University of California
Santa Barbara

Scattering studies of correlated metal phases in iridium and ruthenium oxides

A dissertation submitted in partial satisfaction
of the requirements for the degree

Doctor of Philosophy
in
Physics

by

Zach Porter

Committee in charge:

Professor Stephen D. Wilson, Co-Chair
Professor Andrea F. Young, Co-Chair
Professor Leon Balents

June 2022

The Dissertation of Zach Porter is approved.

Professor Leon Balents

Professor Andrea F. Young, Committee Co-Chair

Professor Stephen D. Wilson, Committee Co-Chair

June 2022

Scattering studies of correlated metal phases in iridium and ruthenium oxides

Zach Porter

still the question sings like saturn's rings

maybe she knows what she won't tell

—Adrianne Lenker

Acknowledgements

I am so grateful to all the people who have helped me along the way in my physics research. I want to start by thanking my advisor Prof. Stephen Wilson who is the one person most responsible for where I am today. Thank you Stephen for your patience and guidance in developing my skills and in supporting me over the years. I appreciate your willingness to pick up your phone at all hours to help me troubleshoot my X-ray or neutron issues. You encouraged me to take big risks that sometimes paid off. Thanks also to Profs. Andrea Young and Leon Balents for serving on my committee and helping hone my written and oral science communication. All three professors, especially Stephen, were instrumental in shaping my graduate projects through grants and collaborations.

Thanks mom and dad for supporting my education and for raising me to be curious, among everything else. I can remember the first time I was dissatisfied with an explanation of how magnets work back in 5^{th} grade. Now that I get most ferromagnets (the ones that stick to the fridge), I've found new magnets to not understand.

I am indebted to a number of incredible mentors over the years. As a high school intern, Prof. Haym Benaroya at Rutgers and his students Sohrob and Tushar were so nurturing to me and encouraged me to shoot for the stars. I'm grateful to Prof. Kyle Shen for being so generous with his time and for being so approachable when he taught my 8am special relativity class. Thanks to Kyle's students Ed, Shouvik, Jacob, Hoafei, Brendan, and Jocienne for their patience and guidance, first in helping me try to design vacuum chambers when I thought I'd be an engineer, and later when I tried to actually learn physics. A huge thank-you to Dr. Apurva Mehta at SLAC National Lab, my summer intern advisor who taught me so much about X-rays and about being a scientist. I cannot say kind enough things about the incomparable Dr. Jacob Ruff at CHESS, he is as talented a mentor as he is a scientist.

I want to thank a great deal of extraordinary people at UCSB who I loved working with. When I was green, Tom, Xiang, Rebecca, Josh, and Ryan got me started and served as great role models. Dr. Julian was a tremendous mentor, built my trusty laser furnace, and instilled me with healthy(?) pessimism. Eli is responsible for my successes in lab more than anyone - it was you who taught me how to write these kinds of equations. I really enjoyed working with all the members of the group, and I want to specifically call out Eli and Julia and Steven and Mitch for their camaraderie. I've had the great pleasure to learn from fabulously smart and kind postdocs: Drs. Paul, Brenden, Juan, Lianyang, and Ganesh. Outside of the group, I need to thank Prof. Ram Seshadri and Drs. Amanda Strom, Rachel Schoeppner, Deryck Stave, Tom Mates, Luca Galletti, Kaveh Ahadi, Collin Holgate, Emily Levin, Sam Teicher, and Ludwig Holleis for taking time to troubleshoot my work with me.

As a national lab user, I had the pleasure to work with some great folks away from UCSB. It was amazing to collaborate with Drs. Ryan Need and Rebecca Dally in their capacities as NCNR employees, thank you both so much and send my best to your cats. Jacob Ruff makes every time at CHESS my favorite. I was grateful to work closely with Zahir Islam, Mary Upton, Yong Choi, and Daniel Haskel at the APS at Argonne. Sasha Kolesnikov and Adam Aczel and Huibo Cao at Oak Ridge National Lab, and Jeff Lynn and Yang Zhao and Zhijun Xu at the NCNR, were each great to learn from. Thanks to the many staff members and engineers I'm neglecting to mention.

My time in grad school was made so much more fun and special by my friends in and around the physics program. My big family is fantastic, thanks for your love and support. Ilana is the best twin ever hands-down, thank you for teaching me core level spectroscopy. Last but not least, Emilie pulled me through. Thank you for letting me be the moon you shine.

Curriculum Vitæ

Zach Porter

Education

2022	Ph.D. in Physics (Expected), University of California, Santa Barbara
2019	M.A. in Physics, University of California, Santa Barbara
2015	B.S. in Engineering Physics, Cornell University

Publications

19. **Z. Porter**, P.M. Sarte, T. Petersen, M.H. Upton, L. Hozoi, and S.D. Wilson. "Spin-orbit excitons and electronic configuration of the $5d^4$ insulator $Sr_3Ir_2O_7F_2$."
Submitted manuscript (2022). [arxiv.org/abs/2206.04721v1]

18. **Z. Porter**, E. Zoghlin, J.L. Schmehr, and S.D. Wilson. "Crystal growth of $Sr_2Ir_xRu_{1-x}O_4$ for $x \leq 0.4$."
Journal of Crystal Growth (2022). [doi.org/10.1016/j.jcrysgro.2021.126432]

17. H. Zhao, **Z. Porter**, X. Chen, S.D. Wilson, Z. Wang, and I. Zeljkovic. "Imaging antiferromagnetic domain fluctuations and the effect of atomic-scale disorder in a doped spin-orbit Mott insulator."
Science Advances (2021). [doi.org/10.1126/sciadv.abi6468]

16. G. Ahn, J.L. Schmehr, **Z. Porter**, S.D. Wilson, and S.J. Moon. "Doping and temperature evolutions of optical response of $Sr_3(Ir_{1-x}Ru_x)_2O_7$."
Scientific Reports (2020). [doi.org/10.1038/s41598-020-79263-5]

15. K.L. Seyler, A. de la Torre, **Z. Porter**, E. Zoghlin, R. Polski, M. Nguyen, S. Nadj-Perge, S.D. Wilson, and D. Hsieh. "Spin-orbit-enhanced magnetic surface second-harmonic generation in Sr_2IrO_4."
Physical Review B (2020). [doi.org/10.1103/PhysRevB.102.201113]

14. E. Zoghlin, **Z. Porter**, S. Britner, S. Husremovic, Y. Choi, D. Haskel, G. Laurita, and S.D. Wilson. "Mapping the structural, magnetic and electronic behaviour of $(Eu_{1-x}Ca_x)_2Ir_2O_7$ across a metal-insulator transition"
Journal of Physics: Condensed Matter (2020).
[doi.org/10.1088/1361-648X/abbf2b]

13. S. Li, E. Drueke, **Z. Porter**, W. Jin, Z. Lu, D. Smirnov, R. Merlin, S.D. Wilson, K. Sun, and L. Zhao. "Symmetry-resolved two-magnon excitations in a spin-orbit-coupled bilayer antiferromagnet."
Physical Review Letters (2020). [doi.org/10.1103/PhysRevLett.125.087202]

12. **Z. Porter**, R.F. Need, K. Ahadi, Y. Zhao, Z. Xu, B.J. Kirby, J.W. Lynn, S. Stemmer, and S.D. Wilson. "Correlating magnetic structure and magnetotransport in semimetal thin films of $Eu_{1x}Sm_xTiO_3$."
Physical Review Materials (2020). [doi.org/10.1103/PhysRevMaterials.4.054411]

11. H. Zhao, S. Manna, **Z. Porter**, X. Chen, A. Uzdejczyk, J. Moodera, Z. Wang, S.D. Wilson, I. Zeljkovic. "Atomic-scale fragmentation and collapse of antiferromagnetic order in a doped Mott insulator."
Nature Physics (2019). [doi.org/10.1038/s41567-019-0671-9]

10. **Z. Porter**, E. Zoghlin, S. Britner, S. Husremovic, J. P. C. Ruff, Y. Choi, D. Haskel, G. Laurita, and S.D. Wilson. "Evolution of structure and magnetism across the metal-insulator transition in the pyrochlore iridate $(Nd_{1x}Ca_x)_2Ir_2O_7$."
Physical Review B (2019). [doi.org/10.1103/PhysRevB.100.054409]

9. J.L. Schmehr, T.R. Mion, **Z. Porter**, M. Aling, H. Cao, M.H. Upton, Z. Islam, R.-H. He, R. Sensarma, N. Trivedi, and S.D. Wilson. "Overdamped antiferromagnetic strange metal state in Sr_3IrRuO_7."
Physical Review Letters (2019). [doi.org/10.1103/PhysRevLett.122.157201]

8. J.L. Schmehr, E.A. Zoghlin, **Z. Porter**, X. Wang, W. Tian, J.P.C. Ruff, Z. Islam, and S.D. Wilson. "Preferential quenching of $5d$ antiferromagnetic order in $Sr_3(Ir_{1-x}Mn_x)_2O_7$."
Journal of Physics: Condensed Matter (2019).
[doi.org/10.1088/1361-648X/ab0ef9]

7. W. Jin, S. Li, J. Liu, Q. Han, **Z. Porter**, C. Peterson, J. Schmehr, I. Boulares, K. Sun, R. Merlin, S.D. Wilson, and L. Zhao. "Polarized Raman spectroscopy study of metallic $(Sr_{1-x}La_x)_2Ir_2O_7$: A consistent picture of disorder-interrupted unidirectional charge order"
Physical Review B (2019). [doi.org/10.1103/PhysRevB.99.041109]

6. C. Peterson, M.W. Swift, **Z. Porter**, R.J. Clment, G. Wu, G.H. Ahn, S.J. Moon, B.C. Chakoumakos, J.P.C. Ruff, H. Cao, C. Van de Walle, and S.D. Wilson.
"$Sr_3Ir_2O_7F_2$: topochemical conversion of a relativistic Mott state into a spin-orbit driven band insulator."
Physical Review B (2018). [doi.org/10.1103/PhysRevB.98.155128]

5. M.W. Swift, **Z. Porter**, S.D. Wilson, and C.G. Van de Walle. "Electron doping in $Sr_3Ir_2O_7$: Collapse of band gap and magnetic order"
Physical Review B (2018). [doi.org/10.1103/PhysRevB.98.081106]

4. K. Ahadi, Z. Gui, **Z. Porter**, J.W. Lynn, Z. Xu, S.D. Wilson, A. Janotti, and S. Stemmer. "Carrier density control of magnetism and Berry phases in doped $EuTiO_3$."
APL Materials (2018). [doi.org/10.1063/1.5025317]

3. X. Chen, J.L. Schmehr, Z. Islam, **Z. Porter**, E.A. Zoghlin, K. Finkelstein, J.P.C. Ruff, and S.D. Wilson. "Unidirectional spin density wave state in metallic

$(Sr_{1-x}La_x)_2IrO_4$."
Nature Communications (2018). [doi.org/10.1038/s41467-017-02647-1]

2. Y. Jia, R. Chopdekar, E. Arenholz, Z. Liu, M. Biegalski, **Z. Porter**, A. Mehta, and Y. Takamura. "Thickness dependence of exchange coupling in (111)-oriented perovskite oxide superlattices."
Physical Review B (2016). [doi.org/10.1103/PhysRevB.93.104403]

1. H. Benaroya, S. Mottaghi, and **Z. Porter**. "Mg as an ISRU-derived resource for lunar structures."
Journal of Aerospace Engineering (2013).
[doi.org/10.1061/(ASCE)AS.1943-5525.0000235]

Abstract

Scattering studies of correlated metal phases in iridium and ruthenium oxides

by

Zach Porter

In the diverse catalog of 'quantum materials' one of the most beguiling parameters is the spin-orbit coupling. This dissertation is concerned with how spin-orbit coupling effects exotic physics in correlated transition metal oxides. The materials described herein are all assembled from corner-sharing octahedra (Ir,Ru)O_6, and are hole-doped from the d^5 configuration, yet they contain a diversity of electronic and magnetic phases. A combination of resonant X-ray scattering and neutron scattering were employed to try to unravel the nature of the order and fluctuations in these materials.

First we examine the unusual Lifshitz transition in metallic $Sr_2Ir_xRu_{1-x}O_4$, where we unveil a transition from itinerant to local moment behavior that might speak to quantum criticality. Second we explore the closely related compound $Sr_3(Ir_{1-x}Ru_x)_2O_7$, where the antiferromagnetism persists to remarkably high Ru content. Third is $Sr_3Ir_2O_7F_2$, which is like a fully hole-doped and distorted analog to $Sr_3Ir_2O_7$; there the spin-orbit excitons are thoroughly compared to theory. Last is $(Ca_xNd_{1-x})_2Ir_2O_7$, a tunable magnetic semimetal with potential for interesting topological states.

Contents

List of Figures

Chapter 1

Introduction

The Coulomb potential is a basic concept that is key to condensed matter physics. Electrons repel each other with a long-range force that goes as the inverse distance $1/r$. But how do we reconcile this idea with materials that conduct electricity? Metals can host an enormous density of delocalized electrons of up to $\sim 10^{29}/\mathrm{m}^3$. Why doesn't the Coulomb repulsion make *every* delocalized electron in the 'Fermi sea' of a metal stay maximally far apart, forming a 'Wigner' crystal? The boiled-down answer is that positive ions and delocalized electrons screen one another, with the result that electrons only feel Coulomb repulsion at very short distances.[1] The Coulomb potential is most consequential within each electronic orbital, where it generates an energy cost to electrons that hop into a half-filled valence orbital. These 'correlation' effects can be significant enough to cause would-be metals to become electrical insulators, as we will soon explore in some depth.

Correlated electron physics is a subset of a rich body of work on electron localization in condensed matter physics. The broader fundamental question about localization goes: why are some materials insulators when they ought to be metals due to a partially-filled valence band? And conversely, under what conditions do such materials remain metallic? Localization is deeply interconnected with some of the organizing principles of condensed

[1] This result is developed in the Lindhard theory, and the specific concept I am invoking is the Thomas-Fermi screening [1].

matter physics like spontaneous symmetry breaking and emergence.[2]

In the first part of this introductory chapter I provide an overview of localization via electronic correlations. The first work on this idea was in 1937 by Nevill Mott, who was motivated by Rudolph Peierls's remarks on NiO [2]. While the foundations of correlated electron physics were developed in the 20$^{\text{th}}$ century, the sub-topic of strong spin-orbit coupling has risen much more recently. This is an exciting arena for theorists and experimentalists alike, where quantum effects directly inform the rich physics. In the second and third parts of the introduction, I more tightly focus on the intersection of these concepts most relevant to the materials described in later chapters.

1.1 Hubbard Model of Correlated Electrons

The Hubbard model is an important way of describing how electronic correlations can lead to insulating behavior and favor certain kinds of magnetism. This is a simple model that captures rich physics, and is still not completely understood. It was developed by John Hubbard in the 1960s and unifies an understanding of both itinerant ferromagnetism and localized antiferromagnetism that is applicable to many important materials families, including the high-T_c superconductors. This topic is well-established so I draw from textbooks; my favorites on the topic are D.I. Khomskii's *Basic Aspects of the Quantum Theory of Solids* and *Transition Metal Compounds* [3, 4]. I assume the reader has some familiarity with condensed matter physics and with the second quantization formalism of quantum mechanics.

The essential idea of the model is that when electron-electron correlations get to be comparable to the kinetic energy of the valence band, the valence charge carriers (either electrons or holes) tend to localize. Here 'correlations' refers generally to the Coulomb

[2] I thank Prof. Paul McEuen for introducing me to the broad topic of localization in his class and inspiring my interest in these sorts of materials puzzles.

repulsion - the reason we do not come out and state this explicitly is because this energy scale is not intuitively encoded in models.

Now to build up to the Hubbard model. Let us start with the band theory of solids. Consider a simplified tight binding Hamiltonian that only considers one valence orbital per lattice site, $\hat{\mathcal{H}}_{\mathrm{TB}}$. We will consider only the matrix element for arbitrary sites i and j indexed from $1, 2, \ldots, N$ in one dimension:

$$\langle j|\hat{\mathcal{H}}_{\mathrm{TB}}|i\rangle = \epsilon\delta_{i,j} - t\delta_{i,j\pm1} \tag{1.1}$$

Here, ϵ is an all-encompassing self-energy term, and t is the hopping term, which parameterizes the overlap between orbitals and thus the likelihood for an electron to hop from one site to another. The shorthand within the subscripts for the Dirac delta functions indicates that only nearest-neighbor hopping is allowed; sometimes this is denoted as $\langle ij\rangle$. While I only wrote the tight binding Hamiltonian explicitly in one dimension, the form is similar for dimensions d>1. There are several relevant features of the tight binding theory for our purposes. The full bandwidth of the band we are describing is $W \equiv 2zt$, with z the number of nearest neighbors. As long as it is not filled, this valence band describes a metal.

Now let us introduce 'correlations' into the tight binding framework. The correlations are parameterized by $U > 0$, a rough approximation of a repulsive Coulomb energy. This 'Hubbard U' penalizes two electrons occupying the same real-space orbital site i (from Pauli exclusion these necessarily have opposite spin states). Correlations compete with the kinetic energy, which is minimized when the Fermi energy is low − that is, when electrons double occupy an orbital.

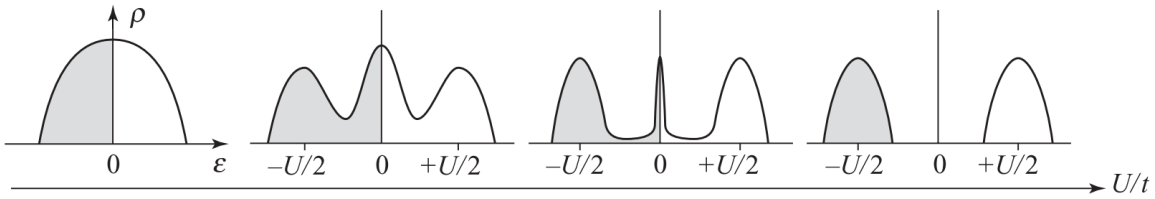

Figure 1.1: Progression of density of states $\rho(\epsilon)$ of a half-filled valence band upon increasing effective correlations U/t. A simple metal turns into a gapped Hubbard insulator. From [4]. Copyright 2014 Daniel I. Khomskii.

The Hubbard interaction $\hat{\mathcal{H}}_{\text{Hubbard}}$ is the last term in the following Hamiltonian:

$$\begin{aligned}\hat{\mathcal{H}} &= \hat{\mathcal{H}}_{\text{TB}} + U\sum_i n_{i,\uparrow}n_{i,\downarrow} \\ &= -t\sum_{\langle ij\rangle,\sigma} c^\dagger_{i,\sigma}c_{j,\sigma} + \sum_i \epsilon + U\sum_i n_{i,\uparrow}n_{i,\downarrow}\end{aligned} \tag{1.2}$$

where these equations are in the second-quantization form, with creation(annihilation) operators $c^\dagger(c)$ that explicitly account for the z projection of the spin operator indexed by σ. Recall that the number operator is defined as $n_{i,\sigma} \equiv c^\dagger_{i,\sigma}c_{i,\sigma}$ and can be 0 or 1.

In this Hamiltonian there are two consequential parameters: the relative interaction strength U/t, and the band filling $n \equiv N/N_{\text{sites}}$ with N either the number of electrons N_e or holes N_h such that n=1 describes a half-filled band. Whenever $U/t \ll 1$ we are in the weakly-correlated regime where the Fermi-liquid picture is valid in d=3. However, when $U/t \gg 1$, we are in the strongly-correlated regime. If we consider the scenario with half-filling (n=1), it costs energy U in order to hop because this necessitates an electron doubly-occupying an orbital. When this energy cost outweighs the hopping energy gain, the correlations open a gap in the excitation spectrum and we find a Mott-Hubbard insulator.[3]

[3]Physicists generically call any insulating phase related to correlation effects a Mott insulator. Calling something a Mott-Hubbard insulator is invoking only the transition metal ions' bands as the starting point [2]. Another Mott insulator is the charge-transfer insulator, a model that directly accounts for hybridized ligand bands.

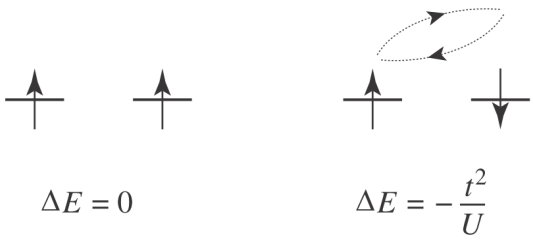

Figure 1.2: In the Hubbard model, due to second-order perturbations, antiferromagnetic couplings are favored over ferromagnetic ones at half-filling. From [4]. Copyright 2014 Daniel I. Khomskii.

Now we may ask, how do the spins align for these fully localized electrons? If electrons cannot hop, they still can make a virtual hop to a neighboring site in the second-order perturbation theory. On a square lattice, close to n=1, such a virtual hop can only happen for anti-aligned spins, in keeping with the Pauli exclusion principle. This virtual hop can be treated as a second-order perturbation of the tight-binding Hamiltonian on the Hubbard Hamiltonian:

$$\begin{aligned} \hat{\mathcal{H}}_{\text{eff}}(\text{square}, n{=}1) &= \hat{\mathcal{H}}_{\text{TB}} \frac{1}{E_0 - \hat{\mathcal{H}}_{\text{Hubbard}}} \hat{\mathcal{H}}_{\text{TB}} \\ \ldots &= \frac{2t^2}{U} \sum_{\langle ij \rangle} \mathbf{S}_i \cdot \mathbf{S}_j + \text{constants} \end{aligned} \tag{1.3}$$

where the result after simplification on the second line is the Heisenberg spin Hamiltonian, which is minimized when the dot product between neighboring spin operators $\mathbf{S}_i \cdot \mathbf{S}_j = -1$. The energy gain from anti-aligned spins compared to aligned spins is $2t^2/U = J$, where J is the exchange interaction.[4] So the antiferromagnetic (AFM) state (in this lattice realization and many others) is often the magnetic ground state in the Mott-Hubbard

[4]This was actually recognized by the legendary P.W. Anderson in 1950, a year after his Ph.D. in molecular physics [5]. Anderson is one of the giants of this field; in 1952 he introduced the revelatory idea of spontaneous symmetry breaking in an article about the quantum nature of antiferromagnetism [6]. I only reference his early work because it was uncharacteristically straightforward. As the theorist Anatoly Larkin said, "God speaks to us through Phil Anderson. The only mystery is why He chose a vessel that is so difficult to understand."

insulating phase! Since the couplings are set by the correlations, the Néel transition temperature from paramagnet to AFM can be very large $T_N \sim t^2/U$. This energy scale is often in the 10s of meV or equivalently 100s of K (e.g. for cuprates), which can be much larger than the uncorrelated spin couplings ∼meV.

1.1.1 Spin and Charge Excitations

The lowest-energy pure spin excitations in an antiferromagnetic state are magnons. Without belaboring the derivation, the familiar result for the dispersion $\omega(k)$ along one direction is $\hbar\omega = 4JS|\sin ka|$ where the crystal momentum $k = |\mathbf{k}|$ along that direction, a is the lattice constant, J is the coupling (here $= 2t^2/U$), and S is the spin quantum number we are considering. Note that near $k = 0$, the dispersion is nearly linear in k. Quantum-mechanical derivations invoke the Bogolyubov transformation [4].

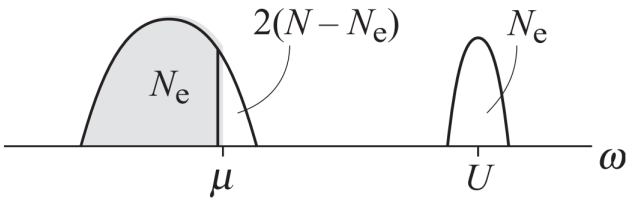

Figure 1.3: Spectral weight transfer in the Hubbard model. The density of states in the LHB and UHB as a function of single-particle energy ω is plotted at arbitrary chemical potential μ. From [4]. Copyright 2014 Daniel I. Khomskii.

What about the low-energy charge excitations? For strong electronic correlations $U/t \gg 1$, the charge gap comes from the interaction between electrons. This Mott-Hubbard insulator ground state has totally different physics from a band insulator. One huge difference is that the Lower and Upper Hubbard Bands (LHB and UHB) are not ordinary bands: when we add electrons, the number of states in each sub-band changes! In normal bands, the total number of states is $2N$. However the LHB has $2N - N_{el}$ states and the UHB has N_{el} states. The consequence of this 'spectral weight transfer' is that it

is difficult to isolate one low-energy excitation from another, because states with a broad range of energies $\sim U$ are admixed.

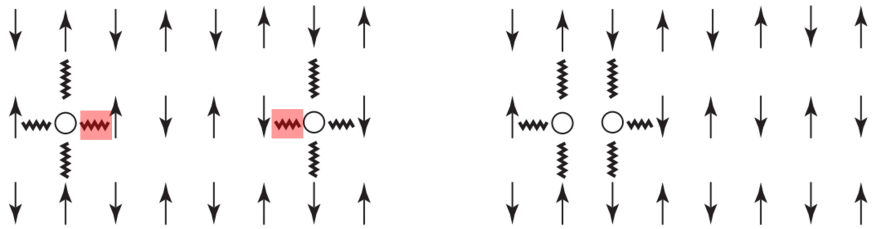

Figure 1.4: Electronic phase separation in Mott antiferromagnets. When doped carriers neighbor each other, it disturbs the antiferromagnetism less by breaking fewer magnetic couplings (squiggly lines). Here, vacancies indicated by circles are shown in a sea of spin-1/2 electron sites on the square lattice. In (a) there are 2 more broken couplings (red) than in (b). From [4]. Copyright 2014 Daniel I. Khomskii.

How do we even describe the charge carriers in the Mott-Hubbard insulator? It is complicated. We can first try to think about how *additional* holes and electrons move in the insulating AFM background. These carriers' motion is strongly hindered by the anti-aligned spins. A mean-field solution yields that the bands become narrower by a factor of $\sqrt{\frac{1}{4} - S^2}$ with $S{=}|\langle|S_i^z|\rangle|$ the sublattice magnetization (slightly less than 1/2 due to quantum fluctuations). A related consequence is that there is generally electronic phase separation in Mott-Hubbard systems. From the magnetic Hamiltonian, it is energetically favorable to have neighboring charge carriers - see Fig. 1.4.

What about the motion of existing charge carriers? This answer is more fascinating. When we start to propagate one electron, we do two things: doubly occupy a site and reverse a pair of spins. It is best in theoretical considerations to deconstruct this process into two quasiparticles: a holon or a doublon (that is, a vacancy or a doubly occupied single site, which carries only charge and no spin) and a separate spinon (which carries no charge). This is called 'spin-charge separation.'

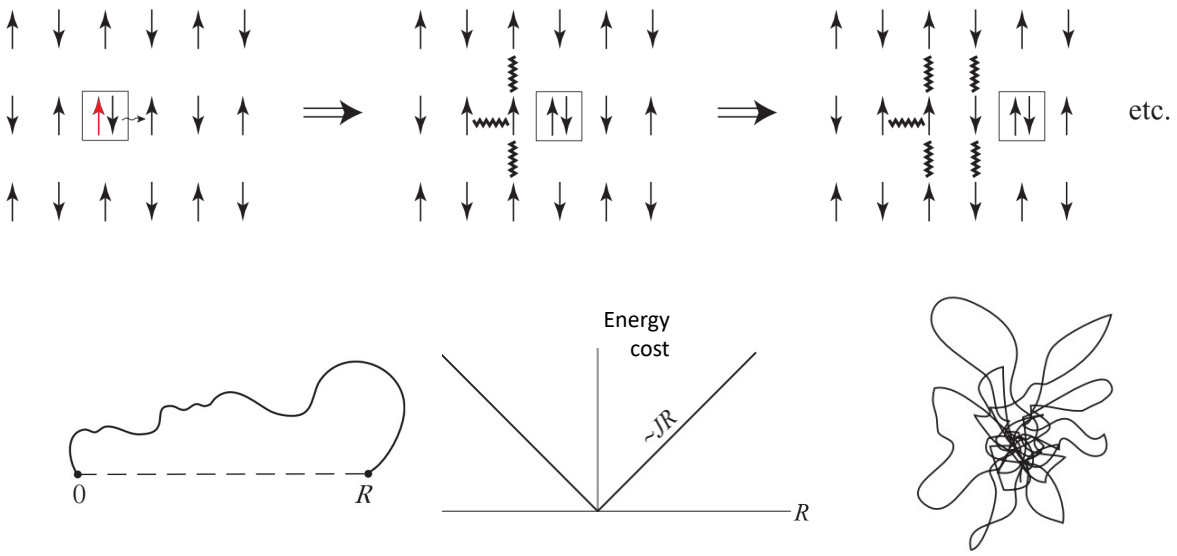

Figure 1.5: Charge excitations in a Mott antiferromagnetic background. *Top panel*: an extra electron (red arrow) causes a doubly-occupied site (or 'doublon', boxed). Each time the charge carrier hops, it disturbs the antiferromagnetism by breaking magnetic couplings, costing $\sim J$ (squiggly lines). *Bottom panel*: since the energy cost of a charge carrier scales with distance R, and couplings can be 'repaired' by backtracking, there is effectively a restoring force that confines the excitations. See the more complete description in the text, and note the same physics applies to a vacancy ('holons'). From [4]. Copyright 2014 Daniel I. Khomskii.

When a doublon propagates, it creates a 'tail' of spins that are aligned with their neighbors in d= 2 or 3, which strongly distorts the AFM background. Each hop has an energy cost $(z-2)J = 4t^2/U$ on the square lattice. Thus as it propagates, a doublon (or a holon) costs more and more energy, which goes as $\sim J\cdot(\text{radius})^{(\geq 1)}$ from the initial position. This acts like a restoring force, which causes wandering charge carriers to be confined, like a magnetic version of polarons. This picture offers a possible (unconfirmed) pairing mechanism for copper-oxide-based superconductors! One holon moving in an AFM background leaves a tail of misaligned spins and becomes localized. But a second holon can move after the first, repairing its damage. So pairs of carriers could reduce the overall kinetic energy of the system, and these attractively paired carriers could move freely, the ingredients for a Cooper pair.

1.1.2 Stoner Instability

Let us return to our consideration of correlated magnetism more generally, beyond the strongly-correlated regime. What kinds of magnetic order might we expect for correlated metals, of the type depicted in the middle panels of Fig. 1.1 where there is density of states peaked both at the Fermi level E_F and at $E_F \pm U/2$?

Consider a scenario where there are a fixed number $0<n<2$ of electrons (or holes) in the Lower Hubbard Band. From mean field theory [7], we can approximate the expectation value of the Hubbard energy as: $E_{\text{Hubbard}} = \langle \hat{\mathcal{H}}_{\text{Hubbard}} \rangle \approx \sum_{i=1}^{n} \frac{1}{4} U(n^2 - (Mv/\mu_{\text{B}})^2)$, where M is the magnetization per unit cell volume v, and each electron carries a magnetic moment of one Bohr magneton μ_{B}. If we consider a system at zero temperature with $\delta\epsilon$ more up-states occupied than down-states, we can approximate the magnetization as $M/\mu_{\text{B}} = -g(E_F)\delta\epsilon/2$ given the density of states g at the Fermi energy E_F, and find that the change in the kinetic energy for this magnetization is $M^2/(2g(E_F)\mu_{\text{B}}^2)$. Thus the change in the total energy per unit volume of the system due to finite magnetization is: $E_{\text{tot}} - E_{\text{tot}}(M{=}0) = \left(\frac{M}{\mu_B}\right)^2 \left[\frac{1}{2g(E_F)} - \frac{vU}{4}\right]$. This means that if:

$$U > \frac{2}{g(E_F)v} \tag{1.4}$$

then the total energy of the interacting electron system is minimized by having a finite magnetization. This relation is known as the Stoner criterion, and it is the reason why having a large density of states at E_F often leads to magnetism (the so-called Stoner instability) [4, 7]. In the case that there are correlations but they are too weak to open a charge gap, the magnetic ground state is most often an itinerant ferromagnet.

Reconsider the $n{=}1$ strongly-correlated system with its antiferromagnetism. As we move away from a perfectly half-filled band and introduce the possibility of hopping, the magnetic ground states can face very fierce competition. Clearly, the Hubbard model

explains a diverse array of interacting electron systems with magnetic order.

1.1.3 Metal-Insulator Transitions

The Mott insulator phase and adjacent metallic phases exhibit strong fluctuations of spin, charge, and/or orbital degrees of freedom. These competing fluctuations have interesting consequences, as developed in Section 1.1.1. Now we talk about the role of these fluctuations in mediating metal-insulator transitions (MITs).

From a theoretical perspective, there are two categories of approaches from a metal to a Mott insulator [2]. One category of MIT is called 'carrier vanishing' and it happens if a degree of freedom is spontaneously broken. The other category is called 'effective mass diverging' and occurs in the absence of spontaneously broken symmetries. Since the number of carriers remains constant, consequently the mass must diverge according to the Luttinger theorem, because U is considered to be an adiabatic perturbation on the Fermi liquid theory.

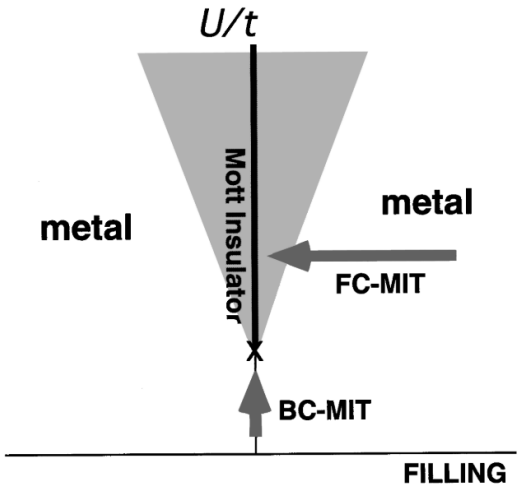

Figure 1.6: Metal-insulator phase diagram based on the Hubbard model. Bandwidth control (BC) is mediated by tuning U/t (vertical axis). Filling control (FC) involves tuning the chemical potential towards half-filling (horizontal axis). From [2]. Copyright 1998 American Physical Society.

There are two tunable parameters in the Hubbard model, and therefore two discrete ways to mediate a Hubbard MIT; see Fig. 1.6. The first is bandwidth control (BC) which involves modifying the bonding environment, and the second is filling control (FC) via carrier doping. BC transitions are often 1st order because the hopping t is discontinuous in the presence of a discrete lattice change. But in the Hubbard theory at half-filling, FC transitions are expected to be continuous (2nd order) barring a charge density wave instability.

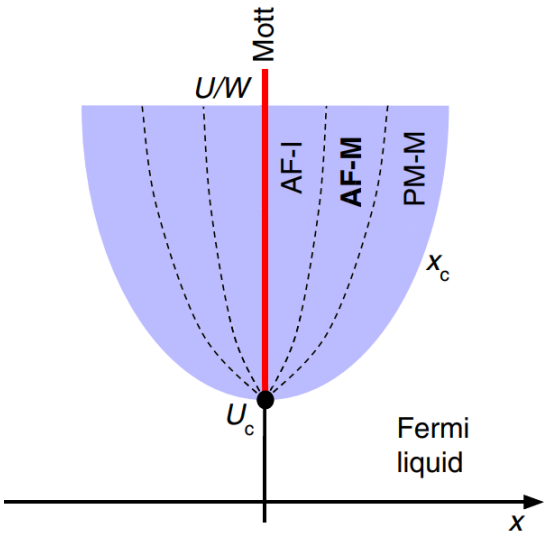

Figure 1.7: Mott phase diagram when bandwidth control mediates a 1st order metal-insulator transition. This depicts a 3-dimensional system with percolation threshold near 1/3 of the critical filling x_c. The abbreviations are paramagnetic (PM), antiferromagnet (AF), metal (M), and insulator (I). Dashed lines indicate phase coexistence. From [8]. Copyright 2015 American Physical Society.

Yet in practice, many Mott insulator phases can survive very far away from half-filling, which is incongruous with this treatment of FC transitions. One instructive theory shows that, in the presence of a 1st order BC transition, the FC transition becomes percolative [8]. Consider a correlated material with filling $x = n-1$ which is less than some critical amount $x < x_c$ that yields perfect metallic behavior. In this doping range, thermodynamics forbids charge densities less than x_c, which yields spatially separated

but coexisting insulating puddles with x=0 and metal puddles with x=x_c. While Fig. 1.4 showed electronic phase separation in the insulating antiferromagnetic phase, this theory extends phase separation to global metals, which have filling that exceeds the percolation threshold.

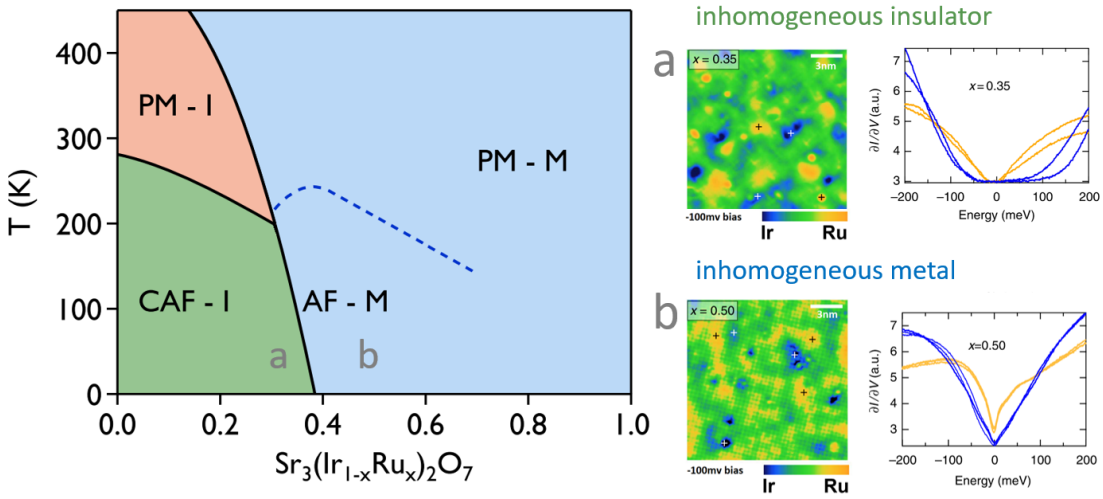

Figure 1.8: The electronic phase diagram for $Sr_3(Ir_{1-x}Ru_x)_2O_7$ on the left; C stands for canted, and the other abbreviations are common to Fig. 1.7. The panels marked (a) are scanning tunneling microscopy and spectroscopy in the global insulating phase, indicating nanoscale regions that are insulating (blue) and conductive (yellow). $\partial I/\partial V$ is an experimental proxy of the density of states. The panels marked (b) show similar inhomogeneity in the global metal phase. Adapted from [9, 10].

There are many experimental examples of electronic phase coexistence in Mott systems, so here is one that is specifically instructive to this dissertation. In $Sr_3(Ir_{1-x}Ru_x)_2O_7$, percolative nanoscale clusters are visible via scanning tunneling microscopy studies [9]. In the globally insulating phase, there are locally metallic clusters embedded within. And even across the percolation threshold in the global metal, there are puddles with markedly reduced density of states near the chemical potential (i.e. more localized character). Magnetic phase coexistence occurs in this system farther from half-filling, which is a central idea in Chapter 4.

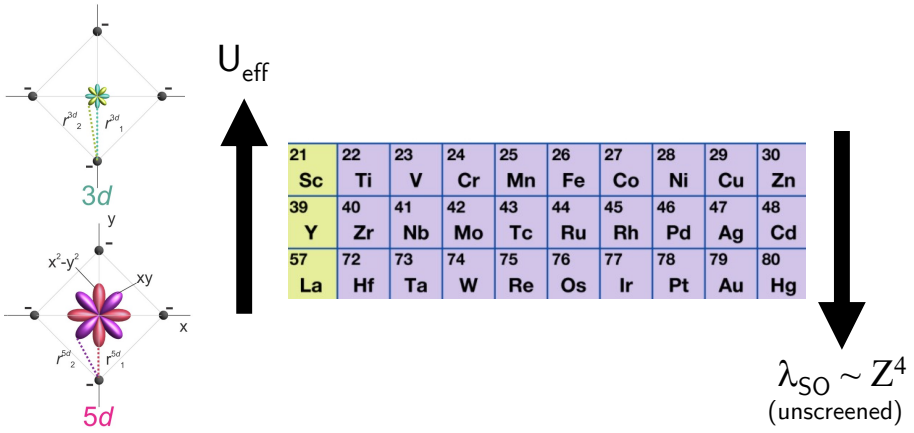

Figure 1.9: Mott insulators are not expected for large $5d$ ions due to the correspondingly large bandwidth which diminishes the effective correlation strength $U_{\text{eff}} = U/W$. However, large spin-orbit coupling for $5d$ elements is responsible for Mott physics.

1.2 Spin-Orbit-Coupled Mott Physics

At first pass, the above picture of Mott physics does not seem to describe the iridates and other $5d$ ions at half-filling. The $5d$ ions have large bandwidth W because they are quite extended compared to $3d$ and $4d$ ions. As a consequence, one might expect metallicity due to the small effective Hubbard U when the bandwidth is taken into account $U_{\text{eff}} = U/W$.

What is missing from this consideration is the effect of spin-orbit coupling (SOC). SOC is parameterized by λ in $\hat{\mathcal{H}}_{SOC} = \lambda \hat{l} \cdot \hat{s}$, and scales with atomic number [5]. While λ is negligible for $3d$ systems, it is as large as 0.5 eV for the iridates, which is comparable to the correlation strength. Interestingly, SOC seems to cooperate with correlations in opening a charge gap [11]. SOC removes degeneracies and narrows bands, which enhances the effective correlation strength. And conversely, correlations act to localize electrons, which can enhance SOC.

[5] The unscreened ionic value of SOC goes as atomic number to the fourth power $\lambda \propto Z^4$, however screening reduces this effect. Empirically the relation seems closer to Z^2.

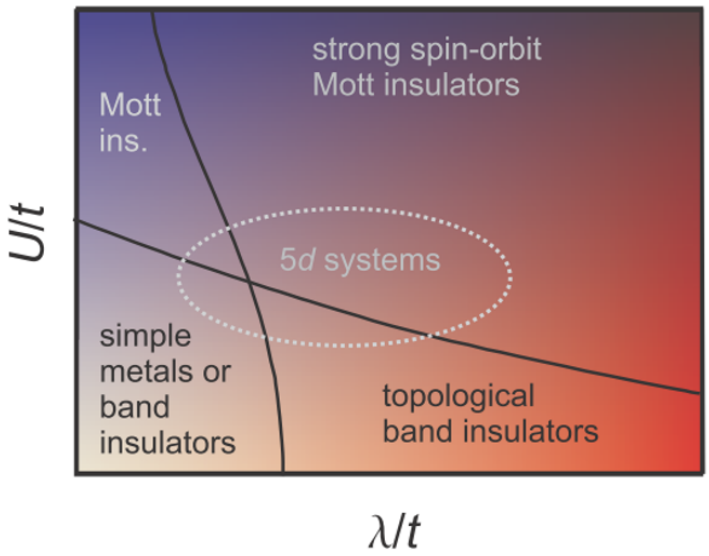

Figure 1.10: Spin-orbit-coupled Mott phase diagram. Effective correlations (y axis) and SOC (x axis) are cooperative, increasing the phase space for unusual insulating phases (top right). Lines are not phase boundaries, just limits for regimes. From [12], adapted from [11].

While much of the focus of this subfield is on Mott insulators, strong SOC also has fascinating consequences for correlated metallic phases. Reconsider the picture of charge excitations in an antiferromagnetic background depicted in Fig. 1.5. SOC allows spins to flip as charges hop, with an energy cost that decreases with SOC strength. So SOC has the consequence that antiferromagnetic order is easier to preserve in the presence of charge excitations, enabling antiferromagnetic order to persist deep into metallic phases. We explore the consequences of this in Chapter 4.

In the following section, we will explore some of the physics that results from this unusual route to insulating behavior. In particular, we will discuss the enigmatic J_{eff}=1/2 electronic ground state and its magnetism. These ideas are the crux of this dissertation.

1.2.1 J_{eff}=1/2 State

For $5t_{2g}^5$ electronic configurations (e.g. arrangements of $Ir^{4+}O_6$ octahedra), the strong SOC completely removes the t_{2g} orbital degeneracy. This idealized picture is known as the J_{eff}=1/2 electronic state. In this state, the entanglement of spin and orbital quantum states is responsible for a slew of exotic phase phenomena.

Let us first briefly review the quantum states for the t_{2g}^5 configuration in the presence of a strong octahedral crystal field. For what follows it is helpful to simply consider the effective hole rather than the 5 electrons. Here, the effective angular momentum $\hat{L}$=1 states for this hole (which is spin-1/2) are linear combinations of $|xy\rangle$, $|xz\rangle$, and $|yz\rangle$ orbitals: $|L_z = 0\rangle = |xy\rangle$,$|L_z = \pm 1\rangle = -\frac{1}{\sqrt{2}}(i|xz\rangle \pm |yz\rangle)$. Now if we consider the total angular momentum operator $\hat{J}$ and the hole spin operator $\hat{S}$, we'll note $\hat{J} = \hat{S} + \hat{L}$. [6] In what follows our Hilbert space is written in the $|L_z\rangle \otimes |S_z\rangle \equiv |L_z, S_z\rangle$ basis. If we account for SOC λ and a tetragonal splitting Δ,then the single ion Hamiltonian is $\hat{\mathcal{H}}_0 = \lambda \hat{L} \cdot \hat{S} + \Delta L_z^2$

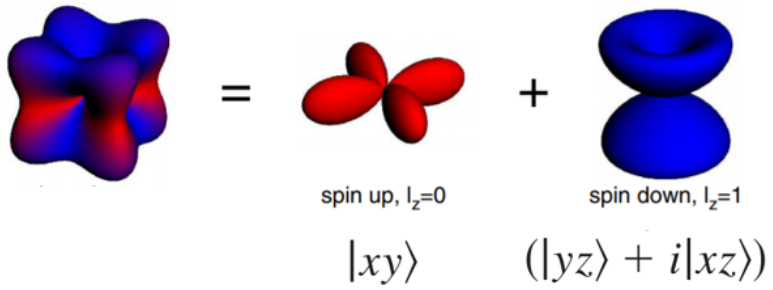

Figure 1.11: The $|\tilde{\uparrow}\rangle$ pseudospin state. It is a linear combination of the t_{2g} orbitals. Shown without tetragonal distortions, it is roughly isotropic. From [13]. Copyright 2009 American Physical Society.

From Kramers Theorem, we know that an odd number of electrons (or in this case,

[6] This is NOT generic for two reasons. First is the "T-P" correspondence [3]: compared to the p orbital manifold, $\hat{l}$ for the t_{2g} manifold has the opposite sign. Sometimes the form $\hat{L}_{\text{eff}} = -\hat{L}$ is used. Second, there is yet another minus sign from spin-orbit coupling: the J_{eff}=1/2 state comes from the J=5/2 manifold, so this minus sign comes from Hund's rules acting upon these states.

one hole) is two-fold-degenerate in the absence of a magnetic field [7]. The resultant Kramers doublet can be viewed in isolation as having an effective spin-1/2 state. But this Hamiltonian $\hat{\mathcal{H}}_0$ is a very different starting point than the conventional one invoked by Hund's rules, because here the stronger SOC term entangles spin and orbital states. The lowest energy levels of this Hamiltonian are a Kramers doublet of 'pseudospin' states: $|\tilde{\uparrow}\rangle = \sin\theta|0,\uparrow\rangle - \cos\theta|+1,\downarrow\rangle$, and $|\tilde{\downarrow}\rangle = \sin\theta|0,\downarrow\rangle - \cos\theta|-1,\uparrow\rangle$. Here, the unitless parameter θ parameterizes the tetragonal splitting via $\tan 2\theta = \frac{2\sqrt{2}\lambda}{\lambda - 2\Delta}$. Even in the presence of small tetragonal distortions, the J_{eff}=1/2 state still is applicable; the SOC trades the Jahn-Teller effect for the entanglement of spin and orbital states [11, 14].

The spin-orbit narrowed J_{eff}=1/2 band is especially susceptible to splitting via correlation effects into Lower and Upper Hubbard bands. The resultant insulating state is generally referred to as the 'spin-orbit-assisted Mott insulator,' though the applicability of the word Mott is strongly debated.

This J_{eff}=1/2 insulting state was first reported in Sr_2IrO_4 in 2008 [15]. Unlike the isostructural 4*d* compound Sr_2RhO_4 which is a paramagnetic metal, Sr_2IrO_4 is instead small-bandgap insulator with canted antiferromagnetism. The initial experimental evidence of this ground state comes from three papers by B.J. Kim and coworkers, Refs. 15–17. I will summarize the evidence in order of clarity:

1. *Band Structure*: The electronic levels for Sr_2IrO_4 can only be justified with SOC. The evidence of the rearrangement of the valence level dispersion (compared to Sr_2RhO_4) and of the circular Fermi surface sheets come from angle-resolved photoemission (ARPES) [15]. The narrow UHB was measured with optical conductivity [15].

2. *Resonant X-ray Diffraction*: Some quantum numbers can be directly probed with resonant scattering. In particular, the Ir L_2-edge can be shown to have perfect

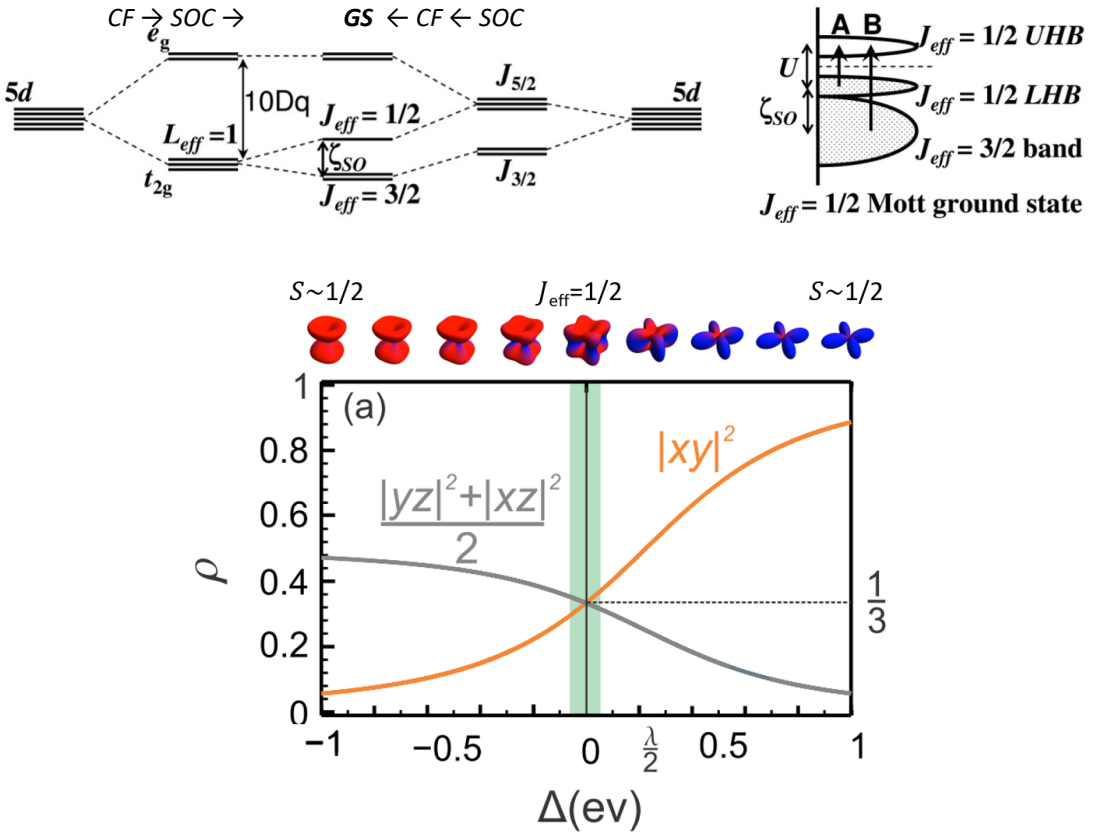

Figure 1.12: *Top panels*: Single-ion energy levels and density-of-states cartoon for the J_{eff}=1/2 spin-orbit-assisted Mott insulator. The ground state (GS) can be achieved starting with either crystal field (CF) or SOC splitting. Transitions 'A' and 'B' have been measured with optical reflectivity; spin-orbit excitons are not shown. *Bottom panel*: Insensitivity of J_{eff}=1/2 state to small tetragonal (or trigonal) distortions Δ. In the ideal case, each of the three t_{2g} orbitals has equal occupation ρ but differing phases. At very large distortions a simple **S**=1/2 state occurs. From [15] and [14] respectively. Copyright American Physical Society.

destructive interference in the ideal J_{eff}=1/2 case [16]. These ideas will be described in Section 2.1.3.

3. *Quantum Numbers via Absorption Spectroscopies*: From the X-ray selection rules $\Delta J = -1, 0, +1$, we can learn about the relative filling of the different J manifolds and also the ratio of L_z/S_z, and match these to predictions. Please see Section

6.4.2 for a detailed explanation.

4. *Spin-Orbit Excitons*: Spin-orbit coupling yields local, bound excitations with mixed spin and orbital character at the SOC energy scale λ. For the J_{eff}=1/2 state the excitations are to a J_{eff}=3/2 band not indicated in level schematics in Fig. 1.12. These excitons are optically forbidden [17]. See Sections 4.4.3 and 5.4 for examples.

5. *Unconventional Magnetic States*: For example, Sr_2IrO_4 has an anomalously large ferromagnetic signal that puzzled researchers for more than a decade. Please see the next Section 1.2.2 for an explanation and extension to other compounds.

6. *Unquenched Orbital Momentum*: For the typical $\mathcal{O}_h$ (octahedral) t_{2g} levels, weak Jahn-Teller distortion in real materials should quench the L_z quantum number. Instead, the J_{eff} levels retain finite L_z. This is measurable in the significantly reduced net moment size via bulk magnetization [18], neutron diffraction [19], and X-ray magnetic circular dichroism [20]. I will note that other effects contribute to the weak moment size, so this piece of evidence is no smoking gun.

The J_{eff}=1/2 state is a somewhat idealized case. It only holds when distortions to the octahedral crystal field symmetry are weak. Additionally, there are several mechanisms of hybridization in real materials that may yield deviations:

1. *Covalency*: In materials with high connectivity, such as the edge-sharing rutile compound IrO_2, covalency with oxygen yields p–d hybridization and results in physics akin to charge-transfer insulators [21].

2. *Dimerization*: Similar to the above point, strong hybridization among isolated iridium-oxygen clusters has been shown to lead to dimerization (e.g. $Ba_3CeIr_2O_9$, with Ir_2O_9 bi-octahedra [22, 23]).

3. *Valence Hybridization*: Substantial itinerancy (hopping) can perhaps yield hybridization between the J_{eff}=1/2 and J_{eff}=3/2 states [24].

4. e_g *Hybridization*: Strong spin-orbit coupling may not be a simple perturbation to the valence bands – it ought to additionally hybridize the e_g manifold with the J_{eff}=3/2 manifold [25]. In a model with realistic parameters for Sr_2IrO_4 (J_H=0.1 eV, λ=0.5 eV) this approach yielded a whopping 0.2 electrons in the e_g manifold, with serious ramifications for the electronic properties. For example, the spin quantum number increases from 0.5 to 0.7 with the above parameters.

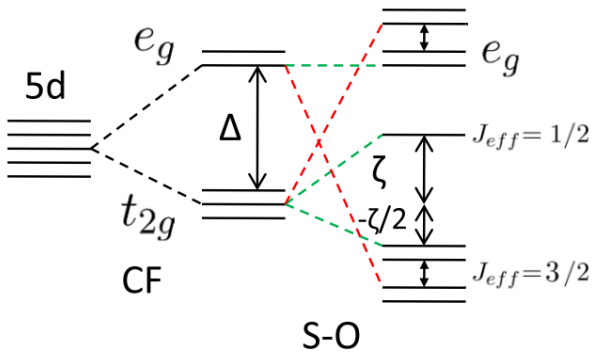

Figure 1.13: When sufficiently strong, spin-orbit-coupling (here ζ) hybridizes the e_g and J_{eff}=3/2 manifolds (red lines). From [25]. Copyright 2018 American Physical Society.

1.2.2 Magnetism and the Quantum Compass Model

In 3*d* ions, the spins are weakly coupled to the lattice, and the phenomenological Goodenough-Kanamori rules broadly describe superexchange[7] interactions [7]. In the strong SOC limit neither of these ideas hold. For the J_{eff}=1/2 state, the spin state is

[7]Superexchange is shorthand for a magnetic coupling across a ligand. In transition metal oxides, often the transition metal ion orbitals overlap strongly with ligands, making superexchange dominant over the direct exchange.

entangled with the orbital angular momentum, so the couplings are explicitly dependent on bonding geometry [13]. Next we will consider different lattice geometries for ions with pseudospin-1/2 states bonded across ligands: TM-O-TM where TM is a transition metal. The following all assumes the idealized J_{eff}=1/2 state with perfect octahedral symmetry ($\Delta = 0$).

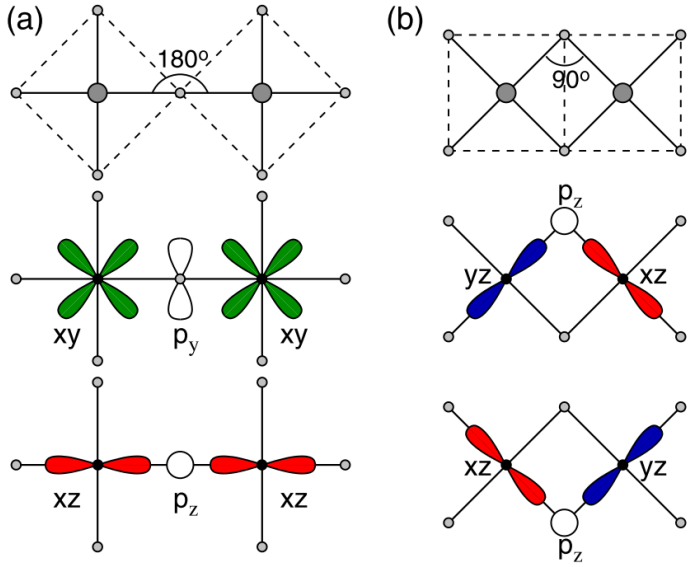

Figure 1.14: Bond-dependent exchange interactions for transition metal ions (big gray circles) with t_{2g} valence orbitals bonded across oxygen ions (little gray circles). These limiting cases are the (a) corner- and (b) edge-sharing bonding geometries. From [13]. Copyright 2009 American Physical Society.

1.2.2.1 Perfect Corner-Sharing

In a 180° bond, seen in corner-sharing octahedra Fig. 1.14a, there is a diagonalized hopping matrix because charges transfer between like t_{2g} orbitals. Unfortunately, the full exchange Hamiltonian necessary to describe this problem is too complicated to consider here; it handles J_H-multiplet splitting in 2$^{\text{nd}}$ order virtual exchange processes. Jackeli and Khaliullin mapped this Hamiltonian in the Kramers basis onto a sum of Heisenberg

and pseudodipolar anisotropic exchange terms:

$$\hat{\mathcal{H}}_{ij} = J_1 \hat{S}_i \cdot \hat{S}_j + J_2 (\hat{S}_i \cdot \mathbf{r}_{ij})(\hat{S}_j \cdot \mathbf{r}_{ij}) \tag{1.5}$$

Note that the operator $\hat{S}_i$ is the spin-1/2 operator for pseudospins, and $\mathbf{r}_{ij}$ is the unit vector along the bond ij. The ratio $J_2/J_1 \sim J_H/U$ due to Hund's splitting, which is typically small, so the Heisenberg term J_1 usually dominates and the pseudodipolar term acts as a perturbation.

This model seems unexotic, in that the isotropic Heisenberg couplings are also found when SOC is weak via the Goodenough-Kanamori rules. But its familiar results derive from entirely different effects. Here, the anisotropic pseudodipolar term comes from the Hund's coupling, whereas for $3d$ ions anisotropy often comes from the SOC.

1.2.2.2 Perfect Edge-Sharing

In a 90° bond, seen in edge-sharing octahedra Fig. 1.14b, the geometry dictates a non-diagonal hopping matrix where charges may only transfer between one $|xz\rangle$ and one $|yz\rangle$ orbital. The two charge transfer paths between the ions, across the upper and lower oxygens, results in destructive interference for the transfer amplitudes. This yields no isotropic exchange terms in the Hamiltonian:

$$\hat{\mathcal{H}}_{ij} = -K \sum_{\alpha=x,y,z} \sum_{\langle ij \rangle \in \alpha} \hat{S}_i^\alpha \hat{S}_j^\alpha \tag{1.6}$$

Where $\hat{S}_i^\alpha$ is the spin-1/2 operator for the pseudospin component along the α axis, with α perpendicular to the plane of the bond (i.e. the xx exchange $\hat{S}_i^x \hat{S}_j^x$ occurs for ions bonded in the yz-plane).

This is known as the *quantum compass* model, wherein the interaction depends on the

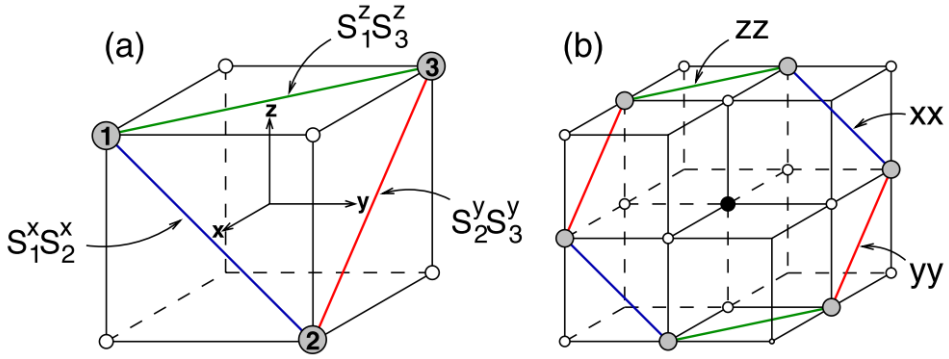

Figure 1.15: The quantum compass model on two corner-sharing bonding geometries. (a) is a triangular lattice and (b) is the honeycomb lattice. From [13]. Copyright 2009 American Physical Society.

bond's spatial orientation. I labeled the exchange interaction as K to allude to the Kitaev Hamiltonian [26]. Kitaev's model may be defined as quantum compass on the honeycomb lattice, shown in Fig. 1.15b. In brief, this model can yield a gapless quantum spin liquid, a phase governed by magnetic frustration and many-body quantum entanglement [27]. The anyonic excitations of this particular flavor of quantum spin liquid have fractional statistics, and may include long-sought topologically-protected Majorana quasiparticles.

In real materials with deviations from perfect 90° bonds, additional Heisenberg and/or pseudodipolar couplings often occur. This leads to exotic low-temperature magnetic orders in materials like $(Na,Li)_2IrO_3$ [28]. At high temperatures these materials' paramagnetic phases seem governed by Kitaev physics [29, 30]. A comprehensive review of these fascinating materials is beyond the scope of this dissertation.

1.2.2.3 Imperfect Corner-Sharing

The coupling between spin and lattice degrees of freedom is a unique consequence of the J_{eff}=1/2 state. In Sr_2IrO_4, the lattice distortions result in spin canting. The combination of a considerable in-plane octahedral tilt of $\alpha = 11°$ and weak Jahn-Teller

elongations gives us the following Hamiltonian:

$$\hat{\mathcal{H}}_{ij} = J\hat{S}_i \cdot \hat{S}_j - D_z\hat{z} \cdot (\hat{S}_i \times \hat{S}_j) + J_z\hat{S}_i^z\hat{S}_j^z \tag{1.7}$$

The third term is a small Ising-like coupling from single-ion anisotropy, and the second is a Dzyaloshinskii-Moriya (DM) interaction. The DM term is what is responsible for the remarkably large ferromagnetic moment $\approx$0.14 μ_B in this canted antiferromagnet with moments oriented in the IrO_2 basal plane. The spin canting angle is set by the ratio $D/J \sim 2\alpha$.

The spin canting angle α was shown to be finely tuned also with the tetragonal distortions, which places this system near a spin-flop transition. The proximity to this spin-flop transition is one reason why the remarkably similar bilayer system $Sr_3Ir_2O_7$ (which has much less oxygen octahedral tilting) has its moments oriented mostly perpendicular to the IrO_2 basal plane.

1.3 Quantum Criticality

Several exotic varieties of quantum critical points (QCPs) have been proposed in the iridates. Some QCPs are developed in the proceeding chapters. Here we will discuss broadly what a QCP is, and then describe just one of the types that may be pertinent to $Sr_2Ir_xRu_{1-x}O_4$ in Chapter 3.

1.3.1 Brief Overview

A QCP is a continuous zero-temperature phase transition [31, 32]. Rather than a typical phase transition driven by thermal fluctuations, a QCP is at T=0 and thus must be driven by quantum fluctuations. The excitement for QCPs comes from their

unconventional excitations and proximity to exotic electronic orders.

The essential ingredient for a QCP is noncommuting competing operators in the microscopic Hamiltonian describing the system; in other words, the ground states away from the QCP have different symmetries. A common example is the Ising model, where the ordered ferromagnetic phase has a $\mathbb{Z}_2$ symmetry not present for the transverse-field-polarized paramagnet.

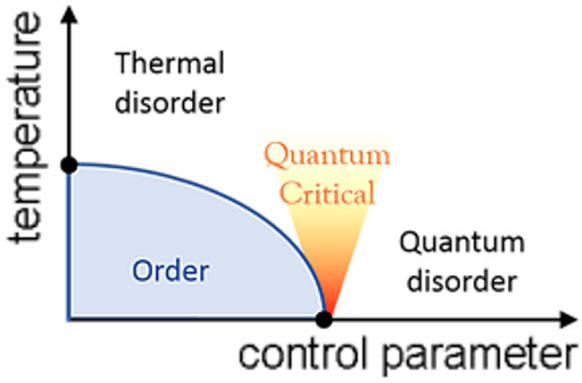

Figure 1.16: A quantum critical point is a zero-temperature phase transition mediated by a parameter like pressure, carrier concentration, or applied field. The quantum critical behavior persists to high temperatures.

This noncommuting operator condition means that, at the QCP, the ground state wavefunction cannot be described by a product state, and is instead a superposition of configurations on all length scales. Counterintuitively, the effects of a QCP are measurable at large temperature scales. This is because the length scale of a wavefunction describing the T=0 QCP is divergently long, but thermal fluctuations act to shorten the length scale that the system can access [33]. Therefore the wavefunction describing the system at finite temperature is effectively quantum critical. Thus the quantum critical regime, where quantum fluctuations with highly entangled degrees of freedom dominate over conventional quasiparticles, can extend over a wide region of phase space.

For metals a QCP yields phase behavior beyond the conventional Fermi liquid theory.

The hallmarks of 'strange metal' physics are linear-in-temperature resistance and poorly defined quasiparticles. Strange metal phases are present in some important materials families including the cuprate, iron-based, and heavy-fermion superconductors [34–37]).

1.3.2 J-freezing Model

The title of this recent theoretical model draws from the idea of angular momentum quenching. In multiorbital materials such as the $3d$ ferromagnets Fe and Ni and Co, the symmetry of the lattice mixes the wave functions with equal contributions of $m_l = \pm 1$ to yield an orbital angular momentum $\langle L_z \rangle \approx 0$. The J-freezing model invokes a similar quenching of local moments under the influence of spin-orbit coupling. Since SOC mixes the spin and orbital quantum states, the moment size here is determined by $\langle J_z \rangle$.

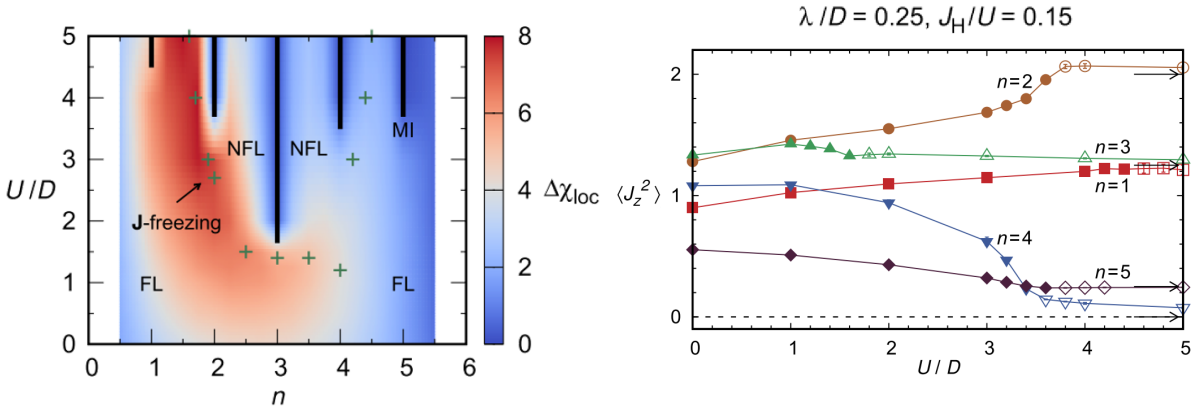

Figure 1.17: On the left is a correlation-filling phase diagram with the effects of spin-orbit coupling included. Plus signs mark J-freezing transitions, where a measure of local fluctuations $\Delta\chi_{\rm loc}$ exhibits a maximum, indicating a transition from an itinerant to a localized phase. Insulating phases are in black. On the right is a more straightforward plot of $\langle J_z^2 \rangle$ at integer fillings. Solid (open) symbols are the metallic (insulating) solutions, and arrows are Hund's rules values. The abbreviations are: D=$W/2$ half-bandwidth, J_H Hund's coupling, U correlations, N/FL Non/Fermi-liquid, MI metal-insulator transition, and n filling in a t_{2g} model. The parameters are the same in both models and are approximate for Sr_2IrO_4. From [38]. Copyright 2017 American Physical Society.

The J-freezing model applies the Hubbard model plus strong SOC to t_{2g} multiorbital

systems [38]. Similar approaches had already shown that multiorbital paramagnets are quite different from single-orbital ones: there is an additional quantum phase transition between a Fermi liquid and an incoherent metallic phase characterized by frozen local moments [39]. A recent study by Aaram Kim and Roser Valentí and coworkers was interested in the dynamical contribution to the local susceptibility $\Delta\chi_{\rm loc}$ as a measure of local fluctuations across a wide range of parameters describing many materials.[8] They found that maxima in $\Delta\chi_{\rm loc}$ indicate a transition from an itinerant to a localized phase, which coincides with a crossover from non-Fermi liquid behavior - i.e. a quantum critical point.

Note in Fig. 1.17 the evolution from n=4 (Ir^{5+} or Ru^{4+}, as in Sr_2RuO_4) to n=5 (Ir^{4+}, as in Sr_2IrO_4). In the model, we learn that itinerant excitations comprise the low-energy magnetic excitations for the highly correlated d^4 ground state, whereas local moment fluctuations dominate as the electron carrier concentration increases and/or as the correlation energy scale decreases. Thus this model is consistent with a mechanism for quantum criticality on carrier-doping compounds like Sr_2RuO_4.

This variety of quantum criticality has been proposed to explain the emergent superconductivity in several compounds including Sr_2RuO_4 and UCoGe [40]. In their normal states, both of these compounds seem to have frozen, itinerant spins. A deeper understanding of this phenomenon may address outstanding issues in the field of unconventional superconductivity. These ideas are perhaps relevant to $Sr_2Ir_xRu_{1-x}O_4$ as discussed in Chapter 3.

[8] This study used a combination of dynamical mean-field theory and the continuous-time quantum Monte Carlo method, applied to the Bethe lattice.

1.4 Chapter Overview

In Chapter 2, we move on to consider scattering methods. After a terse introduction, most of the chapter is devoted to resonant X-ray scattering. Since this is a multi-step process, a full picture of what is measured is complicated. Relevant cross-sections are developed and ultimately pared down with assumptions that are valid for the iridates. I also describe some instrumental setups that were used in later chapters. I conclude by introducing only the parts of the neutron scattering formalism I used in my work.

Chapter 3 is the result of years of synthesis, characterization, and scattering experiments on the compound $Sr_2Ir_xRu_{1-x}O_4$. We focus on the correlated metal phases with low Ir content $x<0.4$. The big picture of this project is that there are strong magnetic fluctuations yet, despite painstaking searches, no evidence of any long-range order. Our evidence is consistent with a peculiar sort of paramagnetic quantum criticality that coincides with a transition from itinerant moments to local moments. I believe this work has the potential to provide insights to other quantum critical metals, perhaps including the unusual superconductor Sr_2RuO_4.

In Chapter 4, we rely on resonant X-ray scattering to flesh out the phase diagram for $Sr_3(Ir_{1-x}Ru_x)_2O_7$. The Ru-rich correlated metal phases are poorly understood. Our studies of the static order and the fluctuations seem to support persistent antiferromagnetism with strongly damped local excitations. We attribute these results directly to the strong spin-orbit coupling. Excitingly, this chapter may prompt more questions than answers.

In Chapter 5, we turn to an insulating d^4 system, where spin-orbit excitons (like Van Vleck transitions) are predicted to yield interesting physics. To this end, I mapped the excitation spectra of $Sr_3Ir_2O_7F_2$ and relied on collaborators to provide *ab initio* and phenomenological models for comparison. Our analysis points to a system with

very strong anisotropy in a spin-orbit singlet ground state. This project gave me a better appreciation of the phenomenal power and complexity of resonant X-ray scattering techniques.

Chapter 6 studies the metal-insulator transition in the pyrochlore iridates. Previous work on $Nd_2Ir_2O_7$ was mostly concerned with bandwidth control. We opted for filling control via Ca substitution in $(Ca_xNd_{1-x})_2Ir_2O_7$. What we find seems consistent with a collapse of the Mott-like state towards a global metal. We also show thermodynamic evidence of the intricate magnetic response. Perhaps the most useful contribution of this work to the field was the careful structural studies, which support a picture of the J_{eff}=1/2 physics and of a set of symmetries that can host the putative topological semimetal phases. In this and all other chapters, I hope to motivate ideas for future work.

Chapter 2

Scattering Methods

Dr. Apurva Mehta at SLAC offered me the following analogy about scattering: you throw a tomato at someone's head, and collect the splatter on a sheet behind them. Perhaps there is little to learn from such an experiment. But this analogy illustrates how people intuitively know about scattering between macroscopic objects. For large condensed matter probes like tomatoes, the scattering is dominated by the electrostatic repulsion (normal force), and this is what dictates the interaction Hamiltonian and resultant cross-section. You are likely familiar with the elastic and inelastic scattering sectors, and their dependence on the incident energy and wavevector of the tomato.

When approaching scattering with other probes, like X-rays or neutrons, it is necessary to establish the mechanism behind a signal's cross-section to achieve a similar intuition. A photon's electromagnetic field interacts with electrons in matter; a neutron's magnetic moment interacts with the magnetic field from the nucleus and unpaired electrons. I will treat scattering with resonant X-rays and neutrons specifically later. First I offer a brief general introduction to the shared concepts of scattering [41, 42].

What we measure with scattering is the differential scattering cross-section $\frac{d\sigma}{d\Omega}$. This is defined as the number of particles detected per second I as a function of the incident flux Φ_0 by a detector that subtends the solid angle $d\Omega$. In the double differential scattering

cross-section, we further restrict the scattering within the energy range E to $E+dE$:

$$\frac{d^2\sigma}{d\Omega dE} = \frac{I}{\Phi_0\, d\Omega\, dE} = \frac{(w \text{ into } d\Omega \text{ and } dE)\rho(E_f)}{\Phi_0\, d\Omega\, dE}. \tag{2.1}$$

Here, the transition rate probability w for a given final density of states $\rho(E_f)$ is given by time-dependent perturbation theory, developed by P.A.M. Dirac and commonly called Fermi's golden rule. This is set by the interaction Hamiltonian $\hat{\mathcal{H}}_{\text{int}}$ acting on the (probe+material) system's initial and final states $|a\rangle, |b\rangle$. To calculate w, the first-order term is sometimes sufficient:

$$w = \frac{2\pi}{\hbar}\left|\langle b|\hat{\mathcal{H}}_{\text{int}}|a\rangle\right|^2 \delta(E_a - E_b) \tag{2.2}$$

where the Dirac delta function $\delta(E_a - E_b)$ ensures conservation of total energy. The energy of a massless photon is given by the Planck-Einstein equation $E = \hbar\omega = \hbar ck = hc/\lambda$, and the energy of a neutron is given by its velocity $E = m_n v_n^2/2 = h^2/(2m_n\lambda^2)$. In the above, ω is frequency, k is wavevector, λ is wavelength, m_n is neutron mass, v_n is neutron velocity, $(\hbar)h$ is (reduced) Planck's constant, and c is the speed of light. At a wavelength of 2 Å, a photon has energy near 6.2 keV in the hard-X-ray regime, and a neutron has energy near 20 meV in the thermal neutron regime.

Now to consider single crystals - see Refs. 41, 43 for a proper derivation. A crystal's periodicity is defined by lattice vectors $\mathbf{R_n} = \sum_{i=1}^{3} n_i \mathbf{a}_i$ where the basis vectors are $(\mathbf{a}_1, \mathbf{a}_2, \mathbf{a}_3)$ and n_i are integers. The reciprocal lattice is defined such that any site $\mathbf{G} = h\mathbf{a}_1^* + k\mathbf{a}_2^* + l\mathbf{a}_3^*$ obeys the relation $\mathbf{G}\cdot\mathbf{R_n} = 2\pi\times$ integer. Working in reciprocal space, the momentum transfer (or scattering vector) is defined as $\mathbf{Q} = \mathbf{k} - \mathbf{k}'$, the difference between the incident and outgoing wavevectors. For elastic scattering $|\mathbf{k}| = |\mathbf{k}'|$ this yields $|\mathbf{Q}| = Q = 4\pi\sin\theta/\lambda$. The diffraction condition is satisfied when $\mathbf{Q} = \mathbf{G}$, and in

the elastic case this can be reduced to Bragg's law $n\lambda = 2d\sin\theta$ for integer n and lattice plane spacing d.

It is easy to consider X-ray or neutron scattering from a free ion, where the isotropic interaction can be described by an atomic form factor f. In going from a free ion to a crystal, we swap the atomic form factor in the cross-section for the crystal form factor F. The crystal form factor is given by:

$$F(\mathbf{Q},\ \hbar\omega) = \sum_j f_j(\mathbf{Q},\ \hbar\omega)\mathrm{e}^{\mathbf{iQ}\cdot\mathbf{r}_j}\sum_n \mathrm{e}^{\mathbf{iQ}\cdot\mathbf{R_n}} \tag{2.3}$$

where the first sum represents the molecular structure factor and sums over the atomic form factor f for each atom j at position $\mathbf{r}_j$ in one unit cell, and the second sum represents the crystal structure factor and sums over the real space lattice vectors $\mathbf{R_n}$. This is in the Born approximation (kinematical scattering); the dynamical scattering theory is outside the scope of this dissertation. For photons the atomic form factors are tabulated accurately in tables, but are imprecise near the resonance energies linking the electronic orbitals. For neutrons the form factors are typically denoted b, which are complex factors tabulated for each isotope.

2.1 Resonant X-ray Scattering Theory

This section provides the relevant theoretical treatment for all forms of resonant X-ray scattering (hereafter abbreviated as RXS). I will later separately consider two different varieties of experiments: resonant in/elastic X-ray scattering (RIXS and REXS).

What sets resonant scattering apart from nonresonant scattering is the increase in scattering length of the targeted element at its absorption edge, through the 2-step process of virtual absorption and emission [41, 44]. This generally increases the relatively

small magnetic scattering signal to measurable amounts. It also helps to elucidate details of the bonding and local structure, which are very briefly discussed in this dissertation.

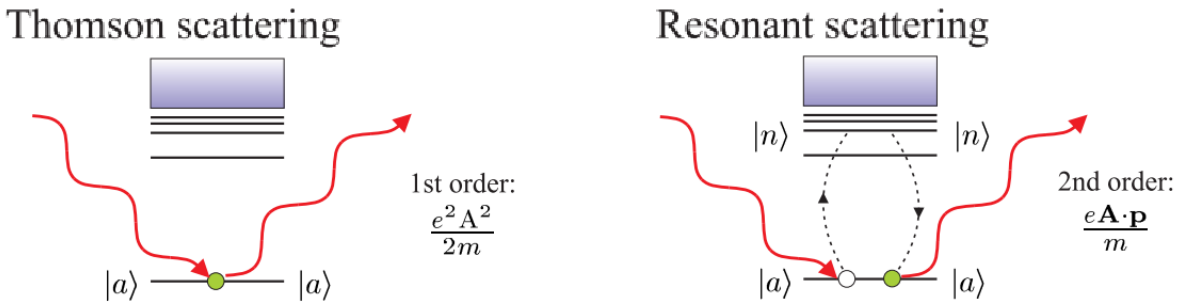

Figure 2.1: Difference between the typical Thomson scattering and resonant scattering processes. Thomson scattering probes electrons in the combined (X-ray + ion) ground state $|a\rangle$. The additional term in the interaction Hamiltonian from the photoexcited electron occupying intermediate states $|n\rangle$ is the basis for the 'anomalous' RXS amplitudes. Adapted from [41]. Copyright 2011 John Wiley and Sons, Ltd.

There are advantages of RXS that are manifest in the literature, which have moved our understanding of quantum materials forward in the past several decades:

+ Fine reciprocal space resolution

+ Element, site, and orbital specificity

+ Large reciprocal space availability; magnetic form factors do not die off with Q so signals can be tracked in multiple Brillouin zones

+ Can measure small samples ($\sim$100 μm^2 areas, ultrathin films [45])

+ Can measure isotopes that are strong neutron absorbers

But RXS also has disadvantages:

– Relatively poor energy transfer resolution >5 meV

– Complicated equipment

– Low signals

– Complicated cross-section

On that last disadvantage, RXS measures the intermediate state which yields the outgoing photon. This state has a "photoexcited electron" (virtual absorption kicks a core electron to the valence) so it is by nature an atypical excited state [44]. This is what complicates the theory, rendering it tractable only with a litany of assumptions. These assumptions are discussed throughout.

In the following theory section, we shall build toward the multipole formalism, an expansion in the rank of the resonant form factors. While nonresonant X-ray scattering can be defined by scalar form factors, the tensors in resonant scattering encode more information about the system in the X-ray's polarization. This is useful for extracting, say, magnetic moment orientation in your sample.

2.1.1 Cross-Sections and Form Factors

We begin our consideration of resonant X-ray scattering with a quantum mechanical treatment of the interaction of photons with matter [41, 46]. The interaction Hamiltonian between photons and electrons is:

$$\begin{aligned}\hat{\mathcal{H}}_{\text{int}} &= \hat{\mathcal{H}}_{\text{total}} - (\hat{\mathcal{H}}_{\text{electron}} + \hat{\mathcal{H}}_{\text{radiation}}) \\ &= \frac{e^2}{2m_e c^2}A^2 - \frac{\hbar e^3}{2m_e^2 c^4}\mathbf{S}\cdot(\dot{\mathbf{A}}\times\mathbf{A}) - \frac{e}{m_e c}\mathbf{A}\cdot\mathbf{p} - \frac{\hbar e}{m_e c}\mathbf{S}\cdot(\nabla\times\mathbf{A}) \\ &\equiv \hat{\mathcal{H}}_1 + \hat{\mathcal{H}}_2 + \hat{\mathcal{H}}_3 + \hat{\mathcal{H}}_4\end{aligned} \tag{2.4}$$

Where $\mathbf{A}$ is the photon vector potential, $\dot{\mathbf{A}}$ is its derivative in time, and $e, m_e, \mathbf{p}, \mathbf{S}$ are the electron charge, mass, momentum operator, and spin operator. We implicitly

consider only one site here.

We have already made several assumptions which make this result only describe experiments with energies below about 20 keV. Namely, this theory is only applicable at energies much less than the electronic rest mass 511 keV, as it disregards the (incoherent, inelastic) Compton scattering which dominates at high energies. Additionally, we consider fields from the beam that are small relative to the electron mass, which is acceptable for synchrotrons but may not hold for focused free electron lasers [46]. Also, we assumed that the core electrons travel non-relativistically (i.e. the Lorentz factor $1/\sqrt{(1-p^2/(m_e c)^2)} \approx 1$), which is acceptable for the $2p$ electrons probed at the L edges, but precludes $1s$ electrons in $4d$ block elements and higher (which is why these are not typically measured). So this theory will only describe L edge and $3d$ K edge scattering. It will be made clear when we later consider the special sub-case of $4d$ and $5d$ L edges.

The vector potential may be expanded as a sum of plane waves. In second-quantization form we express $\mathbf{A}$ as a sum of harmonic oscillator photon creation(annihilation) operators $a^\dagger(a)$ for photon eigenstates $|n_{u,\mathbf{k}}\rangle$ indexed by polarization u and wavevector $\mathbf{k}$:

$$\mathbf{A}(\mathbf{r},t) = \sum_u \sum_{\mathbf{k}} \sqrt{\frac{\hbar}{2\epsilon_0 \mathcal{V}\omega_{\mathbf{k}}}} \left[\boldsymbol{\epsilon}_u a_{u,\mathbf{k}} \mathrm{e}^{\mathrm{i}\mathbf{k}\cdot\mathbf{r}-\mathrm{i}\omega t} + \boldsymbol{\epsilon}_u^* a_{u,\mathbf{k}}^\dagger \mathrm{e}^{-\mathrm{i}\mathbf{k}\cdot\mathbf{r}+\mathrm{i}\omega t}\right] \tag{2.5}$$

where $\mathbf{r}$ is real space, t is time, $\boldsymbol{\epsilon}_u$ is a polarization unit vector for the electric field, $\hbar$ is the reduced Planck constant, ϵ_0 is the vacuum permittivity, $\mathcal{V}$ is some arbitrary volume which will be removed upon Fourier transforming to reciprocal space, and $\omega{=}c|\mathbf{k}|$ is the frequency of the photon. Since electromagnetic waves are transverse, $\mathbf{k}\cdot\boldsymbol{\epsilon}_u = 0$ there are only two orthogonal polarization directions.

Note that the vector potential is along the photon polarization, and is linear in photon creation and annihilation. Thus we can compute how the interaction of the photon with

the material system affects the states, by considering the initial and final states of the combined system. Let us consider the material's electrons prepared in the initial state $|i\rangle$ and an incident photon prepared in the state $|\boldsymbol{\epsilon}, \mathbf{k}\rangle$; the initial state for the entire system is then the product state $|a\rangle \equiv |i\rangle \otimes |\boldsymbol{\epsilon}, \mathbf{k}\rangle = |i; \boldsymbol{\epsilon}, \mathbf{k}\rangle$. Conversely the final state composed of the perturbed material system and the outgoing photon is defined by $|b\rangle \equiv |f; \boldsymbol{\epsilon}', \mathbf{k}'\rangle$.

We use the interaction Hamiltonian to understand the differential scattering cross-section $\frac{d\sigma}{d\Omega}$, which is proportional to the transition rate probability w (see Equation 2.1). I present the relevant second-order result below:

$$w = \frac{2\pi}{\hbar} \left| \langle b|\hat{\mathcal{H}}_{\text{int}}|a\rangle + \sum_m \frac{\langle b|\hat{\mathcal{H}}_{\text{int}}|m\rangle\langle m|\hat{\mathcal{H}}_{\text{int}}|a\rangle}{E_a - E_m} \right|^2 \delta(E_a - E_b) \tag{2.6}$$

where the sum is over all intermediate states m with energy E_m, and the Dirac delta function $\delta(E_a - E_b)$ ensures conservation of total energy. The second-order perturbation term (the sum) describes RXS, which is a two-step scattering process. This will be described in more detail shortly.

The first-order perturbation term $|\langle b|\hat{\mathcal{H}}_{\text{int}}|a\rangle|^2$ describes the Thomson scattering:

$$\begin{aligned} \left(\frac{d\sigma}{d\Omega}\right)_{\text{Thomson}} &\propto |\langle b|\hat{\mathcal{H}}_1|a\rangle|^2 \propto |\langle b|\ A^2\ |a\rangle|^2 \\ &= r_0^2 |\boldsymbol{\epsilon} \cdot \boldsymbol{\epsilon}'|^2 |F(\mathbf{Q},\ \hbar\omega)|^2 \delta(E_a - E_b) \end{aligned} \tag{2.7}$$

(with r_0 the Thomson scattering length) and, to leading order, the absorption:

$$\sigma_{\text{abs}} \propto |\langle b|\hat{\mathcal{H}}_3|a\rangle|^2 \propto |\langle b|\ \mathbf{A} \cdot \mathbf{p}\ |a\rangle|^2. \tag{2.8}$$

These equations reference the $\hat{\mathcal{H}}_{\text{int}}$ terms in Equation 2.4. Absorption is isotropic so we can easily integrate its differential cross-section.

I want to pay particular attention to the atomic form factor f for one particular ion

now. We can experimentally determine the precise energy dependence of f, for richer analysis of scattering results. The convention is to express f as a sum of distinct reciprocal space and energy-dependent terms:

$$f(\mathbf{Q},\ \hbar\omega) = f^0(\mathbf{Q}) + f'(\omega) + \mathrm{i}f''(\omega) \tag{2.9}$$

where $f'(\omega)\equiv\mathrm{Re}[f(\omega)]$ and $f''(\omega)\equiv\mathrm{Im}[f(\omega)]$. $f^0(\mathbf{Q})$ is tabulated for each element and comes simply from the Fourier transform of the electron density.

By definition we have:

$$f''(\omega) = \frac{-\omega}{4\pi r_0 c}\sigma_{\mathrm{abs}}(\hbar\omega) \tag{2.10}$$

Thankfully, the absorption cross-section σ_{abs} is an easily measured quantity. Making use of theory, we can experimentally approximate the real term $f'(\omega)$ from the absorption. We can think of the response of one bound electron to a photon as akin to a damped driven oscillator with position given by $\frac{\boldsymbol{\epsilon}(eE_0/m_e)}{\omega_s^2-\omega^2-\mathrm{i}\omega\Gamma}$, where E_0 is the photon's electric field magnitude, ω_s is the resonance frequency, and Γ is the damping coefficient. The mathematical tool we exploit here is Cauchy's theorem, which relates the form factors to a contour integral in the complex plane. This approach yields the Kramers-Kronig relation:

$$\begin{aligned} f'(\omega) &= \frac{2}{\pi}\mathcal{P}\int_0^\infty d\omega' \frac{\omega' f''(\omega')}{\omega'^2-\omega^2} \\ &= \frac{2}{\pi}\left(\int_0^{\omega_s-\delta} d\omega' \frac{\omega' f''(\omega')}{\omega'^2-\omega^2} + \int_{\omega_s+\delta}^\infty d\omega' \frac{\omega' f''(\omega')}{\omega'^2-\omega^2}\right)\Bigg|_{\delta\to 0} \end{aligned} \tag{2.11}$$

where the principle integral $\mathcal{P}\int$ is defined on the second line. In practice, this quantification is used in the calculation of resonant reflectivity scattering lengths for thin films and heterostructures. Similar concepts are exploited in other resonant scattering analyses.

2.1.2 Multipole Interpretation of Resonant X-ray Diffraction

The full form of the RXS cross-section is unwieldy. To get to a useful formulation, we will apply several assumptions. This section is adapted from Ref. 47 with discussion from other sources [12, 46]. The following is a more complete formalism than is employed in most experimental works, including my own.

The word 'diffraction' in the title of this section is deliberate. In diffraction, the measured signal is a coherent interference of all scattering processes. On the other hand, away from a Bragg peak, all the RXS terms in Equation 2.4 are added incoherently. So the multipole expansion is not applicable to inelastic scattering (RIXS) in its entirety.

One common source of confusion in the terminology: the multipoles derived in this section do NOT directly describe the collective order of the scattered material system. They are *interaction multipoles* describing the photon-electron interaction. For example the "electric dipole" terms describe the magnetic dipole and electric quadrupole orders in the material system. I will elaborate on this point later.

Let us embark by explicitly writing the atomic form factors in Equations 2.4 and 2.9 to leading order $f_j(\hat{\mathcal{H}}_1, \hat{\mathcal{H}}_2, \hat{\mathcal{H}}_3, \hat{\mathcal{H}}_4)$ for one site j [47]. The terms with no explicit energy dependence are straightforward:

$$f^0 = \langle b|\hat{\mathcal{H}}_{1,j}|a\rangle + \langle b|\hat{\mathcal{H}}_{2,j}|a\rangle \equiv f_j^{0,\text{nonmagnetic}} + f_j^{0,\text{magnetic}}. \tag{2.12}$$

As for the resonant form factor terms $f' + \mathrm{i}f''$, these treat the two-step absorption and emission process. Here it is helpful to account for the order of photon creation and annihilation, so we keep note of photon number in each state. In this complicated

notation:

$$f_j' + \mathrm{i}f_j'' = \sum_m \sum_i \frac{\langle b; n|\hat{\mathcal{H}}_{3,i} + \hat{\mathcal{H}}_{4,i}|m; n\pm1\rangle\langle m; n\pm1|\hat{\mathcal{H}}_{3,j} + \hat{\mathcal{H}}_{4,j}|a; n\rangle}{E_a - E_m \mp \frac{\hbar\omega_{\mathbf{k}'}}{\hbar\omega_{\mathbf{k}}}} \tag{2.13}$$

where n is the number of photon states, and the explicit dependence on wavevector and polarization have been dropped for simplicity. We must consider multiple scattering sites i, j because the site may differ in the resonant scattering processes if the photoexcited electron is delocalized. In the above there are two physical scenarios encoded: one in which the incident photon is absorbed before the outgoing photon is emitted (intermediate state $n-1$ with $\omega_{\mathbf{k}}$ in the denominator) where we have resonance; and one in which the outgoing photon precedes the incident one (intermediate state $n+1$ with $\omega_{\mathbf{k}'}$ in the denominator).

Now, for completeness and some helpful redundancy [12], I show the full substitution of $\hat{\mathcal{H}}_{\text{int}}$ into the double differential scattering cross-section:

$$\begin{aligned}
\frac{d^2\sigma}{d\Omega dE} = \quad & \frac{e^4}{m_e^2c^4}\frac{\omega_{\mathbf{k}'}}{\omega_{\mathbf{k}}}\left|\left\langle b\right|\sum_j \mathrm{e}^{\mathrm{i}\mathbf{Q}\cdot\mathbf{r}_j}\left|a\right\rangle\ \boldsymbol{\epsilon}'\cdot\boldsymbol{\epsilon}\ -\right. \\
& \frac{\mathrm{i}\hbar(\omega_{\mathbf{k}}+\omega_{\mathbf{k}'})}{2m_ec^2}\left\langle b\right|\sum_j \mathbf{s}_j\mathrm{e}^{\mathrm{i}\mathbf{Q}\cdot\mathbf{r}_j}\left|a\right\rangle\boldsymbol{\epsilon}'\times\boldsymbol{\epsilon}\ +\ \frac{1}{m_e}\sum_m\sum_{i,j} \\
& \left(\frac{\langle b|(\boldsymbol{\epsilon}'\cdot\mathbf{p}_i - \mathrm{i}\hbar(\mathbf{k}'\times\boldsymbol{\epsilon}')\cdot\mathbf{s}_i)\mathrm{e}^{-\mathrm{i}\mathbf{k}'\cdot\mathbf{r}_i}|m\rangle\langle m|(\boldsymbol{\epsilon}\cdot\mathbf{p}_j - \mathrm{i}\hbar(\mathbf{k}\times\boldsymbol{\epsilon})\cdot\mathbf{s}_j)\mathrm{e}^{\mathrm{i}\mathbf{k}\cdot\mathbf{r}_j}|a\rangle}{E_a - E_m + \hbar\omega_{\mathbf{k}} - \mathrm{i}\Gamma_m/2}\right. \\
& \left.\left. + \frac{\langle b|(\boldsymbol{\epsilon}\cdot\mathbf{p}_i - \mathrm{i}\hbar(\mathbf{k}\times\boldsymbol{\epsilon})\cdot\mathbf{s}_i)\mathrm{e}^{\mathrm{i}\mathbf{k}\cdot\mathbf{r}_i}|m\rangle\langle m|(\boldsymbol{\epsilon}'\cdot\mathbf{p}_j - \mathrm{i}\hbar(\mathbf{k}'\times\boldsymbol{\epsilon}')\cdot\mathbf{s}_j)\mathrm{e}^{-\mathrm{i}\mathbf{k}'\cdot\mathbf{r}_j}|a\rangle}{E_a - E_m - \hbar\omega_{\mathbf{k}'}}\right)\right|^2 \\
& \delta(E_a - E_b)
\end{aligned} \tag{2.14}$$

where the finite lifetime of intermediate states Γ_m helps to remove unphysical divergence at resonance. This has the explicit polarization dependence so the photon number has been dropped from the electron-photon product states $|a\rangle, |b\rangle$, and the intermediate states

$|m\rangle$ now implicitly include the photoexcited electron.

In the above, we can note that the first term is the Thomson cross-section, the second term is a (typically very weak) nonresonant magnetic contribution, and the long terms contain a mix of resonant and nonresonant terms. We can therefore recast this formula in terms of its components:

$$\frac{d^2\sigma}{d\Omega dE} = \frac{e^4}{m_e^2 c^4}\frac{\omega_{\mathbf{k}'}}{\omega_{\mathbf{k}}}\left|\mathcal{A}_{\text{Thomson}} + \mathcal{A}_{\text{nonres}} + \mathcal{A}_{\text{res}}\right|^2 \delta(E_i - E_f + \hbar\omega_{\mathbf{k}} - \hbar\omega_{\mathbf{k}'}) \tag{2.15}$$

where I have here split the Dirac delta function's energies to separately consider the material's and the photon's energies: $E_a - E_b = (E_i + \hbar\omega_{\mathbf{k}}) - (E_f + \hbar\omega_{\mathbf{k}'})$.

To make any progress on the resonant cross-section in Equation 2.14, we employ the multipole expansion [47]. This invokes the approximation in the limit of small $\mathbf{k}\cdot\mathbf{r}_j \sim 0.1$ which is valid for hard X-rays:

$$\begin{aligned} e^{\mathrm{i}\mathbf{k}\cdot\mathbf{r}} &\approx \sum_{l=0}^{\infty} \mathrm{i}^l (2l+1) j_l(kr) P_l(\mathbf{k}\cdot\mathbf{r}/kr) \\ &\approx \sum_{n=0}^{\infty} \frac{(\mathrm{i}\mathbf{k}\cdot\mathbf{r})^n}{n!} = 1 + \mathrm{i}\mathbf{k}\cdot\mathbf{r} - \frac{1}{2}(\mathbf{k}\cdot\mathbf{r})^2 + \dots \end{aligned} \tag{2.16}$$

where we approximate the proper sum of plane waves (in terms of the regular Bessel function j_l and the Legendre polynomials P_l) as a Taylor expansion. The Taylor expansion provides short-term simplicity, but we'd need to rearrange terms to express the transfer matrix in terms of terms of given rank l in this multipole expansion.

Now we wish to express the orbitals in terms of their real-space values for easier mapping onto the electron creation and annihilation operators that describe exciting a core electron into a valence band and its subsequent decay. For this we employ the

following commutators:

$$[x, \hat{\mathcal{H}}_{\text{electron}}] = -\frac{\hbar}{\mathrm{i}m_e} p_x \tag{2.17}$$

$$[xy, \hat{\mathcal{H}}_{\text{electron}}] = \frac{\mathrm{i}\hbar}{m_e}(yp_x + xp_y) = \frac{\mathrm{i}\hbar}{m_e}(2yp_x + L_z) \tag{2.18}$$

$$[xy^2, \hat{\mathcal{H}}_{\text{electron}}] = \frac{\mathrm{i}\hbar}{m_e}(2xyp_y + \mathrm{i}\hbar x + y^2 p_x) = \frac{\mathrm{i}\hbar}{m_e}(2yL_z + \mathrm{i}\hbar x + 3y^2 p_x) \tag{2.19}$$

where L_z is the projection of the angular momentum along z.

If we carry these substitutions through [47], we can solve for one matrix element M_{ma} within $\mathcal{A}_{res} \propto M'_{bm} M_{ma}$:

$$\begin{aligned} M_{ma} \approx & -\frac{\mathrm{i}(E_m - E_a)}{\hbar}\Bigg[\left(1 + \frac{\hbar^2 k^2}{6m_e(E_m - E_a)}\right)\langle m|\boldsymbol{\epsilon}\cdot\mathbf{r}|a\rangle \\ & + \frac{\mathrm{i}}{2}\langle m|\boldsymbol{\epsilon}\cdot\mathbf{r}\mathbf{k}\cdot\mathbf{r}|a\rangle \\ & - \frac{1}{6}\langle m|\boldsymbol{\epsilon}\cdot\mathbf{r}(\mathbf{k}\cdot\mathbf{r})^2|a\rangle \\ & + \frac{\hbar}{2m_e(E_m - E_a)}\langle m|\mathbf{k}\times\boldsymbol{\epsilon}\cdot\left(\hat{L} + 2\hat{S}\right)|a\rangle \\ & + \frac{\mathrm{i}\hbar}{2m_e(E_m - E_a)}\langle m|(\mathbf{k}\times\boldsymbol{\epsilon})\cdot\left(\frac{2}{3}\hat{L} + 2\hat{S}\right)\mathbf{k}\cdot\mathbf{r}|a\rangle\Bigg]\mathrm{e}^{-\mathrm{i}\omega t} \\ = & \ \mathrm{E1} + \mathrm{E2} + \mathrm{E3} + \mathrm{M1} + (\mathrm{M2{+}T1}) + \ldots \end{aligned} \tag{2.20}$$

where we've taken the liberty to define the tensors: electric E, magnetic M, and toroidal T, with rank the number after them. The terms are in order, and the last term is the mixture of T1 and M2 (these are the anti/symmetric parts of the same tensor).

If you think each term in the above equation is unwieldy, remember that for each scattering channel we are actually measuring a permutation of four of these terms. The convention for describing one scattering channel is a combination of two 'couples' of the form (A−B)−(C−D), e.g. (E1−E1)−(E1−E1). Thankfully, it is only in very exotic cases that one considers terms beyond E1 and E2. It is known that the couples (E1−E1)

and (E1−E2) and (E2−E2) have been detected, and it is hypothetically possible that (E1−M2) and E1−T1) and *maybe* the especially weak interaction (E1−M1) could be detected. And, since E2/E1 ratios range from 0.02 to 0.2, typically only the couples (E1−E1) and (E1−E2) are measurable in materials [47].

Rank	Matter Multipole	$\hat{I}$	RXD Couple(s)
0	Electric charge	+	**(E1-E1)**, (E2-E2), (E1-M2)
1	Electric dipole	−	(E1-E2)
2	Electric quadrupole	+	**(E1-E1)**, (E2-E2), (E1-M2)
3	Electric octupole	−	(E1-E2)
1	Magnetic dipole	+	**(E1-E1)**, (E2-E2), (E1-M2)
2	Magnetic quadrupole	−	(E1-E2)
3	Magnetic octupole	+	(E2-E2), (E1-M2)
0	Polar toroidal monopole	+	(E1-M2)
1	Polar toroidal dipole	−	(E1-E2)
2	Polar toroidal quadrupole	+	(E1-M2)
3	Polar toroidal octupole	−	(E1-E2)
1	Axial toroidal dipole	+	(E1-M2)
2	Axial toroidal quadrupole	−	(E1-E2)
3	Axial toroidal octupole	+	(E1-M2)

Table 2.1: Correspondence between multipoles in matter and scattering channels. Tensor rank and parity under spatial inversion $\hat{I}$ are also included. The (typically strongest) dipole term is in bold for clarity. From [47], which contains a description of the matter multipoles that builds on Jackson's *Classical Electrodynamics* textbook.

Recall that the interaction multipoles are distinct from the multipoles that describe matter. Table 2.1 shows which matter multipoles are uncoverable in which channels. The inversion symmetry of each channel is useful for interpreting the data and assigning matter multipoles, in conjunction with the relevant space groups. The rank of each couple is a sum of the ranks of the terms' tensors; e.g. E1-E1 is rank 2 so it can only measure matter multipoles with rank $\leq$2, which includes electric charges, electric quadrupoles, and magnetic dipoles.

Since it is dominant [12], and it can capture magnetic dipolar order, most studies

only treat the dipole term (E1−E1):

$$\mathcal{A}_{\text{res}} \approx \sum_{m} \sum_{i,j} \frac{m_e \big(E_a - E_m\big)^3}{\hbar^3 \omega_{\mathbf{k}}} \left(\frac{\langle b|(\boldsymbol{\epsilon}' \cdot \mathbf{r}_i)|m\rangle\langle m|(\boldsymbol{\epsilon} \cdot \mathbf{r}_j)|a\rangle}{E_a - E_m + \hbar\omega_{\mathbf{k}} - \mathrm{i}\Gamma_m/2} \right) \tag{2.21}$$

where again we explicitly show that resonant scattering can involve a photoexcited state that is delocalized over two separate sites i and j, and we have dropped the small correction factor $\propto k^2$. You will notice that the dipole term has no explicit dependence on the spin state. However, we exploit the selection rules to ensure we are measuring the magnetic valence states. We also can track the polarization, energy, temperature, and reciprocal space dependence and measure the scattering at different edges (say, L_2 and L_3) to learn specific information − please read on for more of this.

2.1.3 Resonant X-ray Scattering for $4d^5$ and $5d^5$

In this section, we employ a more user-friendly approach to the resonant X-ray scattering for $4d^5$ and $5d^5$ ions (iridates and osmates and ruthenates…). In making the theory tractable, we lose a great deal of generality to other ions.

First we apply the "fast collision" approximation [48]. Here, we assume that the width of the excited states is large compared to the excitation spectrum. In effect we are limiting our consideration to edges with supremely short core-hole lifetimes: the L-edges of $4d$-block and higher elements. Often this treatment is used for studies of $3d$ K-edges, but this is probably not valid because their core-hole lifetimes Γ are about as small as the Hubbard energy scale [49].

The second approximation is to treat only dipole transitions (E1−E1) as in Equation 2.21. Under this approximation, throwing out the other interaction multipoles, there is no difference in the theories for all resonant scattering cross-sections. This theory is

therefore applicable to all RXS, RIXS and resonant diffraction alike.[1]

This section is mostly from the treatment by B.J. Kim and G. Khaliullin [49]. This theory only explicitly handles *insulators* with t_{2g} orbitals, because it only considers 1-site terms and not delocalized excitations specifically.

The dipole transitions (E1) can be represented by operators of the form $\hat{\mathcal{D}} \propto \hat{d}^\dagger \hat{p}$ at the L-edges for $2p \rightarrow d$ transitions. More explicitly, for X-ray polarization along z ($\boldsymbol{\epsilon}_z$), the form is: $\hat{d}^\dagger{}_{yz}\hat{p}_y + \hat{d}^\dagger{}_{zx}\hat{p}_x + \frac{2}{\sqrt{3}}\hat{d}^\dagger{}_{(3z^2-r^2)}\hat{p}_z$, with cyclic permutations for the other polarization directions.

With the fast collision approximation, the RXS operator $\hat{R}$ is:

$$\hat{R} = \sum_m \frac{\hat{\mathcal{D}}^\dagger(\boldsymbol{\epsilon}')|m\rangle\langle m|\hat{\mathcal{D}}(\boldsymbol{\epsilon})}{E - E_m + \mathrm{i}\Gamma_m/2} \tag{2.22}$$

with, as a reminder, intermediate states $|m\rangle$ that include the photoexcited electron, incident and outgoing polarization $\boldsymbol{\epsilon}$ and $\boldsymbol{\epsilon}'$, incident X-ray energy E, and core-hole lifetime Γ_m. The measured intensity would be $I \propto \langle b|\hat{R}^\dagger\hat{R}|a\rangle$ measured for the initial and final states $|a\rangle, |b\rangle$ at a particular value of energy and momentum transfer.

The theory breaks the RXS operator into a quadrupole and a dipole channel:

$$\hat{R} = \frac{1}{3}\left(\hat{R}_Q + \mathrm{i}\hat{R}_M\right) \tag{2.23}$$

$$\hat{R}_Q = \sum_\alpha \epsilon_\alpha \epsilon'_\alpha Q_{\alpha\alpha} - \frac{1}{2}\sum_{\alpha>\beta}\left(\epsilon_\alpha\epsilon'_\beta + \epsilon_\beta\epsilon'_\alpha\right)Q_{\alpha\beta} \tag{2.24}$$

$$\hat{R}_M = \frac{1}{2}\left(\boldsymbol{\epsilon}\times\boldsymbol{\epsilon}'\right)\cdot\mathbf{N} \tag{2.25}$$

where the quadrupolar tensor $Q_{\alpha\beta}$ and the magnetic vector $\mathbf{N}$ represent transitions with $\Delta j{=}\pm 2$ and $\Delta j{=}\pm 1$ respectively. These can both be calculated in terms of the $\hat{\mathcal{D}}$ oper-

[1] To reiterate, when we include higher-rank terms the RIXS signal is not described by the multipole expansion because scattering terms may be added incoherently.

	L_3-edge	L_2-edge
Q_{zz} d^5 J_{eff}=1/2	$\big[2L_z^2 - 2L_zS_z\big]$ 0	$\big[L_z^2 + 2L_zS_z\big]$ 0
Q_{xy} d^5 J_{eff}=1/2	$\big[2L_xL_y + 2L_yL_x - 2L_xS_y - 2L_yS_x\big]$ 0	$\big[L_xL_y + L_yL_x + 2L_xS_y + 2L_yS_x\big]$ 0
N_z d^5 $J_{\text{eff}} = 1/2$	$\big[2L_z - 4S_z + 8L_z^2S_z$ $-2L_z(\mathbf{L}\cdot\mathbf{S}) - 2(\mathbf{L}\cdot\mathbf{S})L_z\big]$ $\big[\sqrt{8}\sin 2\theta - 4\cos 2\theta\big]\tilde{S}_z \xrightarrow[\text{cubic}]{} 4\tilde{S}_z$	$\big[L_z + 4S_z - 8L_z^2S_z$ $+2L_z(\mathbf{L}\cdot\mathbf{S}) + 2(\mathbf{L}\cdot\mathbf{S})L_z\big]$ $\big[3 + \cos 2\theta + \sqrt{8}\sin 2\theta\big]\tilde{S}_z \xrightarrow[\text{cubic}]{} 0$
N_x d^5 J_{eff}=1/2	$\big[2L_x - 4S_x + 8L_x^2S_x$ $-2L_x(\mathbf{L}\cdot\mathbf{S}) - 2(\mathbf{L}\cdot\mathbf{S})L_x\big]$ $\big[\sqrt{18}\sin 2\theta\big]\tilde{S}_x \xrightarrow[\text{cubic}]{} 4\tilde{S}_x$	$\big[L_x + 4S_x - 8L_x^2S_x$ $+2L_x(\mathbf{L}\cdot\mathbf{S}) + 2(\mathbf{L}\cdot\mathbf{S})L_x\big]$ 0

Table 2.2: The components of the RXS operator $\hat{R}$ for $4d^5$ and $5d^5$ ions. The corresponding J_{eff}=1/2 result is included in the cubic limit and as functions ofthe tetragonal/trigonal distortion Δ and SOC λ via $\tan 2\theta = \frac{2\sqrt{2}\lambda}{\lambda - 2\Delta}$. Those components not included in the table are related by symmetry. Adapted from [49].

ators. Then the intensities could be expressed as $I \propto \langle b|\hat{R}_Q^\dagger \hat{R}_Q + \hat{R}_M^\dagger \hat{R}_M|a\rangle$.

Table 2.2 has the results for both d^5 and J_{eff}=1/2 states. To calculate $Q_{\alpha\beta}$ and $\mathbf{N}$ in terms of the dipole operators, we assumed that e_g states are negligibly occupied, and that Hund's first rule (maximizing $\hat{S}_z$) is a good starting point. While the result in terms of the spin and orbital momentum operators is useful, we are specifically interested in the case of pseudospin-1/2 operators $\tilde{\mathbf{S}}$ with $|\tilde{S}_z{=}1/2\rangle \leftrightarrow |\tilde{\uparrow}\rangle$. See Section 1.2.1 for relevant definitions.

The specific result for J_{eff}=1/2 in the cubic limit is as follows: $\hat{R}_Q = \hat{R}_{L_2} = 0$, and

$$\hat{R}_{L_3} = 2\big(\boldsymbol{\epsilon} \times \boldsymbol{\epsilon}'\big) \cdot \tilde{\mathbf{S}} \tag{2.26}$$

In this cubic case the resonant X-ray cross-section is *isotropic* and, as we will soon

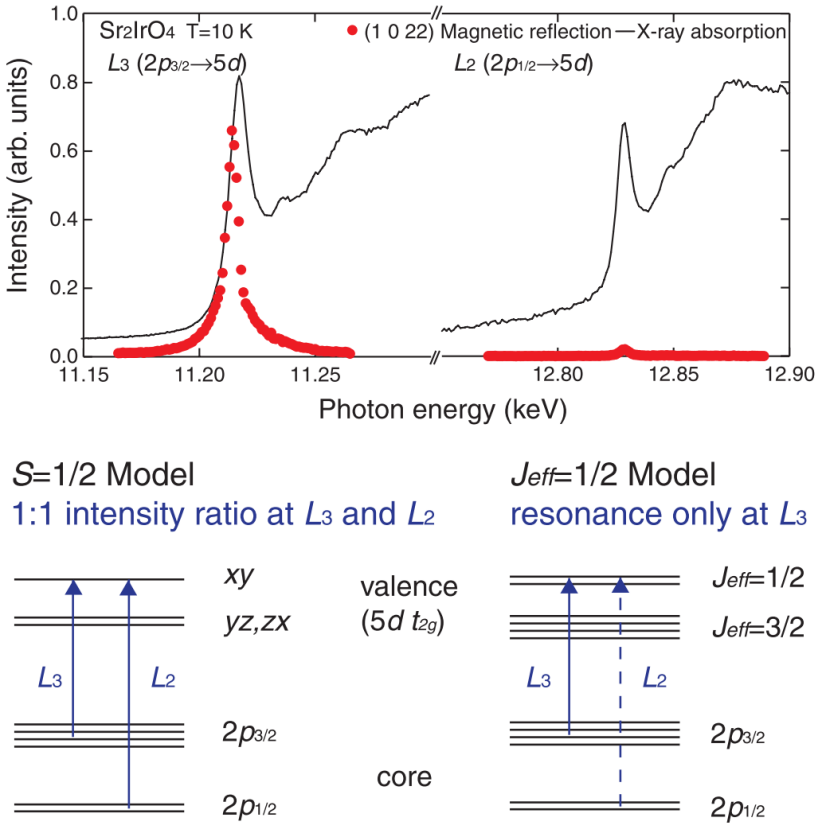

Figure 2.2: Resonant X-ray Scattering can be used to show proof of the J_{eff}=1/2 state, as was done for Sr_2IrO_4. The diffraction at a magnetic Bragg peak is plotted in red for both the L_3 and L_2 edges. From [16]. Copyright 2009 American Association for the Advancement of Science, reprinted with permission.

see, there is a direct correspondence between this and the spin-spin correlation function measured with magnetic neutron scattering.

In REXS one can select the outgoing polarization $\boldsymbol{\epsilon}'$ that points either along or perpendicular to the incident polarization $\boldsymbol{\epsilon}$, to separate this magnetic signal from other possible origins. When the incident polarization is σ, these two channels are dubbed $\sigma - \sigma'$ and $\sigma - \pi'$ respectively. Because $\boldsymbol{\epsilon} \times \boldsymbol{\epsilon}'$ is only finite for $\sigma - \pi'$, this is often called the spin-flip channel. More on this in Section 2.2.1.

Another important result of this theory is the explanation for why J_{eff}=1/2 materials

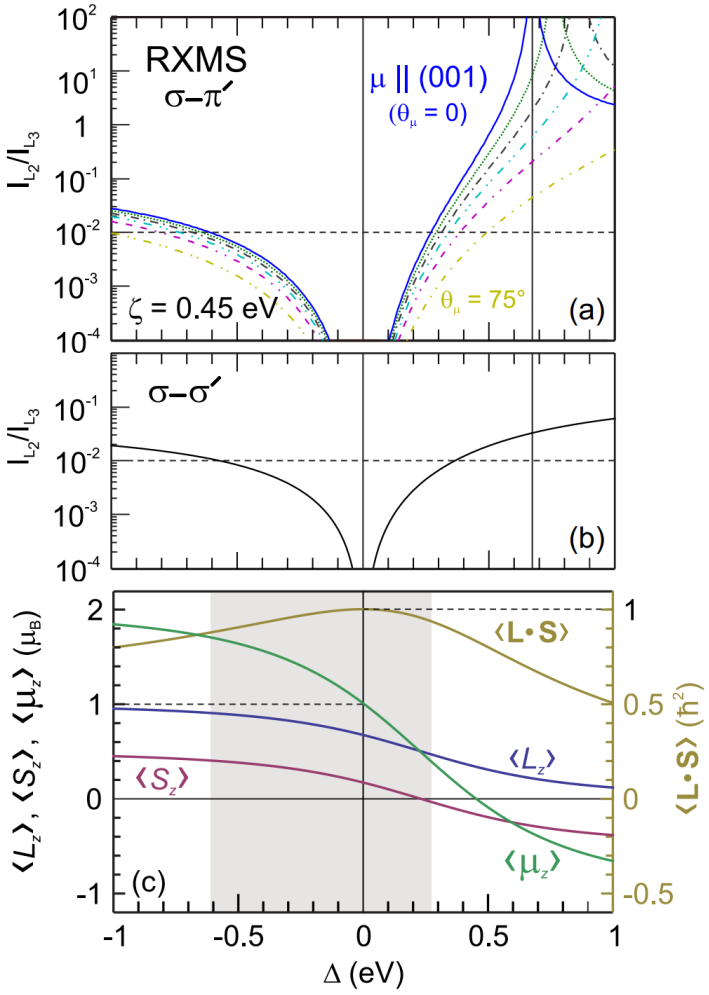

Figure 2.3: Relative intensities of the resonant X-ray scattering near the ideal J_{eff}=1/2 state, as a function of tetragonal/trigonal distortions. In (a) and (b) the ratio of the intensities at the L_2-edge and L_3-edge are plotted for various moment angles θ_μ, with $\boldsymbol{\mu} \,||\, (110)$ defined as having $\theta_\mu = 90°$. While this ratio changes with θ_μ in the spin-flip $\sigma{-}\pi'$ channel, there is no such dependence in the non-spin-flip $\sigma{-}\sigma'$ channel. In (c) are some expectation values. From [14]. Copyright 2014 American Physical Society.

(in particular Sr_2IrO_4) have negligible intensity at L_2 – recall Section 1.2.1, and see Fig. 2.2. This result from Ref. 16 can only be rationalized by the unusual spin and angular momentum states for the J_{eff}=1/2 state. The intensity ratio of out-of-plane pseudospin components $I_c(L_2)/I_c(L_3)$ stays very small <0.01 unless the trigonal or tetragonal dis-

tortion is quite large $\Delta > 0.1\lambda_{SO} \approx 40$ meV for IrO_6. The general results for scattered intensities and expectation values near the J_{eff}=1/2 limit are plotted in Fig. 2.3.

2.1.4 Resonant X-ray Scattering for $4d^4$ and $5d^4$

For $5d^4$ ions in the strong SOC limit, the ground state is J_{eff}=0, and the lowest-energy excitations are to a triplet of $J = 1$ levels. These Van-Vleck-type excitations are of great theoretical interest, as will be discussed in Chapter 5.

Using the same framework as was used for the d^5 derivation, we will consider d^4 in the cubic limit [49]:

$$\begin{aligned}
R_{Q,L_3} =& -\frac{1}{3}\left(\epsilon_x\epsilon'_x + \epsilon_y\epsilon'_y + \epsilon_z\epsilon'_z\right)\tilde{S}_z^2 \\
R_{M,L_3} =& -\frac{\sqrt{6}}{2}\left[\left(\epsilon_y\epsilon'_z - \epsilon_z\epsilon'_y\right)\tilde{S}_x + \left(\epsilon_z\epsilon'_x - \epsilon_x\epsilon'_z\right)\tilde{S}_y\right] \\
R_{Q,L_2} =& +\frac{1}{12}\left(\epsilon_x\epsilon'_x + \epsilon_y\epsilon'_y + 10\epsilon_z\epsilon'_z\right)\tilde{S}_z^2 \\
&+\frac{3}{4}\left[\left(\epsilon_x\epsilon'_x - \epsilon_y\epsilon'_y\right)\left(\tilde{S}_y^2 - \tilde{S}_x^2\right) + \left(\epsilon_x\epsilon'_y + \epsilon_y\epsilon'_x\right)\left(\tilde{S}_x\tilde{S}_y + \tilde{S}_y\tilde{S}_x\right)\right] \\
R_{M,L_2} =& +\frac{3}{4}\left(\epsilon_x\epsilon'_y - \epsilon_y\epsilon'_x\right)\tilde{S}_z
\end{aligned} \tag{2.27}$$

where now $\tilde{\mathbf{S}}$ operators represent the pseudospin-1 basis.

The full derivation, with corrections for tetragonal/trigonal distortions, is in Ref. 49. The relevant point is that for d^4 the resonant X-ray scattering cross-section contains a (matter) quadrupole signal, even when only one site is considered. Thus d^4 RXS could plausibly be used to detect spin quadrupolar (nematic) order, such as the proposed Higgs mode in Ca_2RuO_4 [50].

Another instructive limit, especially for the work in Chapter 5, is that in which compressive distortions are much greater than SOC ($\Delta \gg \lambda_{SO}$). This is the S=1 ground state where the $J = 1$ doublet is brought close enough to mix with the $J = 0$ level.

Here, the pseudospin-1 levels correspond to the 'triplon' Van-Vleck excitations as follows: $\frac{1}{\sqrt{2}}(\tilde{S}_x + \tilde{S}_y) \leftrightarrow \tilde{T}_z$, and $\tilde{S}_z \leftrightarrow \frac{1}{\sqrt{2}}(\tilde{T}_x + \tilde{T}_y)$; see Ref. 51 for a more complete discussion. In this case,

$$\begin{aligned} R_Q &= 0 \\ R_{M,L_3} = -R_{M,L_2} &= -\frac{1}{\sqrt{8}}\left[\left(\epsilon_y\epsilon'_z - \epsilon_z\epsilon'_y\right)\tilde{S}_x + \left(\epsilon_z\epsilon'_x - \epsilon_x\epsilon'_z\right)\tilde{S}_y\right] \\ &= -\frac{1}{\sqrt{8}}\left(\boldsymbol{\epsilon}\times\boldsymbol{\epsilon}'\right)\cdot\hat{z}\tilde{T}_z \end{aligned} \tag{2.28}$$

where, in the last line, I have changed the basis from pseudospin-1 to triplons as defined above. This anisotropic cross-section is a simple starting point for considerations of how the Van-Vleck signal looks like in most $4d^4$ systems, and in $5d^4$ systems with very strong distortions.

2.1.5 Nonmagnetic Resonant Diffraction

The multipole formalism does not just apply to magnetic excitations and order; it is also applicable to other details of the material. For instance, resonant X-ray diffraction has been used in many studies of orbital ordering, by measuring the electric multipoles of the sample; early work was on a variety of samples including Mott insulators like YVO_3 [52].

One especially pernicious nonmagnetic scattering mechanism is termed the Anisotropic Tensor Scattering (ATS, or anisotropic resonant scattering, or Templeton scattering). ATS can yield scattering at structurally allowed *and* 'forbidden' wavevectors as a consequence of nonmagnetic orbitals. A good review of this is by Dmitrienko and co-workers, and it was initially discovered and developed theoretically by Templeton and Templeton [53, 54]. ATS arises from anisotropy in the resonant tensor form factors related to anisotropic charge distributions. For example, in the rare earth pyrochlore iridates,

ATS arises from a slight Jahn-Teller-like distortion of the iridium-oxygen octahedra [55]. While ATS hinders direct interpretation of 'forbidden' peaks as magnetic, it also yields rich information about local electronic symmetries.

The 'forbidden' ATS peaks mainly occur at wavevectors where glide planes or screw axes lead to destructive interference in the nonresonant diffraction when there is a difference in the form factor for scattering along and perpendicular to the local symmetry axis. ATS can also occur for materials with 'special' atomic positions, as with diamond's (222) reflection. For each material, the ATS contribution can have different polarization and azimuthal dependencies as derived by the formalism for each space group. As previously mentioned, ATS can mimic magnetic scattering; for instance, on resonance for a site on a 2_1 screw axis, the dd scattering is purely in the $\sigma - \pi'$ channel [53].

2.2 Resonant X-ray Scattering Experiments

For $4d$ and $5d$ systems, the resonant X-ray scattering (RXS) is manageable to interpret qualitatively (and J_{eff}=1/2 systems are especially straightforward). The main assumptions, (1) of dipole-only scattering terms in the multipole expansion and (2) of 1-site interactions dominating the signal, seem to generally describe most signals in experiments. With these assumptions, there is no difference between the theories for elastic and inelastic scattering.

While RXS techniques share some similarities with diffraction, the key difference is that RXS is inherently a multi-step process. One important example of this distinction is that in RXS measurements of ions arranged like dimers (bilayers, trimers, etc.), the double-slit interference condition can be satisfied. The identity of which ion in the pair yielded the emitted photon, the 'slit' in this double-slit experiment, cannot be determined in principle [56]. This is because the delocalization of the photoexcited electron

in the intermediate state removes the 'which-path' information for the emitted photon [22, 57]. This result was shown in early REXS experiments on magnetic Bragg peaks in $Sr_3Ir_2O_7$ [58]. Recently this finding has proven essential for interpreting new RIXS excitations in $Sr_3Ir_2O_7$ [59] and for the work presented in Chapter 5.

RXS techniques are crucially dependent on the high flux and high energy discrimination available at modern X-ray sources: synchrotrons and free-electron lasers. This is because the measured intensity of magnetic Bragg peaks is often a factor of 10^6 or more weaker than the structural Bragg peaks. The general principle for these varied X-ray sources is to accelerate relativistic charges in order to generate X-rays. Synchrotrons accelerate an electron or positron beam in a ring, radiating a broad spectrum of light tangent to the ring. In either a free-electron laser or an undulator within a synchrotron, arrays of permanent magnets with alternating polarity impart oscillations on the electron/positron beam, leading to the radiation of tunable and highly coherent light with low angular divergence [41].

While resonant diffraction "RXD" is helpful by itself, analyzer crystals used in resonant elastic or inelastic scattering ("REXS" or "RIXS") provide additional information.[2] Scattering from an analyzer crystal selects only energies that satisfy the diffraction condition, which screens out the fluorescence and some spurious signals. In RIXS, an array of low-mosaicity (i.e. low acceptance angle) analyzers are used to sharpen the analyzer's energy resolution. In the case of REXS, a single analyzer in different geometries additionally screens the polarization of the scattered beam. It is best to think about these techniques as akin to neutron scattering: they are flux-limited, so we must compromise between reciprocal space resolution, energy resolution, and count rate. To make these techniques feasible in a few days, REXS analyzers integrate over (relatively) large energy

[2]More acronyms are frequently used. The most common, resonant X-ray magnetic scattering (RXMS) is confusing because it has described experiments both with and without an analyzer crystal (RXD and REXS).

ranges, and RIXS analyzers integrate over (relatively) wide regions of reciprocal space.

2.2.1 Elastic (REXS) and Magnetic Diffraction

The resonant elastic X-ray scattering (REXS) technique is generally performed at instruments with high angular resolution, high flux, incident energy tunability, and the ability to accommodate an analyzer crystal. The power of REXS over other RXS techniques is to select the outgoing X-ray polarization. This is typically measured in two channels, where the outgoing polarization is either along or perpendicular to the incident polarization. When the incident polarization is perpendicular to the scattering plane σ, these two channels are dubbed $\sigma - \sigma'$ and $\sigma - \pi'$ respectively.

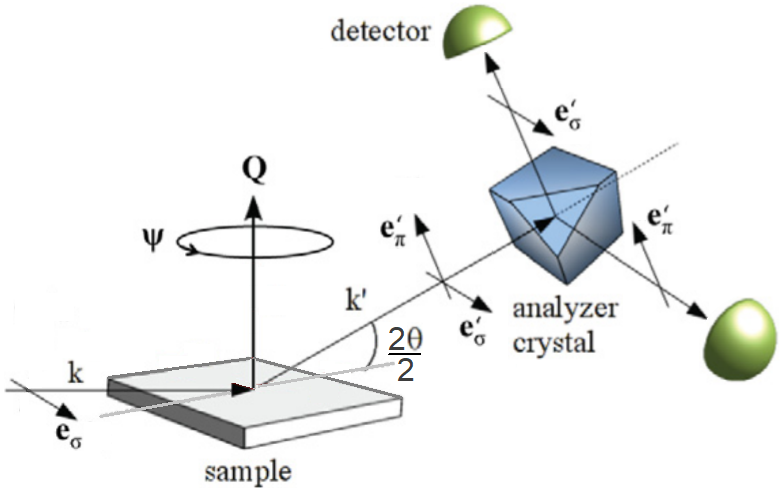

Figure 2.4: The setup of a REXS experiment, highlighting the polarization definitions in a vertical scattering plane. Here the polarization unit vector is labeled $\hat{\mathbf{e}}$, the azimuthal angle is labeled Ψ, and the typical definitions for Q, k, k', and 2θ hold.

Reiterating our finding for J_{eff}=1/2 states in the nearly-cubic limit (Equation 2.26) for the intensity: $I \propto \left|\left(\boldsymbol{\epsilon} \times \boldsymbol{\epsilon}'\right) \cdot \tilde{\mathbf{S}}\right|^2$. We can see that this signal ought to only be measurable in the $\sigma - \pi'$ channel. Thus, in the resonant scattering community, often $\sigma - \pi'$ is called the spin-flip channel.

In REXS, the way polarization is selected is by exploiting Thomson scattering. At scattering angle $2\theta = 90°$, an analyzer crystal only diffracts photons with polarization perpendicular to its scattering plane. Please see the schematic in Fig. 2.4.

Of course, polarization is not the only experimental tool to distinguish and study magnetism in RXS. Below is a description of how other parameters can provide additional information about site-specific magnetism.

1. *Azimuthal Angle*: Since the cross-section has explicit dependence on the magnetic vector's direction, we can use the azimuthal angle to learn about the moment orientation. Here azimuth refers to the angle not defined by momentum transfer **Q**; see Fig. 2.4. For the simple case of the J_{eff}=1/2 state, for a square-lattice G-type antiferromagnet like Sr_2IrO_4, the cross-section specifies that the azimuthal dependence goes as $\cos^2(\psi)$ in the $\sigma-\pi'$ channel, with ψ=0 defined as the angle along the moment direction. The form can of course be more exotic for other lattice symmetries (i.e. three-fold), and is more complicated away from the d^5 configuration. On the other hand, for structurally allowed 'charge' peaks in the absence of ATS, there ought to be no azimuthal dependence. And an overly sharp angular dependence is a strong indication of multiple scattering.

2. *Correlation Lengths*: The width of a magnetic Bragg peak is a measure of the spatial extent of the order. Since resolution ellipsoids are not typically tabulated for X-ray instruments, one must measure nearby structural Bragg peaks; magnetic peak width is calculated by subtracting a charge peak width in quadrature, as with neutron scattering.

3. *Incident Energy*: Magnetic peaks are resonantly enhanced near the L_3 absorption edge, whereas structural peaks are weaker due to absorption. For low-spin $d^{\leq 5}$ ions the absorption maximum is for the e_g manifold, and the magnetic peak is several eV

below in the relevant t_{2g} valence level. The resonance width is typically several eV for Ir (set by many things including beamline resolution, but also by the intrinsic core-hole lifetime).

4. *Temperature*: For magnetic order, the scattered intensity should behave like an order parameter. For the simple case of the J_{eff}=1/2 state, intensity is proportional to the moment squared: $I \propto \langle \hat{R}^\dagger \hat{R} \rangle \propto \tilde{S}^2$.

2.2.2 REXS at APS Diffractometer 6-ID-B

Now we will focus on one instrument optimized for REXS, Beamline 6-ID-B at the Advanced Photon Source (APS) synchrotron at Argonne National Laboratory in Lemont, Illinois, USA. The APS is a highly coherent 3$^{\text{rd}}$ generation (soon to be 4$^{\text{th}}$ generation) 6-7 GeV storage ring with high brightness and flux. As the name abbreviates, 6-ID-B is in the B hutch downstream from an Insertion Device (or an undulator in a straight segment of the synchrotron, as opposed to a bending magnet). This undulator has a length of 2.47 m and a period of 33 mm, which defines the spacing between permanent magnets with alternating polarity. The first undulator harmonic can access about 4-13 keV photon energy, and the monochromator can access up to about 20 keV at higher undulator harmonics. This instrument's incident flux after the monochromator is near 10^{13} photons/s over the focused beam area, which is about 0.1 mm^2 prior to slits. Another useful parameter is that this instrument's incident photons are ≈99% horizontally polarized.

The overall instrumental setup is fairly standard for REXS. From the synchrotron's white beam, a Si(1,1,1) double-bounce monochromator selects an energy with a typical energy resolution of about 1 eV at an incident energy of 11 keV. After several optics tables with slits and mirrors to trim and focus the beam, the beam impinges on the

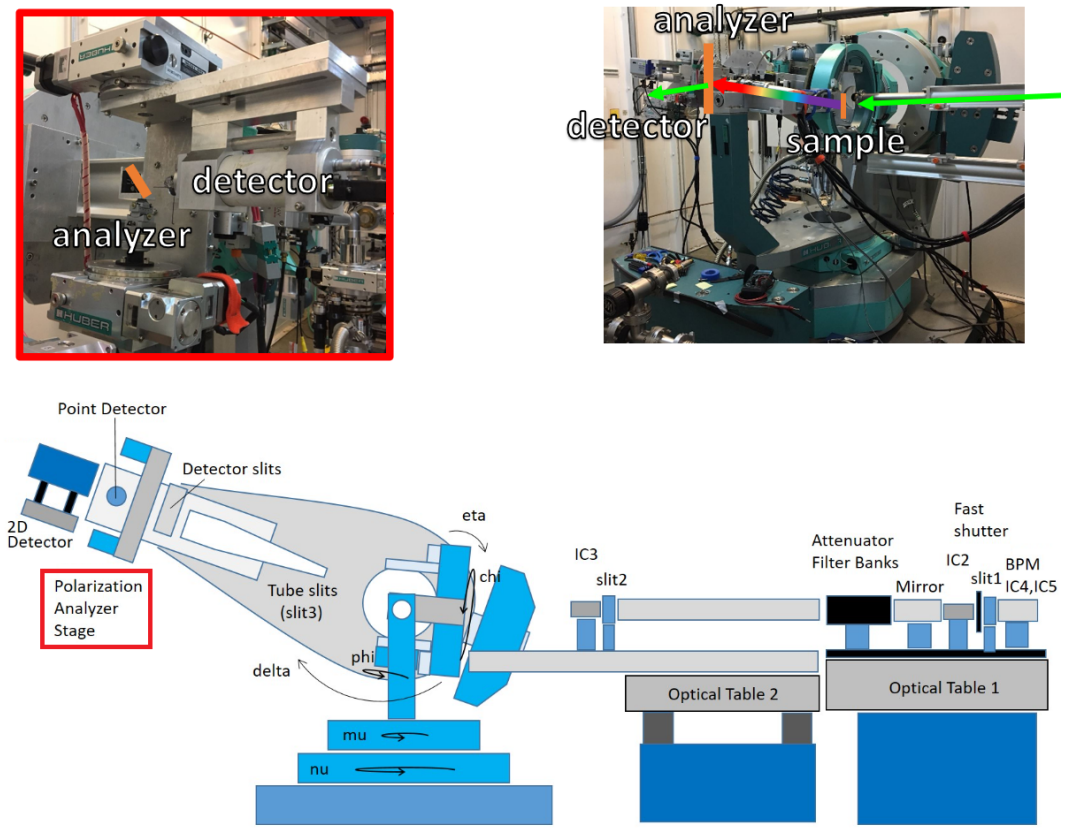

Figure 2.5: An overview of the REXS beamline 6-ID-B at the APS. The top right and bottom panels are a photograph and a schematic of the diffractometer. Green lines indicates the monochromatic incident and analyzed beam, and the narrow rainbow line indicates the outgoing beam scattered from the sample. Ion Chamber is abbreviated as IC. The top left panel highlights the polarization analyzer stage.

sample (here in a 6-circle Huber $\psi-$diffractometer). The sample can be cooled via a cold finger at the end of a cryostat, sealed within a Be dome. After scattering from the sample, the beam scatters from a plane analyzer crystal into a point detector. Each component has many associated linear and angular motors. Flight paths between components are typically evacuated to improve signal-to-noise and flux. Ion chambers passively monitor the flux.

At 6-ID-B specifically, most experiments utilize a graphite analyzer crystal. The reflectivity for graphite is high. Also the angular acceptance is large, which enhances the

flux at some cost to the detected energy resolution.

The supreme angular resolution at 6-ID-B has made great strides in improving correlation length bounds and in pinpointing incommensurate magnetic orders (e.g. Ref. 60). But it also means that measurements on this instrument are challenging. The detected signal is sensitive to the exact crystal orientation, which must be carefully tweaked for small changes in temperature or azimuthal angle.

2.2.3 Inelastic (RIXS) and Magnetic Excitations

The resonant inelastic X-ray scattering (RIXS) technique is generally performed at specialized spectrometers with high energy resolution and high flux. Since it is performed in a backscattering geometry, RIXS does not offer polarization selection.

RIXS can measure many different kinds of excitations, more than neutrons and often more than an experimentalist wants. In addition to magnetic excitations (spin waves i.e. magnons, and dressed varieties like paramagnons and spin-orbit excitons), all sorts of electronic and lattice excitations are accessible, including phonons, plasmons, orbital excitations (like orbitons and charge transfer), and so on. These can typically be distinguished by their energy, momentum, and temperature dependence, and also by measuring in other Brillouin zones. In order to further assess the nature of the excitations, RIXS is typically measured in conjunction with other probes like optical reflectivity.

RIXS is a measure of the scattering function (or dynamic structure factor) $S(\mathbf{Q}, \omega)$ which is proportional to the imaginary part of the susceptibility tensor via the fluctuation-dissipation theorem [42, 61]. However RIXS intensities are typically qualitative; I am not aware of a method for normalizing to 'absolute units' for comparing between different Brillouin zones or between different samples. To compare spectra within one zone apples-to-apples, often experimentalists measure with a fixed scattering angle 2θ to make the

X-ray absorption length in the sample the same, but this does not account for finer corrections.

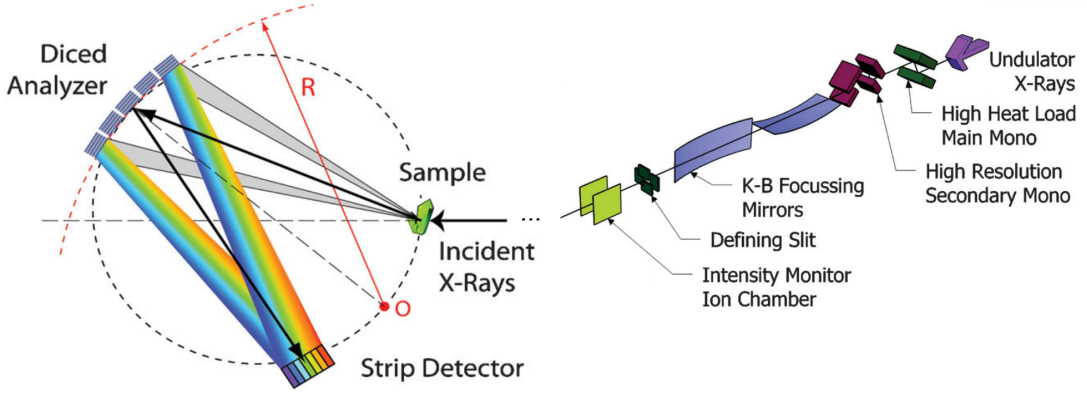

Figure 2.6: The setup of a RIXS instrument, highlighting the circular diced analyzer which focuses to a strip detector. The Rowland circle for the analyzer's diffraction is shown in red. Other upstream components are shown on the right. Adapted from [46]. Copyright 2011 American Physical Society.

2.2.4 RIXS at APS Spectrometer 27-ID-B

Now we will focus on one instrument optimized for RIXS, Beamline 27-ID-B at the APS. This instrument also uses an insertion device (ID). There are actually two 2.4 m long, 30 mm period undulators in this ID.

This instrument is optimized for energy resolution. It utilizes two sets of monochromators (see schematic in Fig. 2.7) to achieve an incredibly fine incident energy resolution of about 10 meV at an incident energy of 11 keV. The first monochromator is a double-crystal diamond(1,1,1) monochromator designed to handle a high heat-load from the considerable incident flux. The second is usually a four-bounce Si(4,4,8) monochromator, but for high-resolution applications a newly developed double-bounce quartz(-3,0,9) monochromator can achieve record-shattering 6 meV overall instrumental resolution [62].

Downstream from the monochromators, the K-B focusing mirrors make the typical

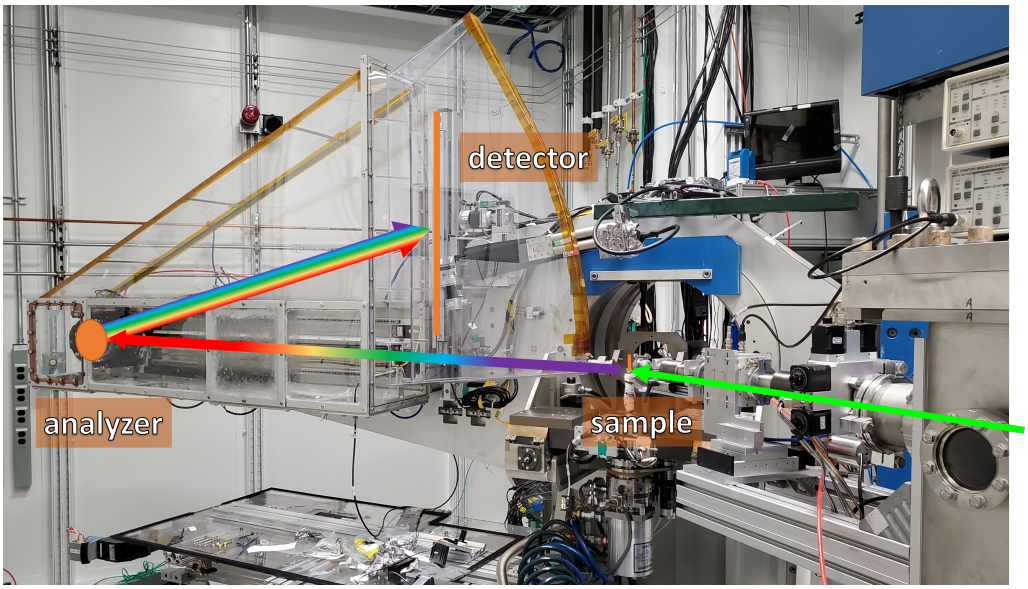

Figure 2.7: The RIXS beamline 27-ID-B at the APS. The overlaid green line indicates the monochromatic incident beam, the narrow rainbow line the outgoing beam scattered from the sample, and the wide rainbow line the analyzed beam.

spot size near 300 μm^2 before slits, which is helpful for the maintaining the overall instrumental resolution and for measuring small samples.

The RIXS measurements in this dissertation used a Si(4,4,8) diced spherical analyzer crystal [63]. With it in place, the overall instrumental energy resolution is about 35 meV. This optic was fabricated by dicing a 100 mm diameter Si wafer on a polycarbonate substrate, and then gluing that to a plano-concave glass lens with a 2 m curvature radius. The result is many pixel-like flat crystals that each have small angular acceptances. The analyzer is at the end of an evacuated 'two-theta arm' shown in Fig. 2.7. Spherical optics focus to a line; this analyzer focuses onto a strip detector with energy discrimination. The large size of the spherical analyzer helps boost the RIXS signal. It accomplishes this gain by its large solid angle, effectively integrating over a large swath of reciprocal space.

For the highest-recorded-resolution RIXS setup on this same beamline, a quartz(-3,0,9) diced analyzer crystal was developed, with an intrinsic resolution of <4 meV [64].

This, along with a Montel mirror and a Si(1,1,1) collimator between the sample and analyzer, enables supreme energy resolution on this beamline [65], which has recently been used to shed light on the hyperhoneycomb iridate [30]. However, there is a trade-off between flux and energy resolution. The Si monochromator and analyzer setup has more flux, which is the limiting factor for many measurements.

2.3 Neutron Scattering Theory

Now we will briefly touch on several neutron scattering cross-sections that will be explored in later chapters. This section is a purposely compact assortment of relevant ideas, which are thoroughly derived in textbooks [42, 66].

The double differential cross-section (Equation 2.1) for neutrons is related simply to the scattering function (or dynamic structure factor) $S(\mathbf{Q},\omega)$ by:

$$\frac{d^2\sigma}{d\Omega dE} = \frac{\sigma}{4\pi\hbar}\frac{k'}{k}S(\mathbf{Q},\omega). \tag{2.29}$$

For neutron scattering from nuclei, the cross-section is related to a site's scattering length b via:[42]

$$\begin{aligned}\sigma = 4\pi b^2 &= 4\pi\bar{b}(\mathbf{Q})^2 + 4\pi(\Delta b)^2 \\ &= \sigma_{\text{coh}} \qquad + \sigma_{\text{incoh}}\end{aligned} \tag{2.30}$$

where the coherent and incoherent components arise from the average $\bar{b}$ and standard deviation $(\Delta b)^2 = \bar{b^2} - (\bar{b})^2$ of the scattering lengths of the various isotopes occupying that site. The incoherent scattering is weakly dependent on the momentum transfer $\mathbf{Q}$ and results in a noisy background. In the case of elastic scattering (diffraction), the dynamic structure factor is just the crystal structure factor with a Debye-Waller factor that accounts for phonons.

2.3.1 Magnetic Neutron Scattering

First we touch on the results for magnetic neutron diffraction. For scattering from electrons' moments, the double differential cross-section is

$$\left(\frac{d^2\sigma}{d\Omega dE}\right)_{\text{mag}} = (\gamma r_0)^2 \frac{k'}{k} S_{\text{mag}}(\mathbf{Q},\omega). \tag{2.31}$$

with γ the neutron gyromagnetic ratio and r_0 the electron radius. But what is the magnetic scattering function? Consider the interaction Hamiltonian $-\boldsymbol{\mu}_n \cdot \mathbf{B}$, a dot product between the neutron's moment[3] and the electrons' magnetic field $\mathbf{B}$. If we consider a sublattice with only a spin contribution to the total angular momentum $\mathbf{M} = 2\mu_{\text{B}}\mathbf{S}$, neutrons therefore are measuring the magnetization density:

$$\mathbf{M}(\mathbf{Q}) = 2\mu_{\text{B}} \sum_j \mathbf{S}_j f_{\text{mag,j}}(\mathbf{Q}) \mathrm{e}^{\mathrm{i}\mathbf{k}\cdot\mathbf{R}_j} \tag{2.32}$$

where the magnetic form factor $f_{\text{mag}}(\mathbf{Q})$ is valence-specific. It is essentially the Fourier transform of the real-space magnetization density $\mathbf{M}(\mathbf{r})$:

$$f_{\text{mag}}(\mathbf{Q}) = \frac{\int d\mathbf{r}' \mathbf{M}(\mathbf{R}+\mathbf{r}') \mathrm{e}^{\mathrm{i}\mathbf{Q}\cdot\mathbf{r}'}}{\int d\mathbf{r}' \mathbf{M}(\mathbf{R}+\mathbf{r}')}. \tag{2.33}$$

With these definitions in place, the elastic magnetic cross-section (without the crystal structure factor) is:

$$\left(\frac{d^2\sigma}{d\Omega dE}\right)_{\text{elastic,mag}} = \left(\frac{\gamma r_0}{2\mu_{\text{B}}}\right)^2 \left|\hat{\mathbf{Q}} \times \mathbf{M}(\mathbf{Q}) \times \hat{\mathbf{Q}}\right|^2. \tag{2.34}$$

So for magnetic diffraction, we can only measure the component of the moment that is perpendicular to the momentum transfer. There is a simple extension of this result for

[3] The neutron's moment is $\mu_n = -1.913\mu_N$, with the nuclear magneton $\mu_N = e\hbar/(2m_p)$.

spin states with finite angular momentum - see Ref. 66. Please note that this result is related to, but quite different from, the resonant X-ray cross-section.

Now we consider the magnetic signals in inelastic neutron scattering. Note that the scattering function in Equation 2.29 is essentially a Fourier transform of the correlation function. So for magnetic signals, this is just the spin-spin correlation function. We can therefore relate $S_{\mathrm{mag}}(\mathbf{Q},\omega)$ to the imaginary part of the susceptibility χ'' through the fluctuation-dissipation theorem and get:

$$\chi''(\mathbf{Q},\omega) = \pi(1 - \mathrm{e}^{-\omega/k_{\mathrm{B}}T})I(\mathbf{Q},\omega)/|f_{\mathrm{mag}}(\mathbf{Q})|^2 \tag{2.35}$$

where the first term that corrects for bosonic filling with temperature is called the detailed balance, and here the measured intensity I has been corrected for the factor k'/k and converted to absolute units. This result is general for powder measurements, to a multiplicative factor. Since the susceptibility is a tensor, for application in single crystals the above equation requires further corrections that account for $\mathbf{Q}$ – see for example Ref. 67.

Chapter 3

Moment Un-freezing in the Monolayer Perovskite $Sr_2Ir_xRu_{1-x}O_4$

[1] This project was designed to explore the fascinating metallic phases that link the correlated metal and unconventional superconductor Sr_2RuO_4 to the J_{eff}=1/2 antiferromagnetic insulator Sr_2IrO_4. We sought to determine how the correlated, itinerant moments for Sr_2RuO_4 evolve into local moments. Based on the existing research, little definitive conclusions could be made about metallic (Ru-rich) samples. Existing crystals were fairly inhomogeneous and small, making them poorly suited for either magnetotransport or neutron scattering studies.

The preliminary thrust of this work was sample synthesis. We endeavored to boost experimental efforts on unconventional correlated metal phases in $Sr_2Ir_xRu_{1-x}O_4$ by improving the sample quality and volume of crystals in the alloy series. Crucially, floating zone synthesis fully opens this class of materials to study via neutron scattering, which enabled more thorough investigation of O positions, magnetic structure, and excitations than previous work on smaller crucible-based flux-grown crystals. Floating zone synthe-

[1] Part of this chapter includes work from one of our publications, Ref. 68: Zach Porter, Eli Zoghlin, Julian L. Schmehr, and Stephen D. Wilson. Crystal growth of $Sr_2Ir_xRu_{1-x}O_4$for $x \leq 0.4$, Journal of Crystal Growth 578, 126432 (2022). Copyright 2021 Elsevier B.V. All rights reserved.

Much of the rest of the chapter is from an unpublished manuscript. My collaborators are: Aaram J. Kim, Paul M. Sarte, Eli Zoghlin, Alexander I. Kolesnikov, Rebecca L. Dally, Jeffrey W. Lynn, Adam A. Aczel, Roser Valentí, and Stephen D. Wilson.

sis also has the potential to improve the alloy homogeneity due its ability to actively mix the melt during the crystal growth process. We found that the resultant gram-sized samples are more uniform in composition than comparable flux-grown crystals.

What we discovered was unusual compared to other substitution series for Sr_2RuO_4: no apparent short-range or long-range magnetic order. Yet the local moment magnetism turns on at a critical Ir concentration x=0.18 in $Sr_2Ir_xRu_{1-x}O_4$. This marks a recently established Lifshitz (quantum phase) transition, and we find a coincident quantum critical response in the magnetotransport and the heat capacity. We interpret this result in the context of moment freezing, a phenomenon that may link this transition to the mechanism for the superconductivity in Sr_2RuO_4.

3.1 Introduction and Previous Work

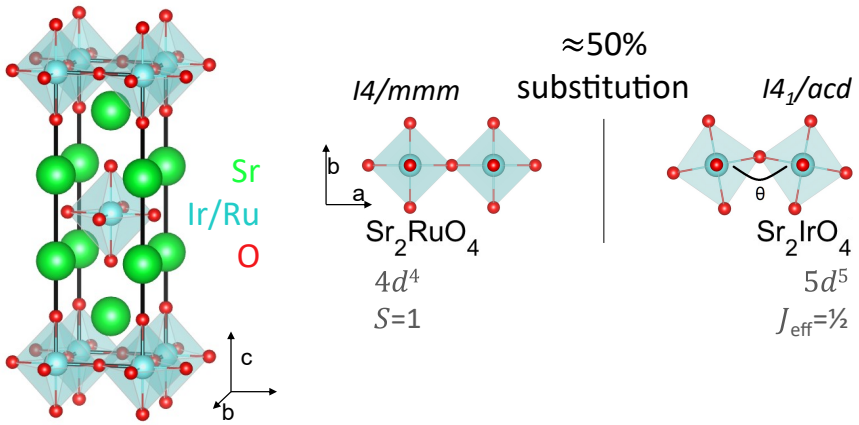

Figure 3.1: Ruddlesden-Popper structure of $Sr_2Ir_xRu_{1-x}O_4$. The $I4/mmm$ unit cell is shown on the left. In-plane tilts are shown schematically on the right for Sr_2RuO_4 and Sr_2IrO_4, along with quantum numbers for the B-site ions.

$Sr_2Ir_xRu_{1-x}O_4$ is an alloy of the single layer member of the Ruddlesden-Popper series; its chemical formula is $Sr_{n+1}(Ir,Ru)_nO_{3n+1}$ with n=1. It consists of alternating layers

of SrO rock salt and perovskite, such that there are separated planes of corner-sharing $(Ir,Ru)^{4+}O_6^{2-}$ octahedra. Hence it is occasionally considered to be a monolayer perovskite.

We studied $Sr_2Ir_xRu_{1-x}O_4$ with the intent to look for 'strange metal' phases. These mysterious phases are the hallmark of a metallic quantum critical point (QCP), a continuous phase transition at zero temperature (see Section 1.3). Strange metals are characterized by linear-in-temperature resistivity which is not captured by the Fermi liquid theory [31, 32]. Such phase behavior has been observed for several families of unconventional superconductor materials, where the superconducting phase is predicted to be related to the quantum critical fluctuations. For the iron-based and heavy-fermion-based superconductors, the QCPs frequently coincide with the end of antiferromagnetic phases, which may suggest that the Cooper pairing is spin-driven (for example, Refs. 35–37). However, the especially strong pairing mechanism for the cuprates has remained a puzzle. The cuprate QCP seems to lie at the end of the enigmatic pseudogap phase, with incoherent quasiparticles and various density wave fluctuations which are difficult to directly study [34]. There seems to be consensus that Mott physics are key to understanding the cuprates, whether within the QCP theoretical framework or other theories [69, 70]. Therefore, uncovering the low-temperature physics of metallic quantum criticality in another system with Mott physics and density waves may provide clues to the nature of the superconductivity in the cuprates.

Sr_2RuO_4 is a paramagnetic correlated metal with an effective moment near 0.5 μ_B/Ru, greatly reduced from the expected value 2.8 μ_B/Ru for $\mathbf{S}$=1 $4d^4$ local moments [71]. This paramagnetic phase lies near an electronic instability, as evidenced by the spin density wave fluctuations [72, 73] and the unconventional superconductivity for ultrapure samples [74]. Dilute substitution of Ru for other d block elements (Ti, Mn, Co, Fe) results in magnetic short-range order at low dopant concentrations ∼1% [67, 75, 76]. To our knowledge, Ir is the only Ru substitute in Sr_2RuO_4 for which no static order has been

demonstrated for x<0.3 (though a possible exception is Rh substitution [77]). Thus, this study is uniquely positioned to explore the nature of the unusual paramagnetic ground state for Sr_2RuO_4.

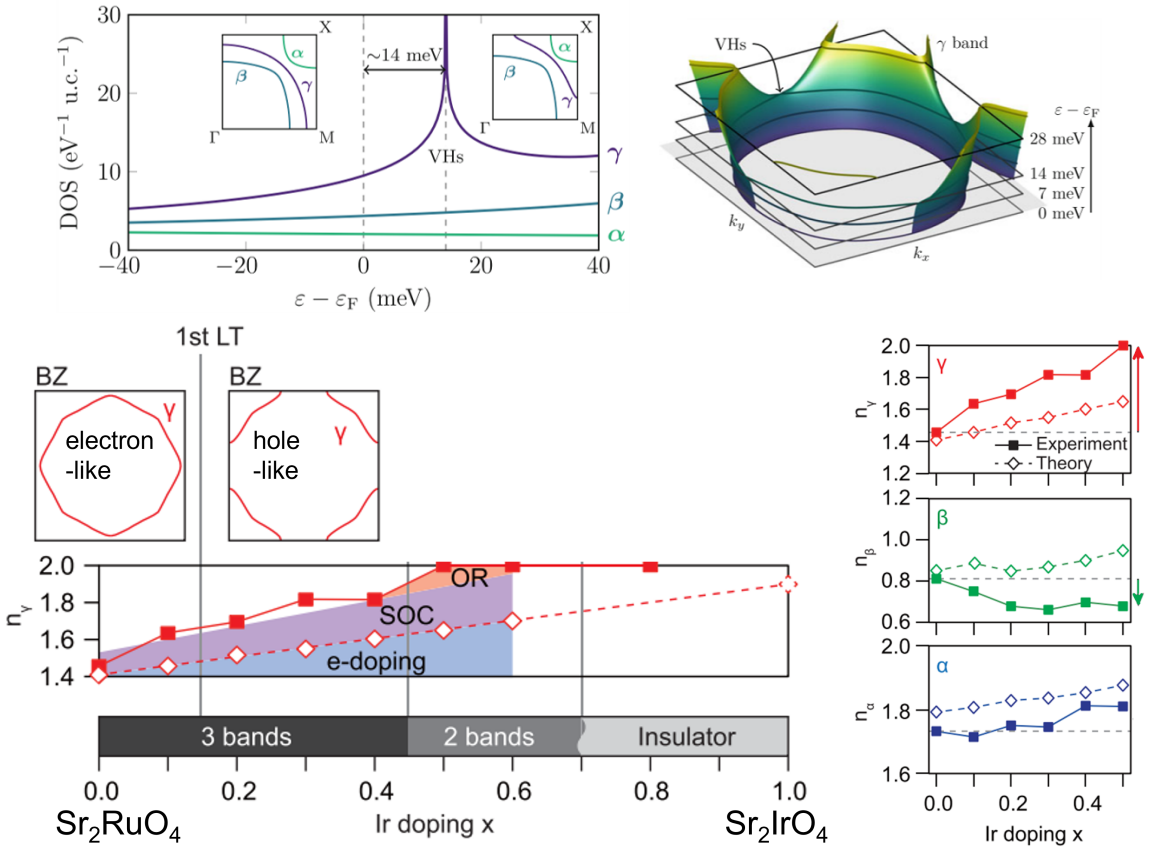

Figure 3.2: *Top panels*: band topology and density of states of Sr_2RuO_4. From [78] Copyright 2018 Springer Nature. *Bottom panels*: orbitally-selective filling in the case of $Sr_2Ir_xRu_{1-x}O_4$. Ir substitution mostly fills the γ-band at low x, rather than rigidly shifting the Fermi level. The Lifshitz transition lies between 0.1<x<0.2. Adapted from [79] Copyright 2021 American Physical Society.

Substitution of Ru for $5d^5$ Ir^{4+} ions in $Sr_2Ir_xRu_{1-x}O_4$ introduces delocalized electrons and J_{eff}=1/2 magnetic impurities into this near-critical metallic phase. Recently, an angle-resolved photoemission (ARPES) study demonstrated a Lifshitz transition in $Sr_2Ir_xRu_{1-x}O_4$ for 0.1<x<0.2 where the topology of the γ-band transitions from electron-like to hole-like; see Fig. 3.2 [79]. This study found that electron doping from Ir substi-

tution is orbitally selective, filling the γ-band more than comparable levels of La substitution [80], an effect which was attributed to the increased effective spin-orbit coupling energy scale.

In the multiorbital metal Sr_2RuO_4, the γ-band is primarily composed of Ru d_{xy} orbitals, and forms a 2-dimensional sheet that has the largest density of states at the Fermi level. The additional filling at low Ir content comes from depleting the β-band, which like the α-band is a nearly 1-dimensional sheet with mixed Ru d_{xz}/d_{yz} character. It is these α- and β-bands which exhibit Fermi surface nesting. The resultant spin density wave fluctuations have the quasi-2-dimensional wavevector (h, k)=$(0.3, 0.3)$ in reciprocal lattice units (r.l.u.) [72].

For the rest of this section we will consider pertinent work in other Sr_2RuO_4 variants, mostly other substitution series. Later in this chapter, after establishing some synthetic and structural details, we explore the thermodynamic signatures of the Lifshitz transition in $Sr_2Ir_xRu_{1-x}O_4$. We present dc magnetization, magnetotransport, heat capacity, and neutron scattering measurements that are suggestive of metallic quantum criticality driven by moment freezing. We demonstrate that spin density wave fluctuations and incoherent quasiparticles seem to be prominent features of this transition, as in the cuprate superconductors.

3.1.1 Comparison to other Sr_2RuO_4 Substitution Series

We need to untangle the effects of the band fluctuations and the local moment magnetism in this study. To do so we start by examining other substitution series. First consider the relatively simple case of La substitution in $Sr_{2-y}La_yRuO_4$, where the electron doping is well-described by a rigid band shift; see Fig. 3.4 [80]. As La content increases toward the γ-band vHs at $y \approx 0.20$, Kikugawa and co-workers measured an

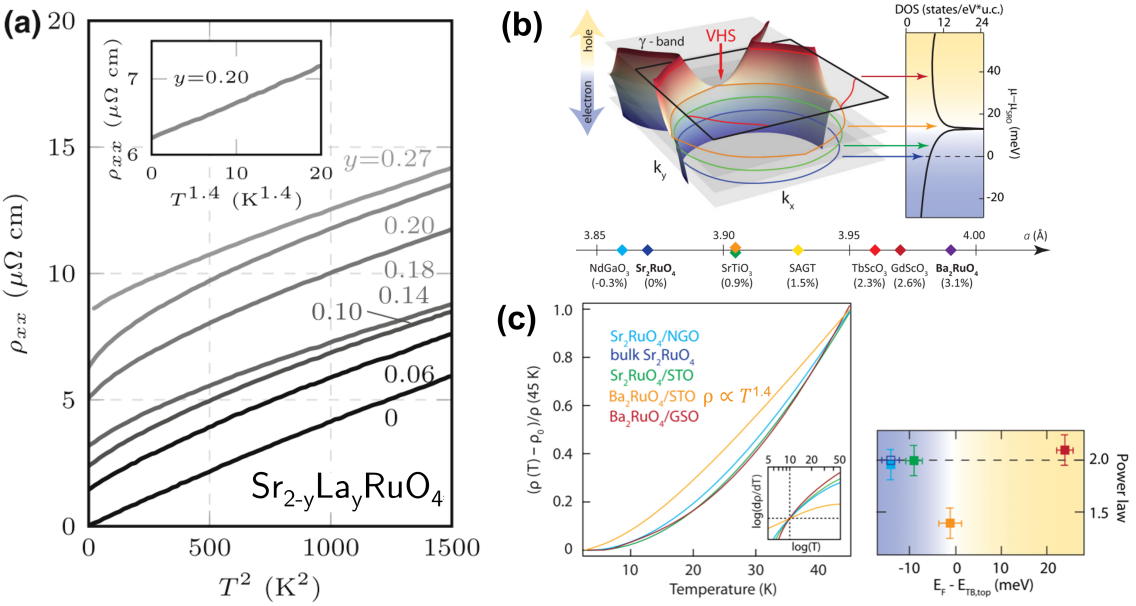

Figure 3.3: Crossing the Sr_2RuO_4 van Hove Singularity via electron doping and biaxial strain. (a) For $Sr_{2-y}La_yRuO_4$, resistivity measurements show a sudden shift to non-Fermi-liquid behavior near $x = 0.2$. From [78] Copyright 2018 Springer Nature, which is adapted from [81].(b) Schematic of van Hove singularity, with various epitaxial substrates and their lattice parameters indicated. (c) resistivity shows non-Fermi-liquid behavior near the putative van Hove singularity sample (Ba_2RuO_4 on $SrTiO_3$, abbreviated as STO). From [82] Copyright American Physical Society.

upturn in the low-temperature heat capacity near the vHs [81], similar to the Ir system. At y=0.20 the resistivity follows the form $\rho_{ab} = \rho_0 + AT^n$ with n=1.4 which may be evidence of quantum criticality (Fig. 3.3a). Interestingly, similar critical resistivity behavior was demonstrated for strained films of pure Sr_2RuO_4 and isostructural Ba_2RuO_4 (Fig. 3.3c) [82]. There, Burganov and co-workers produced and measured the ARPES for a sample near the vHs using +0.9% biaxial strain and $\Delta c/c$=+4.7%. (For comparison, the Ir sample near the vHs is minimally strained: biaxial strain is +0.1% and $\Delta c/c$=+0.3%.) This finding demonstrates that this form of criticality may be inherent to the vHs of Sr_2RuO_4, reached either via electron-doping or strain.

Regarding the magnetism in $Sr_{2-y}La_yRuO_4$, there is no static order and the suscep-

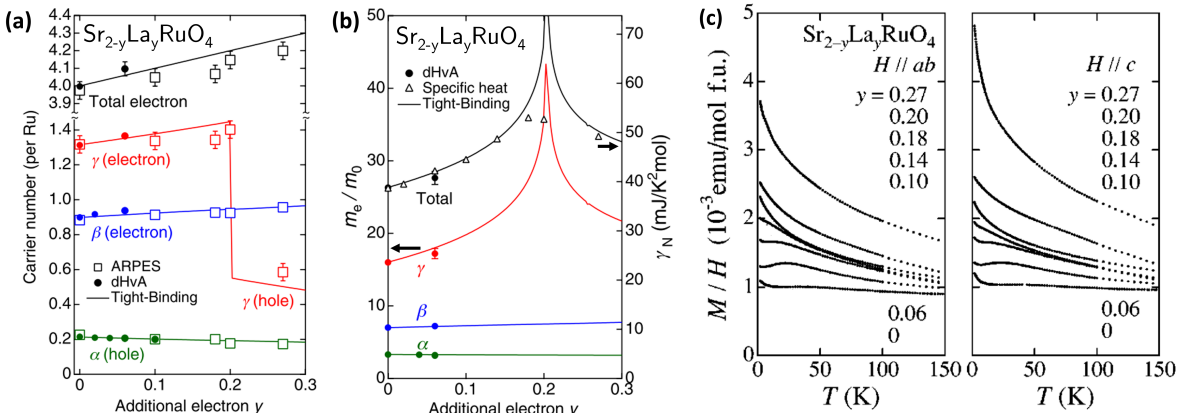

Figure 3.4: Rigid band shift-driven van Hove singularity in $Sr_{2-y}La_yRuO_4$. (a) Angle-resolved photoemission spectroscopy (ARPES) results suggest that the bands are filled fairly evenly. Across the Lifshitz transition $\gamma \approx 0.2$ the γ-band switches from electron-like to hole-like. (b) The Sommerfeld coefficient of the heat capacity γ_N, here approximated via C_p/T at T=0.5 K, is shown in empty triangles. Effective mass for each valence band (colors) and their sum (black) is extracted from the de Haas−van Alphen effect (dVhA) and shown in solid dots. (c) The dc susceptibility (field cooled, measured at 1 T) is shown both along ab and c, and is much more isotropic than for Ir substitution. Low-temperature glassy features are present. From [80, 81]. Copyright American Physical Society.

tibility isotropically increases toward the vHs; see Fig. 3.4. This magnetic response has been attributed to ferromagnetic fluctuations from the increase in density of states at the Fermi level, without direct evidence. Indirect experimental clues of the ferromagnetic fluctuations come an NMR study of pure Sr_2RuO_4 which suggests the γ-band's fluctuations are ferromagnetic [83]. Yet the susceptibility enhancement persists beyond the vHs, which is inconsistent with this explanation. Note that La substitution introduces Ru^{3+} J_{eff}= 1/2 moments. A local-moment picture of the magnetism captures the gradual increase in the Curie-Weiss effective moment μ_{eff} and the gradual decrease in the temperature-independent paramagnetism χ_0. Unfortunately the susceptibility has only been reported at a lower temperature range than our measurements, so it is hard to compare our Curie-Weiss results directly.

Another interesting substitution series is that with $3d^0$ Ti^{4+}, which does not seem to

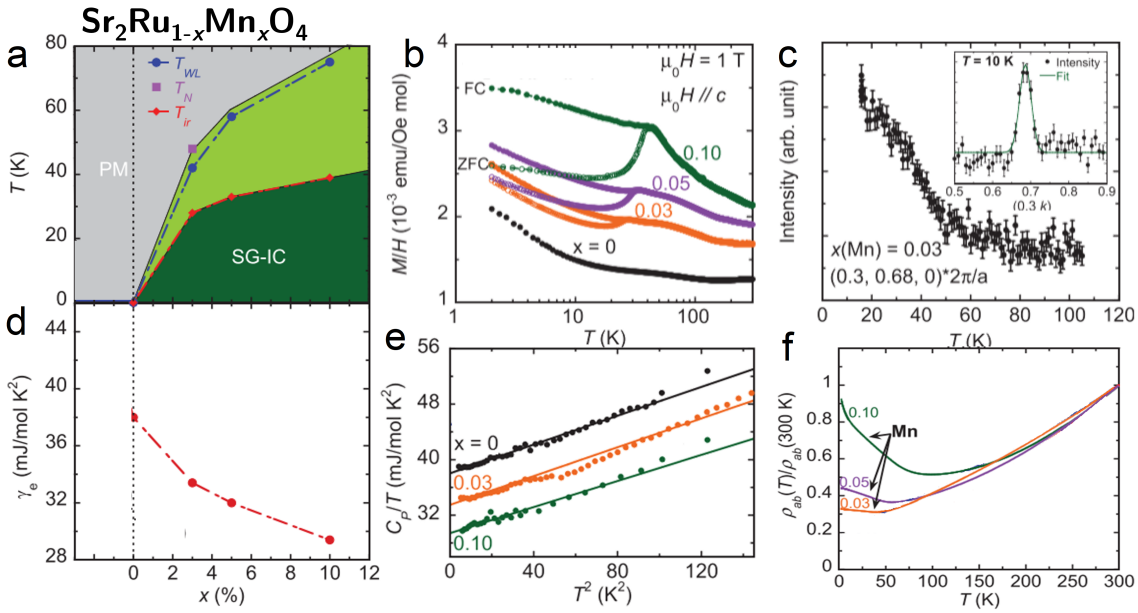

Figure 3.5: Close proximity to antiferromagnetism in $Sr_2Ru_{1-x}Mn_xO_4$. (a) The phase diagram, which evolves from paramagnetism (PM) to incommensurate spin-glass antiferromagnetism (SG-IC). The antiferromagnetic transition T_N (purple square, extrapolated to light-green region) and the resistivity upturn $T_{\rm WL}$ (blue circles) are not coincident with irreversibility in the bulk magnetization $T_{\rm ir}$ (red diamonds). (b) Bulk susceptibility M_c/H shows strong irreversibility on field cooling versus zero-field cooling (closed and open symbols). (c) Neutron diffraction intensity shows an elastic signal at the incommensurate wavevector associated with the spin-density wave in undoped Sr_2RuO_4. The K-scan in the inset has a large correlation length indicating short-range order. (d) Sommerfeld coefficient extracted from fitting the heat capacity C_p/T in (e), which decreases with Mn content. (f) Weak localization in the in-plane resistivity ρ_{ab} under increasing Mn content. From [75]. Copyright 2013 The Authors.

dope carriers. For $Sr_2Ru_{1-z}Ti_zO_4$, short-range and glassy antiferromagnetic order sets in at z=0.03, which demonstrates how close the ruthenate is to an electronic instability. The antiferromagnetism is marked by hysteresis along the c easy axis, and has the same ordering wavevector as the SDW for the parent Sr_2RuO_4 [84, 85]. With increasing Ti content z>0.03, the low-temperature heat capacity decreases [86, 87], and the resistivity shows insulating upturns, consistent with localization. Now, please compare nonmagnetic Ti with magnetic Mn, which additionally acts as a hole-dopant (Fig. 3.5) [75].

Notably, both Ti and Mn substitution yield the same phase behavior. Mn doping yields higher transition temperatures than Ti, which suggests that local moment magnetism strengthens the antiferromagnetic order. While no ARPES or inelastic neutron scattering is published for Mn, Ortmann et al. conjecture that Mn may stabilize the AFM order by enhancing nesting between the α and β Fermi surface sheets, possibly by hole-doping the α band selectively [75]. Taken together, these two substitution series suggest that enhanced itinerant fluctuations are what yield their long-range order.

3.2 Synthesis: High-Pressure Floating Zone

Synthesis of crystalline samples of $Sr_2Ir_xRu_{1-x}O_4$ was accomplished with a floating zone growth technique. This work owes its success entirely to the high-pressure floating zone furnace (named LAPIS) that my colleagues Julian, Michael, Eli, and Stephen designed, built, and commissioned [88].[2] We found that the use of a high pressure gas environment (70 bar mixed O_2 and Ar) greatly decreases the volatility and loss of the IrO_2 and RuO_2 reactants. In effect, this gas environment is what enabled record incorporation of iridium oxide (≈20 wt%) into the molten zone.

3.2.1 Synthesis Overview

Below I describe the growth of $Sr_2Ir_xRu_{1-x}O_4$ crystals with $0 \leq x \leq 0.4$ on the Ru-rich side of the solid solution between Sr_2IrO_4 and Sr_2RuO_4. I discuss the evolution of the average structure of crystals in the alloy series, and additionally comment on composite two-phase structures that form under certain conditions. They include lamellae of (Ir,Ru) metal alloy, and also dendrites of a seemingly metastable phase $Sr_9(Ir,Ru)_3O_{17}$, both embedded in the bulk phase. The metastable phase is removed (within detection limits)

[2]For more information on using this furnace, please see Eli Zoghlin's dissertation.

by annealing, and the (Ir,Ru) alloy is diminished by annealing. Based on these products we are confident that the bulk phase is not transition metal-deficient.

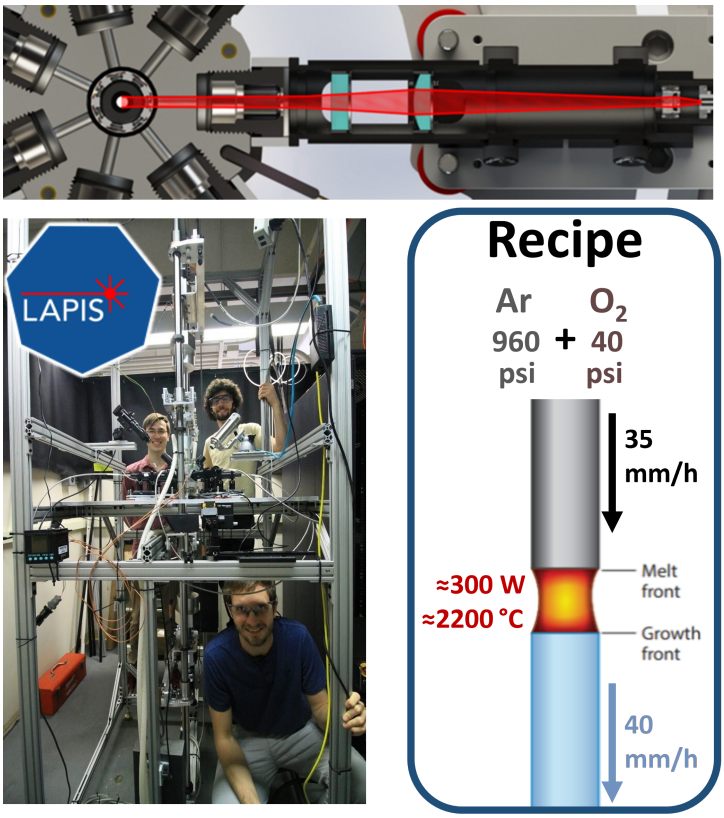

Figure 3.6: The LAPIS high-pressure floating zone furnace. *Top panel*: Schematic of the laser optics. Lasers are radially distributed and focused so that their spots overlap slightly. In this furnace the separate camera and pyrometer ports are at an angle. Adapted from Ref. 10. *Left panel*: Photograph of LAPIS with designers (from bottom) Julian, Michael, and Eli. Picture credit S.D. Wilson. *Right panel*: Approximate synthesis parameters for $Sr_2Ir_xRu_{1-x}O_4$.

Crystals of $Sr_2Ir_xRu_{1-x}O_4$ were grown with a floating zone (FZ) technique with an $(Ir,Ru)O_2$ self-flux. In our apparatus, we first melt the tip of the seed rod (affixed from below) and then lower the feed rod (suspended from above) into the melt, establishing a connected molten zone. We pull a crystal from the $(Ir,Ru)O_2$-rich molten solution by lowering both rods through the fixed optical heating source. For this work we used a custom furnace with a laser-based heating source designed to accommodate high gas

pressures, which is described elsewhere [88]. The relevant details of the furnace are that the molten zone is approximately 4 mm tall and 6-7 radially distributed laser beams are used to heat the zone with an optical wavelength in the range 800-820 nm.

The synthesis steps are as follows:

1. **Solid state synthesis of powder**

   (a) *Prepare Reactants*: $SrCO_3$ (99.99% excluding Ca or Ba) and IrO_2 (99.99% metals basis) and RuO_2 (99.95% metals basis) were used as starting materials, all sourced from Alfa Aesar. We found some as-purchased IrO_2 and RuO_2 powders to be O-deficient, so these precursors were initially heated in a tube furnace to 700 °C for 18 h with O_2 flow at 30 SCCM to ensure full O occupation.

   (b) *Dry Reactants*: The reactants are stored in alumina crucibles in a ≈200 °C drying oven, but they are hygroscopic and Santa Barbara is humid. We used box furnaces to dry the IrO_2 and RuO_2 at 700 °C, and the $SrCO_3$ at 400 °C for at least 18 h in air prior to weighing. The input stoichiometries are reported in Table 3.1.

   (c) *Initial Sinter*: To prepare the initial powder, mix the reagents in an agate mortar for >25 minutes, pack them into a clean latex balloon, and press into a pellet at 300 MPa within an isostatic press. Remove the pelletized powder from the balloon, place in an alumina crucible on a thick layer of reactant powder, and sinter at 1100 °C for 18 h in air. Store this pellet in a glove box until the next step to minimize water content.

2. **Rod Preparation**: Since our laser furnace only accommodates ≈5 mm diameter rods, it is especially hard to prepare straight rods without breaking them.

(a) Regrind the (dry) sintered pellet into powder. Tightly and uniformly pack the powder into a water-cleaned cylindrical latex balloon with diameter 5 mm and length up to 120 mm. The packing process involves compressing small additions of powder and frequently rolling the balloon to ensure the latex is relaxed, the diameter is uniform, and there are no lightly packed segments with trapped air pockets.

(b) Evacuate the air from the balloon with a rough pump and tie it off. Straighten the balloon by rolling it on a clean surface and compressing it from two sides with boxes. Then wrap the balloon tightly with paper, fastening with tape radially to prevent bending. Suspend the balloon with string within the isostatic press so that it does not touch any walls, and press at 300 MPa for 3 minutes.

(c) On removal, the rod is incredibly delicate and difficult to extract from the balloon. Remove the paper by gently slicing the tape, and then rinse the balloon with ethanol to weaken the latex. Tape the (dry) balloon with many strips of scotch tape width-wise onto a flat surface, such that there is tension in the tape. Carefully cut the tape and balloon incrementally length-wise with a sharp curved #12 stainless steel blade so that the tape expands the incision and allows for easier removal of the pressed rod.

(d) Place the rod on a conforming bed of reactant powder within a long alumina boat so that the rod does not bend when it softens. Sinter at 1380 °C for up to 12 h in air using a box furnace.

3. **Floating zone growth procedure**

(a) Mount and align the seed and feed rods in the furnace so as to minimize rod precession.

(b) Seal and pressurize the chamber.

(c) Ramp up optical power over approximately 40 minutes to gradually heat the seed's tip. During this, counter-rotate the seed and feed rods at ≈10 rpm.

(d) When the seed becomes fully molten (nearly 2150 °C) lower the feed rod slowly to establish a connected molten zone.

(e) Start pulling slowly and ramp up the rates. The translation rates need to be closely monitored, especially because the feed rate ≈40 mm/h is quite fast.

(f) When the growth is complete, disconnect the molten zone by slowly translating the feed rod away from the zone.

(g) Ramp the optical power down slowly with the crystal in the beam to avoid quenching and breaking the crystal.

(h) De-pressurize the furnace and remove the 'as-grown' sample when the system is cold. For synthesis feedback only, some 'as-grown' samples were measured with diffraction and microscopy below.

(i) Clean and inspect the furnace for damage. The evaporation did slightly discolor the quartz inner shroud which is closest to the growth zone, but each shroud was usable for about 10 such syntheses before absorption effects were noticeable.

4. **Anneal**: prior to any electronic or magnetic measurements, samples were annealed in air on powder beds for 4 to 6 days at 1380 °C. This is slightly lower than the temperature used for the pure ruthenate [89], but we note that Sr_2IrO_4 is reported to decompose near 1400 °C [90].

Here are some additional notes on this floating zone procedure. The low surface tension and/or melt viscosity made the molten zone unstable, so in some cases it spilled

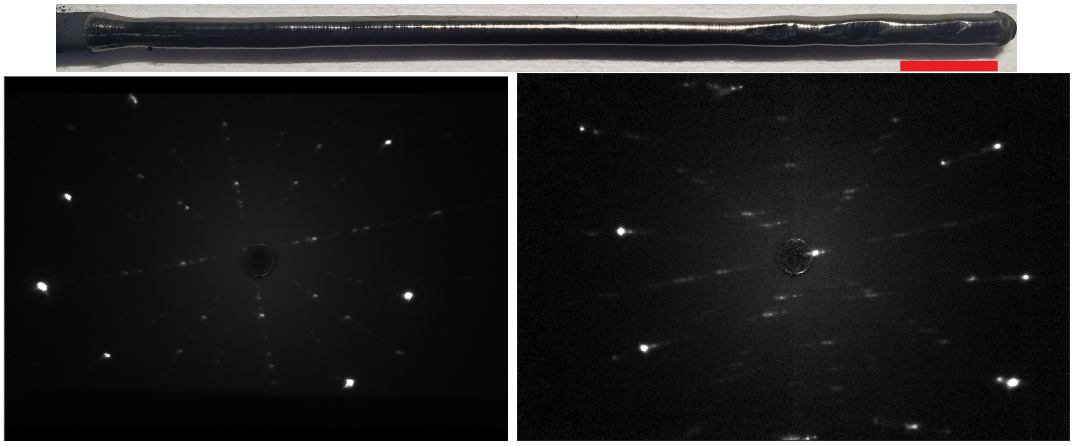

Figure 3.7: *Top panel*: Photograph of a representative sample: batch 'x0.25c'. Exterior facets are visible toward the end of the growth (right). The red scale bar is 1 cm. *Bottom panels*: We oriented crystals and assessed the crystal quality with a Photonic Science back reflection Laue Crystal Orientation System. Backscattered Laue detector images of cleaved surfaces of annealed $Sr_2Ir_xRu_{1-x}O_4$. These images are of two batches: *(left)* 'x0.10c' and *(right)* 'x0.40c' and confirm that they are crystalline. The samples are mounted with the growth direction vertical and c approximately along the beam, so the rotation of the patterns indicates that the a axis is 10-15 degrees away from the growth direction. The sample on the right is more mosaic due to the oxidizing synthesis environment.

downward violently. Preventing this required a low sample volume in the beam. We accomplished this by using a lower translation speed for the feed rod relative to the seed rod; i.e. the volumetric flow rate into the zone was less than the rate of the crystal pulled out, as others reported for Sr_2RuO_4 e.g. Refs. [89, 91]. This caused the crystal boule's diameter to be less than the polycrystalline rod's diameter. As such, the zone narrowed after the initial join, so the power and translation speeds were adjusted after the beginning of the growth. Part of this had to do with the low polycrystalline rod density 72(5)%; we note that we followed the optimized sintering conditions reported by Ref. 89. We report the final values of the crystal growth parameters in Table 3.1.

batch	x_{nom}	x	input stoichiometry	RuO_2 excess [mol%]	IrO_2 excess [mol%]	P_{melt} [W]	P_{end} [W]	p_{O_2} [bar]	p_{Ar} [bar]	v_{feed} [mm/h]	v_{seed} [mm/h]	as-grown (Ir,Ru) [wt%]	as-grown '9-3-17' [wt%]	annealed (Ir,Ru) [wt%]
x0a	0	-	$Sr_2Ir_{0.00}Ru_{1.03}O_{4.1}$	3	-	210	198	3	66	33	40	0.6	-	
x0.10a	0.10	0.09	$Sr_2Ir_{0.12}Ru_{0.93}O_{4.1}$	3	2	210	216	3	66	35	40	1.1	-	
x0.10b	0.10	0.08	$Sr_2Ir_{0.11}Ru_{0.93}O_{4.1}$	3	1	234	228	3	66	35	40	0.1	-	
x0.10c	0.10	0.09	$Sr_2Ir_{0.10}Ru_{0.91}O_{4.1}$	1	0	240	228	3	66	33	40	0.1	-	0.1
x0.15a	0.15	0.15	$Sr_2Ir_{0.17}Ru_{0.86}O_{4.1}$	1	2	234	228	3	66	32	40	1.2	-	0.7
x0.18a	0.18	0.18	$Sr_2Ir_{0.20}Ru_{0.83}O_{4.1}$	1	2	234	228	3	66	55	40	0.1	-	0.1
x0.20a	0.20	0.20	$Sr_2Ir_{0.23}Ru_{0.81}O_{4.1}$	1	3	276	252	14	55	25	40	0.1	3.5	0.1
x0.20b	0.20	0.20	$Sr_2Ir_{0.23}Ru_{0.81}O_{4.1}$	1	3	300	276	3	66	25	40	0.2	-	0.2
x0.25a	0.25	0.23	$Sr_2Ir_{0.26}Ru_{0.76}O_{4.1}$	1	1	240	240	3	66	34	40	0.5	-	
x0.25b	0.25	0.23	$Sr_2Ir_{0.28}Ru_{0.76}O_{4.1}$	1	3	240	222	3	66	36	40	0.7	-	
x0.25c	0.25	0.24	$Sr_2Ir_{0.28}Ru_{0.76}O_{4.1}$	1	3	240	240	3	66	31	40	0.9	-	0.9
x0.32a	0.32	0.32	$Sr_2Ir_{0.37}Ru_{0.69}O_{4.1}$	1	5	282	264	14	55	29	40	0.2	-	0.2
x0.40a	0.40	0.31	$Sr_2Ir_{0.41}Ru_{0.61}O_{4.1}$	1	1	264	276	3	66	32	40	2.1	8.1	
x0.40b	0.40	0.38	$Sr_2Ir_{0.46}Ru_{0.61}O_{4.1}$	1	6	258	252	3	66	33	40	3.0	6.9	
x0.40c	0.40	0.39	$Sr_2Ir_{0.46}Ru_{0.61}O_{4.1}$	1	6	276	258	14	55	34	40	0.1	4.0	0.1

Table 3.1: Crystal growth parameters: batch name, nominal and EDS-measured Ir substitution x, input stoichiometry, excess reactant, total beam power during melting and at the end of the growth P, partial pressure p, feed and seed translation speed v. The last columns contain the impurity phase fractions of the (Ir,Ru) alloy and the '9-3-17' phase $Sr_9(Ir,Ru)_3O_{17}$ as attained from laboratory PXRD refinements before and after annealing crystals at 1380 °C for 4 to 6 days in air. Note that as-grown and annealed samples are ground from similar regions of the boule but are not the same samples, which accounts for some of the variation in alloy phase fraction.

3.2.2 Synthesis Optimization

Nearly phase-pure samples were produced by optimizing the sample stoichiometry and the gas environment used during crystal growth. Other growth parameters throughout the series of samples were held fixed, to the best of our ability. A typical image of an as-grown $Sr_2Ir_xRu_{1-x}O_4$ boule is shown in Fig. 3.7a. A crystal grain is typically selected within 2 cm of growth when seeded from a polycrystalline rod, as evidenced by facets on the exterior and interior of the boule and confirmed by Laue measurements (Fig. 3.7b,c). As observed for the parent compound Sr_2RuO_4, the $(Ir,Ru)O_2$ layer direction (*ab* basal plane) is typically along the growth direction (cylinder axis)[89, 92]. Samples readily cleave along the basal plane.

For consistency, a fixed chamber pressure of 69(4) bar at room temperature was used. The optimal gas environment in our syntheses was found to be a ratio of 96:4

Ar:O_2.[3] However, for several syntheses of samples with higher Ir content, a more oxidizing environment with a ratio of 80:20 Ar:O_2 was utilized to decrease the Ir metal content. This led to high-phase-purity samples but also resulted in crystals that are highly friable and exfoliate easily. The gas environment for each growth attempt for an array of Ir concentrations is shown in Table 3.1.

To prepare the nominal chemical formula $Sr_2Ir_xRu_{1-x}O_4$, the optimal input stoichiometry contains 15 mol% excess IrO_2 and 1 mol% excess RuO_2; that is, $Sr_2Ir_{1.15x}Ru_{1.01(1-x)}O_{4.02+0.28x}$. The input stoichiometries and reactant excess values are summarized in Table 3.1; some batch stoichiometries are not optimal. Note that, at lower pressures, earlier reports required far greater excesses of IrO_2 and RuO_2 within starting stoichiometries. For example, in a FZ study by N. Kikugawa and co-workers with Ir $x \leq 3\%$ grown in 2.2 bar of 90:10 Ar:O_2, the reported starting stoichiometry contains an excess of about 300 mol% IrO_2 and 15 mol% RuO_2 [93].

For the samples reported here, there are two impurities detected via powder X-ray diffraction collected on crushed crystals. The first is an alloy of Ir and Ru metal that, for samples with $x>0$, adopts the Ir $Fm\bar{3}m$ space group. The second phase seems to be an Ru-substituted form of the recently reported phase $Sr_9Ir_3O_{17}$ [94]. Electron microscopy for these impurities is shown in Figure 3.10 and discussed later.

In Table 3.1 we summarize growth parameters for a variety of trial growths and the composition of the resulting boules. We note that the variance in the feed translation speed compensates for differences in the feed density and diameter. The required power for melting is a relative metric only and depends on a number of parameters; however the overall trend is to increase with Ir content. We do not report the pyrometer-measured temperature because it primarily varies with the pyrometer reticle position and with

[3]The procedure was to fill the chamber to 14 bar with pre-mixed 80:20 Ar:O_2 gas after purging several times, then to fill the rest of the way with pure Ar gas.

the amount of volatilized powder that coats the sapphire inner shroud in front of the pyrometer.

3.3 Structural Characterization

Most of the structural characterization detailed below comes from our publication in the *Journal of Crystal Growth* [68]. Powder X-ray diffraction and electron microscopy were used as feedback for the growth optimization described above. Mostly what we found were indications of very high sample quality and low impurity content up to Ir substitutions of 40%.

The last section describes new work on the subtleties of the oxygen positions. Additional weak peaks were found using single crystal neutron diffraction. Along with indirect evidence from thermal expansion, these peaks indicate oxygen octahedral tilts and/or rotations similar to those in Sr_2IrO_4. The space group is unclear from our limited studies. This slight deviation from the $I4/mmm$ unit cell is not expected to make much of a difference in the electronic properties, especially when pitted against considerable carrier doping and disorder that come with Ir substitution.

3.3.1 Powder X-ray Diffraction

Preliminary powder X-ray diffraction (PXRD) was performed with a Panalytical Empyrean diffractometer using lab-source Cu K-α radiation. Follow-up high-resolution synchrotron measurements were taken at Beamline 11-BM of the Advanced Photon Source at Argonne National Laboratory with a fixed wavelength of 0.458 Å. 11-BM samples were diluted with SiO_2 powder to optimize the transmission to >10%. The PXRD patterns were refined using the `TOPAS` software package [95]. The refinements were straightforward for extracting lattice constants, thermal parameters, and site occupation.

I applied standard particle size and strain corrections with the 'LVol_FWHM_CS_G_L' macro. Preferred orientation was an issue for this layered compound, so corrections were handled with the 'PO_Spherical_Harmonics' macro to capture this and the anisotropic peakshapes such as the broader $(00L)$-type peaks.

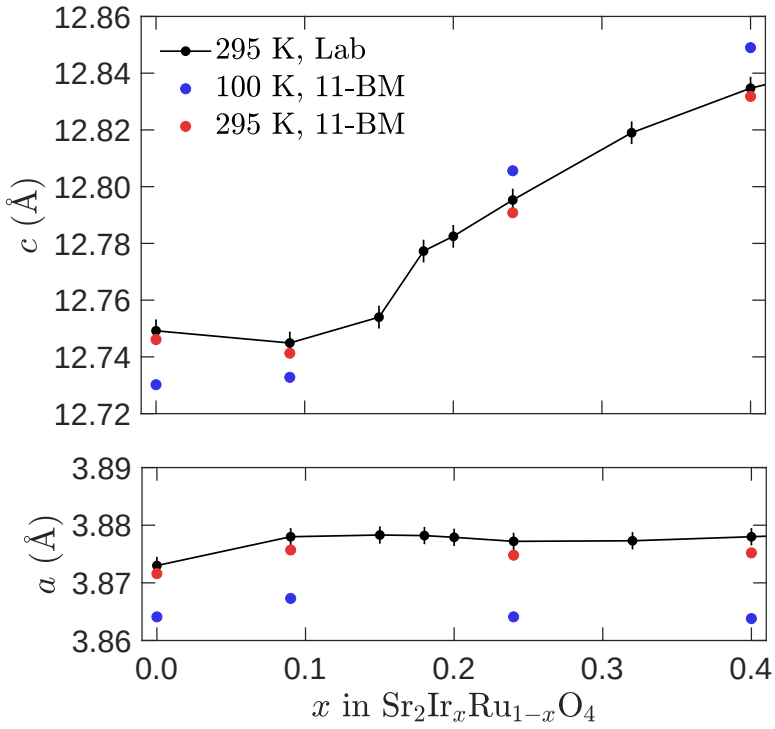

Figure 3.8: Tetragonal lattice parameters from PXRD refinements. Lab-source data (black) is indicated as 'Lab' and synchrotron data is indicated as '11-BM' in the figure. Approximate uncertainties are either indicated with error bars or are smaller than the data markers. Lines are a guide to the eye.

The evolution of the bulk crystallographic parameters across the substitution series is shown in Table 3.2 and lattice parameters are plotted in Figure 3.8. The samples are indexed to the $I4/mmm$ tetragonal space group commonly used for Sr_2RuO_4, and the atomic displacement parameters increase with x as expected for substitutional disorder. While the out-of-plane lattice constant c trends up with x, the in-plane lattice constant a only weakly depends on x.

There are two free coordinates for this compound in the $I4/mmm$ space group, O(2) z and Sr(1) z; both are $4e$ Wyckoff positions with $x = y = 0$. These free coordinates parameterize the positions of the apical O ions and Sr ions along c. In the refinements, the O(2) z positions are unreliable, but there is a weak trend down in Sr(1) z with increasing x, which indicates that Sr ions are positioned farther away from the (Ir,Ru)O_2 planes with Ir content. In other words there is a small Jahn-Teller elongation with increasing x.

batch		x0a	x0.10c	x0.25c	x0.40c
x_{nom}		0	0.10	0.25	0.40
x		0	0.09	0.24	0.39
100 K					
a	[Å]	3.8641	3.8673	3.8641	3.8638
c	[Å]	12.730	12.733	12.806	12.848
Sr(1) z		0.3536	0.3536	0.3519	0.3513
O(2) z		0.161	0.162	0.169	0.167
Sr U_{iso}	[Å^2]	0.004	0.004	0.003	0.005
B U_{iso}	[Å^2]	0.003	0.003	0.004	0.006
R_{wp}	[%]	9.79	8.06	8.61	10.22
χ^2		1.15	1.50	1.25	1.61
295 K					
a	[Å]	3.8716	3.8757	3.8749	3.8749
c	[Å]	12.746	12.741	12.791	12.830
Sr(1) z		0.3535	0.3535	0.3522	0.3512
O(2) z		0.160	0.164	0.168	0.169
Sr U_{iso}	[Å^2]	0.007	0.008	0.007	0.006
B U_{iso}	[Å^2]	0.004	0.005	0.007	0.009
R_{wp}	[%]	9.76	8.88	9.14	10.51
χ^2		1.19	1.35	1.19	1.09

Table 3.2: Select bulk crystallographic data from Rietveld refinement of synchrotron PXRD data on as-grown samples. First, batch name, nominal and measured x from EDS measurements. Next, refined values at 100 K and at 295 K: a and c tetragonal lattice parameters; Sr(1) z and the O(2) z free parameters; isotropic atomic displacement parameters U_{iso} for the Sr and B sites (B=Ir/Ru); and Rietveld goodness-of-fit parameters R_{wp} and χ^2. Note all occupancies were set to the stoichiometric values. U_{iso} for oxygen sites was fixed at 0.008 Å. The O(2) z positions are not reliable in that their refined positions have minimal effects on the goodness-of-fit, because the X-ray diffraction signal is dominated by the heavier elements. If not indicated, uncertainties are smaller than half of the last significant digit.

3.3.2 Scanning Electron Microscopy

A ThermoFisher Apreo C scanning electron microscope was utilized for energy-dispersive X-ray spectroscopy (EDX) and backscattered electron imaging (BSE) with a typical configuration of 20 kV accelerating voltage and 1.6 nA beam current.

The homogeneity of the Ir substitution x was measured with EDX mapping. The Ir/Ru atomic ratios are homogeneous on the $\sim$10 μm scale; i.e. the variation in x is within measurement uncertainty $\sigma_x \approx 0.2\%$. The variation in x on the $\sim$5 mm scale (i.e. radially across the crystal boule) is within $\sigma_x \leq 0.5\%$.

This alloy homogeneity for FZ-synthesized samples is an improvement compared to previously reported flux-synthesized samples. In the ARPES study on the same compound grown via a flux method by J. Kwon and co-workers, the reported EDX-measured variance in x is about 3% on the 100 μm scale [79]. This value is consistent with measurements reported on the related compound $Sr_3(Ir,Ru)_2O_7$, for which the variation in x for the highest-quality flux samples is typically near 2% on both the μm and mm length scales - see e.g. Ref. [9].

3.3.3 Impurity phases

We now comment on impurity phases that result and are amplified away from optimal growth conditions, which we indicate in the ternary phase diagram sketched in Figure 3.9. There are two reactions that lead to chemical inhomogeneity and likely drive unwanted phase formation: (a) $(Ir,Ru)O_2$ reduces to form (Ir,Ru) metal just below the liquidus temperature[96] and also (b) $(Ir,Ru)O_2$ reacts with oxygen gas to briefly form $(Ir,Ru)O_{3,4}(g)$, which effectively evaporates the oxide from the molten zone.

The small (typically <1 wt%) (Ir,Ru) metal impurity detected in diffraction measurements is primarily caused by the reduction of the oxides, during both the solid state

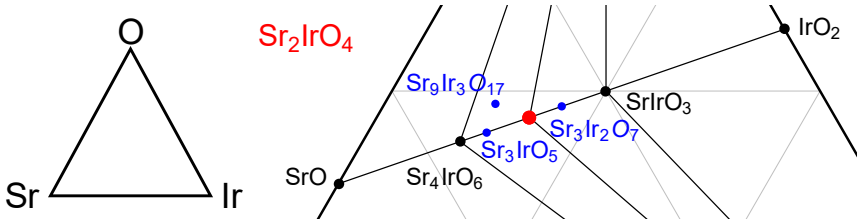

Figure 3.9: The approximate isothermal ternary phase diagram for Sr-Ir-O at 2200 °C, which captures mixed (Ir,Ru) phase formation. The red dot is Sr_2IrO_4. Known phases are in black and other possible phases are in blue.

reaction as well as during FZ growth. The observed ∼1 μm size lamellar alloy formation in unannealed samples is shown in Figure 3.10. The alloy is predominantly Ir even for low Ir content, and EDS measurements indicate compositions of $Ir_{0.85}Ru_{0.15}$ for the x≈0.1 batches and closer to $Ir_{0.95}Ru_{0.05}$ for samples with x≈0.2.

In unannealed samples, a perovskite-like impurity phase is identified most closely matching the structure of $Sr_9(Ir,Ru)_3O_{17}$ as seen in Figure 3.10b. Our diffraction data are most consistent with this phase and unannealed samples show a weak 11 K feature in susceptibility (not shown) resembling the reported antiferromagnetism of $Sr_9Ir_3O_{17}$. An alternative model for this impurity phase could be $Sr_3(Ir,Ru)O_{5+\delta}$ (related to double perovskites like Sr_3WO_6 but with O vacancies [91]). For visualization these phases are included in the ternary phase diagram Figure 3.9. This phase disappears upon annealing, suggesting it is metastable. The phase fraction of this impurity scales with excess Ir content in unannealed crystals, and it seems to form upon rapid cooling in locally Ir/Ru poor regions in an oxidizing environment - see Ref. [91].

Other Ruddlesden-Popper phases such as the bilayer $Sr_3(Ir,Ru)_2O_7$ and the trilayer $Sr_4(Ir,Ru)_3O_{10}$ compounds were not observed in PXRD or SEM measurements. However, a dilute quantity <0.1 mol% of the ferromagnetic $Sr(Ir,Ru)O_3$ phase is detectable solely via magnetization. This perovskite phase is also not directly visible in PXRD or SEM data, similar to reports on the parent system Sr_2RuO_4 [91]. It has a saturated moment

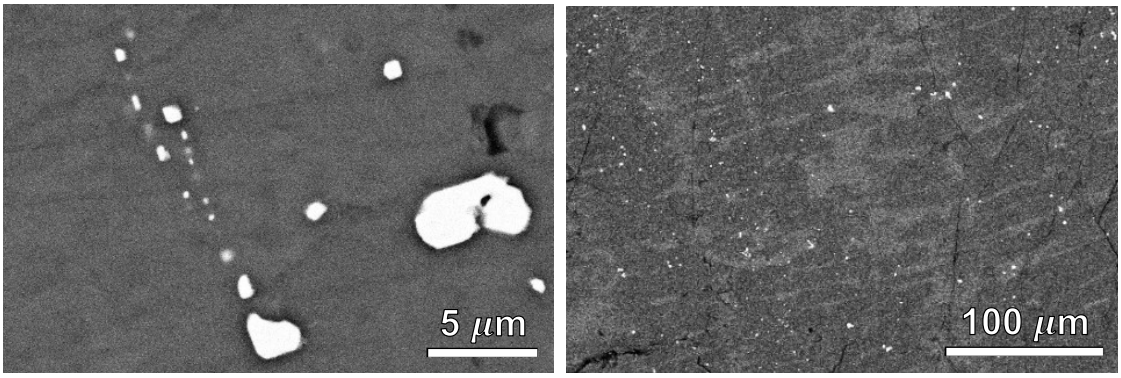

Figure 3.10: Scanning electron microscope backscattered electron images for polished as-grown samples: (a) batch 'x0.10b' with inclusions and lamellae of the (Ir,Ru) alloy phase that appears brighter than the bulk; and (b) batch 'x0.40a' which additionally contains a dendritic phase that appears slightly brighter than the bulk. The Sr:(Ir,Ru) ratio of this phase is near 3:1 from EDX analysis.

as high as 1.5 μ_B/Ru, so even ppm impurities of $Sr(Ir,Ru)O_3$ can be resolved via low-field magnetization measurements [97, 98].

3.3.4 Weak Oxygen Distortions

From the X-ray powder diffraction, the volumetric thermal expansion is positive for all samples. Interestingly, there is a changeover in the coefficient of thermal expansion along c, from thermal expansion for x=0 and 0.09 to thermal contraction for x=0.25 and 0.40 − see Figure 3.8. This change is likely related to a subtle symmetry change that we do not observe in laboratory PXRD at room temperature. There is one unindexed peak in the synchrotron PXRD for the x=0.25 and 0.40 samples near Q=2.55 Å^{-1} that is stronger at 100 K than at 295 K. This may be the disallowed (1 1 2) peak which is allowed for the Sr_2IrO_4 $I4_1/acd$ space group.

Recent single crystal neutron diffraction (SCND) studies helped confirm the nature of the thermal contraction along the c-axis, plotted for one sample in Fig. 3.11. SCND was measured down to $T < 5$ K and without an applied field. First I summarize data on

the x=0.25 sample, then I move on to the x=0.09 sample, which both have $I4/mmm$-disallowed half-order peaks. We associate these weak peaks with oxygen octahedral rotations and/or tilts.

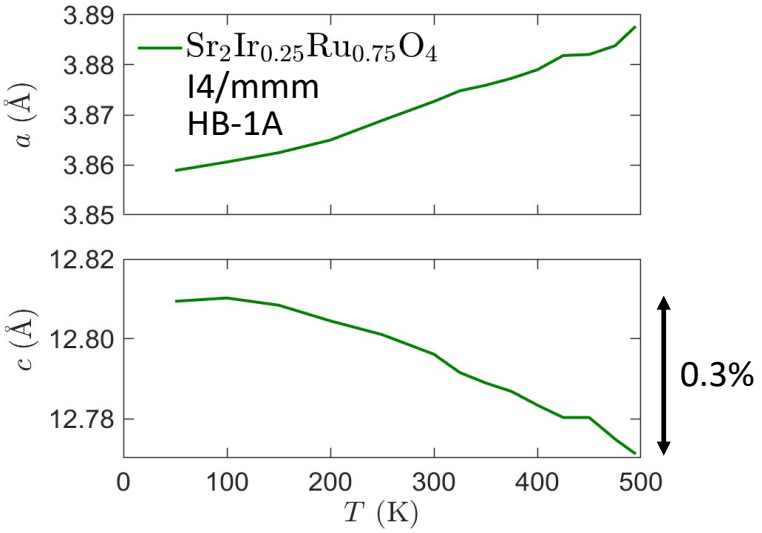

Figure 3.11: Thermal expansion probed via single crystal neutron diffraction. $Sr_2Ir_xRu_{1-x}O_4$ with x=0.25 was measured in the (HHL) plane at beamline HB-1A at HFIR. These are the approximate lattice parameters from the lattice orientation, calculated by Adam A. Aczel. While there is an overall 1.4% thermal expansion over this temperature range 50-500 K, the c lattice parameter decreases with temperature.

A 0.2 g sample of x=0.25 was measured in the (H, H, L) plane on the HB-1A triple-axis spectrometer, located at the High Flux Isotope Reactor (HFIR) at Oak Ridge National Laboratory (ORNL). The setup entailed a 14.64 meV double bounce monochromator, pyrolitic graphite (PG) filters before and after the sample, and then an analyzer before the point detector to minimize higher harmonics. We used the tight collimator configuration 40'-40'-40'-120' to improve angular resolution. A series of weak half-order peaks with [1/2,1/2,1/2] wavevectors was found. The transition above 500 K does not coincide with magnetic signals (based on magnetization measurements in the range 400-850 K). We cannot rule out a magnetic component for the low-Q peaks such as $(0.5, 0.5, 0.5)$.

But stronger signal at $(0.5, 0.5, 7.5)$ and the high onset temperature (much higher than Sr_2IrO_4) indicate a primarily structural origin for these peaks.

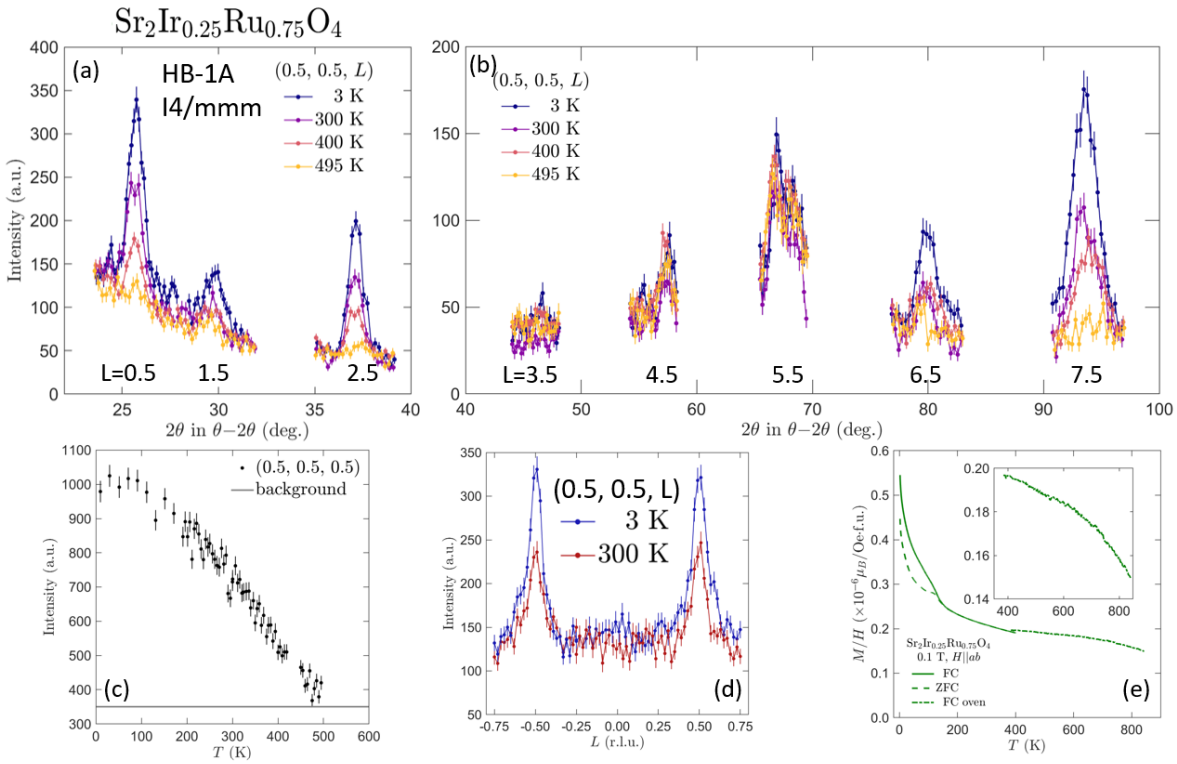

Figure 3.12: Weak oxygen distortions tracked with single-crystal neutron diffraction. Please note these signals are ∼10,000× weaker than allowed $I4/mmm$ reflections. $Sr_2Ir_xRu_{1-x}O_4$ with x=0.25 was measured in the (H, H, L) plane. (a-b) [1/2,1/2,1/2]-type peaks are evident. The onset temperature is near 550 K. (c) is an order parameter. (d) is an L scan that demonstrates there is no reflection at (0.5,0.5,0) - more detailed scans indicate possible low-Q scattering from the CYTOP epoxy. (e) shows magnetization - note the lack of a feature in the range 500-600 K. For this sample there is a ∼10 ppm ferromagnetic impurity, hence the feature near 100 K.

A 0.4 g sample of x=0.09 was measured in the $(HK0)$ plane at NCNR on the BT-7 triple-axis spectrometer. The setup entailed a fixed E_f=14.7 meV, a vertical bounce monochromator, and 1 PG filter before and 2 after the sample. Most scans were measured with a velocity selector (to further reduce higher harmonics) and the open-80'-80R-open-point detector configuration, because flux was limited. A series of weak half-order peaks

[1/2,1/2,0] was found, with a transition near room temperature that does not coincide with magnetic signals. We cannot rule out a magnetic component for the low-Q peaks such as $(0.5, 0.5, 0)$ but stronger signal at $(7.5, 0.5, 0)$ and the order parameters indicate a primarily structural origin for these peaks. The correlation length for $(0.5, 0.5, 0)$ stays at 25(4) Å over the range 3 K to 200 K.

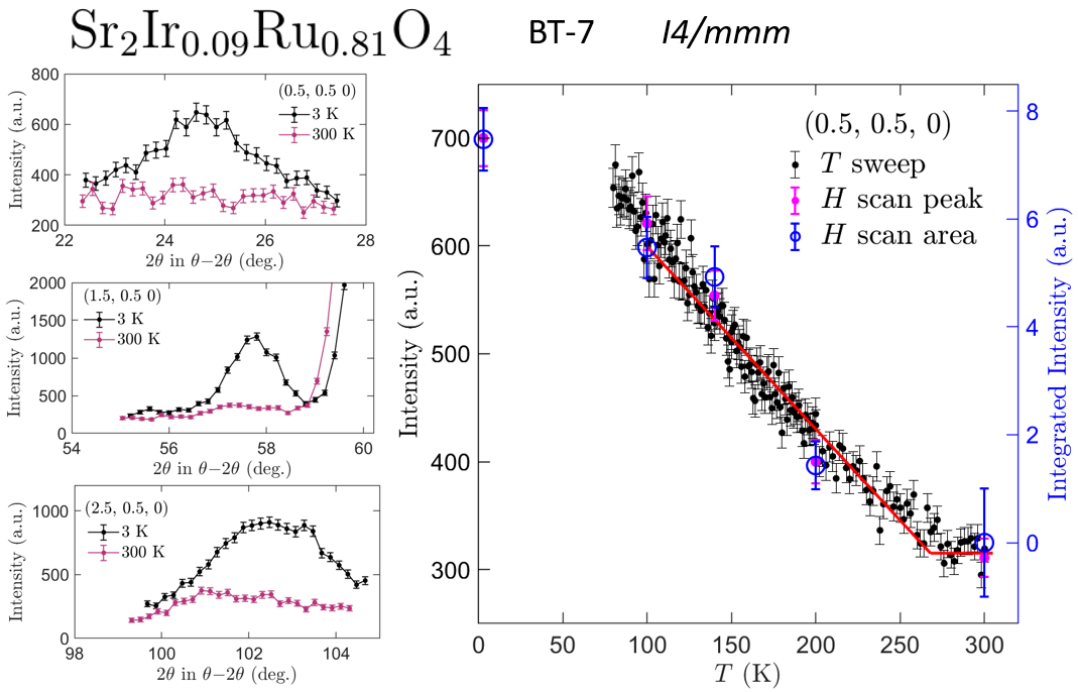

Figure 3.13: Weak oxygen distortions tracked with single-crystal neutron diffraction. Please note these signals are ∼10,000× weaker than allowed $I4/mmm$ reflections. $Sr_2Ir_xRu_{1-x}O_4$ with x=0.09 was measured in the $(H, K, 0)$ plane. [1/2,1/2,0]-type peaks are evident. The onset temperature is near 280 K. In the order parameter, the black and magenta symbols are peak intensities, and blue symbols are the integrated intensities from (H,0.5,0) scans.

Confusingly, we do NOT observe the $[\frac{1}{2}\ \frac{1}{2}\ 0]$-type peaks for the x=0.25 sample, only the ones with half-integer L. These peaks are observed for x=0.09 and also for x>0.5, since they are allowed in the $I4_1/acd$ space group. This likely points to a different variety of oxygen rotations and/or tilts at intermediate Ir content.

Now I briefly share another piece of evidence for a subtle structural change. The

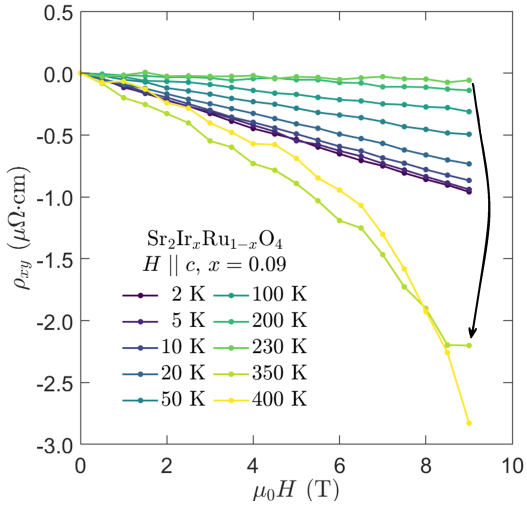

Figure 3.14: Subtle Fermi surface change tracked with Hall effect measurements. Compare with the order parameter in the right panel of Fig. 3.13. Data between 230 and 350 K show an order-of-magnitude difference in the Hall resistivity ρ_{xy}, suggesting a change in the carrier number.

Hall effect is sensitive to the number of carriers and the mobility, and thus is a (tricky-to-interpret) probe for changes in the Fermi surface. In Fig. 3.14 we show Hall effect data across the transition temperature where the order parameter turns on. This sample is from the same batch as the neutron diffraction measurements shown in Fig. 3.13. The Hall resistivity changes drastically across this transition. Our understanding of this phenomenology is preliminary, especially since most samples' transitions are well above the 400 K limit of our apparatus.

In summary, I want to reiterate how these half-order peaks are very weak, too small to be observed in synchrotron X-ray diffraction. We cannot point to a definite origin but it is likely a small structural perturbation that marginally affects the low-temperature physics. Note how angle-resolved photoemission (ARPES) studies do not detect the effects of octahedral rotations until x>0.4 [79]. Future work to refine precise structural solutions would entail single-crystal diffraction with several orientations, measured on a neutron diffraction instrument like TOPAZ or HB-3A.

3.4 Heat Capacity

The heat capacity is perhaps the most convincing evidence for quantum criticality in $Sr_2Ir_xRu_{1-x}O_4$. We present data and analysis of the temperature and field dependence for samples spanning the van Hove singularity.

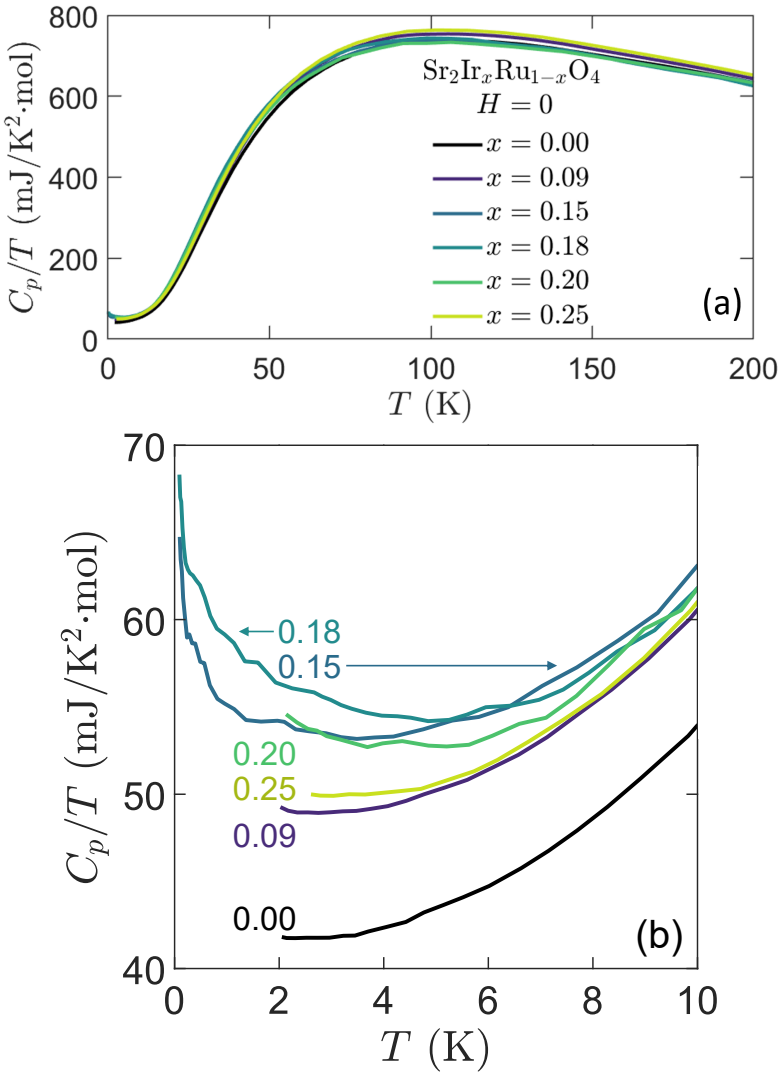

Figure 3.15: Quantum critical fluctuations and the low-temperature degrees of freedom. Panel (a) shows the zero-field heat capacity C_p/T for the substitution series, with no clear evidence of phase transitions. Panel (b) shows C_p/T at low temperatures; for samples near $x \approx 0.18$ there is an upturn.

Heat capacity was measured with a Quantum Design PPMS with a dilution refrigerator insert. Measurements used the pulse method, which involves heating with a constant-power pulse and fitting the heating and cooling curves. Addenda measurements were run before inserting the sample, which measured the puck with small amounts of Apiezon N grease. The typical procedure was to measure several repetitions at each temperature and to bin the measurements with a weighted mean.

We argue that the abrupt change in local magnetic moments and fluctuations as x increases from 0.15 to 0.20 is indicative of a quantum critical point. The corresponding increase in the low-temperature degrees of freedom is captured by the increase in the heat capacity C_p (Fig. 3.15) at low temperatures for samples near x=0.2. In other words, the Sommerfeld coefficient, which scales with the effective electron mass, is maximized at this Ir concentration.

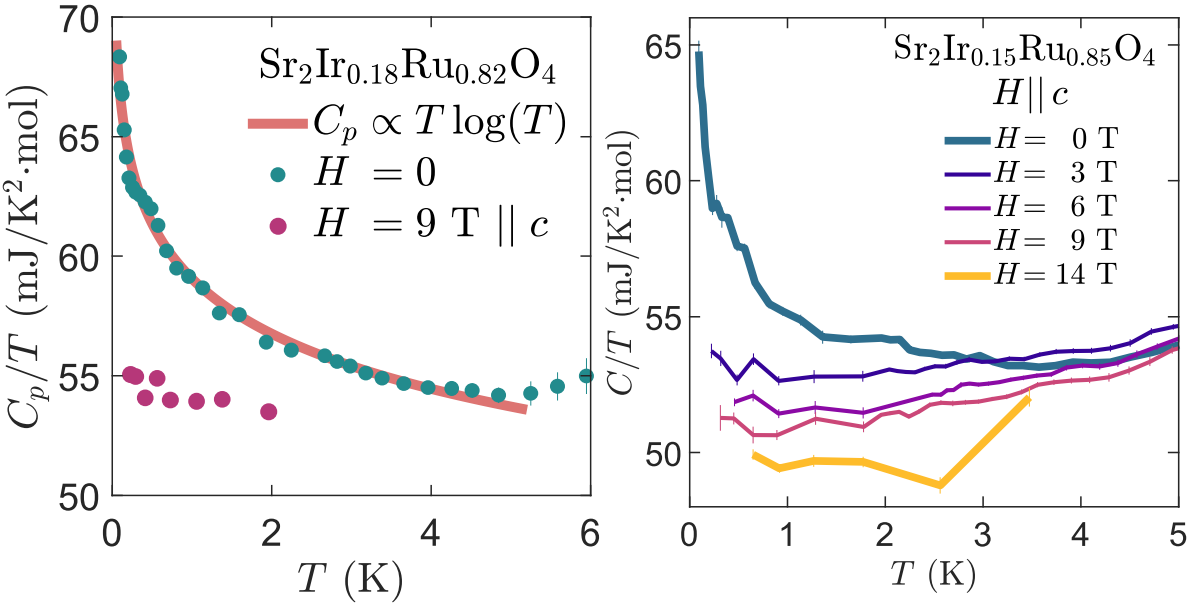

Figure 3.16: Quantum critical fluctuations and the low-temperature degrees of freedom. The panels show the field-dependence of the heat capacity for the x=0.18 and x=0.15 concentrations, with field applied along the c axis.

Focusing on the near-critical concentration x=0.18, we observe a >20% increase in

C_p/T over the range 0.1 K $< T <$ 5 K. The data are well-described by the phenomenological form $C_p/T \propto \log(T)$, as shown in Fig. 3.16. The fit to another critical form $C_p/T \propto \sqrt{T}$ is only valid over a limited temperature range $2 - 4$ K. Interestingly, the low-temperature upturn in the heat capacity is strongly suppressed with magnetic field. Similar field dependence was observed for the x=0.15 sample.

3.5 Magnetization

As a quick overview, magnetization studies show no evidence of long-range order. Some low-temperature glassy behavior likely reflects the quantum critical fluctuations. The most striking evidence of these fluctuations is in the Curie-Weiss fits, which show a sharp change near the reported Lifshitz transition.

Magnetization was measured with a Quantum Design MPMS3 SQUID magnetometer on cleaved samples adhered to a quartz paddle with GE varnish.

Surprisingly, no long-range order was detected via magnetization. This is consistent with single crystal neutron diffraction measurements of samples with x=0.09 and x=0.25 that show no order. Additionally, there are no clear peaks in the heat capacity (Fig. 3.15a) which confirms a lack of magnetic ordering in the ground state. For the x=0.20 sample, the inelastic neutron scattering revealed no magnon modes below 60 meV at 5 K. Thus all samples reported here for $x \leq 0.25$ are considered to have paramagnetic ground states.

Magnetization measurements in $Sr_2Ir_xRu_{1-x}O_4$ (Figs. 3.17 and 3.18) reveal an intriguing substitution-driven un-freezing of the moments. The parent ruthenate Sr_2RuO_4 demonstrates Pauli-like paramagnetic susceptibility with a weak temperature dependence, which increases slightly above 300 K and thus cannot be described by the Curie-Weiss model. The non-monotonic susceptibility dependence on temperature persists to

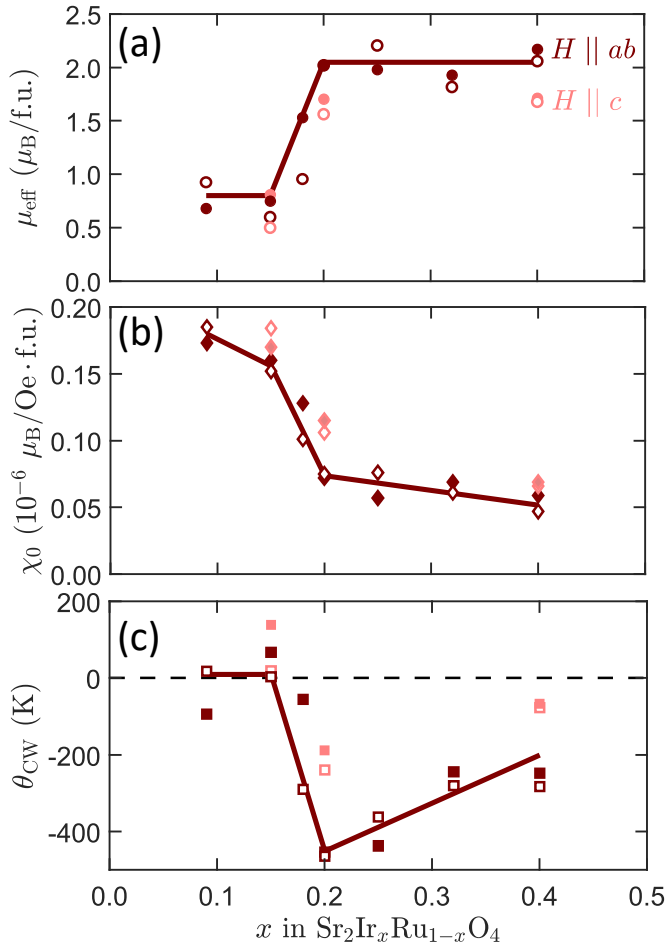

Figure 3.17: Moment freezing gives way to local moment magnetism with Ir substitution. Panels (a)−(c) summarize the effective moment $\mu_{\rm eff}$ (circles), temperature-independent paramagnetism χ_0 (diamonds), and Curie-Weiss temperature $\theta_{\rm CW}$ (squares), respectively. All change abruptly near x=0.2. Lines are guides to the eye. These values are from Curie-Weiss fits over the ranges 200−400 K (empty markers) and 300−400 K (filled markers) with $\mu_0 H$=0.1 T applied within the ab plane (dark red) and along the c axis (light red).

low Ir substitution x=0.05. At higher Ir concentrations $x \geq 0.09$, local moments become evident within the largely temperature-independent susceptibility [71].

Remarkably, on increasing the Ir content x from 0.15 to 0.20 we observe:

1. a three-fold increase in the Curie-Weiss effective moment $\mu_{\rm eff}$;

2. a sharp decrease in the temperature-independent paramagnetism χ_0; and

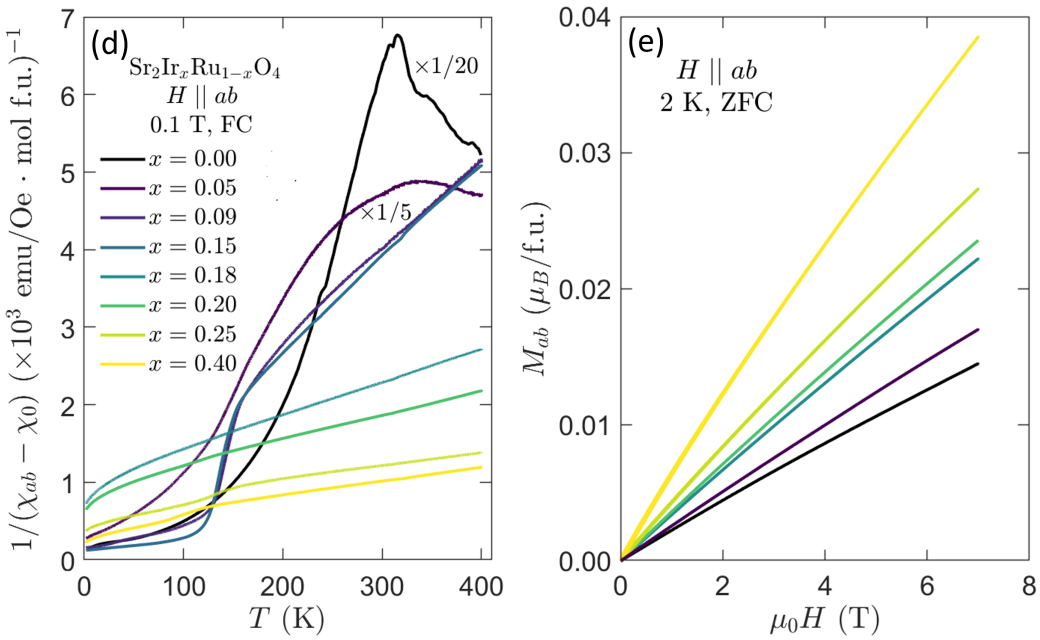

Figure 3.18: Moment freezing gives way to local moment magnetism with Ir substitution. The dc susceptibility is shown in panel (d); some samples have 100−150 K features due to ppm impurities of the ferromagnet $SrIr_xRu_{1-x}O_3$. Panel (e) shows the isothermal magnetization at T=2 K for select samples with undetectable ferromagnetic impurities. The abbreviation (Z)FC stands for (zero) field cooling.

3. an order-of-magnitude change in the Curie temperature θ_{CW}, from ∼10 K to −450 K, indicative of strong antiferromagnetic spin fluctuations [4].

Based on the ensuing measurements, we argue that the abrupt change in local magnetic moments and fluctuations as x increases from 0.15 to 0.20 is indicative of a quantum critical point.

To understand the nature of this low-temperature field-driven magnetic response, we carefully measured the dc magnetization for the high-purity x=0.20 sample. There are no cusps and negligible ≈1% irreversibility for this sample above 1.8 K. However, there is a clear inflection feature in $M(T)$ with large applied fields >1 T along c (Fig. 3.19). The inflection temperature $T_{\mathrm{inflection}}$ increases with increasing field, from 3 K at 1.2 T to 12

[4] While some samples' $|\theta_{\mathrm{CW}}|$ values lie outside the temperature range of the fit and thus are unsuitable for interpretation with the mean-field Curie-Weiss model, they qualitatively point to strong fluctuations.

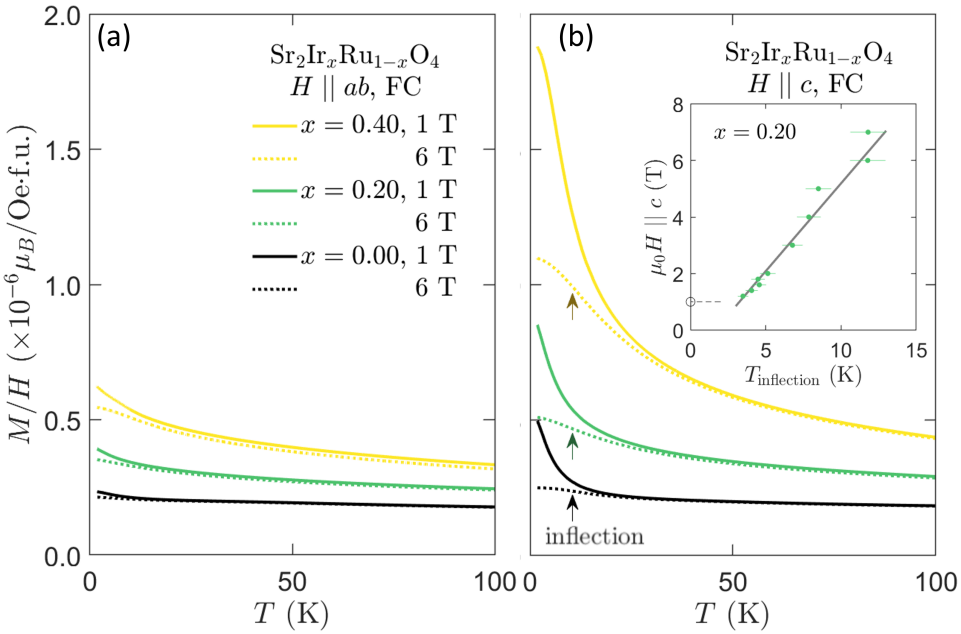

Figure 3.19: Field-driven freezing is observed across the substitution series. The field-cooled susceptibility is shown with field oriented along (a) the ab plane and (b) the easy c axis. Note that below $T \approx 30$ K the susceptibility differs strongly with field for all samples. Arrows in panel (b) show an inflection in the susceptibility. The inset tracks the inflection temperature $T_{\mathrm{inflection}}$ with field for the x=0.20 sample; no inflection is observed for $T > 2$ K below 1.2 T.

K at 7 T. A similar feature is observed for all of our samples for the range $0 \leq x \leq 0.40$. This suggests that applied fields suppress electronic degrees of freedom via spin freezing in this entire substitution series.

The magnetization becomes very anisotropic from Ir substitution, with c the easy axis. The low-temperature susceptibility is much larger and the inflection is much clearer with $H \parallel c$ as compared to $H \parallel ab$ (Fig. 3.19). Also the magnitudes of μ_{eff} and θ_{CW} are lower with $H \parallel c$ (Fig. 3.17a-c). This anisotropy contrasts with the isotropic susceptibility for La substitution [81].

One clear magnetic feature shared by all samples is that the susceptibility for different applied fields starts to diverge below 30−50 K (Fig. 3.19). This temperature scale is explored more in the magnetotransport results below.

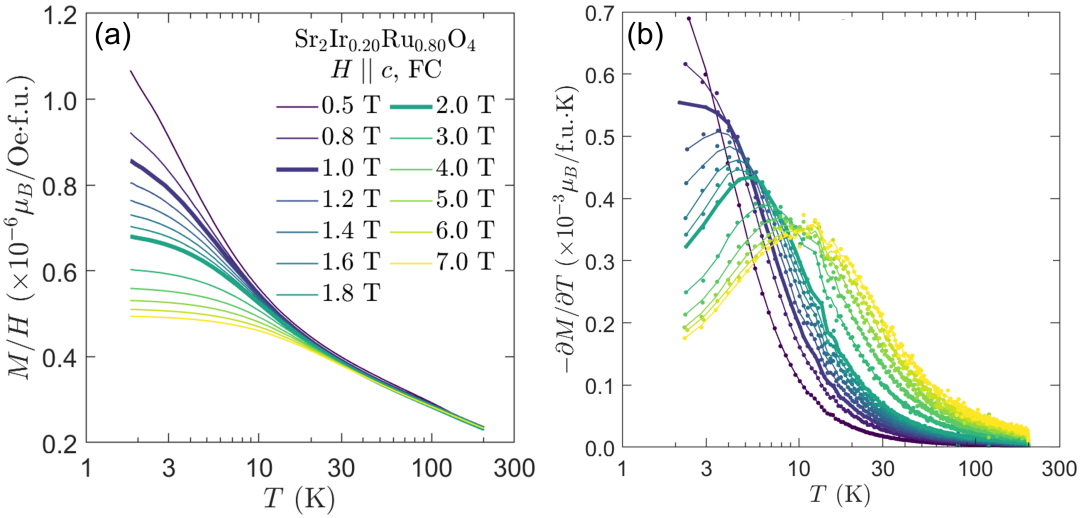

Figure 3.20: Field-driven freezing, focusing on the x=0.20 sample. (a) The field-cooled susceptibility is shown with field oriented along the easy c axis. (b) The slope of the same data are in dots; smoothed lines are guides to the eye. The 1 T and 2 T data are heavier for clarity.

3.6 Magnetotransport

Magnetotransport measurements reveal features for all samples in the range $30 - 50$ K. The resistivity also strongly deviates from typical Fermi-liquid behavior.

Electron transport was measured with a Quantum Design PPMS with a dilution refrigerator insert. Transport samples were cleaved with a blade, diced into long bars with a diamond saw, and then mechanically polished to <100 μm using diamond lapping paper and water. Surface roughness was about 5 μm. Samples were glued to insulating cigarette paper atop gold puck surfaces with GE varnish. Contacts were made with silver paint and gold wirebonding wire. All measurements were repeated on multiple samples of each composition.

The most important set of transport measurements are of the temperature dependence of the resistivity $\rho \propto AT^n$. We found these to be a supporting piece of evidence for quantum criticality. In our transport measurements, the in-plane resistivity $\rho_{ab}(T)$ is

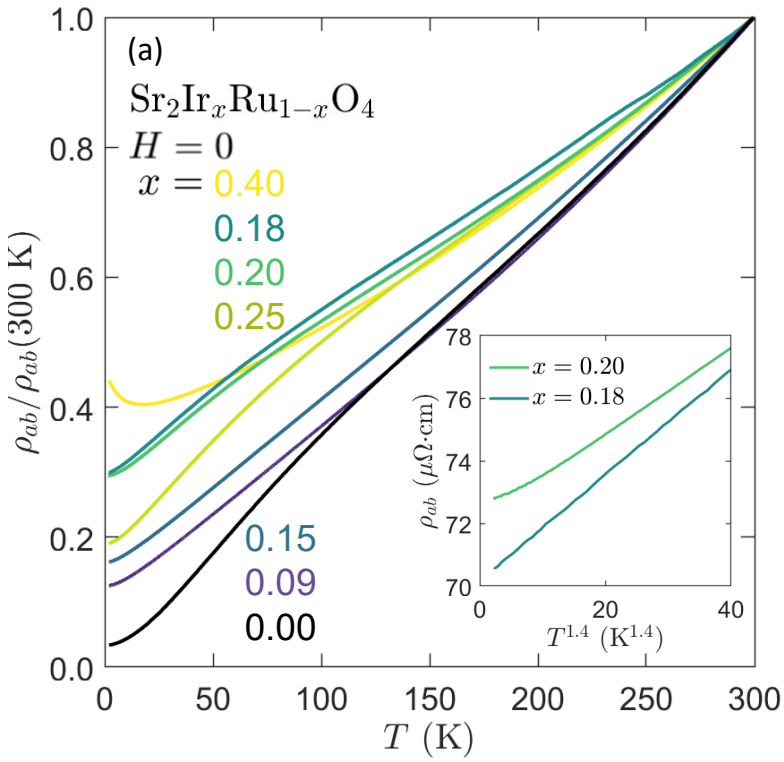

Figure 3.21: Magnetotransport near quantum criticality. Panel (a) shows the normalized resistivity ρ_{ab} for $Sr_2Ir_xRu_{1-x}O_4$, which is nearly linear in temperature above 100 K. For samples with $0<x<0.3$, $\rho_{ab}(2\ \mathrm{K})\approx 100\ \mu\Omega$·cm, whereas $x=0.40$ samples have $\rho_{ab}(2\ \mathrm{K})\approx 2$ mΩ·cm. The inset shows the $T^{1.4}$ dependence of the $x=0.18$ sample over the range $2<T<14$ K.

observed to follow $n\approx 1.4$ for the near-critical sample $x=0.18$ (inset to Fig. 3.6) over a wide temperature range $2 < T < 20$ K. This divergence from Fermi Liquid $n=2$ behavior may be an indication of one of several types of quantum criticality [81, 99, 100]. Additionally, the high-temperature linearity $n=1$ has an onset temperature that is lowest near $x=0.2$. This linearity indicates non-Fermi liquid excitations with diverging relaxation time scales. The resultant 'quantum critical fan' is shown in the substitution-temperature phase diagram (Fig. 3.6d).

This is the temperature below which the magnetoresistance turns on and the resistivity shows an inflection in temperature (Fig. 3.6). We suggest that a poorly understood

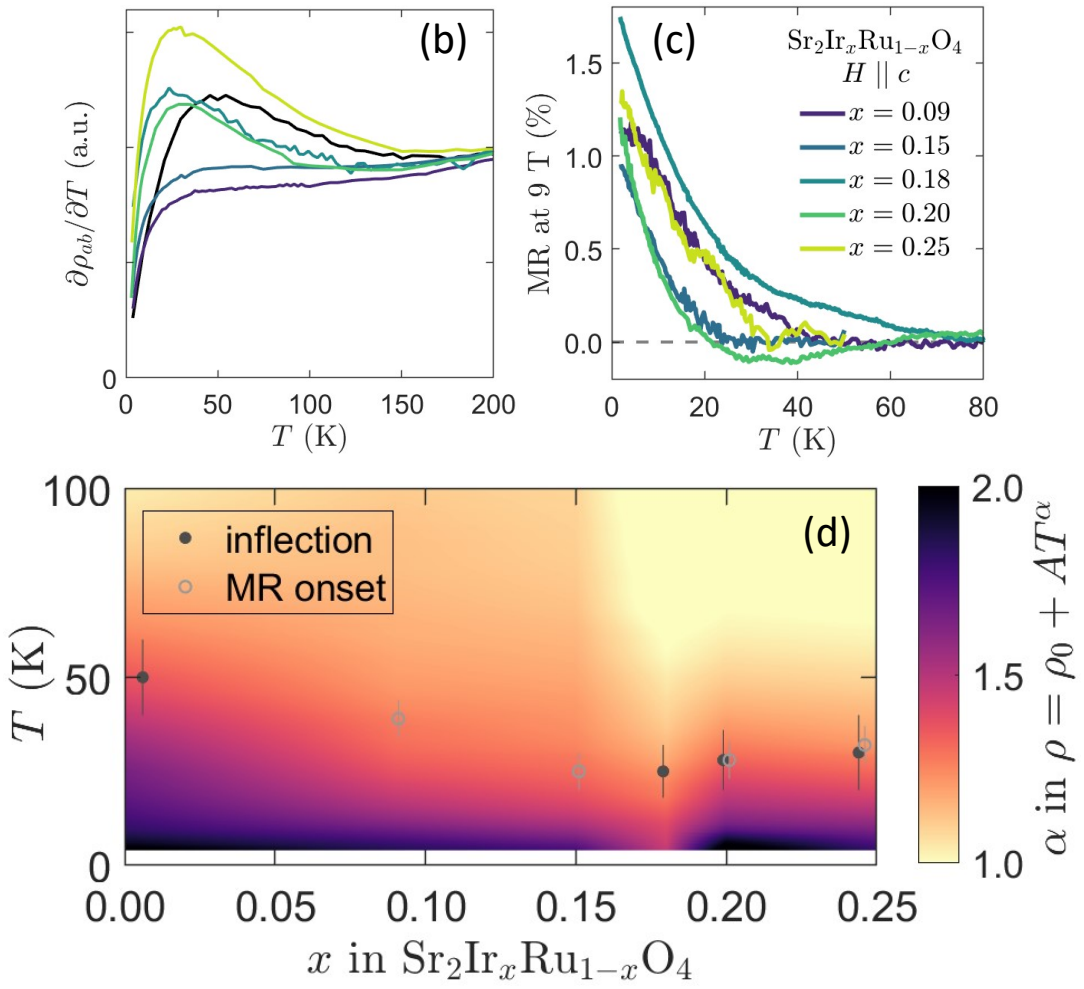

Figure 3.22: Magnetotransport near quantum criticality. Panel (b) shows the normalized slope of the resistivity. Panel (c) shows the magnetoresistance. Panel (d) is a false-color map of the exponent in temperature α, calculated from fits to the zero-field resistivity of the form $\rho_{ab} = \rho_0 + AT^\alpha$. All these panels highlight the inflection in temperature and the onset of the magnetoresistance near $T = 30{-}50$ K.

change in electronic properties is responsible for this significant response. The most relevant electronic detail seems to be the vicinity of all samples to the van Hove singularity (vHs) and its flat band physics. In the parent compound Sr_2RuO_4, above this temperature the resistance dependence on temperature changes qualitatively [101], the Hall coefficient dramatically changes sign [102], and for lightly strained films the electronic nematicity turns on [103].

A recent theoretical work by Herman and coworkers presents numerical simulations of Sr_2RuO_4 that match many of our magnetotransport observations [104]. Theirs is a Boltzmann equation approach to quasiparticle scattering for the γ-band. By tracking a crossover in scattering time near the vHs, they simulate the feature we call an inflection in the resistivity. This feature has a temperature scale of ∼40 K that decreases with doping towards the vHs, which gives way to transport with exponents $n<2$ near the vHs. Notably, they also predict that the low-temperature resistivity is maximized near the vHs. The applicability of these theoretical results may suggest that the non-Fermi Liquid transport arises from well-defined quasiparticles. However, that study considers neither the magnetic response nor SDW excitations from the α- and β-bands explicitly.

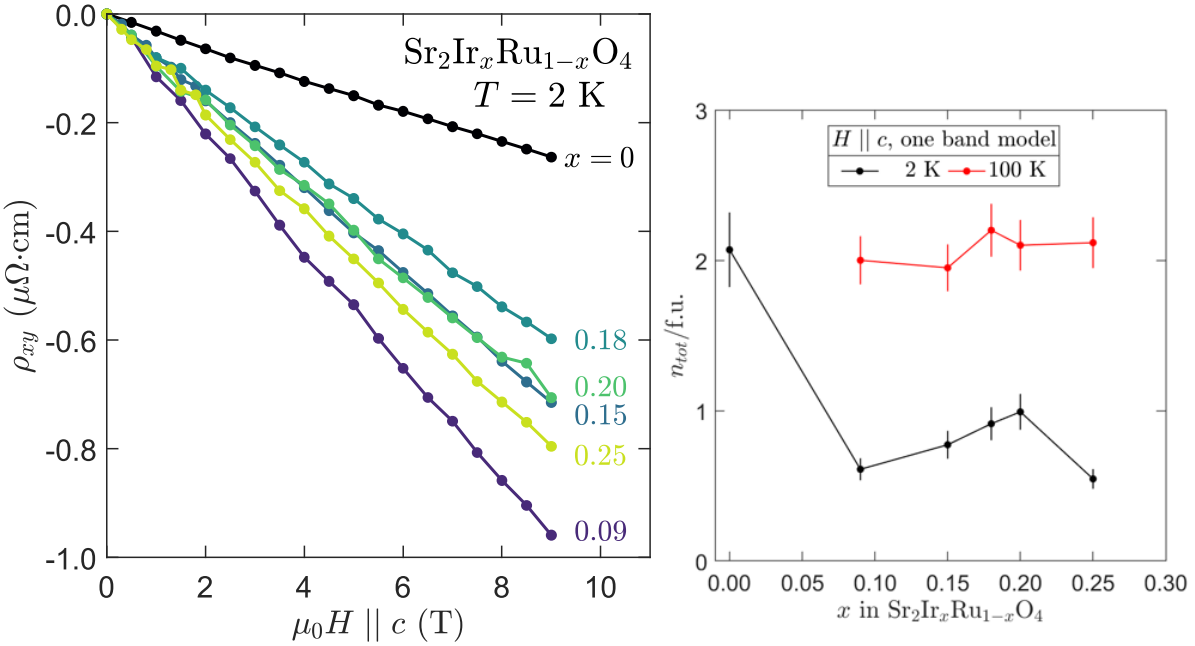

Figure 3.23: Hall resistivity near quantum criticality. The left panel shows the symmetrized Hall resistivity ρ_{xy} at 2 K. In the right panel, the number of carriers $n_{\rm tot} \propto H/\rho_{xy}$ was calculated by averaging the Hall data in field over the range 5 to 9 T. This analysis invokes an oversimplified one-band model. More data are in Fig. 3.14.

We turn our attention now to the Hall resistivity, shown in Fig. 3.6. As the samples approach the vHs there is a local maximum in $\rho_{xy}(H)$. This is unsurprising since the

density of states is maximized when the chemical potential sits at the vHs. Similar observations of extrema in ρ_{xy} hold under both La doping and uniaxial strain [78, 105]. In our case the value of ρ_{xy}(2 K, 9 T) is near -0.9 $\mu\Omega$·cm away from the vHs and -0.6 $\mu\Omega$·cm at x=0.18; assuming a simple one-band model, the latter corresponds to about one electron per formula unit. Since we know from ARPES that the number of carriers increases more or less continuously across the vHs [79], these results are broadly consistent with expectations and the other measurements.

To make further claims from the Hall data we would need to tread carefully. It is hard to compare the precise values of ρ_{xy} because of the inherent uncertainties from the polishing procedure, which yielded typical thicknesses 50±3 microns. And as was reported for other substitution series, it is hard to make meaningful claims from the Hall coefficient in this multiband, disordered system [105]. For pure Sr_2RuO_4, the $\rho_{xy}(\mu_0 H)$ is famously nonlinear and changes sign with temperature [102]. In our case, Ir-substitution yields short scattering times (ρ_{xx} is relatively large), so ρ_{xy} is linear in field and negative as a function of temperature.

3.7 Neutron Scattering

No long-range order was detected via single crystal neutron diffraction measurements of samples with x=0.09 and x=0.25. Instead we only found peaks with a structural origin - see Section 3.3.4. For the x=0.20 sample, the inelastic neutron scattering revealed no magnon modes below 60 meV at 5 K. Thus all samples reported here for $x \leq 0.25$ are considered to have paramagnetic ground states.

We did, however, track the spin density wave (SDW) fluctuations using inelastic neutron scattering (INS). We were motivated to look for magnetic fluctuations but found no clear evidence of magnons. For Sr_2RuO_4, there are gapped SDW fluctuations present,

as previously mentioned. The generalized susceptibility exhibits non-Fermi-liquid-like ω/T scaling above 30−50 K for pure Sr_2RuO_4 [67]. So measurements of the SDWs could stand to teach us about the electronic features we see in this temperature range.

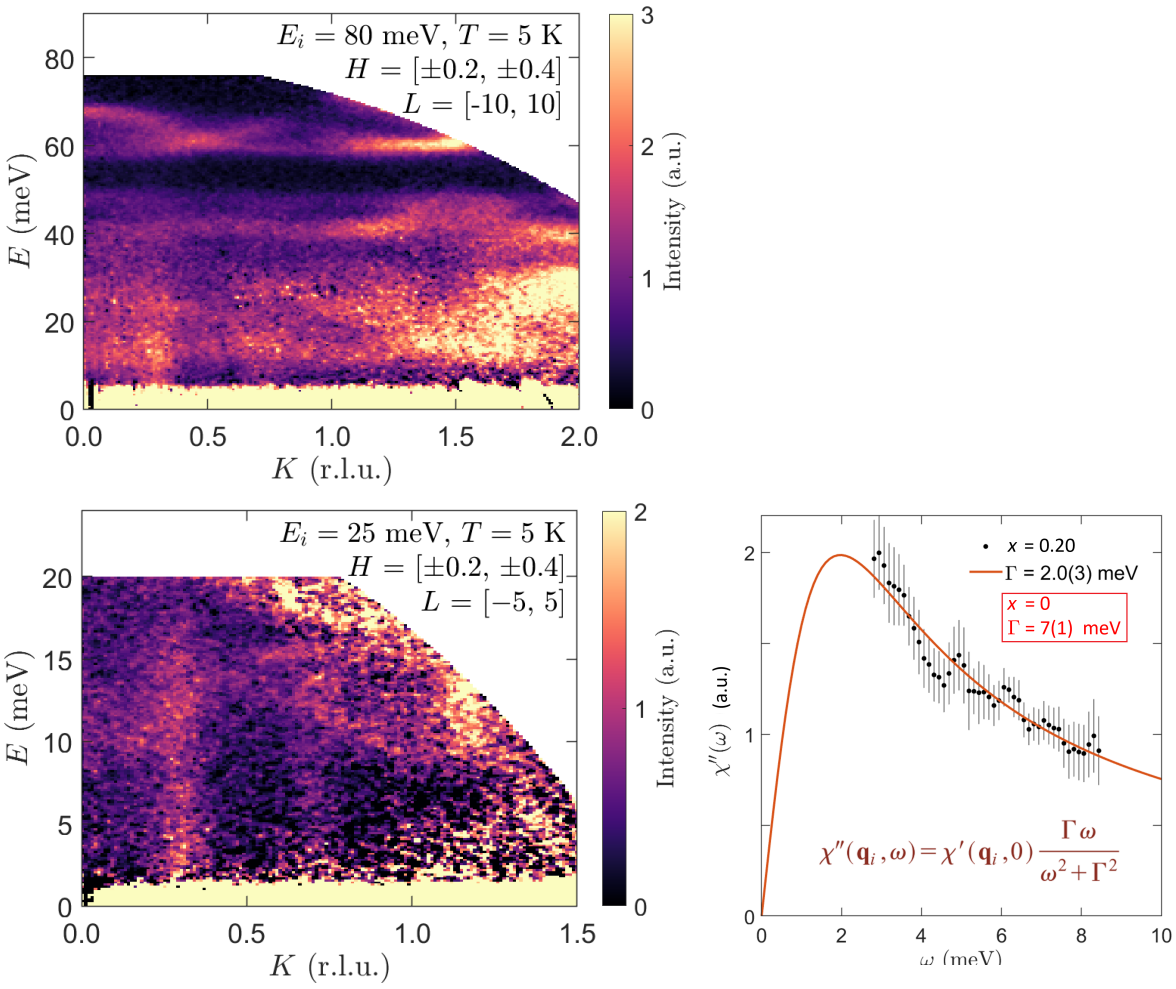

Figure 3.24: Spin density waves persist with Ir substitution. Both panels on the left show false-color maps of the inelastic neutron scattering of an x=0.20 sample measured on the SEQUOIA spectrometer. The integration ranges of the crystal momenta are reported in reciprocal lattice units, and the maps are symmetrized in H and K. The panel with E_i=80 meV shows no dispersing spin wave features, only the phonon modes reported for Sr_2RuO_4 [106]. In the panel with E_i=25 meV it is easier to distinguish the spin density wave (SDW) fluctuations with wavevector (0.30, 0.30) in the quasi-2-dimensional Brillouin Zone. On the right is the imaginary part of the susceptibility. The fit is described in the text.

INS was measured at the SEQUOIA direct geometry time-of-flight spectrometer at the Spallation Neutron Source (SNS) at Oak Ridge National Laboratory (ORNL). One 1.8 g crystal of the x=0.20 sample was mounted on an aluminum plate with aluminum wire and CYTOP epoxy within a closed-cycle cryostat. The sample was aligned with the incident beam along the tetragonal c axis (k_i || c) to measure the scattering in the ab basal plane, and the high flux Fermi chopper settings were utilized. For a measurement of the background, the aluminum sample can was measured under the same conditions with slits covering the sample.

As demonstrated in our INS spectra in Fig. 3.24, there are qualitatively similar SDW excitations for the x=0.20 sample compared to the parent Sr_2RuO_4. The quasi-2-dimensional SDW wavevector (0.30, 0.30) is the same as in Sr_2RuO_4. From our measurements we can set an upper bound for the SDW excitation gap at 2 meV, but lower-energy measurements are needed to determine whether the excitations are gapped.

The imaginary part of the susceptibility $\chi''(q,\omega)$ was calculated by first integrating for the energy dependence: the data were integrated and symmetrized as in Fig. 3.24 and then were further integrated by fitting energy cuts along K to Gaussians centered at the SDW wavevector with a constant background term. Then we accounted for the detailed balance and magnetic form factor. The Ru^{4+} form factor is not tabulated, so it was approximated by the International Tables for Crystallography value for Ru^{1+}, as is standard in the literature [107–109]. The resultant susceptibility data (black dots in Fig. 3.24) was fitted to single-relaxor behavior $\chi''(q,\omega) \propto \Gamma\omega/(\omega^2+\Gamma^2)$ (orange line) where the free parameter Γ is the characteristic energy scale associated with damping.

One important finding is that the damping of $\chi''(q,\omega)$ for the x=0.20 sample is in the range 2.0(5) meV, whereas for the parent sample the damping is near 7(1) meV [67]. This buildup of susceptibility at lower energies indicates that Ir pushes the electronic response towards criticality.

3.8 Discussion

What do La, Ti, and Mn teach us about Ir substitution? Let us revisit the results shown in Section 3.1.1. First, most qualitative experimental phenomena are shared between the Ir and La systems, except the magnetic anisotropy. Therefore we can attribute this difference to the orbitally-selective filling, since Ti and Mn are both highly anisotropic. It is interesting, then, that an easy c axis susceptibility does not render long-range order, as happens also under electron doping in the case of Co [75]. Clearly some additional competition or different chemistry occurs for Ir substitution that favors paramagnetism.

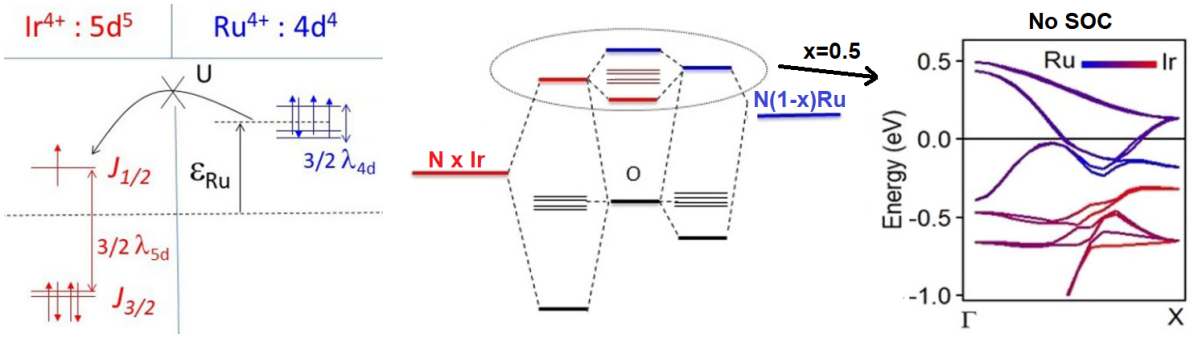

Figure 3.25: A self-energy (ε) consideration of the Ir substitution in $Sr_2Ir_xRu_{1-x}O_4$. On the left is a cartoon showing how correlations (U) prohibit electron transfer from Ru to Ir. In the center is a molecular extrapolation of these levels, and at right is a band structure calculation (without spin-orbit coupling and at x=0.5) showing that valence bands have primary Ru character. Adapted from [110]. Copyright 2021 American Physical Society.

Along the lines of different chemistry, we advance a simple self-energy argument proposed by Brouet et al. [110], shown in Fig. 3.25. If Ir has a lower self-energy than Ru, then correlations prohibit Ru from transferring an electron to Ir and forming the mixed valent Ru^{5+}/Ir^{3+} configuration (in a purely local, oversimplified picture). Instead it seems like the valence bands have dominant Ru character, which may be part of the puzzle of this unusually persistent paramagnetism under Ir substitution.

Before we assert our QCP claims, we offer one alternative explanation for the change in the high-temperature magnetic response with Ir substitution. Consider an oversimplified model in which isolated Ru ions have negligibly small magnetic moments, and Ir sites can magnetically polarize their nearest-neighbor Ru sites. In this model, according to percolation theory, the square lattice site percolation threshold $p_c \approx 0.59$ lies near x=0.16; in other words, magnetic clusters would begin to span large domains above this substitution value. Without further work it is unclear how well Ir polarization captures the high-temperature susceptibility behavior in Fig. 3.17a-c. However this polarization framework does not describe the low-temperature magnetism: there is a simple linear trend with Ir substitution for the magnetization M(2 K, 7 T) in Fig. 3.18e, which demonstrates that Ir ions do not polarize neighbors' moments at low temperatures.

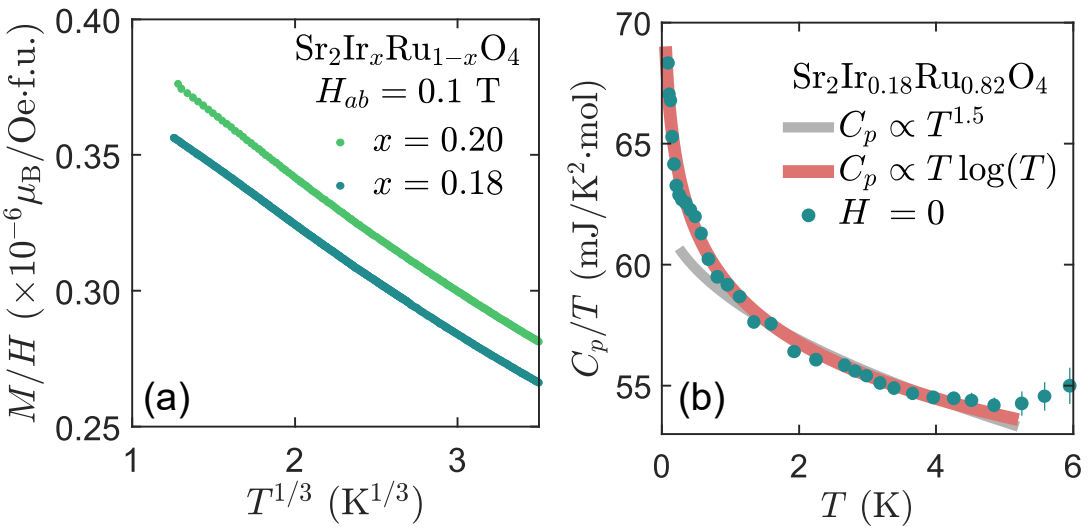

Figure 3.26: Possible quantum critical scaling. (a) shows the low-field susceptibility, plotted to show an approximate $M/H \propto T^{1/3}$ dependence. (b) is a reminder of the approximate $C_p \propto T \log T$ dependence in Fig. 3.15.

Instead we assert the presence of a quantum critical point to explain the thermodynamics, and in particular the low-temperature divergence of the heat capacity which is much greater than La substitution. The scaling of the heat capacity and the suscepti-

bility in Fig. 3.8 might be consistent with expectations for metallic QCPs (e.g. Ref. 100):

(a) $d = 3, z = 3$ antiferromagnetic QCP with $C_p \propto T \log T$ and $M/H \propto T^{1/3}$,

(b) $d = 3, z = 2$ antiferromagnetic QCP with $C_p \propto -T^{1.5}$ and $M/H \propto T^{1/4}$,

where d is the spatial dimension and z is the dynamical exponent. The nature is not definitive in our measurements, but there is some consistency with (a). The heat capacity is most consistent with (a) below 5 K when no corrections are made for the phonons (e.g. subtraction of a Debye fit). But the susceptibility is amenable to both options. The susceptibility is best fit by $T^{1/3}$ over the range 2 to 14 K, but it is best fit by $T^{1/4}$ over the wider range 2 to 40 K. Future theoretical collaborations will hopefully shed light on other possibilities, with special attention to theories in 2 spatial dimensions that may be more applicable.

This system's QCP may arise from moment freezing in the presence of strong spin-orbit coupling, as some of us and our co-workers predicted for multiorbital $4d$ and $5d$ compounds [49]. In this "J-freezing" model, itinerant excitations comprise the low-energy magnetic excitations for the highly correlated d^4 ground state, whereas local moment fluctuations dominate as the electron carrier concentration increases and/or as the correlation energy scale decreases. This variety of quantum criticality has been proposed to explain the emergent superconductivity in several compounds including Sr_2RuO_4 and UCoGe [39, 40]. A deeper understanding of this phenomenon may address outstanding issues in the field of unconventional superconductivity.

This proposed J-freezing quantum criticality seems applicable to a range of metals that host broad paramagnon bands, resulting in slow spin excitations prone to localization rather than long-range magnetic order. One common route to magnetic localization might be flat electronic bands. One example is the paramagnetic state in the flat band

metal URuGe, and reports of quantum criticality in U(Co,Ru)Ge [111, 112]. For another example, we point to recent experimental work on the kagome metal Ni_3In [113], which does not seem to order in spite of strong antiferromagnetic fluctuations $\theta_{CW}\approx-70$ K. Lastly, we suggest that these physics might be at play in $GaTa_4Se_8$, where moment freezing and flat bands have been associated with unconventional superconductivity [114, 115]. In these systems, like in $Sr_2Ir_xRu_{1-x}O_4$, the flat (yet delocalized) electronic bands lead to increased effective electronic mass (and perhaps reduces the bandwidth, increasing effective correlations), which may tune toward magnetically localized quantum criticality.

Lastly, we return to the connection between moment freezing in Sr_2RuO_4 and the cuprate superconductors. There, the bulk magnetization is qualitatively unique for each compound, but there is generally an onset in Curie-Weiss local magnetism for overdoped strange metal samples; for instance, above hole content $p_c\approx0.19$ for $(La,Sr)_2CuO_4$ (LSCO) [116]. LSCO is a charge transfer insulator and antiferromagnet at p=0, so it is best to compare Sr_2RuO_4 to strongly overdoped cuprates (e.g. $p\approx0.3$ in LSCO) with dominant Pauli paramagnetism and Fermi Liquid physics [117]. Without attempting to smooth over any subtleties, it is difficult to compare the magnetic responses because of the nature of the hole doping and the Lifshitz transitions particular to each cuprate system. Instead, we choose to elaborate on the density waves common to $Sr_2Ir_xRu_{1-x}O_4$ and LSCO. Recently charge density waves (CDWs) were shown to exist to at least p=0.25 in the strongly overdoped regime [118]. At temperatures above the CDW order, density wave fluctuations seem to have a strong effect on the thermodynamics. We echo claims that the density wave fluctuations and Mott physics are central to the strange metal phases of both the cuprates and $Sr_2Ir_xRu_{1-x}O_4$.

3.9 Conclusions

In conclusion, we show how the correlated, itinerant moments for Sr_2RuO_4 seem to evolve into local moments for $Sr_2Ir_xRu_{1-x}O_4$ for x>0.18. Some hallmarks of strange metal behavior in the paramagnetic metal phase were observed. The possibility of a quantum critical point was discussed and extended to other materials. The discussion highlighted ideas for future theory work. I will now explicitly describe some future experimental directions.

On the synthesis end, of course ever-higher-quality samples are sought in the field of quantum materials. It would be good to measure samples with a tighter control of Ir content x across the phase diagram. In the cuprates, minute changes in carrier concentration $\approx$0.01 are sufficient to traverse phase regions, like the anomalies seen in $La_{1.875}Ba_{0.125}CuO_4$ and near the pseudogap phase's endpoint. As a parallel effort, several researchers have requested high-quality samples traversing the metal-insulator transition at large Ir content $x\sim$0.5. I am invested in this question, but so far it has proven very difficult to prepare higher-Ir-content samples via the floating zone technique. We report evidence of weak localization for samples with x=0.40, but it is unclear if this is a consequence of mediocre sample quality.

I briefly identify some next steps regarding measurements on current samples. We performed few measurements below 2 K where the quantum critical fluctuations are strong; ac susceptibility and neutron scattering might find interesting fluctuations or perhaps other orders. Magnetoresistance at higher fields might yield more insights about the strange metallicity. We did not measure resistivity along the interplane c direction so we cannot speak much to the transport anisotropies. Collaborations with measurements sensitive to fluctuating density wave orders, like terahertz spectroscopies, could be complementary to our inelastic neutron studies. Muon spectroscopy and X-ray magnetic

circular dichroism have the potential to yield insights about the magnetism. Measurements of the electronic nematicity could also be insightful. Near the vHs, uniaxial strain might be an interesting parameter to tune.

Chapter 4

Persistent Antiferromagnetism in the Bilayer $Sr_3(Ir_{1-x}Ru_x)_2O_7$

[1] The substitution series $Sr_3(Ir_{1-x}Ru_x)_2O_7$ is closely related to $Sr_2Ir_{1-x}Ru_xO_4$, the compound explored in Chapter 3.[2] $Sr_3(Ir_{1-x}Ru_x)_2O_7$ is the bilayer in the Ruddlesden-Popper series, so each $(Ir/Ru)O_6$ octahedron ion has an additional interplane nearest neighbor, for a total of 5. The resultant increase in bandwidth (or, if you like, dimensionality) manifests in a smaller band gap for the insulating antiferromagnetic endmember $Sr_3Ir_2O_7$. On the other end of the phase diagram, the fully Ru-substituted system $Sr_3Ru_2O_7$ is a metallic paramagnet near both ferromagnetic and antiferromagnetic instabilities [120, 121].

While they share commonalities, much of the physics of this bilayer compound are different from the monolayer. $Sr_3Ir_2O_7$ has small octahedral tilts relative to Sr_2IrO_4, so it has its spins oriented along the long axis in its antiferromagnetic ground state; see Section 1.2.2. And, relatedly, there is no structural transition between $Sr_3Ir_2O_7$ and $Sr_3Ru_2O_7$,

[1] Part of this chapter is based on one of our publications, Ref. 10: Julian L. Schmehr, Thomas R. Mion, Zach Porter, Michael Aling, Huibo Cao, Mary H. Upton, Zahirul Islam, Rui-Hua He, Rajdeep Sensarma, Nandini Trivedi, and Stephen D. Wilson. Overdamped antiferromagnetic strange metal state in Sr_3IrRuO_7, Physical Review Letters 122, 157201 (2019). Copyright 2019 American Physical Society.
Other measurements reported here were collaborative efforts with several of the above scientists.
We also reference some of the work published in Ref. [119]: Gihyeon Ahn, Julian L. Schmehr, Zach Porter, Stephen D. Wilson, and Soonjae Moon. Doping and temperature evolutions of optical response of $Sr_3(Ir_{1-x}Ru_x)_2O_7$, Scientific Reports 10, 22340 (2020). Copyright 2020 The Authors.

[2] Note we are using a different definition of x from the previous chapter, for consistency with the literature.

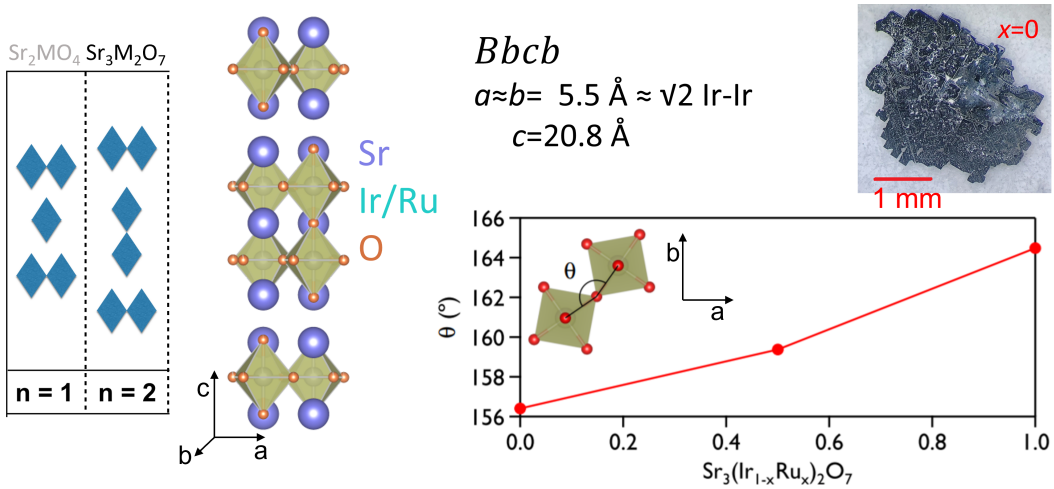

Figure 4.1: Structural overview of $Sr_3(Ir_{1-x}Ru_x)_2O_7$. The n=2 (bilayer) Ruddlesden-Popper structure is shown on the left, and the orthorhombic cell (close to tetragonal) is briefly described. The in-plane bond angles are shown on bottom right, adapted from Ref. [10]. A representative iridate sample is shown on the top right.

according to the neutron diffraction in Refs. 10, 122. Accordingly the bandstructures of the monolayer and bilayer vary. The bilayer ruthenate $Sr_3Ru_2O_7$ is incredibly close to a spin density wave (SDW) instability, and these gapped fluctuations seem to dominate the low-energy physics. $Sr_3Ru_2O_7$ can be tuned across a metamagnetic quantum critical point with applied magnetic fields [123–127].

In this chapter we present evidence for a correlated electron system hosting substitution-driven metallic quantum criticality. We demonstrate an antiferromagnetic ground state in $Sr_3(Ir_{1-x}Ru_x)_2O_7$ that persists to at least $x = 0.70$, deep in the strange metallic phase where quasiparticles are highly incoherent. Long-range Ir J_{eff}=1/2 antiferromagnetism with a large transition temperature $T_N > 200$ K is revealed via resonant X-ray scattering, but it is not evident in the bulk magnetization due to dominant Ru S=1 local fluctuations. Spectroscopies suggests that damped fluctuations could play a role in stabilizing the magnetic order. Our linear-in-temperature resistivity measurements may point to a quantum critical point near x≈0.8.

4.1 Introduction

$Sr_3(Ir_{1-x}Ru_x)_2O_7$ has a rich yet partially unexplored phase diagram [9, 128]. The parent system, $Sr_3Ir_2O_7$, is a J_{eff}=1/2 Mott insulator with long-range G-type antiferromagnetic (AF) order. Upon alloying Ru^{4+} (S=1) on the Ir^{4+} sites, there is a percolative metal-insulator transition near Ru fraction x=0.4, yet long-range AF order persists well into the metallic state, beyond x=0.7. To date, the AF endpoint in the $Sr_3(Ir_{1-x}Ru_x)_2O_7$ phase diagram has not been established.

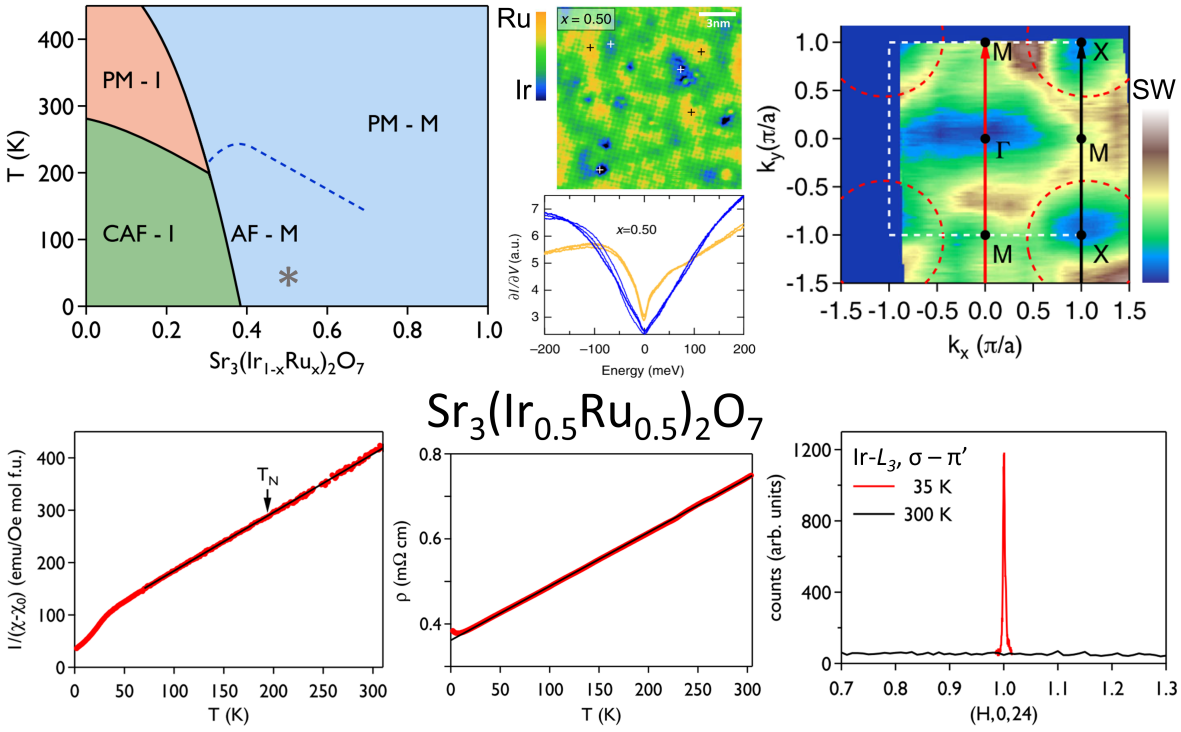

Figure 4.2: Strange metal physics of Sr_3IrRuO_7. From top left, first we present the phase diagram; then we repeat the scanning tunneling results shown in Fig. 1.8 from Ref. 9 that demonstrate phase segregation on the nanoscale. The proceeding results were published in Ref. 10: incoherent Fermi surface with poorly-defined quasiparticles (SW stands for spectral weight); inverse susceptibility $1/\chi$ is featureless near the Néel transition; the in-plane resistivity ρ is roughly linear-in-temperature; and the Ir-L_3 resonant elastic X-ray scattering (REXS) shows a low-temperature signal in the magnetic $\sigma - \pi'$ channel at the antiferromagnetic wavevector (1, 0, 24). All results are indexed to the tetragonal $I4/mmm$ space group.

Our resonant X-ray scattering (RXS) studies were targeted at determining the details of the magnetic structure for samples with high Ru content. To summarize our main results, at 50% Ru substitution, Sr_3IrRuO_7 is an inhomogeneous metal marked by an incoherent Fermi surface with no well-defined quasiparticles [10]. Surprisingly, long-range AF order survives in this electronically incoherent state, even though the large background of local Ru moment magnetism makes the onset of AF order too weak to be detected via dc magnetization measurements. Perhaps the ARPES spectral weight at the M-point, the magnetic zone center, reflects a spin density wave instability toward this order; see Fig. 4.2 top right. Recent Ir-L_3 resonant elastic X-ray scattering (REXS) measurements of $Sr_3(Ir_{0.3}Ru_{0.7})_2O_7$ directly confirm long-range G-type AF order with an isotropic correlation length of about 100 nm, about the same as in earlier measurements of Sr_3IrRuO_7. This prompts the question of how far long-range magnetic order survives with increasing Ru content.

This question of the magnetic phase boundary is vital for understanding recent observations of strange metal transport behavior in these samples. It is unclear exactly how long-range magnetic order is tied to the strange metal phases as a function of temperature, though we present some preliminary order parameters. A bigger open question as of this writing is whether strange metallicity stems from a continuous global AF-paramagnetic phase transition at zero temperature − a quantum critical point; see for example Refs. 129, 130. There may be a relation to the well-established quantum critical transition in $Sr_3Ru_2O_7$ (x=1) under an applied magnetic field [126].

Regarding the strange metallicity, recent optical spectroscopy measurements unambiguously reveal a state with a non-Fermi-liquid scattering rate $1/\tau \propto \omega$ [119]. The intraband response was shown to be dissipative, indicating poorly defined quasiparticles. The effective mass enhancement was further evidence of the highly correlated nature of this strange metal state for samples spanning x=0.49-0.77. These findings are comple-

mentary to the ARPES measurements reported in Ref. 10, shown in Fig. 4.2.

4.1.1 Relevant Work on $Sr_2Ir_{1-x}Ru_xO_4$

Few studies have focused on $Sr_3(Ir_{1-x}Ru_x)_2O_7$, so we now present previous work that may be relevant. Since some of the physics are shared, I will describe a small subset of the results of X-ray and neutron scattering studies of the excitations in $Sr_2Ir_{1-x}Ru_xO_4$ (note how x in this chapter describes Ru content).

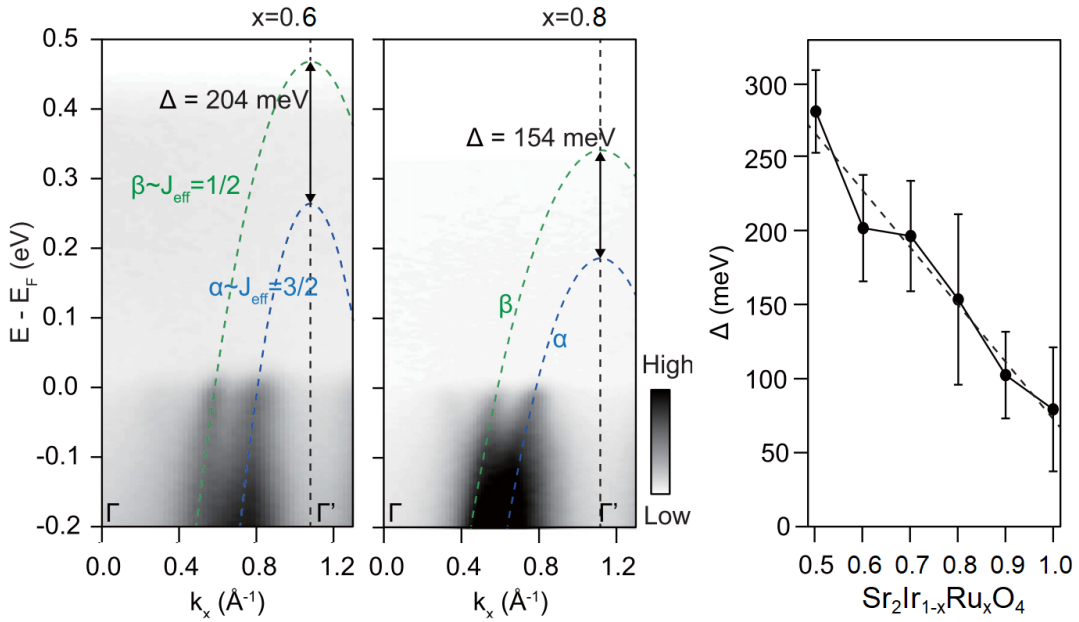

Figure 4.3: Band structure corroboration for spin-orbit excitons. These angle-resolved photoemission (ARPES) data are for the closely related compound $Sr_2Ir_{1-x}Ru_xO_4$. In the left panels, band dispersions along $\Gamma - \Gamma'$ are shown, with fits for the J_{eff}=1/2 and 3/2 bands. On the right is the fitted splitting Δ between these bands extrapolated to Γ'. The ≈200 energy scale of the splitting at x=0.7 seems relevant for the excitations presented in Section 4.4.3. Adapted from Ref. 79. Copyright 2021 American Physical Society.

First, some band structure results from ARPES, which I touched on in Section 3.1. J. Kwon and co-workers estimated the splitting between the J_{eff}=1/2 and 3/2 manifolds, shown in Fig. 4.3 [79]. This ≈200 meV energy scale for Ru substitutions x≈0.7 may be

relevant to the spin-orbit excitons. The trend down with Ru matches expectations for the change in effective spin-orbit energy scales for Sr_2MO_4 with M=Ir d^5 $\lambda\approx$400 meV to M=Ru d^4 $\tilde{\lambda}\approx$40 meV. Because spin-orbit coupling is tied to the local physics, it seems fair to assume a similar trend for $Sr_3(Ir_{1-x}Ru_x)_2O_7$.

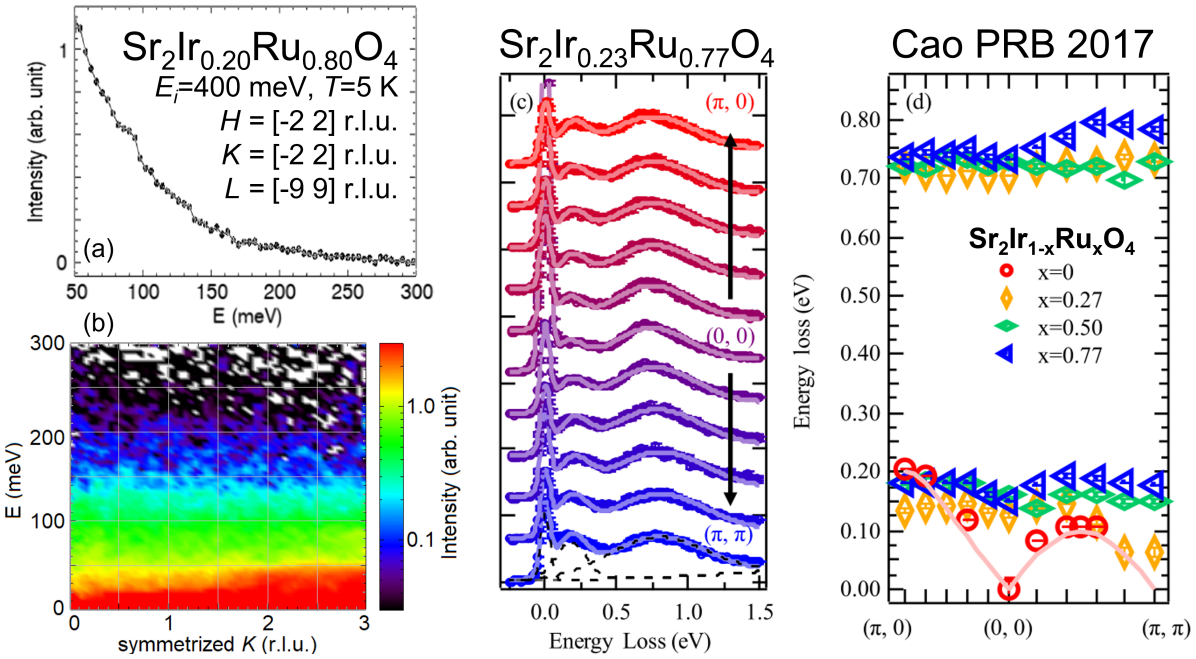

Figure 4.4: Scattering corroboration for spin-orbit excitons. These data are for the closely related compound $Sr_2Ir_{1-x}Ru_xO_4$. In (a,b) is our own inelastic neutron scattering (INS) measurements at incident energy of E_i=400 meV. Integration bounds for both the cut and the false-color slice with a logarithmic color scale are indicated in (a). In (c,d), resonant inelastic X-ray scattering (RIXS) spectra and fits are shown, adapted from Ref. 131, Copyright 2017 American Physical Society.

Now we move on to a salient resonant inelastic X-ray scattering (RIXS) study of $Sr_2Ir_{1-x}Ru_xO_4$. Y. Cao and co-workers reported RIXS studies of samples spanning from Sr_2IrO_4 nearly to Sr_2RuO_4 see Fig. 4.4c-d [131]. The two highly-Ru-substituted samples both have similar spectra. Their Gaussian fits for $x = 0.77$, which capture some but not all of the energy dependence, show a weakly dispersive band of excitations peaked near 180 meV. These results are clearly similar to ours on $Sr_3(Ir_{1-x}Ru_x)_2O_7$ in Section 4.4.3.

Note how this energy scale is very similar to the one in ARPES.

Contrast this RIXS result with the high-energy inelastic neutron scattering (INS) of $Sr_2Ir_{1-x}Ru_xO_4$. The measured sample has a high Ru content of $x = 0.80$, very near the stoichiometry of the RIXS sample. The measurement setup at the SEQUOIA time-of-flight spectrometer was reported in Section 3.7. In measurements with an incident energy of 400 meV, we were unable to resolve any features in the spectra in the range 100-300 meV. This is evidence that the excitations measured by RIXS are not magnetic. We take this to imply that the RIXS signal is instead more consistent with spin-orbital excitons.

4.2 Synthesis: Unconventional Flux

Single crystal synthesis was accomplished using a flux technique. It is unconventional mainly in the sense that the flux boils off during synthesis, which changes the flux ratio over time. As such, sample size and homogeneity are finely sensitive to the furnace settings and to the input flux ratio.

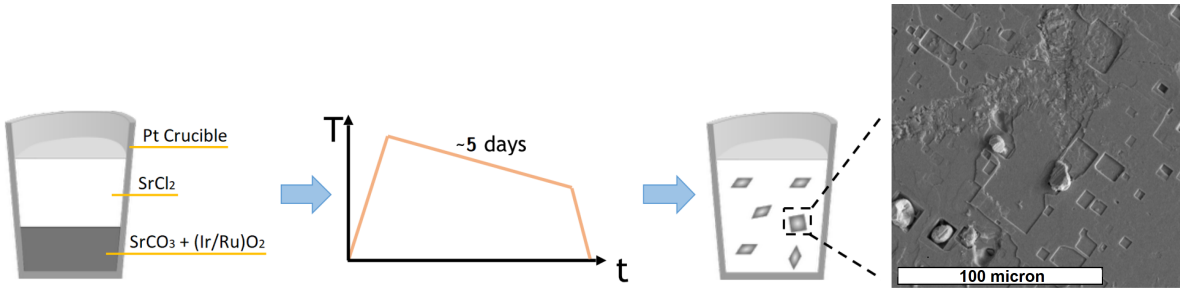

Figure 4.5: Flux synthesis technique for $Sr_3(Ir_{1-x}Ru_x)_2O_7$. First reactants are placed in a Pt crucible, then heated and slowly cooled. The resultant ~1 mm^2 plate-shaped crystals adopt a square habit, with rectangular ~10 μm features visible in the secondary electron image on the right.

Crystals were grown in platinum crucibles using $SrCO_3$, IrO_2, and RuO_2 (all >99.9%, Alfa Aesar) in a stoichiometric ratio. These powders were dried overnight, weighed, mixed

for about 20 minutes with an agate mortar and pestle, and then poured into the crucible. Then dried anhydrous $SrCl_2$ (99.5%, Alfa Aesar) flux was added in a 15:1 molar ratio, for a total mass of about 10 g. The crucibles were affixed with a Pt lid and further contained inside alumina crucibles. Mixtures were heated up to 1650 K over several hours in a box furnace, reacted there for 3-5 hours, then slowly cooled to 1120 K at a rate of about 3.5 K per hour. Finally the reaction was furnace-cooled to room temperature; below the melting point of the flux the final cooling rate seems unimportant. The resulting crystals were etched from the solidified flux mixture with warm deionized water to reveal shiny, black, rectangular-prism-shaped samples. The encrusted chloride salt was scraped with fine nonmagnetic tools (dental probe and needles) and rinsed with water. To cleave fresh surfaces, samples were pressed onto Scotch double-sided tape and lifted off, then rinsed in acetone and isopropanol to remove residue.

Sample composition was checked with X-ray diffraction using a Panalytical Empyrean diffractometer. Each batch's lattice parameters were checked by finely grinding several crystals, diffracting over a wide range, and using a Pawley fit. Each studied crystal was additionally screened for phase purity with the diffractometer by placing it flat on a zero-diffraction plate; since the crystals cleave in the basal plane the $\theta-2\theta$ scans along the long axis. In the oversimplified $I4/mmm$ tetragonal space group this means we measured the $[00L]$ reflections. This type of measurement is insensitive to misoriented grains but it is a fairly sensitive measure of whether there was intergrowth of other Ruddlesden-Popper phases like the monolayer $Sr_2Ir_{1-x}Ru_xO_4$ which is synthesized under similar conditions. Since the Cu-K_α X-rays have a penetration depth of several tens of microns, samples were checked on both sides.

To measure Ru substitution, we used a ThermoFisher Apreo C scanning electron microscope for energy-dispersive X-ray spectroscopy (EDX) and backscattered electron imaging (BSE) with a typical configuration of 20 kV accelerating voltage and 1.6 nA

beam current. Ruthenium is incorporated somewhat homogeneously into the bulk crystal matrix, as confirmed by lattice parameters and energy dispersive spectroscopy. The variance of x for one sample on the 50 μm length scale is typically near $0.04x$.

One peculiar finding is that the batches' stoichiometries were difficult to tune and somewhat insensitive to the input stoichiometry. Of hundreds of EDX measurements, only several samples were found with compositions between x=0.52 and 0.64. Large gaps in x are common across the substitution series.

4.3 Electron Transport

Electron transport was measured with a Quantum Design PPMS. Samples were glued to insulating cigarette paper atop gold puck surfaces with GE varnish. 4-wire contacts were made with silver paint and gold wirebonding wires onto flat unpolished crystal facets. Paint was applied with an eyelash due to small sample size.

Fig. 4.6 shows the in-plane resistivity $\rho_{ab}(T)$ for the series $Sr_3(Ir_{1-x}Ru_x)_2O_7$. Largely linear-in-temperature behavior ($\rho_{ab} \propto T^{\alpha}$ with α=1) was observed near 100 K, which is consistent with strange metallicity. The overall trend with x is for the residual resistivity ratio ρ_{ab}(100 K)/ρ_{ab}(2 K) to increase, as site disorder decreases towards the metallic endmember $Sr_3Ru_2O_7$. At Ru concentrations near x=0.5, weak upturns were observed at low temperatures. Fitting above these upturns, the resistivity is nearly quadratic (α=2) at low temperatures and becomes nearly linear at high temperatures.

As x increases, the onset temperature for the linearity decreases until about x=0.74 and subsequently increases, as is readily observed in the resistivity. For a more quantitative analysis, we calculated a false-color map of α values. In the map, this trend is exhibited by the solid black lines, which cut very approximately through α=1.4. The samples in the range $0.66 \leq x \leq 0.82$ are best fit by $\alpha = 1.3(1)$ below about 15 K.

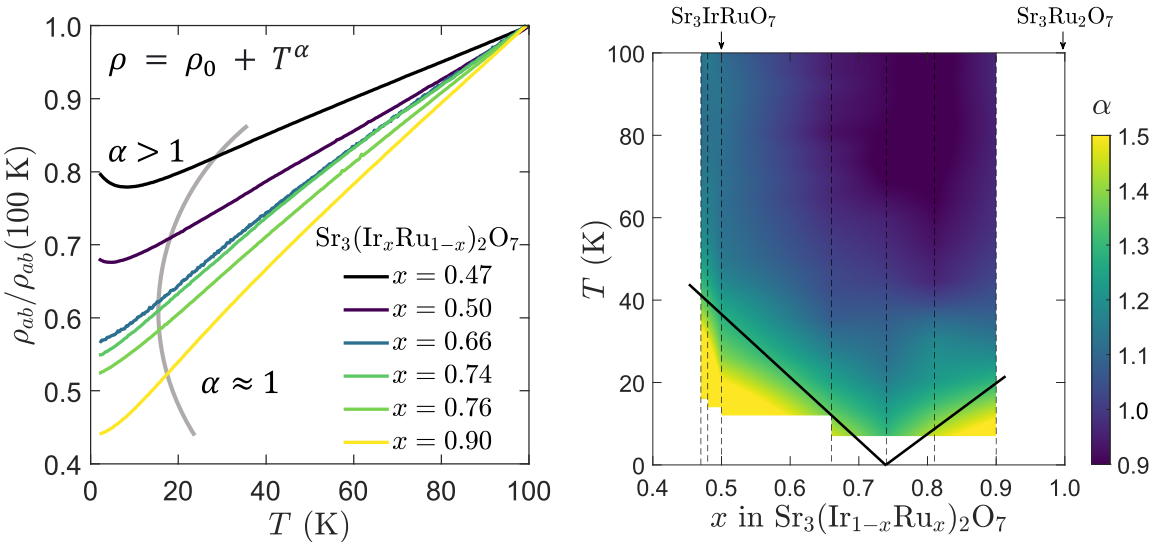

Figure 4.6: Strange metal transport for Ru-rich $Sr_3(Ir_{1-x}Ru_x)_2O_7$. In the left panel, the normalized in-plane resistivity ρ_{ab} is plotted for several samples. The gray line coarsely marks the onset of linear-in-temperature behavior: $\rho = \rho_0 + AT^\alpha$ with $\alpha \approx 1$. On the right is a calculated, interpolated false-color map of α for select samples. Measured x values are indicated by dashed lines. Black solid lines are guides to the eye.

We associate this temperature dependence with a possible quantum critical point in the range near x=0.75.

As a follow-up, we attempted heat capacity measurements to explore this possibility. But the <1 mg sample masses with mediocre thermal conductivity made quantitative analysis and sample-to-sample comparison difficult. Magnetization was similarly difficult, in part due to dilute impurity phases.

4.4 Resonant X-ray Scattering

Our Ir L_3-edge RXS measurements may show long-range antiferromagnetism to at least x=0.7. Recent results include correlation lengths and partial temperature order parameters. These measurements are challenging because of the dilute Ir concentrations.

The signals are more than $10^3\times$ weaker than in the parent iridate $Sr_3Ir_2O_7$.

As for the resonant inelastic X-ray spectroscopy (RIXS), the discussion of Ref. [10] claims that the lowest-energy excitations near 200 meV are overdamped magnons. Our recent work on $Sr_3Ir_2O_7F_2$ instead suggests a subtle distinction, that these are spin-orbit excitons; see Chapter 5. Since spin-orbit excitons are highly local, this hypothesis addresses how incredibly isotropic these excitations appear. Also, excitons better explain why the low-energy excitations' energy scale increases with Ru content from x=0.17 to 0.48, as the Ir ions are hole-doped towards the $5d^4$ J_{eff}=0 state. The energy scale of the excitations seems to match the ≈200 meV J_{eff} manifold splitting measured by ARPES; see Fig. 4.3. The magnons that must be present in these antiferromagnetic samples are likely at lower energies ∼10 meV inaccessible by our RIXS measurements.

First I will summarize the resonant elastic X-ray scattering (REXS) studies of x=0.5 samples (Sr_3IrRuO_7). Then I will discuss higher-Ru content samples with x=0.7; these were measured on a RIXS beamline but we pay particular attention to measurements in the elastic channel. For comparison to the scattering, magnetization was measured on the same samples with a Quantum Design MPMS3 SQUID magnetometer on cleaved samples adhered to a quartz paddle with GE varnish.

4.4.1 x=0.5 Magnetic Diffraction

Samples with x=0.5 (Sr_3IrRuO_7) are known to have G-type antiferromagnetic order. A neutron diffraction study found a (1 0 3) magnetic peak persists to this Ru concentration, with an onset temperature >150 K [9]. Since no evidence of a structural transition was resolved with high-resolution neutron diffraction at T=4 K on HB-3A at the High Flux Isotope Reactor (HFIR), we are confident in this result [10].

The results of resonant elastic X-ray scattering (REXS) measurements at APS 6-ID-B

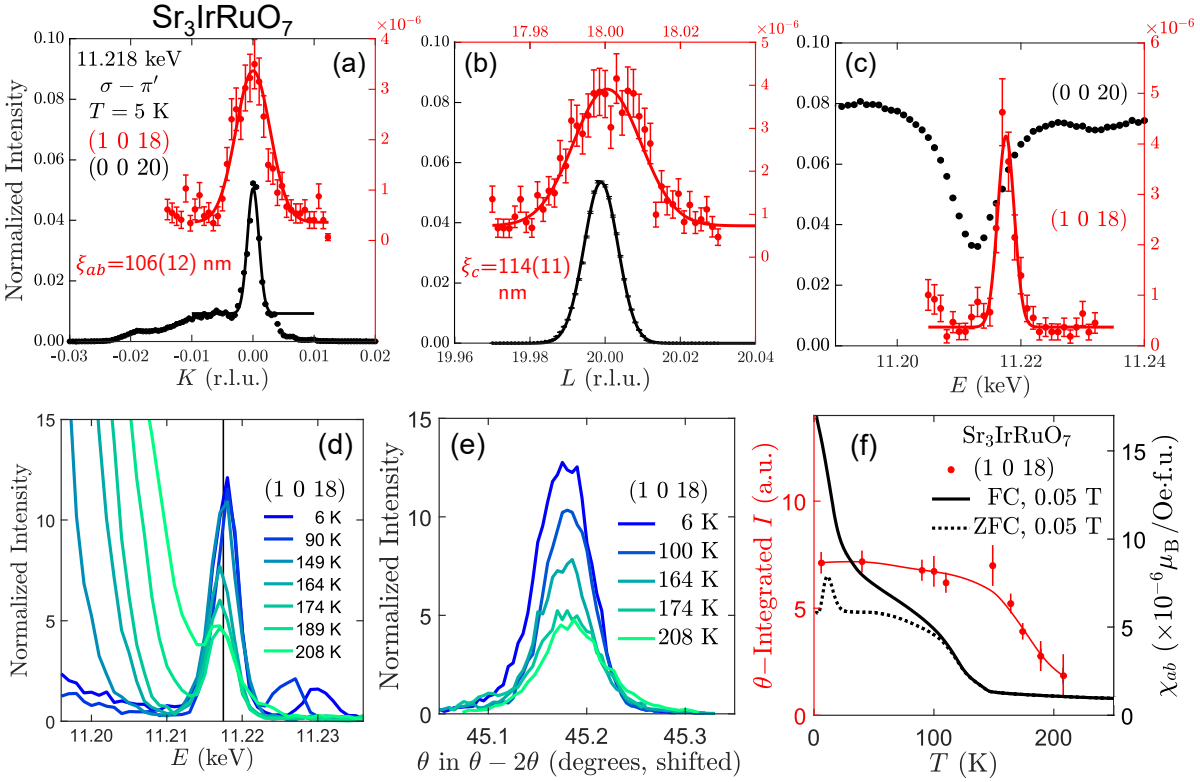

Figure 4.7: Resonant elastic X-ray scattering (REXS) measurements exploring the long-range G-type antiferromagnetism in Sr_3IrRuO_7. (a,b,c) are K, L, E scans of a magnetic (red) and a structural (black) Bragg reflection. (d) shows energy scans at the magnetic Bragg reflection with encroaching multiple scattering (MS). (e) shows the θ–2θ scans; widths are roughly constant in temperature. (f) shows the θ-integrated order parameter (left axis, red) after subtracting an approximate MS contribution. Compare this to the bulk magnetization (right axis, black) for the same sample. All results are indexed to the tetragonal $I4/mmm$ space group.

are shown in Fig. 4.7. Some information about the setup is in Section 2.2.2. These are the results from two different experiments on samples with similar Ru content x. All the measurements are on resonance unless otherwise indicated, and analyzed with a flat Si(1,1,1) crystal in the $\sigma - \pi'$ polarization channel.

The top panels in Fig. 4.7 indicate results already known about the putative G-type antiferromagnetic order from Ref. [10]. The correlation lengths ξ are near 100 nm along

K and L, indicating long-range order.[3]

The most confusing finding is that the incident energy that maximizes the magnetic reflection ≈11.218 keV (see Fig. 4.7c) is about 4 eV *above* the absorption maximum (AM). If this is a trustworthy value, it is perhaps at odds with measurements of d^5 iridates e.g. Sr_2IrO_4 and $Sr_3Ir_2O_7$ [16, 58], where the resonant enhancement occurs 3-4 eV *below* the AM. We are unaware of another Ir compound with this exact behavior, but a similar peak was recently observed on a mixed structural and magnetic reflection in the trimer antiferromagnet $Ba_4Ir_3O_{10}$ [132]. For t_{2g}^5 ions, the AM typically corresponds to the e_g manifold since it has the most available states for the photoexcited electron. So the conventional wisdom goes that the magnetic state in the t_{2g} manifold ought to lie below the AM. By this logic our signal is 6-7 eV above the valence states, which casts the origin of this in doubt. We rule out anisotropic tensor scattering (ATS, Section 2.1.5) because that is expected within the e_g manifold, and such peaks usually do not exhibit much temperature dependence (e.g. Ref. [133]). Instead this energy scale is on par with expectations for charge transfer to hybridized O $2p$ states [134, 135]. What if the magnetism is on the Ru sites, only probed at Ir sites by transferring electrons to Ru over the oxygen ions? We suspect some such complication or another experimental issue at play. Therefore, based on the neutron diffraction, we will assume this is a magnetic signal.

Now we turn our attention to the partial order parameter (bottom panels of Fig. 4.7) which is currently unpublished. The $\theta-2\theta$ scans do not seem to change significantly in width (correlation length) with temperature, possibly consistent with long-range order remaining through at least 180 K. The energy scans at the (1, 0, 18) magnetic Bragg reflection show a strong multiple scattering (MS) peak moving in from low energy to obscure the signal. The effect is quite significant above 180 K. To deal with this we

[3]The H direction was not sharp with the analyzer crystal in place.

fit the energy scans and approximately subtracted the MS contribution from the order parameters. The order parameter (red data in Fig. 4.7f) seems uncorrelated with the measured susceptibility for this exact same sample. In the susceptibility there are no clear features above 150 K, when the REXS order parameter is already saturated. The susceptibility is potentially picking up a dilute ferromagnetic impurity such as sub-percent contamination of $Sr(Ir,Ru)O_3$.

4.4.2 x=0.7 Magnetic Diffraction

The results of resonant X-ray scattering (RXS) measurements at APS 27-ID-D are shown in Fig. 4.8. Some information about the setup is in Section 2.2.4. All the measurements are at 11.215 keV. The scattering was analyzed with a Si(4,4,8) diced spherical analyzer crystal and detected in the elastic channel of the strip detector. This setup allowed us to minimize the fluorescence background while integrating the peak over a fairly large solid angle, vastly improving signal-to-noise. But since the scattering was performed in a backscattering geometry, all scattered polarizations were detected.

The x=0.71(3) sample was mounted with GE varnish to an aluminum mount on a cold finger, and cooled in an evacuated cryostat within two Be windows. The alignment was performed using a $C2/c$ unit cell with a=20.92 Å, b=5.481 Å, c=5.463 Å, and β=90.045°, but all the values in this thesis reference the tetragonal $I4/mmm$ space group with c as the long axis. I aligned at base temperature using the (0, 0, 24), (2, 0, 24), and (1, 1, 25) structurally allowed Bragg peaks. The (0, 0, 24) rocking curve's width was about 0.07 degrees, which is fairly sharp and indicates a good sample mosaic. The analyzer crystal (100 mm diameter) integrated over a wide range of 2θ values.

Intensity was observed at the wavevector (3, 0, 24) which lies near normal incidence. This is consistent with G-type antiferromagnetic order. Due to time constraints this is

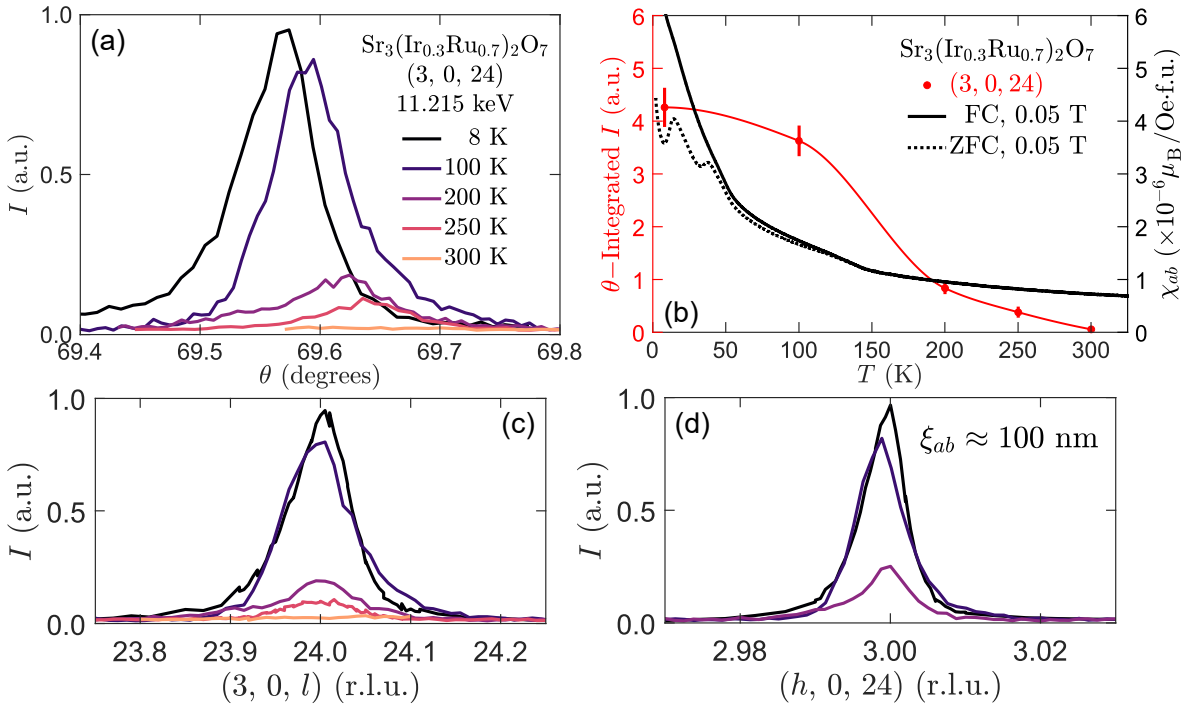

Figure 4.8: Resonant X-ray scattering (RXS) measurements exploring the long-range G-type antiferromagnetism in $Sr_3(Ir_{0.3}Ru_{0.7})_2O_7$. (a,c,d) are θ, L, H scans of a magnetic Bragg reflection at various temperatures. (b) shows the θ-integrated order parameter (left axis, red) and the bulk magnetization (right axis, black) for the same sample. All results are indexed to the tetragonal $I4/mmm$ space group.

the only disallowed reflection that I tracked.

The rough order parameter for $Sr_3(Ir_{0.3}Ru_{0.7})_2O_7$ in Fig. 4.8b is qualitatively similar to the x=0.5 sample (Fig 4.7f): nearly saturated by 100 K and diminished to ≈1/4 of the intensity at 200 K without a large change in correlation length. At low temperatures the in-plane correlation lengths ξ_{ab}≈100 nm for both samples. Again the long-range order seems to be largely uncorrelated to the bulk susceptibility. Electronic phase segregation (coexisting antiferromagnetic and paramagnetic metal phases) is the likely culprit.

Above 200 K, at temperatures above those probed for x=0.5, there is a gradual decrease in intensity. We note there is no significant change in correlation length or the

width in the θ scans to 250 K. This is an unusual order parameter that warrants finer temperature steps and measurements in other zones. As a final precaution for interpreting this result, I reiterate that there is no polarization analysis and that we did not track the energy or azimuthal dependence, so we cannot be certain that this is a magnetic signal.

4.4.3 x=0.7 Excitations

The results of resonant inelastic X-ray scattering (RIXS) measurements at APS 27-ID-D are shown in Fig. 4.9. This is the same experiment, sample, and setup as were employed in the previous section, except that the scattering was measured in the inelastic channels.

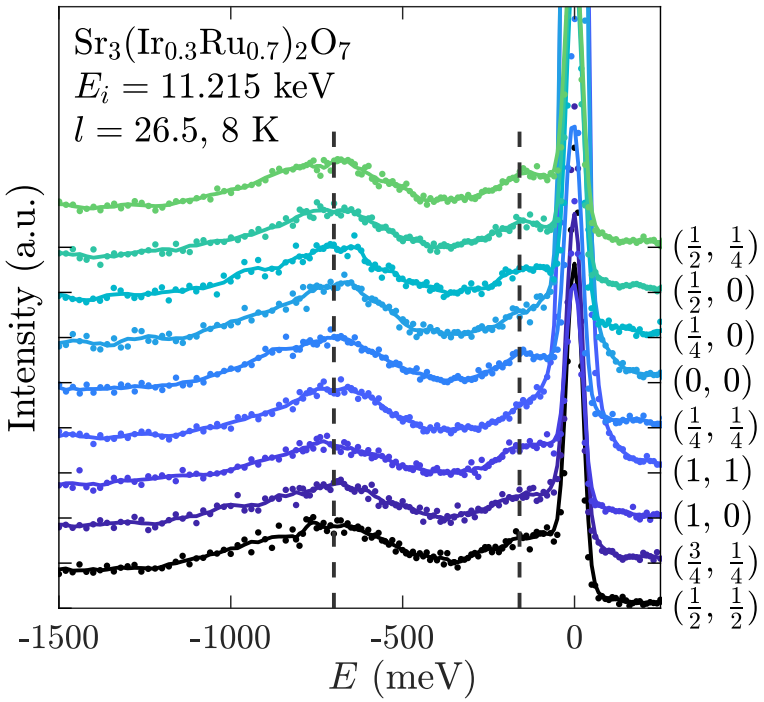

Figure 4.9: Resonant inelastic X-ray spectroscopy (RIXS) measurements of low-energy excitations in $Sr_3(Ir_{0.3}Ru_{0.7})_2O_7$. The incident energy is tuned to the Ir-L_3 edge. Spectra are indexed to the tetragonal $I4/mmm$ space group.

Spectra were measured at several (h, k) wavevectors in the $l = 26.5$ plane. Detected energy resolution was ≈35 meV (the width of the elastic peak from a piece of Scotch magic tape). We observed relatively strong scattering near energy transfer E≈0. This 'elastic' feature convolves many different signals, including phonons and possibly magnons. At the wavevectors (0, 0) and (1, 1) the elastic signal is strong, likely indicating crystal truncation rods from the integer-l allowed structural Bragg peaks.

At higher energies, several broad features are present, indicated by dashed lines in Fig. 4.9. These features are peaked near 200 and 700 meV and show very little dispersion. Because changes were so small across the quasi-2-dimensional Brillouin zone, coarse momentum steps were chosen despite the fine angular resolution of the sample and apparatus ($\Delta\theta \approx 0.07^\circ$ for the structural Bragg peaks).

The ≈200 meV excitations appear to follow a damped oscillator form. Following the analysis in Ref. [10], we modeled the scattering $\chi''(\omega)$ by the form:

$$\chi''(\omega) = \chi_0'' \frac{\gamma\omega}{(\omega^2 - \omega_0^2)^2 + \gamma^2\omega^2} \tag{4.1}$$

where $\chi'', \omega_0, \gamma/2$ are the momentum integrated intensities, characteristic energy scales, and damping rates (widths) of the magnetic excitations, respectively. We use the symbols $-E, \omega$ interchangeably to refer to the energy transfer.

We fitted the elastic signals with a Voigt function, and the lowest-resolvable-energy features with the damped form above, modified so that it was zero at and above the elastic line. Since the higher-energy feature is asymmetric we fitted it with two Gaussians maximized near 700 and 900 meV. All fit parameters (intensities, widths, peak energies) were not fixed.

The fit results for the x=0.70 spectra indicate a weakly dispersive band of excitations peaked near 180 meV, with comparable damping rates. These fits are very similar to

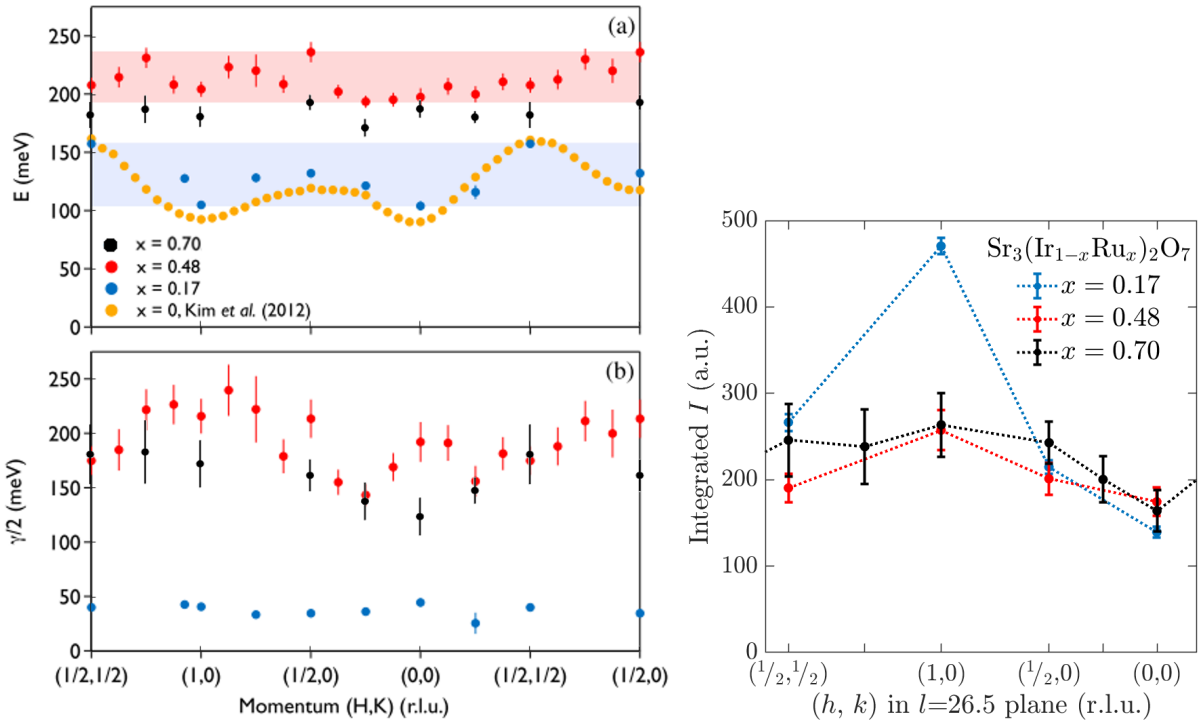

Figure 4.10: Fits of the lowest-resolvable-energy excitation of $Sr_3(Ir_{1-x}Ru_x)_2O_7$ from the RIXS measurements. Results for $Sr_3(Ir_{0.3}Ru_{0.7})_2O_7$ are plotted in black over the results from Refs. 10, 136. (a) shows the fitted peak energy and (b) shows the damping rate (width) for a peak of the form given by Equation 4.1. (c) shows the intensity. Spectra are indexed to the tetragonal $I4/mmm$ space group and were all measured in the $l = 26.5$ plane.

those for the x=0.48 sample measured in Ref. [10]. For both samples, the intensity is largely isotropic, but it is maximized at the (1, 0) zone center and minimized at (0, 0).

This band might be magnons damped by charge excitations, as was asserted for Sr_3IrRuO_7. However, we suggest a subtly different assignment for these metallic samples: damped spin-orbit exciton modes. It does not seem plausible that a magnon energy scale would change so little after such a drastic change in the carrier doping, and that there would be so little dispersion for a statically ordered system. Highly local excitations with orbital character seem to better address these discrepancies; see Fig. 4.3 for more details. These fluctuations merit further investigation with complementary probes.

4.5 Conclusions

In summary, we have shown evidence of long-range magnetism in $Sr_3(Ir_{1-x}Ru_x)_2O_7$ for unintuitively large Ru substitution, exceeding 70%. Our theory collaborators hypothesized that this finding is directly attributable to the spin-orbit coupling, which decreases the energy cost for charge carriers in the antiferromagnetic background; see Section 1.2 [10]. Our other main result was that similar ≈200 meV fluctuations, with a slightly lower energy scale, were found for $Sr_3(Ir_{0.3}Ru_{0.7})_2O_7$ compared to Sr_3IrRuO_7.

Our RIXS study is one of the very first to track an exciton dispersion for a d^{4-5} metal. Other examples of spin-orbit excitons in metals are the pyrochlore iridates and osmates e.g. Refs. 133, 137. These reports indicated highly localized excitons too. The dispersion of another more similar metal would provide a helpful comparison. While it was not directly resolved, a 36 meV energy scale was inferred for Ca_2RuO_4 [135].[4]

The excitations in $Sr_3(Ir_{0.3}Ru_{0.7})_2O_7$ are strongly damped, and coupled charge excitations seem likely to play a large role in this damping. This is a complicated scenario to consider, and we are hopeful our experimental work will motivate theories that piece together the thermodynamics at play. Similar excitations might be present in other correlated metal systems such as the cuprate superconductors.

Several experimentally-answerable questions remain regarding these excitations. Does the exciton energy scale decrease farther with more Ru content x? Follow-up RIXS measurements at an even higher Ru concentration x≈0.9 using a higher-resolution setup could help distinguish whether these excitations decrease as expected from the ARPES in Fig. 4.3. A related question is, could we resolve magnons if samples with x≥0.5 were able to be studied with inelastic neutron scattering? This would be a difficult measurement, and the continuum of states expected for a magnetic metal (the Stoner continuum) might

[4]Recent advances in spectrometers have made the spin-orbit exciton energy scale directly resolvable in ruthenates at the Ru L-edge [138, 139].

impede experimental efforts, but there is much that could be learned. As for the static magnetism, neutron diffraction or even Ru L-edge REXS studies could be well-suited to explore the unusual incident energy dependence observed in the Ir L-edge REXS.

Our incomplete picture of the physics in $Sr_3(Ir_{1-x}Ru_x)_2O_7$ would be rounded out by higher-quality samples. Flux-synthesized samples are somewhat inhomogeneous, which hinders magnetotransport and scattering studies. More crucially, it is hard to prepare samples with fine and controllable Ir/Ru content.

Chapter 5

Spin-orbit Excitons in $Sr_3Ir_2O_7F_2$

[1] The J_{eff} model describes how spin-orbit coupling can preserve an unusual ground state even in the presence of small distortions. This chapter represents an opposite limit. $Sr_3Ir_2O_7F_2$ has such large distortions that it cannot achieve the predicted J_{eff}=0 ground state for its $5d^4$ configuration. Interestingly, it still has low-energy excitations owing to its strong spin-orbit coupling.

We report on the energy and momentum dependence of low-energy excitations in the Ir^{5+} band insulator $Sr_3Ir_2O_7F_2$, as revealed by resonant inelastic X-ray scattering (RIXS). This material is composed of corner-sharing planes of IrO_6 arranged in bilayers as in the precursor material $Sr_3Ir_2O_7$. Quantum chemistry simulations suggest that the strong departure from octahedral symmetry results in a spin-orbit singlet ground state, where S and J are not good quantum numbers. In what follows I sometimes slip and describe this by a closely related S=1 (L=1, J=0) ground state. Weakly dispersive modes $\leq$ 0.6 eV are well-described by spin-orbit excitons. The couplings between excitons are too weak to yield gapless excitations yet they are relevant to the thermodynamics of this d^4

[1] Part of this chapter is based on one of our publications, Ref. 140: Christi Peterson, Michael W. Swift, Zach Porter, Raphaële J. Clément, Guang Wu, G. H. Ahn, S. J. Moon, B. C. Chakoumakos, Jacob P.C. Ruff, Huibo Cao, Chris Van de Walle, and Stephen D. Wilson. $Sr_3Ir_2O_7F_2$: Topochemical conversion of a relativistic Mott state into a spin-orbit driven band insulator, Physical Review B 98, 155128 (2018). Copyright 2018 American Physical Society.

Much of the rest of the chapter is from an unpublished manuscript. My collaborators are: Paul M. Sarte, Thorben Petersen, Mary H. Upton, Liviu Hozoi, and Stephen D. Wilson.

system.

5.1 Introduction

Recently, a great experimental effort has begun to explore the magnetism of previously unconsidered $4d^4$ and $5d^4$ systems with octahedral ligand coordination. Such systems host J=0 singlet ground states, which naïvely yield band insulators without static magnetic order. But lately researchers have been searching for a material example, motivated by a transformative theoretical framework by Khaliullin [141], which proposed that with strong spin-orbit coupling (SOC) the Van Vleck-type bosonic J=0 to J=1 excitations can condense into so-called 'excitonic' magnetism. One exciting aspect of this proposal is the proximity to a quantum critical point with high energy scales [142]. And, for some material realizations, the condensed phase itself could support novel spin-liquid ground states. Even though the materials studied so far (including the one in this study) may lack static magnetism arising from spin-orbit excitons, the thermodynamic signatures and phase phenomena of this fascinating class of materials is rich and little explored.

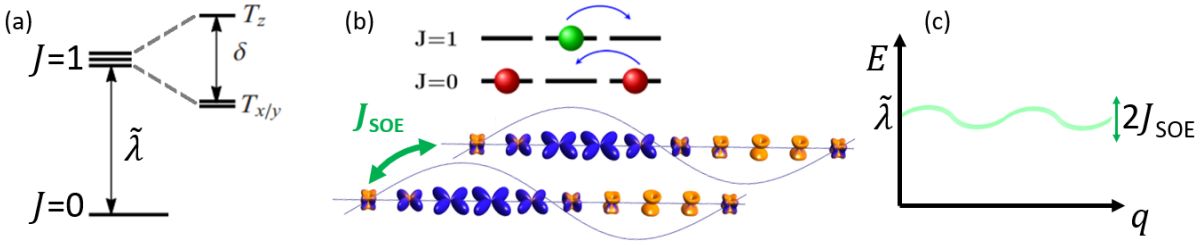

Figure 5.1: Overview of Van Vleck excitations in J=0 ground states. (a) shows how the J=1 triplet state is split from the J=0 singlet by spin-orbit coupling $\tilde{\lambda}$; it is further split by tetragonal/trigonal compression $+\delta$ to the triplon states $T_{x,y}$ and T_z. (b) is two cartoons of J=1 excitations, schematically and then in real space. Couplings between excitons lead to dispersion in (c); if couplings are strong enough then the band could become gapless.

Even under perfect octahedral crystal fields, for $4d^4$ and $5d^4$ materials there are

uncertainties regarding the electronic configuration, which draws into question the applicability of theoretical predictions for spin-orbit excitons and the broader magnetic phase behavior. Generally, the ground states for these systems are considered in two limits:

1. when SOC is much weaker than correlations, the triply degenerate t_{2g} manifold hosts a S=1 (L=1, J=0) state;

2. when SOC is much stronger than correlations, the J_{eff}=3/2 doublet is filled yielding a J_{eff}=0 state.

However, the comparable energy scales of SOC (parameterized as $\tilde{\lambda}\equiv\alpha'\lambda$ with $\alpha'=\frac{1}{2}$ for d^4 and α'=1 for d^5)[2] and correlations (considered via the Hund's coupling J_H or the unscreened on-site Coulomb interaction U) for $4d^4$ and $5d^4$ compounds are difficult to reconcile with either of these limits. As additional sources of complication, ligand hybridization has been predicted to modify filling;[134] itinerancy can mix ground state wavefunctions; [24] and distortions from the octahedral crystal field are known to split states. The effects of these deviations from the ideal case are especially noticeable in excited states. Thus, without relying on sophisticated quantum chemistry calculations, it is difficult to compare experimentally observed electronic excitations to theoretical predictions of d^4 magnetism.

Here we study a compound derived from the well-studied Ir^{4+} material $Sr_3Ir_2O_7$. Via a topochemical transformation on single-crystalline samples, fluorine layers are intercalated between the bilayers of corner-sharing IrO_6 octahedra [140]. The fluorine ions act to hole-dope each Ir ion to the 5+ valence. The magnetic ground state is near-fully quenched, amounting to about 1% of Ir sites with spin-1/2 moments. Crucially, this hole-doping is accomplished without diluting the lattice; each Ir ion is still nearest-neighbor

[2]In other words the effective spin-orbit coupling of d^4 ions is reduced by a factor of 2 from d^5 ions; see Ref. 143.

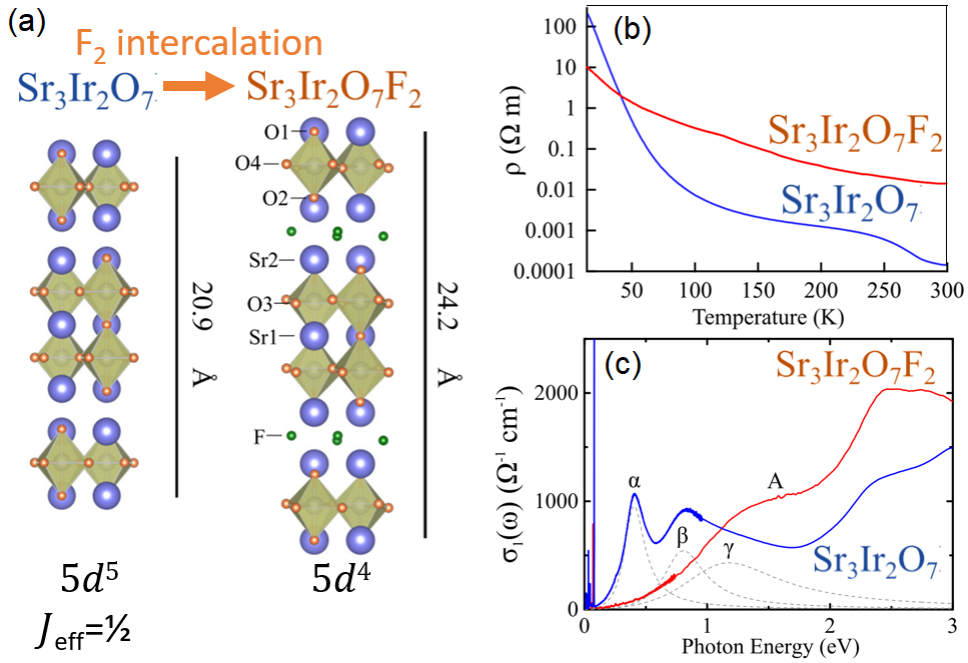

Figure 5.2: Overview of $Sr_3Ir_2O_7F_2$. In (a) the fluorine intercalation is depicted pictorially. In (b) the dc resistivity measurements show a band insulator, rather than a Mott state. In (c) the optical conductivity is consistent with this assignment. From [140].

coupled to 1 interlayer and 4 intralayer Ir ions (via superexchange across oxygen ions). And, owing to the constituent elements, we expect negligible Ir antisite defects. The resultant compound $Sr_3Ir_2O_7F_2$ has a strong deviation from an octahedral crystal field, in contrast to $Sr_3Ir_2O_7$ [140]. Its spin-orbit singlet ground state, with its first excited states resembling the S_z=±1 states, makes the present system relevant to other tetragonally distorted compounds such as Ca_2RuO_4 with its S=1 (L=1, J=0) state [50].

We use resonant inelastic X-ray spectroscopy (RIXS) to measure low-energy excitations in $Sr_3Ir_2O_7F_2$. Through this study, we measure weakly coupled spin-orbit excitons and $d-d$ excitations to establish the energy scales of SOC, correlations, and crystal field splitting in this novel material. This work may allow for quantitative comparisons to other d^4 materials like Ca_2RuO_4 and $(Sr,Ba)_2YIrO_6$.

5.1.1 Other efforts to hole-dope $Sr_3Ir_2O_7$ (and Sr_2IrO_4)

Some hole-doping studies of $Sr_3Ir_2O_7$ have been performed. I have personally studied Ru substitution (Chapter 4). But above 40% Ru substitution these samples have metallic ground states. Since this metallicity seems to be a consequence of Ru^{4+} ground state and percolation, this is not a great system to understand Ir^{5+} physics. Therefore, to get at the insulating behavior relevant to $Sr_3Ir_2O_7F_2$, other dopants merit consideration.

One very important system that seems to entail Ir^{5+} physics is Rh-substituted Sr_2IrO_4. I will only briefly discuss $Sr_2Ir_{1-x}Rh_xO_4$ here because it is incredibly complicated. The Rh ions seem to hole-dope Ir sites in a manner that may involve a rigid band shift [144]. By $x = 0.2$ the Rh drives this insulator into a global metal [145]. Rh substitution seems to involve a great deal of site disorder that complicates interpretation. At high Rh content, some of the physics of the Ir^{5+} valence is obscured by the mixed $Rh^{3+/4+}$ sites.

Are there ways to significantly hole-dope without diluting the iridium lattice? A-site doping (substitution for Sr) is a good approach. J.N. Nelson and co-workers studied hole doping under K substitution in $Sr_{1.93}K_{0.07}IrO_4$ [146]. There it was found that light hole-doping collapses of the Mott gap and yields a global metal, with surprisingly similar bandstructure to electron-doped Sr_2IrO_4 (with a few subtle differences). In this and many other A-site dopants, the structural stability limits the how many holes can be doped into the system.

This leaves few ways to achieve even more hole-doping. Substitution of oxygen for nitrogen-group elements does not seem feasible. Therefore, intercalation of anions was our chosen route to insulating d^4 physics.

5.1.2 Other J=0 Systems

I will briefly introduce several systems with singlet ground states. The most relevant to $Sr_3Ir_2O_7F_2$ are those with S=1. From one S=1 example, I will summarize a few putative J_{eff}=0 compounds that shape the context for our results.

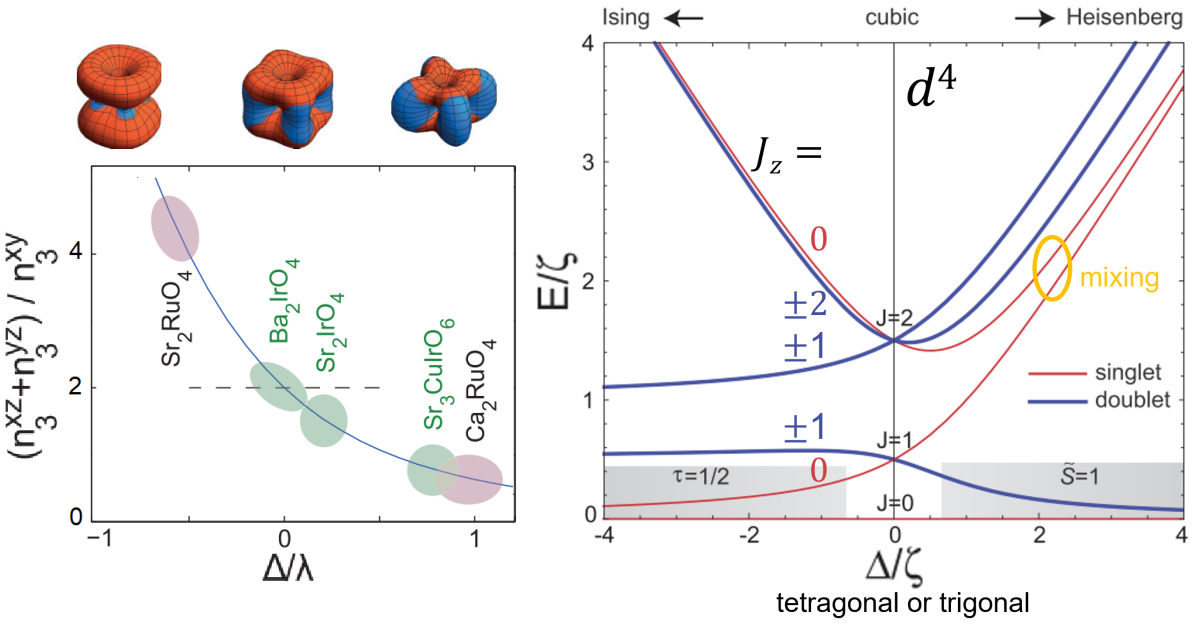

Figure 5.3: On the left, relative orbital filling from the tetragonal distortion. Iridate compounds are in green and ruthenates are in red. Deviation from J_{eff} orbitals is shown above the plot. Adapted from [147]. On the right is the specific case of d^4 levels. J and J_z quantum states are indicated. In this figure, $+\Delta$ is tetragonal compression, n is orbital filling, λ and ζ are spin-orbit coupling, and E is energy relative to the ground state. From [49]. Copyright American Physical Society.

Among all possible S=1 systems I will focus on Ca_2RuO_4 because it is well-studied and perhaps most applicable. Ca_2RuO_4 is an exotic $4d^4$ Mott antiferromagnetic insulator [148], which is especially tunable with pressure or light e.g. Refs. 148, 149. At low energies accessible by neutron scattering there is significant magnon dispersion [50]. But at higher energies the orbital excitations accessible by RIXS weakly disperse, owing to their local character [135]. As seen in Fig. 5.3, the RuO_6 octahedra are strongly

tetragonally compressed, so Ru d_{xy} orbitals are occupied more than d_{xz} and d_{yz}. This yields a situation where the doublet of J=1 states ($\langle J_z \rangle = \pm 1$) is brought down in energy towards the S=1 ground state, mixing with it. This effective $\tilde{S} = 1$ state is predicted to yield its excitonic magnetic order, exemplified by a putative Higgs (amplitude) mode [50]. This electronic state is analogous to the J_{eff}=0 state under strong exciton coupling.

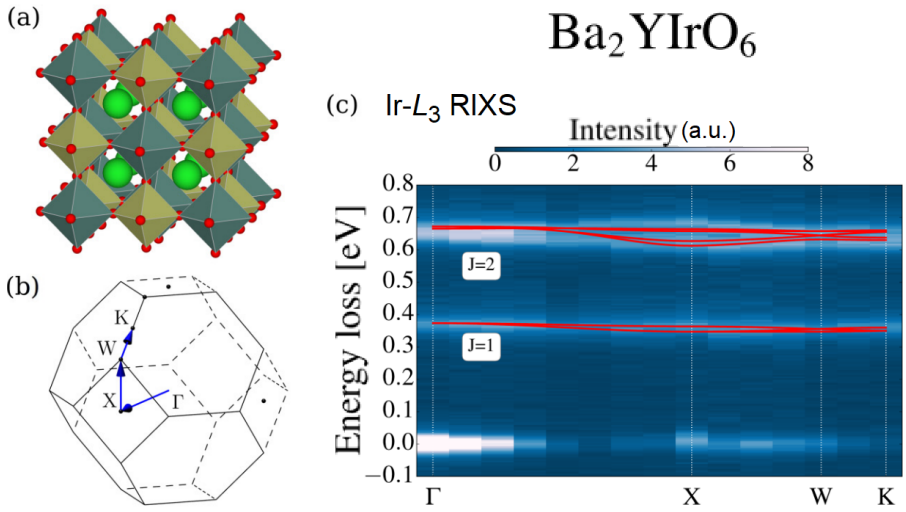

Figure 5.4: The weakly dispersive J_{eff}=0 system Ba_2YIrO_6. (a) and (b) show the cubic unit cell and Brillouin zone. (c) shows a false-color RIXS map of the spin-orbital excitations. From [150]. Copyright 2018 American Physical Society.

Several putative J_{eff}=0 compounds have been studied in the past decade. Currently there is scant evidence of excitonic magnetism in these systems. The preferred candidates have nearly-perfect octahedral crystal fields. $Y_2Os_2O_7$ [151] and K_2RuCl_6 [138] and several double perovskite iridates like $(Ba,Sr)_2YIrO_6$ [150] are some examples of this. In each of these systems the exciton bands very weakly disperse; see Fig. 5.4. For the osmate and iridate above, bulk magnetism has been attributed to glassy, impurity-driven behavior. However, the excitonic nature of the magnetism, particularly in the double-perovskite iridates, has been fiercely debated.

5.2 Synthesis: Topochemical Reaction

The topochemical reaction was hard to control and often inconsistent. The technique we employ has strong variability in resulting O and F stoichiometry, probably because of changes in reactant dryness and precise furnace conditions. Therefore, each sample needed to be individually checked, both for crystal structure and fluorine content.

For the RIXS study, I reacted a ∼1 mg sample of single crystalline $Sr_3Ir_2O_7$. I produced this with the flux technique described in Section 4.2. I placed this sample in an alumina boat and buried it under about 1 g of CuF_2, handled in a glovebox for safety and to prevent water absorption. The reaction was performed in a tube furnace, at 550 K for 3 h under flowing argon gas at 30 sccm. I checked that this sample was phase-pure by laboratory X-ray diffraction (Panalytical Empyrean and Rigaku Smartlab diffractometers).

After the RIXS measurements, the sample was ground into powder onto double-sided tape and measured with X-ray photoemission spectroscopy (XPS) using a Thermo Fisher Escalab Xi+ instrument. The `CasaXPS` software was used to fit the XPS intensities, and without using standards we found the Sr:F ratio was 3:2.1 which is nearly stoichiometric within the large expected uncertainty.

I sent collaborators powder to perform nuclear magnetic resonance (NMR) and X-ray absorption spectroscopy (XAS) measurements. Some of these measurements on well-prepared samples are described in Ref. 140. Measurements on differently-prepared samples showed evidence of incomplete intercalation and also substitution of fluorine ions for oxygen ions.

5.3 Magnetization

The bulk dc magnetization was measured with a Quantum Design MPMS3 magnetometer. The sample was affixed with GE varnish to a quartz paddle, oriented with field along the basal plane.

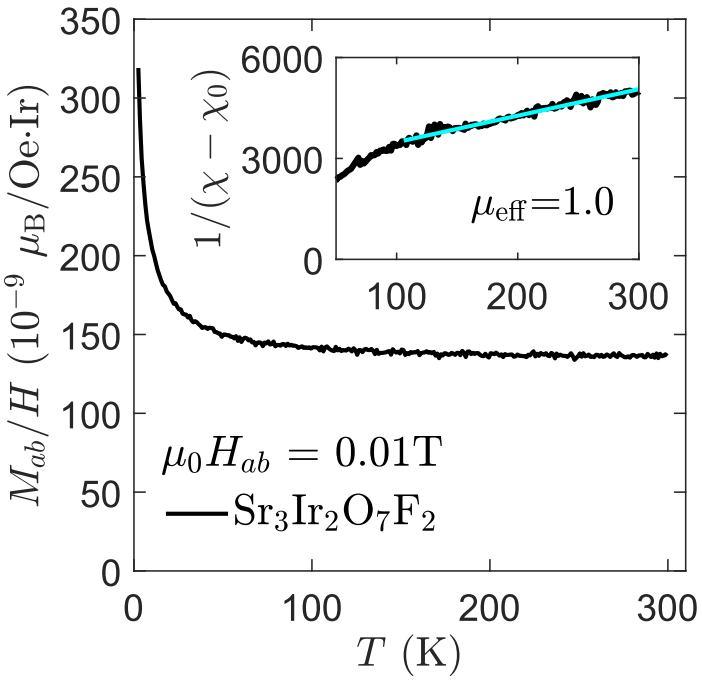

Figure 5.5: Weak bulk magnetization in $Sr_3Ir_2O_7F_2$. The low-temperature upturn is consistent with dilute impurities. The inset is the inverse susceptibility, in units of (Oe·mol formula unit / emu). The cyan line is a Curie-Weiss fit.

As seen in Fig. 5.5, the magnetization is incredibly weak. The dominant temperature-independent Van Vleck contribution to the susceptibility is about $1.1(1)\times10^{-3}$ emu/mol. From Curie-Weiss fits, several similarly prepared samples had <1 mass percent μ_{eff}=1 paramagnetic impurities. We ascribe this to dilute Ir^{4+} impurities, either from fluorine substitution for oxygen or from oxygen vacancies.

5.4 Resonant Inelastic X-ray Scattering

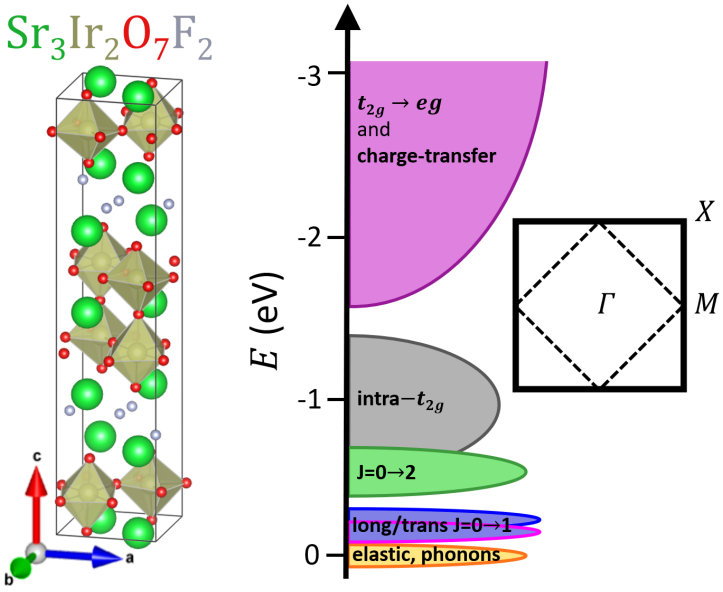

Figure 5.6: Orthorhombic *Bbcb* unit cell (left) and quasi-2D Brillouin zone (right) for $Sr_3Ir_2O_7F_2$. Ir−O bond lengths are appreciably compressed along c near the fluorine planes. Cartoon of the excitations observed in RIXS measurements (center). Details are in the text. J is not a good quantum number so transitions are approximate.

Resonant inelastic X-ray scattering (RIXS) measurements were performed at Beamline 27-ID of the Advanced Photon Source at Argonne National Laboratory. See Section 2.2.3 for more details of the experimental setup. For the exact sample measured with X-ray scattering, X-ray photoelectron spectroscopy (XPS) measurements confirm accurate stoichiometry and diffraction confirmed the correct structure. The incident photons were tuned to the Ir L_3 absorption edge (E = 11.215 keV) and final energies were selected with the Si(4,4,8) reflection of a spherical analyzer crystal array in a horizontal scattering geometry. Excitations were mapped primarily in the quasi-2D l=30.5 Brillouin zone (BZ). This l value was chosen because it is far from Bragg peaks and near 2θ=90° where Thomson scattering (i.e. elastic charge scattering) is minimized.

Momentum space positions are indexed using an orthorhombic *Bbcb* unit cell with

lattice parameters a=5.45 Å, b=5.51 Å, and c=24.21 Å; see Figure 5.6. This simplification from the proper $C2/c$ cell was chosen for comparison to other quasi-2D samples. Due to twin structural domains, we do not distinguish between a and b axes. RIXS measurements were sample-resolution-limited in momentum, approximately 0.2 $Å^{-1}$, due to the high mosaicity of samples after the topochemical conversion. Detected energy resolution was ≈35 meV. Unless otherwise stated, measurements were performed at 8(2) K.

RIXS spectra are shown at individual $\mathbf{Q}$ positions in Fig. 5.7, and as a map in the quasi-2D Brillouin zone in Fig. 5.4. All measured excitations disperse weakly. We label the features (Table 5.1 and Fig. 5.7) as elastic at energy loss E=0, A at E≈170 meV, B at E≈220 meV, and C at E≈500-900 meV. A, B, and C are spin-orbit excitons. The A and B features match qualitatively with the *ab initio* model; see Table 5.1. We note that no sharp features were observed in the optical conductivity from 0 to 1 eV [140], consistent with feature C being composed of optically-forbidden spin-orbit excitons.

Near 1.3 eV, there is a broad excitation in the optical conductivity, so the scattering may begin to include transitions across the charge gap. We call these intra-t_{2g} excitations. Some of the ambiguity in interpreting this feature stems from difficulty in modeling the electron-hole continuum; see for example Ref. 152.

Higher energy features are visible in the spectra with a wider energy window shown in Figure 5.4. In the spectra there is a broad peak at 3.2(1) eV, and at higher energies the scattered intensity is nearly flat. This is consistent with expectations for excitations to the e_g manifold, and establishes an approximate energy for the octahedral crystal field splitting. The high energy features also include contributions from O $2p$−Ir t_{2g} charge-transfer scattering channels [153, 154].

Next we comment on the widths of the low-energy RIXS features. For the A and B modes, the full width at half maximum (FWHM) values are very near 60 meV. This is near the 35 meV instrumental resolution and is much sharper than the other features,

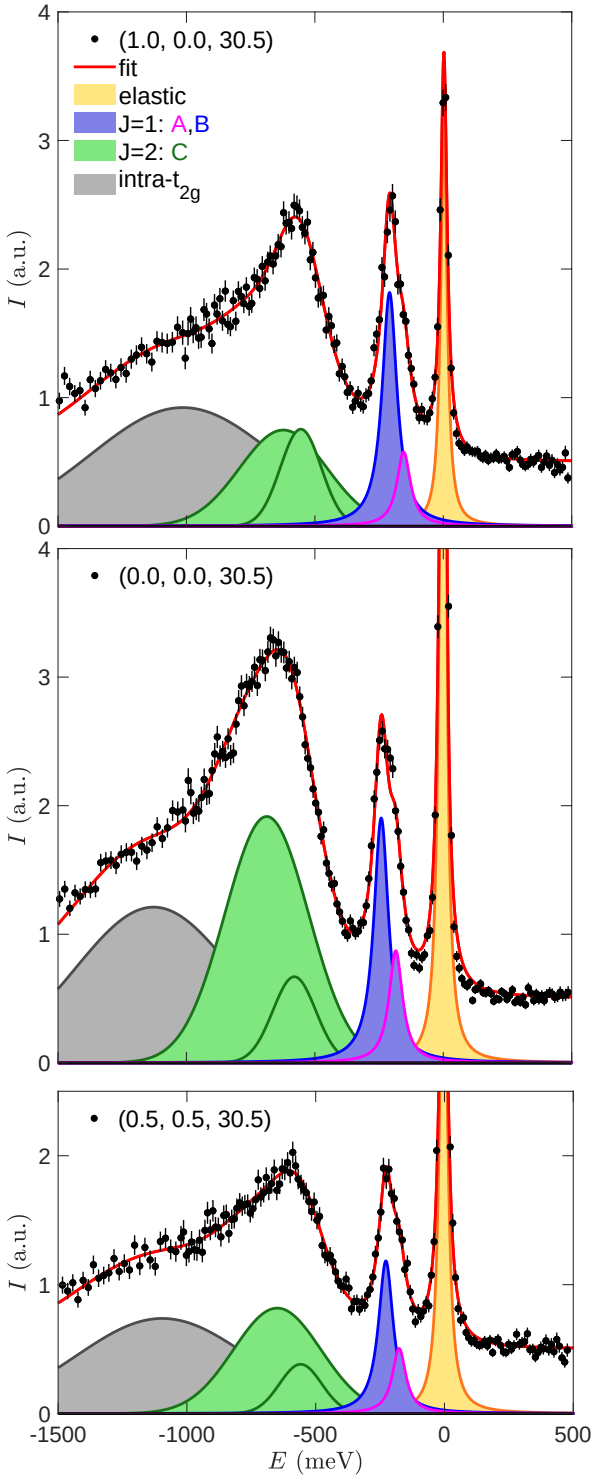

Figure 5.7: Representative RIXS spectra (black dots) for several **Q**. Fits to the spectra (solid red lines) utilize the spectral components discussed in the text. J values are approximate.

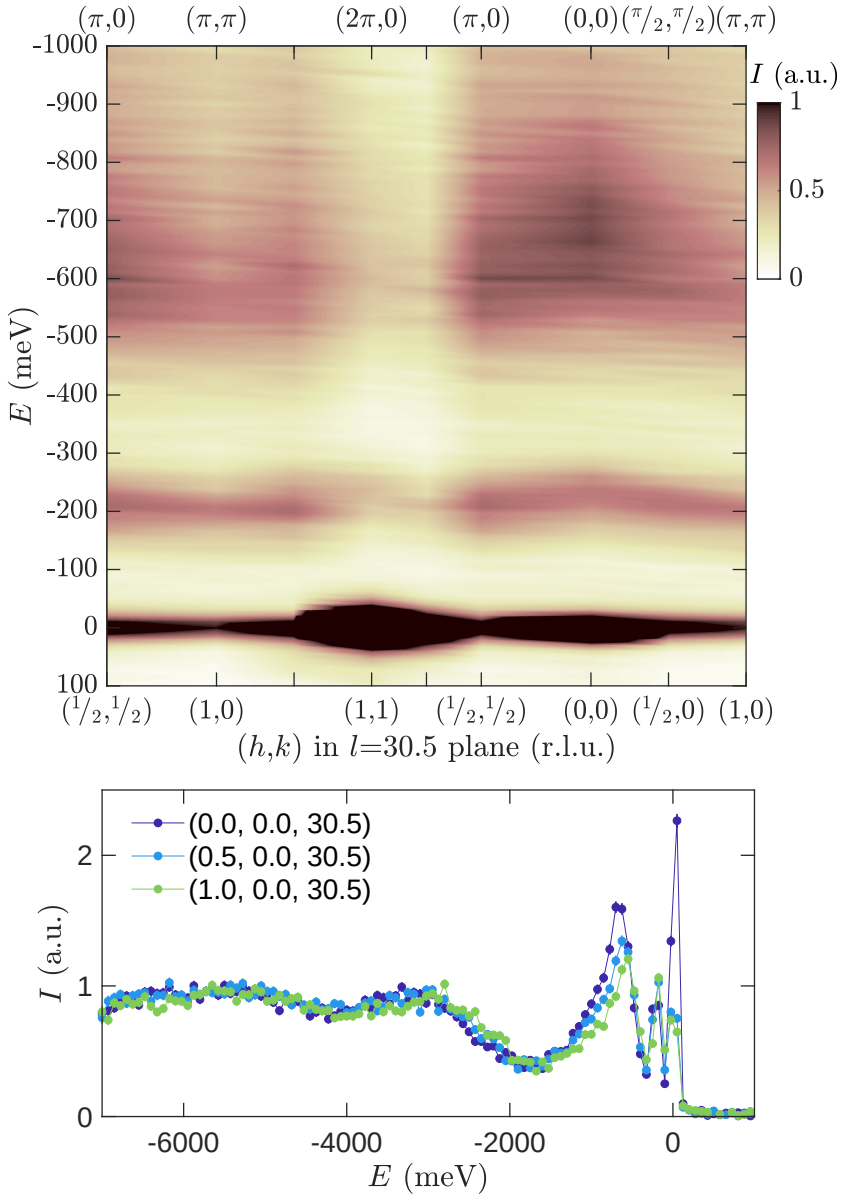

Figure 5.8: *Top Panel*: RIXS false-color map of raw intensities in the quasi-2-dimensional Brillouin zone. Ticks indicate the **Q** positions where spectra were measured; the map was generated by interpolation. *Bottom Panel*: Representative spectra for several **Q** over a wide energy range to show higher-energy excitations. A constant background was subtracted from all scans in this figure.

so it seems to preclude a collection of many distinct modes. The bandwidth for the A and B modes is about 15-35 meV, which points to weakly coupled excitations (i.e. high effective mass). The C feature has FWHM values near 100 meV, and a bandwidth of about 80 meV, consistent with a collection of many dispersive modes (confirmed from the many nearby modes in the quantum chemistry models).

To analyze these RIXS features, the elastic line was fitted to a Voigt function, A and B were fitted to Lorenztians, and all other features were fitted to Gaussians, on a constant background. These peak shapes were chosen to empirically match the data. To attain well-behaved fits we found it appropriate to fix the A and B peaks' widths throughout this paper. The reduced chisquared χ_r^2 (goodness-of-fit) values are nearly equal for fits where these parameters were fixed or free. For the special case of tracking the l dependence of the A and B intensities at fixed h and k, the modes seem nondispersive so we fixed the A and B peak energies as well, corroborated by the goodness-of-fit.

Using the fits as described above, we now consider the RIXS integrated intensities. Most features' intensities are nearly constant as functions of $\mathbf{Q}$, with the exception of the A and B modes, which are nearly constant across each quasi-2D BZ yet exhibit a strong sinusoidal l dependence; see Fig. 5.9. The A mode intensity appears well-described by the functional form $\sin^2(\pi l d/c)$, with d the bilayer Ir-Ir spacing and c the lattice constant. For the B mode the intensity variation is $\pi/2$ phase-shifted (to $\cos^2$) with an added constant background. We attribute this sinusoidal behavior of A and B to a double-slit-like interference for two different excited states that are delocalized across the bilayer. This interference effect results from the emission process in RIXS [57], so it should be expected for RIXS spectra of all ions arranged like dimers, and it will not occur in the inelastic neutron scattering. A more detailed description of the physical origin and alternative explanations are provided below in Section 5.4.1.

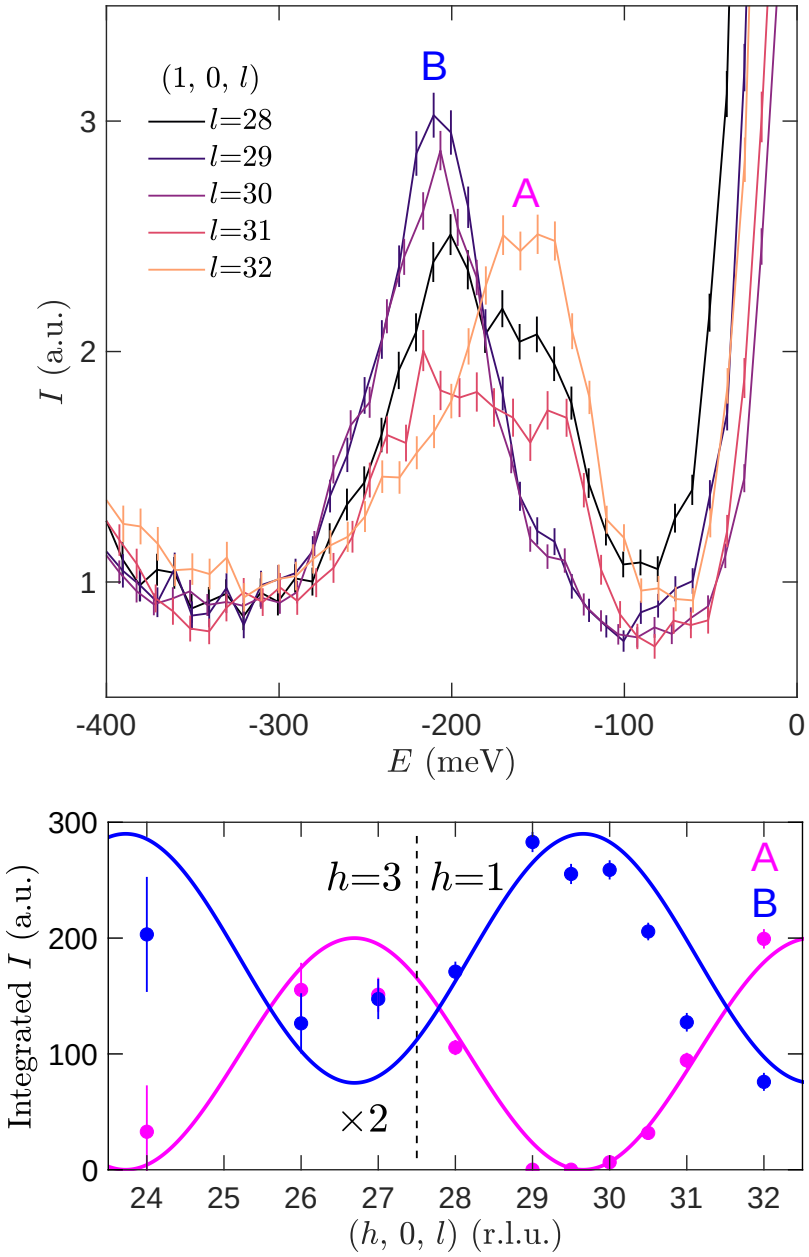

Figure 5.9: Interference pattern in the RIXS spectra along l. *Left Panel*: Raw RIXS spectra at (1, 0, l) show the change in spectral weight of the A and B features (magenta and blue, respectively). *Right Panel*: Integrated intensities of the Lorentzian fits to these features reveal sinusoidal dependence in l. The functional form of the magenta line is $sin^2(\pi ld/c)$, as is described in the text. Note that for l<28 the fitted scans were measured at (3, 0, l) which was closer to normal incidence, where self-absorption effects were larger due primarily to the scattering geometry. The h=3 scans were scaled by a factor of 2 to make the intensity values comparable.

5.4.1 Sinusoidal intensity dependence

Now we return to our consideration of the sinusoidal intensity dependence of the A and B modes along the l direction. When we consider possible explanations, we must satisfy the following observations:

- First, this effect must come from the Ir interactions along c such as across the bilayers, as it cannot be reconciled with isolated ab planes of Ir ions.

- Second, we note that these modes are large in magnitude and that the A intensity goes to zero within uncertainty at certain l values. Therefore, any explanation for the l dependence of the A and B features must be a significant effect that invokes the bulk d^4 state rather than defects.

- Third, given how dilute the RIXS-excited ions are in the measured sample,[3] we do not consider pairs of excitations on nearest-neighbor ions since these comprise weak scattering channels.

Based on these considerations for the sinusoidal l intensity dependence, we accredit the A and B features to spin-orbit excitons which form molecular orbitals that are delocalized across the bilayer. A similar conclusion was described with little clarification in a recent paper describing excitons in $Sr_3Ir_2O_7$ [59]. I choose to spell this out here because it is a point of confusion for many in the field.

In X-ray emission measurements of ions arranged like dimers, such as RIXS performed on bilayers, the double-slit interference condition can be satisfied: the identity of which ion in the pair yielded the emitted photon, the 'slit' in this double-slit experiment, cannot be determined in principle. An essential ingredient for the interference is delocalization

[3]Here, flux $\sim 10^{12}$/s and the excited volume contains $\sim 10^{15}$ Ir ions. These values imply that pairs of excitations caused by the incident photons are infrequent for realistic final excited state lifetimes $\ll$ s.

of the photoexcited electron in the state intermediate to the absorption and the emission processes, which removes the 'which-path' information for the emitted photon. For more ideal $5d^4$ J=0 materials, triplon (J=1) excitations are considered to be very delocalized. Delocalized excitons certainly propagate in-plane, yet the geometry of the Ir-O planes does not allow for double-slit interference.

The most natural microscopic picture for the observed A and B features is symmetric and antisymmetric molecular orbital excited states that form across the bilayer. For visualization purposes these orbitals can improperly be considered as akin to bonding and anti-bonding states. The most consistent scenario is one of the two crystal field split S_z=±1 states hybridizing with the S_z=0 ground state; however we note that this is not explicitly captured in the *ab initio* simulations, which reveal a singlet where S and J are not good quantum numbers.

To explain the phase shift between these two features that yields the $\sin^2$ and $\cos^2$ dependence along l, we derive the RIXS scattering amplitudes. The derivation that follows is a slightly modified reproduction of the supplemental materials to Ref. 22. In the dipole and fast-collision approximations [46, 49], the Ir L_3 RIXS scattering amplitude $\mathcal{A}_f(\mathbf{Q},\omega)$ of one final state $|f\rangle$ is:

$$\mathcal{A}_f(\mathbf{Q},\omega) \propto \langle f| \sum_{\boldsymbol{R}} \mathrm{e}^{\mathrm{i}\mathbf{Q}\cdot\mathbf{R}} [\hat{\mathcal{D}}^\dagger(\boldsymbol{\epsilon}')\hat{\mathcal{D}}(\boldsymbol{\epsilon})]_R |i\rangle \tag{5.1}$$

where $|i\rangle$ denotes the initial (ground) state, $\boldsymbol{\epsilon}(\boldsymbol{\epsilon}')$ the polarization of incident(outgoing) photons, $\hat{\mathcal{D}}$ the local dipole transition operator, and R runs over all Ir sites that contribute to the final state $|f\rangle$. This is essentially Equation 2.22 where we explicitly include the crystal structure factor.

If we consider a final state that accounts for two Ir sites across the bilayer at $\mathbf{r}_{1,2} = (0,0,\pm d/2)$ then, since they are equivalent sites, the matrix elements may only differ in

sign. If we measure the dependence along l at $|\mathbf{Q}| = 2\pi l/c$ we get:

$$\mathcal{A}_f(\mathbf{Q},\omega) \propto e^{i\mathbf{Q}\cdot\mathbf{r}_1} \pm e^{i\mathbf{Q}\cdot\mathbf{r}_2} \propto \begin{cases} \sin(\pi l d/c) \\ \cos(\pi l d/c) \end{cases} \tag{5.2}$$

The intensity (scattering cross section) is $I(q,\omega) = \sum_f |\mathcal{A}_f(\mathbf{Q},\omega)|^2 \delta(\hbar\omega - E_f)$ where $\hbar\omega$ is the outgoing photon energy and E_f is the excited state energy. Therefore, symmetric and antisymmetric levels yield $\sin^2$ and $\cos^2$ dependences along l, as observed for the A and B features respectively.

An interference phenomenon was measured in detail for structural dimer systems including $Ba_3CeIr_2O_9$, with Ir_2O_9 bi-octahedra that have small Ir-Ir separations d=2.5Å along the c axis [22, 23]. The dimerized Ir sites' molecular orbitals are delocalized, giving rise to interference among several distinct excited states in RIXS measurements. As a result, the intensity of transitions to the excited states for $Ba_3CeIr_2O_9$ modulates sinusoidally along l, where symmetric intermediate states vary as $\sin^2(\pi l d/c)$ and antisymmetric intermediate states vary as $\cos^2(\pi l d/c)$ [22]. In contrast to $Sr_3Ir_2O_7F_2$, this dimer example has much closer Ir ions with a different valence and wildly different electronic configurations. Crucially the dimer system has a much larger orbital overlap parameterized by the hopping $t\approx$1 eV along c. However, we propose that the excitons in the present study are delocalized, with the Ir-O-Ir bonding providing enough orbital overlap to result in modest hopping for the exciton.

Instead of the proposed electronic configuration, one could envision magnetic or orbital dimerization as a means of interpreting the sinusoidal intensity dependence. For instance, if there are many O vacancies then there could be interlayer-dimerized Ir^{4+} defects, since these may not have a strong signature in the bulk susceptibility. However, this magnetic dimerization seems unrealistic based on how dilute unpaired Ir^{4+} ions are

<1 mol percent and also the structural refinements. On the other hand, we cannot rule out Ir^{5+} orbital ordering and dimerization based on the existing evidence. In the $3d^2$ compound $Sr_3Cr_2O_7$, the proposed ground state is an interlayer orbital singlet state which yields a qualitatively similar crystal field environment [155]. Orbital ordering or dimerization could plausibly explain why the bilayer Ir spacing d does not decrease significantly with holes from $Sr_3Ir_2O_7$ to $Sr_3Ir_2O_7F_2$, even though the Ir free ionic radius decreases 9% from the 4+ to the 5+ valence.

Yet another explanation for the sinusoidal intensity variation is acoustic and optical transverse paramagnon modes, which could possibly exist along with a longitudinal mode. Acoustic(optical) modes are known to have a $\sin^2(\cos^2)$ dependence on the wavevector along the bilayer direction l [156]. In this explanation, the oberved splitting 50 meV translates to intra-bilayer coupling $J_c \approx 25$ meV.[157] This sizeable interlayer coupling (much greater than $J_{1,2}$) would imply dimer excitations that are weakly coupled in-plane. However, the primary inconsistency with this interpretation lies in the room-temperature coupling J_c which is at odds with the established paramagnetic ground state for 2 K $< T <$ 400 K. Also, it is difficult to imagine such strong anisotropy for the paramagnons, since in-plane and out-of-plane Ir-Ir distances are comparable.

5.5 Modeling

To determine the ground state and excited states measured via RIXS, collaborators performed *ab initio* quantum chemistry calculations on an isolated $(IrO_6)^{7-}$ monomer as well as a cluster $(Ir_2O_{11})^{12-}$. This effort was led by Thorben Petersen, Satoshi Nishimoto, Ulrich K. Rößler, and Liviu Hozoi. The input structure was solved from powder X-ray diffraction refinements [140]. First, the Ir t_{2g} orbitals were considered for the initial complete-activespace self-consistent-field (CASSCF) optimization. Then these levels and

t_{2g}^4 terms	MRCI+SOC		RIXS	
${}^3T_{1g}$	0	($\approx S_z$=0)	0	elastic
	370, 440	($\approx S_z$=$\pm$1)	170, 210	A, B
	580	($\approx J$=1)	$\approx$550	C
${}^1T_{2g}$, ${}^1E_g$	790, 820, 850		$\approx$750	C
	960			intra-t_{2g}
	1700, 1730, 1780			intra-t_{2g}

Table 5.1: Low-energy Ir^{5+} $5d^4$ multiplet structure for $Sr_3Ir_2O_7F_2$ from *ab initio* calculations of a monomer $(IrO_6)^{7-}$ site and from RIXS experiments, approximated from Fig. 5.7. Values are in meV.

the O $2s$, $2p$ electrons were correlated in multireference configuration interaction (MRCI) computations, which additionally take spin-orbit coupling (SOC) into account. The details of these computations are beyond the scope of this dissertation.

We first discuss the results of the quantum chemistry simulations from the model of the isolated $(IrO_6)^{7-}$ monomer (see Table 5.1). Here the anisotropy and strong spin-orbit coupling are dominant. The singlet ground state and first excited states are within the spin-orbit-split ${}^3T_{1g}$ manifold, so they are linear combinations of the d_{xy}, d_{xz}, and d_{yz} orbitals. The *ab initio* ground state has dominant in-plane orbital occupation. The first excited states are two spin-orbit-split levels akin to S_z=$\pm$1 near 300-400 meV. Another distinct ${}^3T_{1g}$ level is near 600 meV. At higher energies there are more intra-t_{2g} transitions to strongly spin-orbit-mixed ${}^1T_{2g}$, ${}^1E_g$ configurations in the ranges 0.8-1.0 and 1.6-2.0 eV. These states' levels are likely an overestimation from neglecting partial occupation of the e_g manifold.

The quantum chemistry model of the cluster $(Ir_2O_{11})^{12-}$ reveals that each of the lowest-energy modes is split by about 10 meV compared to the isolated $(IrO_6)^{7-}$ monomer. This supports our assertion that the dispersion is due to exchange coupling.

To supplement the quantum chemistry calculations, Paul Sarte modeled our experimental dispersion relations with a spin-orbit exciton model that relies on a single-ion

Hamiltonian $\hat{\mathcal{H}}_{\text{S.I.}}$. This model for $Sr_3Ir_2O_7F_2$ employs the same formalism that was established [61] for the d^4 multiorbital Mott insulator Ca_2RuO_4. This Hamiltonian is parameterized by: $\alpha'\lambda$, H_{MF}, and δ, corresponding to the individual contributions from spin-orbit coupling, an internal mean molecular field, and a uniaxial (either tetragonal or trigonal) distortion of the local octahedral coordination environment, respectively. The resulting eigenstates of $\hat{\mathcal{H}}_{\text{S.I.}}$ are then coupled by the Fourier transform of the exchange interaction $J(\mathbf{Q})$, where both an isotropic nearest neighbor J_1 and next nearest neighbor exchange J_2 are considered. Before getting to the results, we note that the model does not capture the sinusoidal variation in intensity along l because it is restricted to the (a, b) basal plane, so it only describes the quasi-2D BZ.

The model assumes an idealized S=1 (L=1, J=0) regime. By employing the refined parameters (Table 5.2), the model produced two distinct modes with calculated dispersion relations in excellent agreement with the experimental data. As illustrated in Fig. 5.10, the A mode corresponds to transverse fluctuations ($\alpha\beta = +-$ and $-+$) within the basal plane of the pseudo-tetragonal unit cell, whereas the B mode at higher energy transfers corresponds to longitudinal zz fluctuations along the Ir^{5+} moment's axis. As summarized in Table 5.2, the refined values for each of the five parameters exhibit close agreement (within 20%) with their initial values.

The refined value of 187(5) meV for the spin orbit coupling $\alpha'\lambda$ is comparable to values reported for other d^4 iridates [158]. The presence of one, rather than two, transverse modes can be understood by the negligible molecular field. According to the model, H_{MF} has a refined value of 0.2(2) meV, and this implies no splitting between the two plausible $\alpha\beta$= $+-$ and $-+$ transverse modes. The lack of a molecular field is also consistent with the absence of magnetic long-range order.

In such a case where the molecular field is absent, the gap between the longitudinal and transverse modes results from a uniaxial distortion of the coordination environment

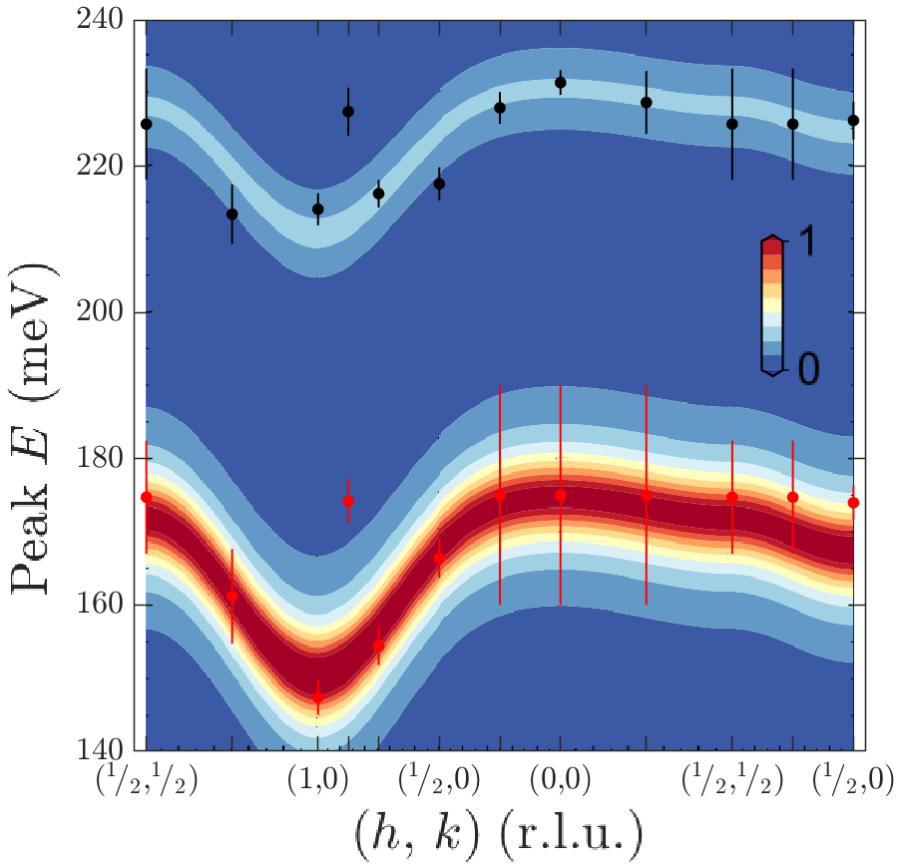

Figure 5.10: Spin-orbit exciton model (solid colors and lines) in comparison to the fitted data (points). Energy transfers of transverse (lower energy) and longitudinal (higher energy) modes overplotted on $S(\mathbf{Q})$. Note that the RIXS intensity is not equivalent to $S(\mathbf{Q})$, and intensities have not been scaled to account for the scattering geometry. Error bars only account for peak energy uncertainty, and do not incorporate fixed widths ≈60 meV.

Parameter	Initial Value	Range	Refined Value
$\alpha'\lambda$	200	[150,250]	187(5)
H_{MF}	0	[-5,5]	0.2(2)
δ	82	[40,120]	100(5)
J_1	2.1	[0,5]	2.1(1)
J_2	-1	$[-2,2]$	-0.80(5)

Table 5.2: Refined parameter values of the spin-orbit exciton model for $Sr_3Ir_2O_7F_2$. All values are reported in meV and numbers in parentheses indicate calculated uncertainties.

for a magnetic ion with unquenched orbital angular momentum. The large magnitude of δ with a refined value of 100(5) meV yields a significant gap of $\delta/2$. The positive sign fixes the longitudinal mode to higher energy transfers than the transverse mode. It can be shown [61] that the dispersion relation illustrated in Fig. 5.10 is indicative of an antiferromagnetic $J_1 > 0$ whose magnitude is greater than the ferromagnetic $J_2 < 0$.

To summarize, we interpreted the two lowest energy excitations as one transverse and one longitudinal S=1 exciton branch, split by a tetragonal distortion, with negligible molecular field. The modes disperse weakly according to weak couplings $J_{1,2}$. This interpretation was used an oversimplified starting point.

5.6 Conclusions

In conclusion, we measured resonant inelastic X-ray scattering for the $5d^4$ band insulator $Sr_3Ir_2O_7F_2$ and interpret the low-energy excitations with quantum chemistry simulations as well as a spin-orbit exciton model. We comment on the electronic configuration of the system and the relevant energy scales including effective spin-orbit coupling, tetrag-

onal distortion, exchange coupling, and correlations, in the context of related systems based on Ir, Ru, and Os sites. The strong interference effect along the bilayer direction is a consequence of X-ray emission. We echo previous predictions that interference effects can be significant in dimer, bilayer, and related systems studied via RIXS.

As a next step, if would be of great interest to tune the fluorine content, and for instance study $Sr_3Ir_2O_7F$ with $Ir^{4.5+}$. Others in my research group and I have failed to modify the intercalation reaction to control the fluorine content. As predicted by density functional theory, our solid state reaction is all-or-nothing; my reactions invariably yielded some mix of $Sr_3Ir_2O_7$ and $Sr_3Ir_2O_7F_2$. Maybe wet chemistry methods are better-suited to achieve this goal. In addition, it remains to be seen if the topochemical reactions could be made gentler; single crystals with a better mosaic that are less damaged would be better able to answer open questions about the electron transport and structure. As a parallel effort, it would be incredibly valuable to have large volumes of sample, even in polycrystalline form, for neutron diffraction and thermodynamic measurements. The current roadblock is that there is no synthetic technique for producing high-quality polycrystalline $Sr_3Ir_2O_7$, so our powder studies were performed on crushed single crystals.

Chapter 6

Tuning the Pyrochlore Iridate $(Ca_xNd_{1-x})_2Ir_2O_7$

[1] While the pyrochlore iridates neatly fit into this dissertation centered around J_{eff}=1/2 states in iridium oxides, they are quite different from materials like Sr_2IrO_4. Due to a significantly larger bandwidth, the pyrochlores are in the weak to intermediately correlated regime where semimetal states exist [11]. This leads to an itinerant picture of spins, where the Quantum Compass model in Section 1.2.2 is not directly applicable (especially for these Ir-O-Ir bonds near 130° where neither 90° nor 180° models are applicable).

We were motivated to study the pyrochlore iridates by a host of studies demonstrating topological semimetal phases [160–163] and predicting associated quantum criticality [164–168]. Unfortunately a complete discussion of the topology is beyond the scope of this dissertation, but for the experts I include some helpful figures below. The requirements for this particular Weyl semimetal phase are that time reversal symmetry must be broken (by short- or long-range magnetism) and that inversion symmetry remains; as such, the existing theories assume a cubic structure and minimal local disorder.

[1] This chapter is based on one of our publications, Ref. 159: Zach Porter, Eli Zoghlin, Samuel Britner, Samra Husremovic, Jacob P.C. Ruff, Yongseong Choi, Daniel Haskel, Geneva Laurita, and Stephen D. Wilson. Evolution of structure and magnetism across the metal-insulator transition in the pyrochlore iridate $(Ca_xNd_{1-x})_2Ir_2O_7$, Physical Review B, 100, 054409 (2019).

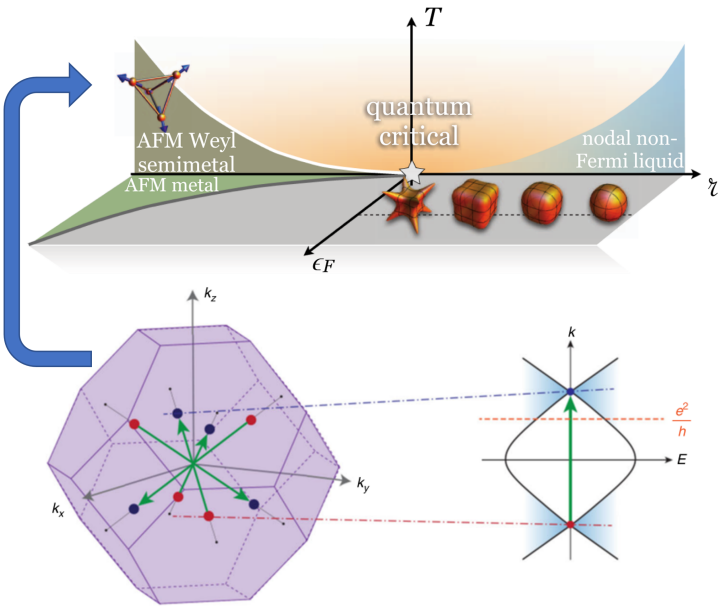

Figure 6.1: Pyrochlore iridate topology. *Top panel*: predictions of a quantum critical point from tuning the AFM Weyl semimetal phase. *Bottom panels*: the eight Weyl nodes (Fermi level crossings) are pictured in the Brillouin zone. Pairs of nodes with opposite chirality (blue/red) are protected by the broken time-reversal symmetry. From [164, 168]. Copyright American Physical Society.

We sought to tune the promising material $Nd_2Ir_2O_7$ via hole doping across a metal-insulator transition (MIT). We attempted to resolve some of relations between lattice, spin, and charge degrees of freedom across this unusual MIT. Our data establish a complex interplay between magnetism and the formation of the metallic state in hole-doped $(Ca_xNd_{1-x})_2Ir_2O_7$.

Another primary goal of this work was to answer open questions about the chemistry in the pyrochlore iridates: does doping affect the local structure symmetries, which are important for the topological properties? And is the electronic state described by the minimal $J_{\text{eff}} = 1/2$ model? To these ends, we collaborated with local structure expert Prof. Geneva Laurita and with X-ray staff scientists skilled in absorption spectroscopies. Our answers to these questions encouraged future studies of this material family.

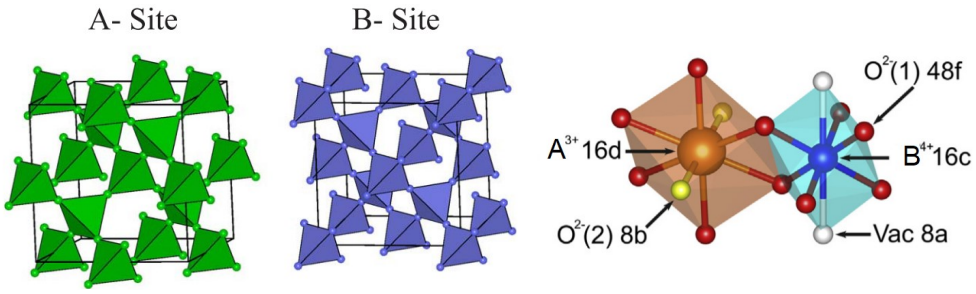

Figure 6.2: Pyrochlore oxide structure. There are 4 crystallographic sites $A_2B_2O_6O'$ in the cubic space group $Fd\bar{3}m$. The left panel separately shows the interpenetrating corner-sharing tetrahedral A and B sublattices. The right panel shows one $AO_6O'_2$ scalenohedron (puckered cube) and one BO_6 octahedron. From [169]. Copyright 2010 American Physical Society.

6.1 Introduction

The pyrochlore oxide structure $A_2B_2O_7$ is decorated with interpenetrating A and B sublattices of corner-sharing tetrahedra composed of AO_8 and BO_6 coordination complexes. Pyrochlores host a variety of electronic and magnetic phases owing in part to geometric frustration in the presence of antiferromagnetic exchange interactions [169] and the diversity of cation species which can be accommodated within this structural framework. This is a highly stable structure, for better or worse; it can accommodate large levels of cation disorder and ligand vacancies.

We focus on the lanthanide iridium oxide pyrochlores $Ln_2Ir_2O_7$ (with Ln^{3+} and Ir^{4+}) because they have small energy gaps between quadratic bands. Upon varying the lanthanide site, this series exhibits a metal-insulator transition (MIT) [170] where the gap monotonically decreases with increasing ionic radius [171] until a metallic state is reached between A=Nd and A=Pr lanthanide ions [172]. Our current theoretical understanding of this transition is that it is bandwidth-driven: larger Ln ions decrease the trigonal compression of the oxygen octahedra, increasing the Ir-O orbital overlap [11]. This

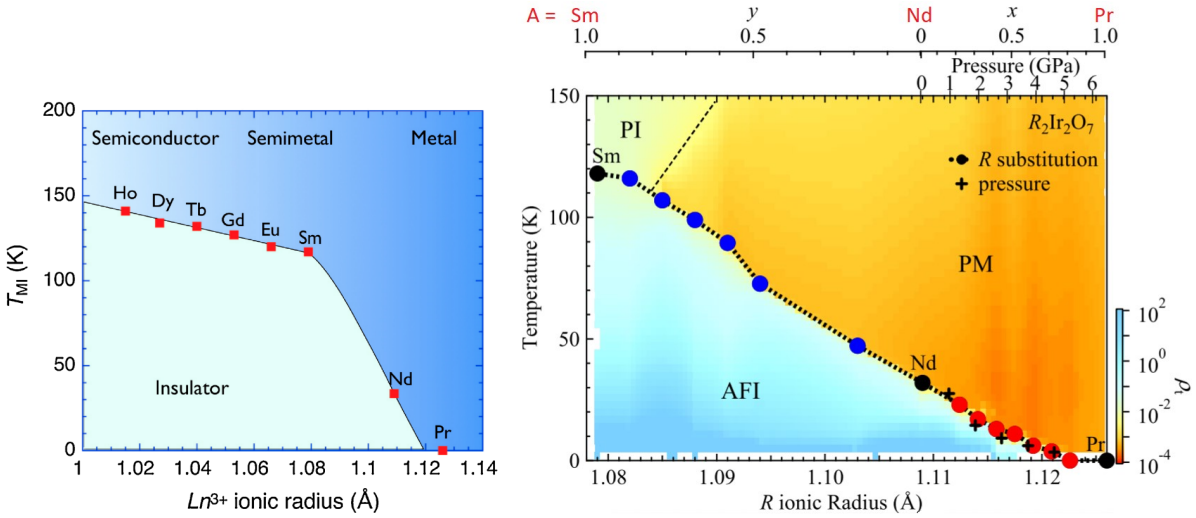

Figure 6.3: Bandwidth-controlled metal-insulator transition in $Ln_2Ir_2O_7$. *Left panel*: Transport behavior for the lanthanide series. The MIT tracks with Ln radius, which changes Ir-O bonding. *Right panel*: hydrostatic and 'chemical' pressure on Ln = (Sm,Nd,Pr) samples. From [171] Copyright 2011 Physical Society of Japan, and from [173] Copyright 2015 American Physical Society.

bandwidth-driven picture has been established by studies of both hydrostatic and 'chemical' pressure. Pressure has a relatively gradual effect on the MIT [173]. As of yet there have been no detailed structural studies of $Nd_2Ir_2O_7$ under pressure, which could be insightful.

Interestingly, the pyrochlore iridates' MIT coincides with the formation of all-in-all-out (AIAO) antiferromagnetic order of the J_{eff}=1/2 moments on the Ir magnetic sublattice, while magnetic A site lanthanide cations may establish the same order at lower temperatures. The role of magnetism in the MIT is unresolved. Unexpectedly, chiral spin textures are reported to persist into the metallic regime [174]. Additionally, while $\mathbf{q}$=0 AIAO order coincides with the opening of a charge gap [11], the MIT shows evidence of both Mott and Slater (or mean-field) character [175]. The electronic response may be tied to the magnetism on each sublattice.

Our study aimed to get at some of the ambiguities regarding the mechanism of this

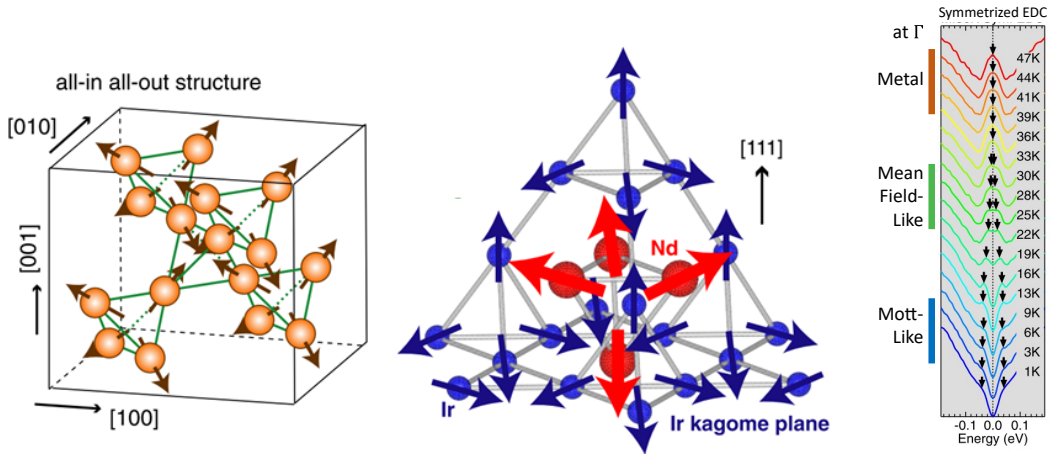

Figure 6.4: Coupled magnetic and electronic transitions in $Nd_2Ir_2O_7$ specifically. *Left panel*: All-in-all-out (AIAO) antiferromagnetic ground state. *Center panel*: A different perspective on the AIAO state, highlighting relations to kagome structures. This picture also includes the Nd sublattice explicitly. *Right panel*: Temperature-driven progression from metal to mean-field-like-insulator to Mott insulator via the energy distribution curves (EDCs, essentially the density of states as probed by angle-resolved photoemission). Note how the first transition is coincident with the Ir AIAO order, and the second coincides with alleged Nd order. From [176] Copyright 2012 American Physical Society, and from [175] Copyright 2016 Physical Society of Japan.

unusual MIT. As an alternative to bandwidth control of the MIT with A-site isoelectronic substitution, filling control via carrier doping has the potential to access metallic states in the $A_2Ir_2O_7$ phase diagram with thermodynamically distinct magnetic and electronic properties.

One of the chief mysteries of filling control in the pyrochlore iridates is the wide variety of magnetic responses. For some compounds and synthesis conditions, the MIT and magnetic transition are coupled, and in others they are decoupled. In the present study and in recent work on $(Eu_{1-x}Ca_x)_2Ir_2O_7$, the MIT and AIAO transition temperatures remain coincident [177], and this transition is rapidly suppressed with increasing x until a metallic ground state is realized between x=0.05 and x=0.10. Yet our own work on the exact same A=(Eu,Ca) system yielded different behavior entirely: while the MIT temperature decreases rapidly with x, the magnetic transition is decoupled in temperature and slowly decreases with x [178]. This is especially vexing because our Ca-doped Nd and Eu compounds were synthesized under nearly-identical conditions. A similar decoupling of the MIT and magnetism was demonstrated in other studies on A=(Y,Ca) and A=(Eu,Sr) [179, 180]. The discrepancies between these naïvely similar materials, and the relation between their synthesis conditions and magnetic properties, warrants further investigation.

6.2 Synthesis: Solid State

Polycrystalline samples of $(Nd_{1-x}Ca_x)_2Ir_2O_7$ were synthesized by a conventional solid-state reaction:

- Dry: Prepare reactant powders (99.99%, Alfa Aesar) of Nd_2O_3, $CaCO_3$, and IrO_2 by drying them in alumina crucibles in air at 1370, 570, and 970 K respectively. This step is very important in humid places like Santa Barbara California.

- Weigh: Use a precision scale to weigh out stoichiometric amounts of the reactants Nd:Ca:Ir in (2-2x):2x:2 ratios, ignoring oxygen stoichiometry. Typical batch size was 2-5 grams.

- 1st reaction: mix and grind powders for > 25 minutes in a clean agate mortar and pestle, and heat at 1070 K in an alumina crucible in air for 18 h. In this initial reaction step, pelletization seemed unimportant.

- 2nd reaction: regrind and remix powder, funnel into a large clean latex balloon, remove air with a rough pump before tying a knot, and press into a pellets at 300 MPa within an isostatic press. Remove the balloon, then place in an alumina crucible and heat at 1270 K in air for 8 days with one intermediate grinding.

- 3rd reaction: Repeat previous step, sintering at 1320 K $-$ 1370 K. This step always resulted in several mol% unreacted Nd_2O_3. Further repetition was not shown to have any improvements in pyrochlore phase fraction. Higher sinter temperatures were avoided as they were thought to evaporate the IrO_2 more quickly or yield other products like the defect fluorite Nd_3IrO_7.

- Vacuum anneal: For several samples, the remaining Nd_2O_3 was reacted by adding 4 mol% additional IrO_2 to the powder, then sintering the pellet at 1370 K in an alumina crucible sealed in a quartz tube under vacuum for 8 days with one intermediate grinding. For these samples, the final pellet was sintered at 1170 K for 2 days in air. These samples had improved electronic homogeneity, as evidenced by the removal of 120 K features in the resistivity and the magnetization. We were unable to resolve any structural differences from vacuum annealing. We suppose without direct evidence that the vacuum anneal improved oxygen stoichiometry. For this chapter, I will be describing only the properties of vacuum annealed samples

for clarity.

As an aside, we note that we attempted single crystal flux synthesis. $SrCl_2$ fluxes resulted in ∼0.1 mm crystals with high Sr content on the A site. We also tried to replicate reported KF flux methods but were unable to produce crystals.[2]

After solid state synthesis, laboratory powder X-ray diffraction was performed to track phase composition and lattice constants. For preliminary measurements we used a Panalytical Empyrean diffractometer using lab-source Cu K-α radiation with standard settings. Finely ground samples were tamped down on a zero diffraction plate. Preferred orientation was not much of an issue.

Refinements of the data exhibit the expected pyrochlore phase as well as small (<1.5%) impurity fractions of each of the reactants and Ir metal. The reactants are all paramagnetic, which enabled study of magnetic order. But for magnetotransport it was unfortunate that we could not prepare purer (and denser) samples.

We quantified the Ca content using a Rigaku ZSX Primus IV wavelength-dispersive X-ray fluorescence (WDXRF) spectrometer. Pressed pellet samples were quantitatively analyzed against standards composed of unreacted powders of known stoichiometry. This is a labor-intensive method but it is more repeatable and precise than similar measurements without standards. It was especially necessary for low Ca content $< 5\%$, where energy dispersive X-ray spectroscopy (EDS) on a scanning electron microscope (SEM) is imprecise.

[2]Because of the dangers of boiling fluorine compounds, our KF flux technique involved weighing and filling the platinum crucible in a glovebox, and sealing it in an alumina crucible with high-temperature cement. A piece of string in the cement would burn away at high temperatures to vent gas in a controlled way. The reaction furnace was placed within a fume hood, and sacrificial alumina shrouds were used to protect the heating elements.

6.3 Lattice Structure

Beyond just reporting lattice constants, we sought a more complete structural characterization of our samples. First we employed synchrotron powder diffraction measurements of the average structure, which revealed minimal changes in bond lengths and bond angles as Ca is alloyed into the pyrochlore matrix. Second, we used pair distribution function (PDF) measurements of the local structure, which showed that Ca enters the lattice homogeneously with no resolvable clustering.

6.3.1 Average Structure

Several samples were characterized by synchrotron powder X-ray diffraction (XRD) measurements at Beamline 11-BM of the Advanced Photon Source (APS) at Argonne National Laboratory. Sample preparation is important for this experiment. Because of the incredibly short absorption lengths I should have diluted the samples (e.g. with silica powder), but instead I loosely filled the kapton tubes with pyrochlore powder. The data quality was much better than is possible with Cu K_α lab-based instruments, but poorer than it could have been. Our transmission was much less than 1%, and I have since learned that transmission $> 10\%$ (or equivalently $\mu R < 1$) is optimal.

The diffraction patterns were refined using the `TOPAS` software package [95]. We observed unusually asymmetric and difficult-to-describe peakshapes, which are perhaps typical of pyrochlore powders (e.g. Ref. 181). I opted for a refinement that captured the desired parameters: lattice constants, thermal parameters, and site occupation. My model was perhaps slightly unphysical in terms of particle strain distribution: in addition to strain and size terms I included a small 'Tube Tails' correction. In addition to the built-in absorption correction, I found it necessary to manually broaden peaks as a function of scattering angle, which is not standard.

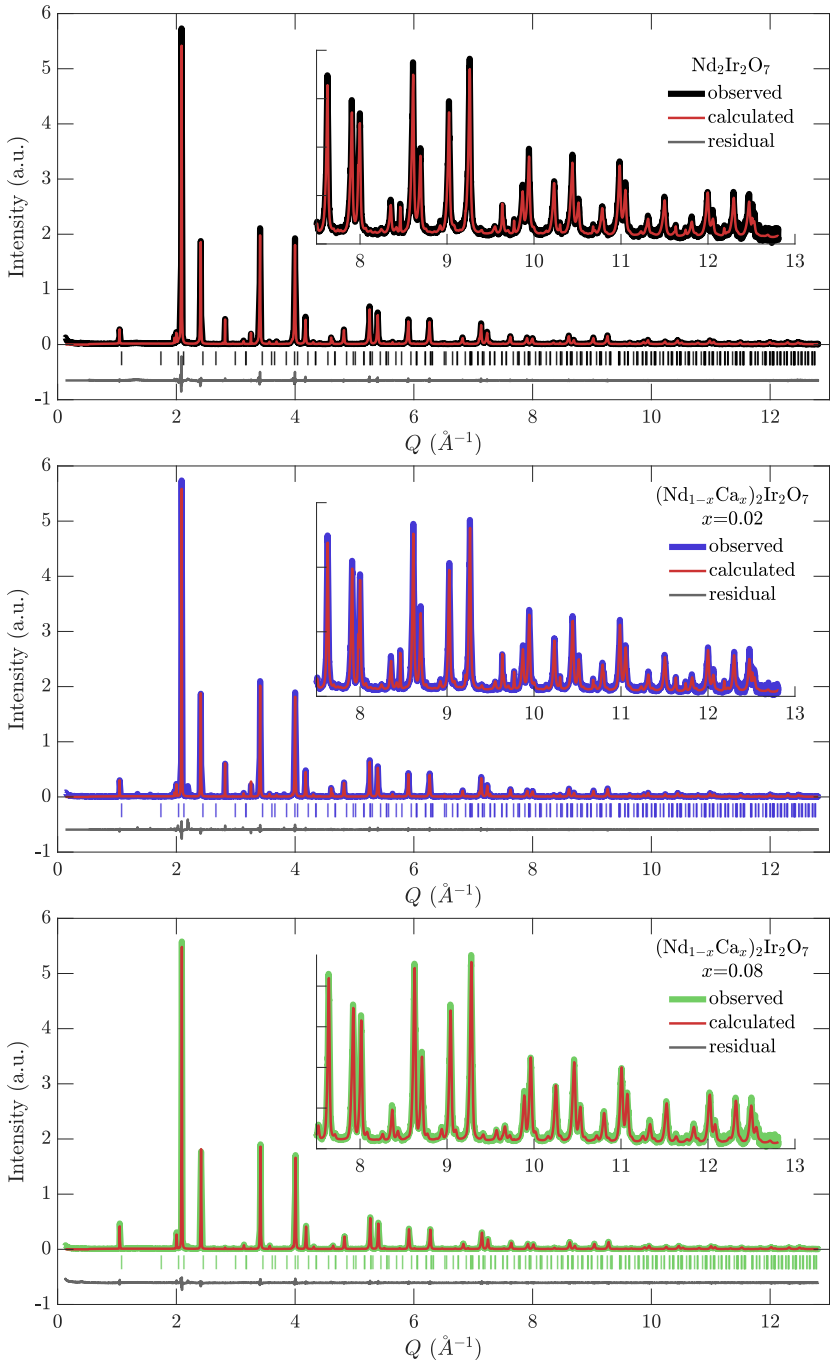

Figure 6.5: $(Ca_xNd_{1-x})_2Ir_2O_7$ synchrotron XRD patterns, all taken at 300 K. Calculated curves include the pyrochlore phase and the impurity phases Ir, IrO_2, and Nd_2O_3. Lines above the residual curves index only pyrochlore peaks.

In the pyrochlore structure there are four sites $A_2B_2O_6O'$, which are located at the $16d$, $16c$, $48f$, and $8b$ Wyckoff positions respectively. The cubic lattice constant a decreases with Ca substitution, as expected. Occupancies of Nd and Ir indicate slight 3% 'stuffing' through anti-site defects of excess Nd cations on the B-sites. Refinements of the O and Ca occupancies were unreliable because they are light elements. For O ions we had no available way to fit occupancy. But for Ca we used the WDXRF-measured values and fixed the Ca ions on the A-sites. We justify this from the thermal parameters, and the finding that refinements with Ca on the B-sites had inferior fits.

An important result from the refinements was the finding that the bandwidth change from the Ir-O bonding was small. We gathered this from the free coordinate u for O $48f$ sites, which decreases marginally with Ca content. This trend signifies a reduction in trigonal compression of the IrO_6 octahedra toward octahedral symmetry (u=0.3125). This reflects a 0.5(2) degree increase in the Ir-O-Ir bond angle from x=0 to x=0.08. The x=0.08 sample's angle is much less than the bond angle in the metallic A=Pr system [182]. We infer, then, that the electronic bandwidth change from Ca is less significant than the effects of carrier doping and disorder in driving the metal-insulator transition.

6.3.2 Local Structure

Synchrotron total scattering data for pair distribution function (PDF) analysis were collected at Beamline 6-ID-D at the APS using powder taken from the same batches as the 11-BM samples. Prof. Geneva Laurita led the experiments and analysis with help from Eli Zoghlin, Samuel Britner, and Samra Husremovic. Sieved powders with <44 μm particle size were sealed into Kapton tubes using copper wire and epoxy in a He-filled glove-bag to provide a thermal exchange gas. The samples were measured in transmission using an area detector. The 2D data were integrated to 1D diffraction data utilizing the

x		0	0.02	0.08
x_{WDXRF}		0	0.0245(9)	0.0755(9)
a(6 K)	[Å]	10.3719(7)	10.3667(9)	10.3497(9)
a(25 K)	[Å]	10.3712(9)	10.3680(9)	10.3497(9)
a(45 K)	[Å]	10.3726(9)	-	10.3489(9)
a(300 K)	[Å]	10.3877(12)	10.3783(12)	10.3631(11)
100 K				
$u(\mathrm{O}_{48f})$		0.3323(2)	0.3325(3)	0.3309(2)
∠Ir-O-Ir	[°]	129.7(2)	129.5(2)	130.4(2)
∠O-Ir-O	[°]	82.28(7)	82.16(8)	82.76(7)
Nd A Occ.		1.000(16)	0.975(17)	0.925(11)
Ir A Occ.		0.000(16)	0.000(17)	0.000(11)
Ir B Occ.		0.988(23)	1.000(25)	1.000(17)
Nd B Occ.		0.012(23)	0.000(25)	0.000(17)
A U_{iso}	[Å^2]	0.00262(9)	0.00305(9)	0.00339(6)
B U_{iso}	[Å^2]	0.00344(7)	0.00329(6)	0.00228(4)
$\mathrm{A_2B_2O_7}$	[%]	96.48	95.59	98.39
R_{wp}	[%]	10.54	12.83	9.45
χ^2		2.32	3.00	2.24
300 K				
$u(\mathrm{O}_{48f})$		0.3313(2)	0.3312(2)	0.3298(2)
∠Ir-O-Ir	[°]	130.6(2)	130.1(2)	131.1(2)
∠O-Ir-O	[°]	82.87(8)	82.55(8)	83.19(7)
Nd A Occ.		1.000(14)	0.975(16)	0.925(10)
Ir A Occ.		0.000(14)	0.000(16)	0.000(10)
Ir B Occ.		0.974(21)	0.978(23)	1.000(16)
Nd B Occ.		0.026(21)	0.022(23)	0.000(16)
A U_{iso}	[Å^2]	0.00660(9)	0.00729(9)	0.00749(6)
B U_{iso}	[Å^2]	0.00268(6)	0.00272(6)	0.00292(3)
$\mathrm{A_2B_2O_7}$	[%]	96.68	96.04	99.00
R_{wp}	[%]	10.01	12.12	8.69
χ^2		2.20	2.88	2.04

Table 6.1: Select crystallographic data from Rietveld refinement of synchrotron powder XRD data. First, nominal sample x and sample x_{WDXRF} from quantitative WDXRF analysis. Second, cubic lattice parameters a at several temperatures. Next, refined values at 100 K and 300 K: u for the O 48f site; nearest-neighbor Ir-O-Ir bond angles; intra-tetrahedron O-Ir-O bond angles; occupancies of Nd and Ir on the A and B sites; isotropic atomic displacement parameters U_{iso} for A- and B-sites; pyrochlore phase fractions less Ir, $\mathrm{IrO_2}$, and $\mathrm{Nd_2O_3}$; and Rietveld goodness-of-fit parameters R_{wp} and χ^2. Note oxygen occupancies and U_{iso} were fixed to 1 and 0.001, respectively.

`Fit2D` software [183]. Corrections to obtain $I(Q)$ and subsequent Fourier Transform with $Q_{\max}$=24 $\AA$ to obtain $G(r)$ were performed using the program `PDFgetX2` [184]. Analysis of the total scattering data was performed using the `PDFgui` software suite [185] over the range 1.75 Å − 10.0 Å.

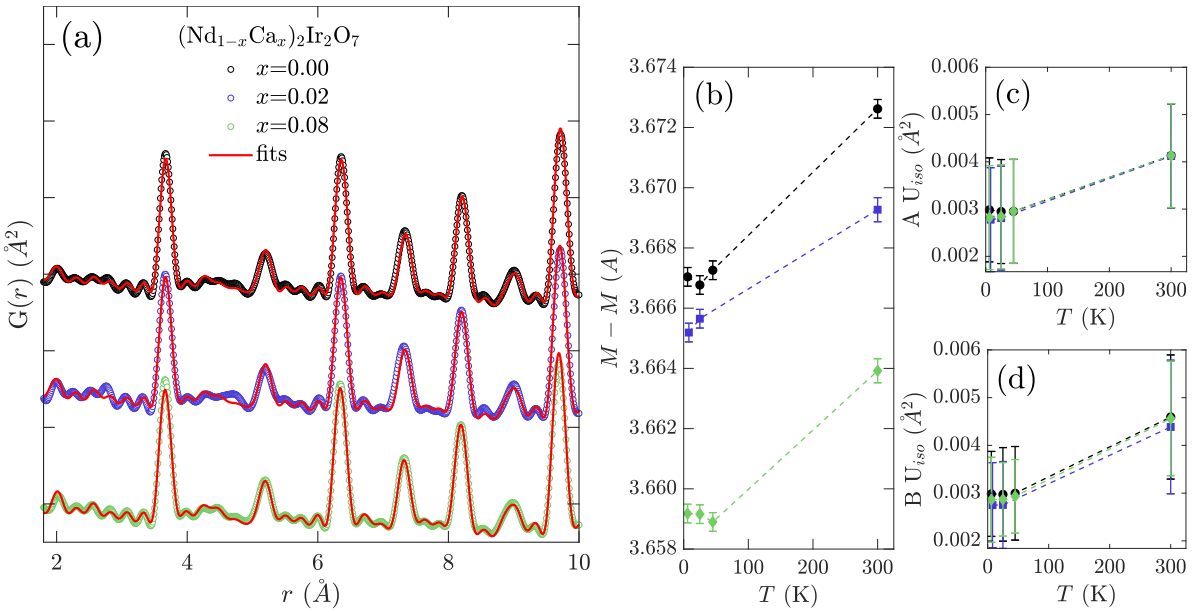

Figure 6.6: X-ray PDF refinement of the $(Ca_xNd_{1-x})_2Ir_2O_7$ local structure: (a) 300 K PDF data in circles, offset vertically, with fits in red solid lines. (b) Metal-metal distances between A and B sites. (c) A- and (d) B-site isotropic atomic displacement parameters U_{iso}. Dashed lines are guides to the eye.

To summarize, the PDF experiments showed that the local structure does not change much as functions of either temperature or Ca. No new atomic correlations (i.e. peaks in $G(r)$) were observed as Ca was introduced into the lattice or as the lattice was cooled through the MIT. Short-range order of the A- and B-sites is unchanged within experimental resolution for the measured samples for 6 K $\leq T \leq$ 300 K. All PDF measurements fit well to the site symmetry of the parent pyrochlore structure, with goodness of fit R_w values between 9% and 15%. This is consistent with a previous synchrotron XRD study that reported no symmetry change for $Nd_2Ir_2O_7$ upon cooling to 4 K [186]. Notably,

the A- and B-sites' isotropic displacement parameters, as determined from PDF refinements, are also unchanged under varying Ca content within (significant) uncertainty. This precludes Ca clustering effects or nanoscale chemical phase separation. Furthermore, metal-metal distances track well with lattice constants, indicating that minimal site disorder is introduced with Ca substitution.

6.4 Electronic Structure

To get at the electronic structure, we performed electron transport (resistivity) measurements. As Ca substitution levels increase, the MIT is pushed downward in temperature and coincides with the onset of magnetic order. For doping levels greater than $x = 0.05$, the ground state switches to a metal with a weak upturn in the low temperature resistivity coupled to Nd magnetism.

To complement the electron transport studies, we performed X-ray absorption spectroscopy (XAS) studies at the Ir L edges to pin down the Ir electronic configuration and valence magnetic state. XAS showed that the metallic state retains a strong spin-orbit coupled character with branching ratios little altered with doping. Magnetic circular dichroism data reveal an anomalous, weak net Ir moment that survives across the MIT. Taken together, these spectroscopies support the idea that the $J_{\text{eff}} = 1/2$ state remains valid on carrier-doping through the MIT.

6.4.1 Transport

Transport measurements were carried out in a Quantum Design DynaCool Physical Property Measurement (PPMS) system. Cut portions of sintered pellets were mounted with GE varnish in a four-wire configuration using silver paint and gold wire to create contacts. Current was driven perpendicular to the applied magnetic field, and voltage

was measured with the standard resistivity option.[3]

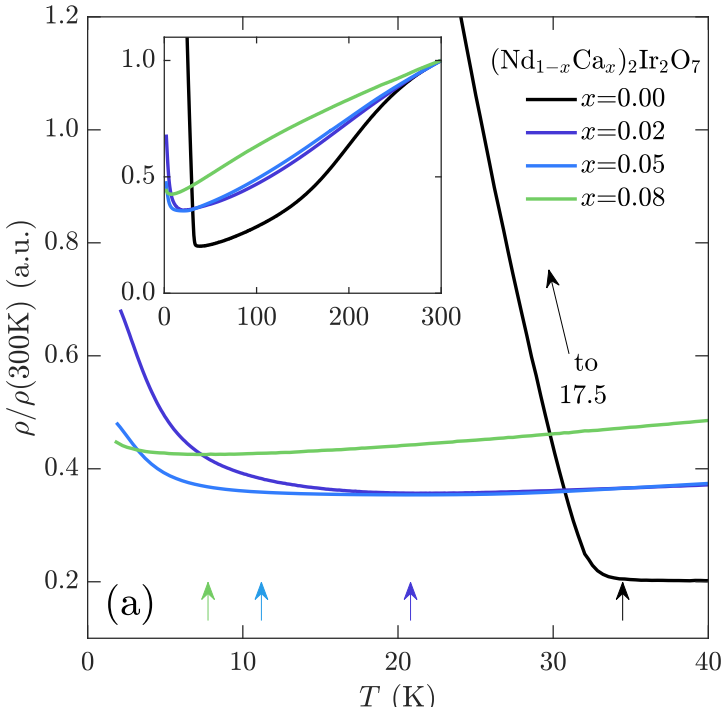

Figure 6.7: $(Ca_xNd_{1-x})_2Ir_2O_7$ resistivity measurements: (a) Relative resistivity from 2 K to 300 K, all at 0 T on zero field cooling. Arrows indicate the onset of $\frac{\delta\rho}{\delta T} > 0$. Resistances are normalized due to variation in pellet densities; typical values are ρ(300 K)≈10 mΩ·cm.

Resistivity measurements showed that all $(Ca_xNd_{1-x})_2Ir_2O_7$ samples are metals at high temperatures, defined via the positive slope $\frac{\delta\rho}{\delta T}$>0. The pure x=0 sample enters a well-defined insulating state with a sharp T_{MIT}=34 K. This transition weakens and drops in temperature quickly with the addition of carriers. For samples with $x\geq$0.05, the insulating state becomes ill-defined, and scattering is only weakly enhanced below 10 K. And this weak residual upturn in resistivity at large x is strongly suppressed with the application of a magnetic field (though this is not observed for $x\leq$0.02). We suggest that this upturn could arise from an RKKY-type coupling of itinerant carriers to the

[3]For this type of measurement on semimetallic samples, the built-in 'ETO' option that uses an ac resistance bridge has superior signal-to-noise.

Nd moments in the samples. This observation is in keeping with muon spin resonance (μSR) features linked to ordering or freezing of the Nd magnetic sublattice [187, 188]. We speculate that this additional scattering channel associated with Nd magnetism could be obstructing the full T_{MIT} suppression to 0 K. This would mean that there may still be quantum criticality if the MIT and coincident Ir sublattice order is suppressed to T=0, but it might not be evident in the transport.

6.4.2 X-ray Absorption

X-ray absorption spectroscopy (XAS) and X-ray magnetic circular dichroism (XMCD) measurements were performed at Beamline 4-ID-D at the APS. Sieved powders with ≈5 μm particle size were brushed on about 10 layers of scotch tape to achieve a uniform sample thickness corresponding to nearly two absorption lengths, where signal is optimum. Care was taken to avoid gaps that would yield 'pinholing' (diffraction) effects. Measurements were collected at the Ir $L_{2,3}$ absorption edges ($2p_{1/2,\,3/2} \rightarrow 5d$) in transmission geometry. The incident energy was selected using a double-crystal Si(1,1,1) monochromator. Circularly polarized X-rays were generated in helicity-switching mode at 13 Hz using a diamond phase retarder, and the absorption was detected using a diode with lock-in amplification [189]. To better handle spurious signals, XMCD measurements were repeated under $\mu_0 H$=±5 T oriented along the incident wave vector.

In the XAS spectra, qualitatively all samples are quite similar. This is consistent with the small structural and valence changes at low levels of Ca substitution; Ca-doping does not radically change the bandwidth. As for hole-doping, x values were too small to cause measurable changes in peak energies. Some evidence of doping comes from the increase in the XAS-calculated number of holes n_h, estimated from the increase in I_{L_2}+I_{L_3} with x.[4]

[4] The XAS L_2 and L_3 white line intensities are defined as $I_{L_{2,3}} = \int[\mu(E) - \Theta(E)]dE$, where $\mu(E)$

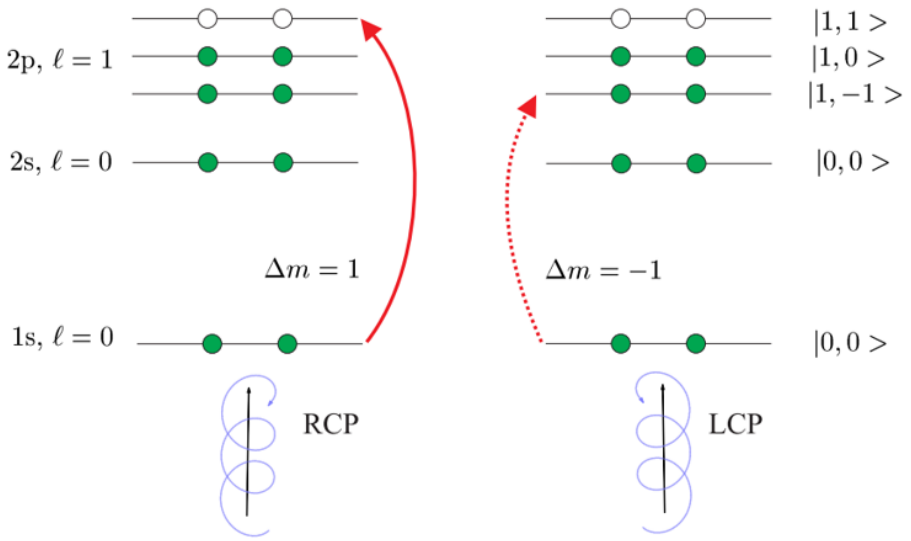

Figure 6.8: Overview of X-ray magnetic circular dichroism (XMCD). XMCD is absorption with circularly polarized light. Right- and left-circularly polarized photons (LCP, RCP) have different angular momenta m. The selection rules limit the valence orbitals that the photoelectron can occupy in each case. This example shows a simple $2p^4$ K-edge, where only one set of orbitals with $j = +1$ can be occupied; the contrast between RCP and LCP would reveal the electronic configuration. From [41]. Copyright 2011 John Wiley and Sons, Ltd.

From the very weak XMCD signal, we calculate the Ir total net moment m_{tot}=0.004 μ_B/Ir at 5 K and 5 T. This small value is unchanged within uncertainty for the x=0 and x=0.08 samples. This magnitude is similar to the bulk magnetization values of other pyrochlore iridates that do not have magnetic A sites.

The ratio of angular to spin moment $L_z/S_z \approx 3$ and the high branching ratio BR≈6 both provide strong indications of an Ir J_{eff}=1/2 ground state [15, 191].

is the XAS signal, $\Theta(E)$ is a broadened step function centered on the inflection energy as expected for isolated ions, and the integration range is over the white line feature [190].

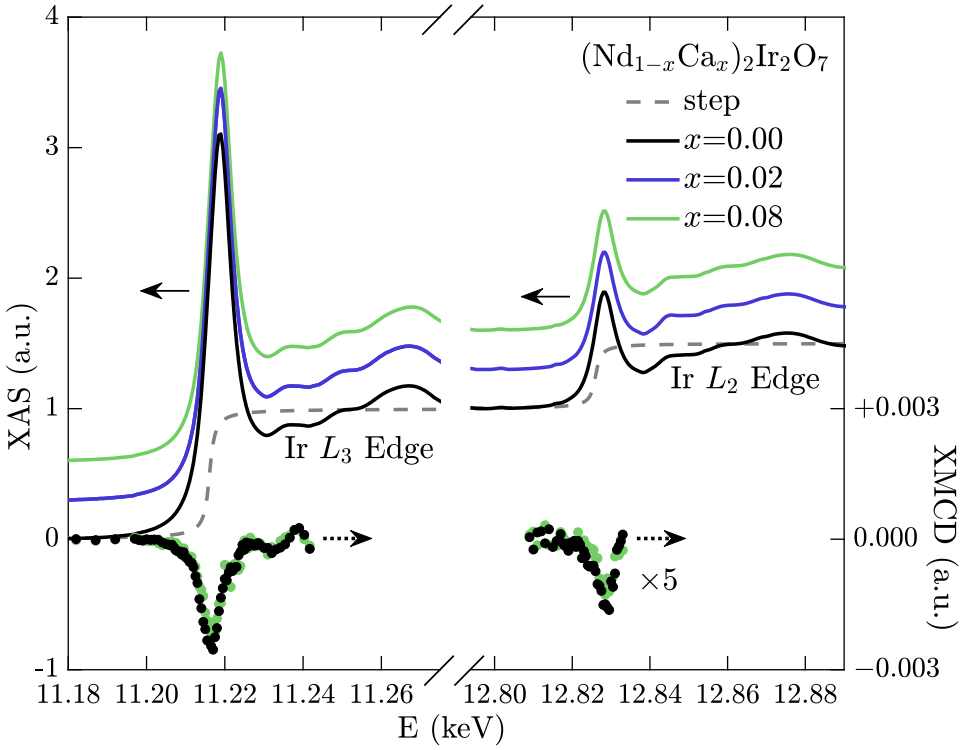

Figure 6.9: $(Ca_xNd_{1-x})_2Ir_2O_7$ X-ray spectroscopic measurements: Ir L-edge XAS is indicated with solid lines, and XMCD with dots. XAS lines are offset by 0.3 for clarity. XMCD was measured at 5 K and ±5 T and normalized to the corresponding XAS edge jump.

To calculate the spin and orbital moments, we applied the XMCD sum rules [192]:

$$\begin{aligned}
\langle L_z \rangle &= \frac{I_{L_3}^{\mathrm{XMCD}} + I_{L_2}^{\mathrm{XMCD}}}{I_{L_2} + I_{L_3}} \times \frac{2}{3} n_h \\
\langle S_{\mathrm{eff},z} \rangle &= \frac{I_{L_3}^{\mathrm{XMCD}} - 2 I_{L_2}^{\mathrm{XMCD}}}{I_{L_2} + I_{L_3}} \times \frac{3}{2} n_h \\
m_l &= -\langle L_z \rangle \\
m_s &= -2 \langle S_z \rangle = -2 \langle S_{\mathrm{eff},z} \rangle + 7 \langle T_z \rangle
\end{aligned} \tag{6.1}$$

where L_z and S_z are angular and spin momentum operators along z, T_z is an additional magnetic dipole term,[5] and m_l and m_z are the corresponding moment sizes. XAS white

[5] As is standard practice, we included a magnetic dipole term $\langle T_z \rangle \approx 0.2 \langle S_z \rangle$. This value is the same strength as in other iridate systems like Sr_2IrO_4 [20]. Configuration Interaction calculations (from

line intensity $I_{L_{2,3}}$ calculations are described in Footnote 4. Simple integrated XMCD intensities $I_{L_{2,3}}^{\mathrm{XMCD}}$ are normalized to the XAS intensities. To get quantitative values in units of μ_{B}/Ir, these results are compared to data on well-studied systems.

As for BR, it comes from careful analysis of the XAS intensities, which I fit in the `ATHENA` software package [193] and subsequently integrated in `MATLAB`. BR is a relative measurement of spin-orbit coupling for similarly prepared samples. From the selection rules $\Delta J{=}0, \pm 1$, the branching ratio BR$= I_{L_3}/I_{L_2}$ ought to be 2 for free ions (just from considering the $2p$ orbital occupations). So BR$>$2 indicates that unoccupied $5d$ states are primarily $5d_{5/2}$ rather than $5d_{3/2}$, which is consistent with a $J_{\mathrm{eff}} = 1/2$ state.

x	n_h $[q_e]$	XAS n_h $[q_e]$	BR	$\langle L{\cdot}S\rangle$ $[\hbar^2]$	m_{tot} $[\mu_B/\mathrm{Ir}]$	L_z/S_z
0.00	5.00	5	5.7(2)	2.8(1)	0.0042(9)	3.0(4)
0.02	5.02	5.06(6)	5.7(2)	2.8(1)	–	–
0.08	5.08	5.10(6)	5.5(2)	2.7(1)	0.0036(9)	2.8(4)

Table 6.2: Calculations for $(Ca_xNd_{1-x})_2Ir_2O_7$ from Ir L-edge XAS and XMCD, as described in the text: stoichiometric and XAS-calculated number of holes n_h; branching ratios BR; spin-orbit expectation values $\langle L{\cdot}S\rangle$; total moments m_{tot} at 5 K and 5 T; and $L_z/S_z = 2m_l/m_s$.

The very large BR values we attain are large, as is typical for the pyrochlore iridates. A few words of caution are warranted here. First, this by itself is not proof of a J_{eff}=1/2 state. A high branching ratio is seen in a range of Ir oxidation states and ligand environments, including the d^4 compound $Sr_3Ir_2O_7F_2$ [140]. Another word of caution is that in most reports, researchers forego an approximate uncertainty, which is problematic because the fitting and integration procedure is highly subjective. In my analysis the most sensitive and subjective parameter is the inflection energy where the broadened step function is centered – this is subtracted from the raw spectrum $\mu(E)$. The choice of inflection energy is inherently inaccurate, and can be stymied by experimental $<$0.1

quantum chemistry) are needed for a precise value.

eV shifts in a spectrum's energy, which occur even on the best XAS instruments. To handle this, my uncertainties assume some miscalibration in energy and span values with reasonable offsets for our instrument.

6.5 Magnetic Properties

The subtle magnetic properties for $(Ca_xNd_{1-x})_2Ir_2O_7$ are especially difficult to disentangle because there are multiple magnetic sublattices: Nd and Ir. We first show bulk magnetization, where by changing temperature and field and tracking hysteresis, we can learn about the changes in the populations of the magnetic domains and metamagnetism. Many of these findings are also reflected in the magnetotransport, but only at low temperatures, so this maybe points to the Nd response. To tie it all off, we analyze our Ir site-specific circular dichroism. This final result is especially subtle and points to very weak net polarization.

6.5.1 Bulk Magnetization

Magnetization data were collected with a vibrating sample magnetometer (VSM) within a DynaCool PPMS or a MPMS3 Quantum Design SQUID magnetometer. The maximum field is 7 T. 10-40 mg of powder was placed in polypropylene capsules that fit inside brass holders.

Magnetization measurements reveal a weak irreversibility (here the difference between (zero-)field cooling sweeps FC-ZFC) that persists across the doping range. This effect in the pyrochlore iridates is conventionally ascribed to spin canting within the all-in-all-out (AIAO) networks of Ir and Nd spins, but may instead be related to domain wall formation. Irreversibility in magnetization data appears at the same temperature where the low temperature resistivity changes slope. This connects the onset of magnetic

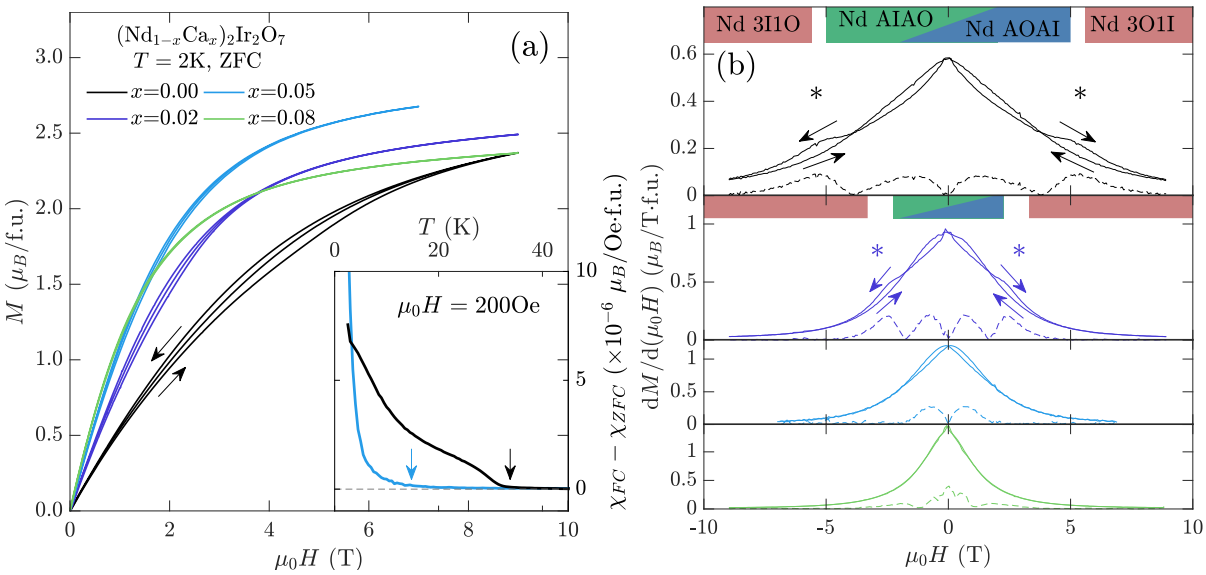

Figure 6.10: $(Ca_xNd_{1-x})_2Ir_2O_7$ magnetization measurements: (a) Field dependence of the isothermal dc magnetization, swept as in Fig. 6.11, with just $H>0$ shown. Arrows indicate field sweep direction. Inset: Irreversibility of the dc susceptibility (field cooling minus zero-field cooling) taken at 200 Oe. T_{MIT} values are indicated with arrows. (b) Solid lines are numerical derivatives of magnetization with respect to field, highlighting the hysteretic splitting. The initial 0→+9 T sweeps (virgin curves) are not shown. Dashed lines are the absolute differences between sweep directions, magnified for clarity.

correlations or freezing with the onset of the MIT for the low doping regime ($x\leq0.02$) as well as with the low temperature increase in resistivity for the high doping regime ($x\geq0.05$).

At $T = 2$ K, isothermal magnetization $M(H)$ is dominated by the Nd sublattice [171, 194], and as such hysteretic differences appear between sweeps of increasing and decreasing field. The splitting is illustrated by plots of dM/dH. In the ordered state of the parent system, applying a magnetic field polarizes the Ising-like domains of both sublattices toward either AIAO or all-out-all-in (AOAI) order [195].

At higher fields, a second hysteretic feature appears, consistent with a spin-flop transition likely into the Nd 3-in-1-out (3I1O) state reported for the single crystals of

$Nd_2Ir_2O_7$ [194, 195]. Upon Ca substitution, this higher field spin-flop feature decreases in onset field and vanishes for x=0.05. This is consistent with the destabilization of long-range Nd antiferromagnetism at high hole-doping and substitutional disorder. The remaining magnetization in these metallic samples may arise from short-range freezing of Nd/Ir moments coincident with the low temperature upturn in $\rho(T)$.

6.5.2 Magnetotransport

The aforementioned hysteretic features in the magnetization mirror those in the magnetoresistance (MR). The critical fields are equal within measurement uncertainty, which suggests that the magnetoresistance changes are governed by magnetic domain scattering effects.

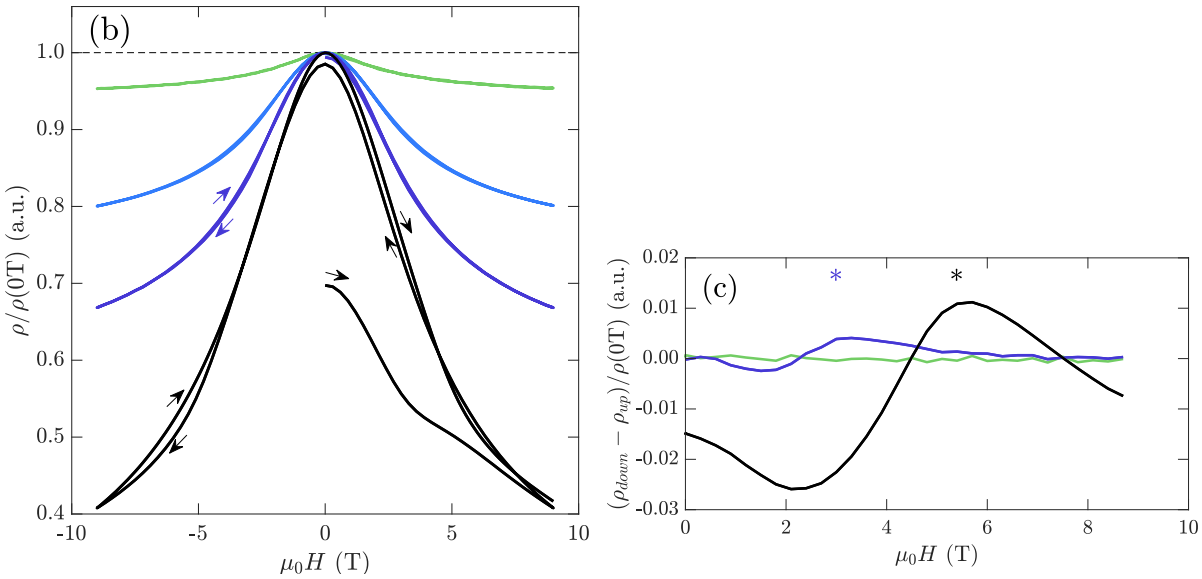

Figure 6.11: $(Ca_xNd_{1-x})_2Ir_2O_7$ magnetotransport measurements: (b) Relative magnetoresistance at 2 K on zero-field cooling, swept from $\mu_0 H$=0→+9→−9→+9 T, with arrows to indicate field sweep direction. Note the hysteretic splitting, which is largest for the x=0 sample. (c) Hysteretic differences of the magnetoresistance in b, for sweeps after the initial 0→+9 T sweeps (virgin curves).

Magnetoresistance is negative at low temperatures for all samples. The low tempera-

ture MR decreases in magnitude with Ca, consistent with the suppression of long-range magnetism in the system. Field-induced 'training' or hysteretic behavior is observed in the parent system and is consistent with previous studies of conducting domain walls [194, 196] in the parent material; yet this behavior is rapidly suppressed with Ca-doping.

6.5.3 X-ray Magnetic Circular Dichroism

An open question remains regarding the origin of the weak, but finite, Ir moment present in both the insulating parent x=0 and metallic x=0.08 samples. That the XMCD net Ir moment from both samples is identical within error and suggests that the weak local Ir moment is not trivially tied to the AIAO state.

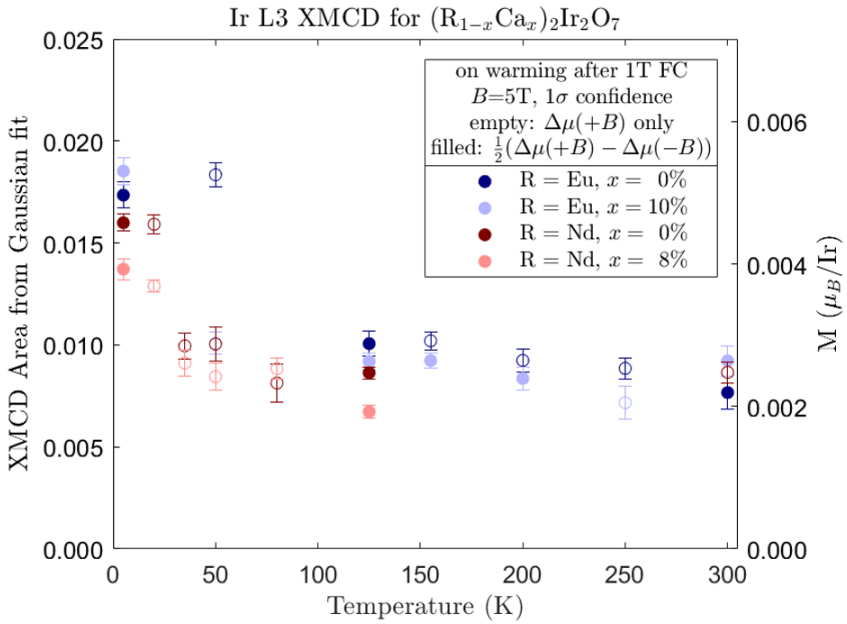

Figure 6.12: X-ray magnetic circular dichroism versus temperature for $(Ca_xNd_{1-x})_2Ir_2O_7$ (red) and the Eu analog (blue). Solid points subtract values at positive and negative fields and are thus more trustworthy. There are no significant differences versus temperature or between the Nd and Eu series. It is not clear how the Ir net moment is related to the magnetic phase behavior.

XMCD picks up both ferromagnetic and reversible (paramagnetic) responses to the

field; like in bulk probes, these are only distinguished by hysteresis loops, which we tried but had insufficient signal. If the signal is ferromagnetic, our signal could be tied to antiferromagnetic domain walls in the parent insulating phase, where domains persist locally in an electronically phase separated state even to high temperatures ∼100 K.

6.6 Conclusions

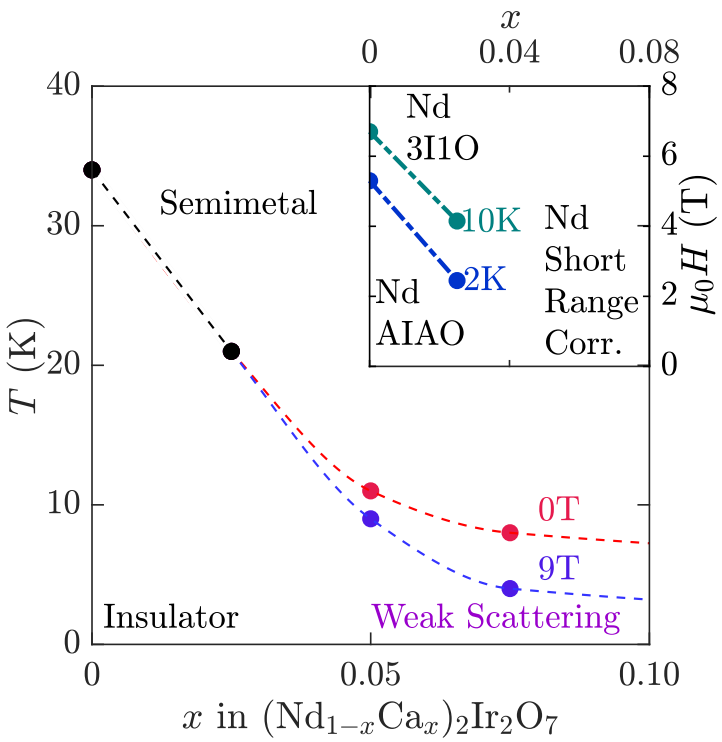

Figure 6.13: Temperature-concentration phase diagram for $(Ca_xNd_{1-x})_2Ir_2O_7$ based on resistivity measurements. Inset: field-concentration phase diagram, indicating magnetism on the Nd sublattice. All lines are guides to the eye.

In conclusion, we performed a litany of measurements to better understand the MIT and magnetic transitions in $(Ca_xNd_{1-x})_2Ir_2O_7$. We reported on the suppression of both T_{MIT} and the AIAO T_N on the Ir sublattice. We attribute this mostly to hole-doping. From a combined analysis of diffraction, PDF, and XAS data, we present evidence of Ca

incorporation without clustering or phase separation on both local and average length scales. Calcium ions only weakly perturb the underlying structure with minimal changes inferred to the corresponding bandwidth, and hole carriers associated with replacing Nd^{3+} with Ca^{2+} cations instead drive the suppression of the low temperature MIT. For $x > 0.02$, as the system enters a metallic ground state, both the charge transport and magnetism remain influenced by fluctuations and disorder on the Nd magnetic sublattice. Our results point toward the coincident suppression of long-range magnetic order and the charge gap in $Nd_2Ir_2O_7$ as the parent spin-orbit Mott state is suppressed via carrier doping.

Since our study was published three years ago, a large number of related studies on the pyrochlore iridates have been published. Hole-doping work has continued, though no doped single crystals have been reported to our knowledge. Single crystal samples would be best-suited to explore the phase phenomena associated with hole doping, including the possible quantum critical transition associated with the suppression of the antiferromagnetism. Since we were able to (accidentally) produce Sr-substituted single crystals with a $SrCl_2$ flux, it seems plausible that a flux with Ca cations would dope samples. It would be of interest, not only from a solid-state chemistry perspective, to see if the Ca content could be controlled during synthesis and/or homogenized post-growth.

There remain open questions about the low-energy excitations in the pyrochlore iridates, especially their evolution across the metal-insulator transition. Great progress has been made recently from optical studies (probing at the Γ point) e.g. Refs. [197] that built upon existing work. But the dispersion is of particular interest. To my knowledge, the highest-energy-resolution RIXS studies to date have had 25 meV resolution [55, 198], which is quite coarse and certainly unsuitable for low-T_N compounds like $Nd_2Ir_2O_7$. The record-breaking 6 meV resolution setup at the APS could possibly uncover more physics; see Section 2.2.3. In addition, it would be interesting to observe the evolution of the

excitations in a magnetic field. Currently-accessible static fields of 2 T [30] may be sufficient to polarize the 3-in-1-out phase for certain carrier dopings. Polycrystalline samples might be usable for such a study, but single crystals would be preferable.

Bibliography

[1] N. W. Ashcroft and N. D. Mermin. *Solid State Physics*. Saunders College Publishing, 1976.

[2] M. Imada, A. Fujimori, and Y. Tokura. Metal-Insulator Transitions. *Reviews of Modern Physics*, 70(4):1039, 1998. doi: 10.1103/RevModPhys.70.1039.

[3] D. I. Khomskii. *Transition Metal Compounds*. Cambridge University Press, 2014.

[4] D. I. Khomskii. *Basic Aspects of the Quantum Theory of Solids: Order and Elementary Excitations*. Cambridge University Press, 2010.

[5] P. W. Anderson. Antiferromagnetism: Theory of superexchange interaction. *Physical Review*, 79(2):350, 1950. doi: 10.1103/PhysRev.79.350.

[6] P. W. Anderson. An approximate quantum theory of the antiferromagnetic ground state. *Physical Review*, 86(5):694, 1952. doi: 10.1103/PhysRev.86.694.

[7] S. J. Blundell. *Magnetism in Condensed Matter*. Oxford University Press, 2001.

[8] C.-H. Yee and L. Balents. Phase separation in doped Mott insulators. *Physical Review X*, 5(2):021007, 2015. doi: 10.1103/PhysRevX.5.021007.

[9] C. Dhital, T. Hogan, W. Zhou, X. Chen, Z. Ren, M. Pokharel, Y. Okada, M. Heine, W. Tian, Z. Yamani, C. Opeil, J. S. Helton, J. W. Lynn, Z. Wang, V. Madhavan, and S. D. Wilson. Carrier localization and electronic phase separation in a doped spin-orbit-driven Mott phase in $Sr_3(Ir_{1-x}Ru_x)_2O_7$. *Nature Communications*, 5:1–7, 2014. doi: 10.1038/ncomms4377.

[10] J. L. Schmehr, T. R. Mion, Z. Porter, M. Aling, H. Cao, M. H. Upton, Z. Islam, R. H. He, R. Sensarma, N. Trivedi, and S. D. Wilson. Overdamped Antiferromagnetic Strange Metal State in Sr_3IrRuO_7. *Physical Review Letters*, 122(15):157201, 2019. doi: 10.1103/PhysRevLett.122.157201.

[11] W. Witczak-Krempa, G. Chen, Y. B. Kim, and L. Balents. Correlated quantum phenomena in the strong spin-orbit regime. *Annual Review of Condensed Matter Physics*, 5:57–82, 2014. doi: 10.1146/annurev-conmatphys-020911-125138.

[12] S. Boseggia. *Magnetic order and excitations in perovskite iridates studied with resonant X-ray scattering techniques*. PhD thesis, University College London, 2015.

[13] G. Jackeli and G. Khaliullin. Mott insulators in the strong spin-orbit coupling limit: from Heisenberg to a quantum compass and Kitaev models. *Physical Review Letters*, 102(1):017205, 2009. doi: 10.1103/PhysRevLetters102.017205.

[14] M. Moretti Sala, S. Boseggia, D. F. McMorrow, and G. Monaco. Resonant X-Ray Scattering and the J_{eff}=1/2 Electronic Ground State in Iridate Perovskites. *Physical Review Letters*, 112(2):026403, 2014. doi: 10.1103/PhysRevLetters112.026403.

[15] B. Kim, H. Jin, S. Moon, J.-Y. Kim, B.-G. Park, C. Leem, J. Yu, T. Noh, C. Kim, S.-J. Oh, J.-H. Park, V. Durairaj, G. Cao, and E. Rotenberg. Novel J_{eff}=1/2 Mott state induced by relativistic spin-orbit coupling in Sr_2IrO_4. *Physical Review Letters*, 101(7):076402, 2008. doi: 10.1103/PhysRevLett.101.076402.

[16] B. J. Kim, H. Ohsumi, T. Komesu, S. Sakai, T. Morita, H. Takagi, and T. Arima. Phase-Sensitive Observation of a Spin-Orbital Mott State in Sr_2IrO_4. *Science*, 323 (5919):1329–1332, 2009. doi: 10.1126/science.1167106.

[17] J. Kim, D. Casa, M. H. Upton, T. Gog, Y. J. Kim, J. F. Mitchell, M. van Veenendaal, M. Daghofer, J. van den Brink, G. Khaliullin, and B. J. Kim. Magnetic excitation spectra of Sr_2IrO_4 probed by resonant inelastic X-ray scattering: Establishing links to cuprate superconductors. *Physical Review Letters*, 108(17):177003, 2012. doi: 10.1103/PhysRevLett.108.177003.

[18] G. Cao, J. Bolivar, S. McCall, J. Crow, and R. Guertin. Weak ferromagnetism, metal-to-nonmetal transition, and negative differential resistivity in single-crystal Sr_2IrO_4. *Physical Review B*, 57(18):R11039, 1998. doi: 10.1103/PhysRevB.57.R11039.

[19] F. Ye, S. Chi, B. C. Chakoumakos, J. A. Fernandez-Baca, T. Qi, and G. Cao. Magnetic and crystal structures of Sr_2IrO_4: A neutron diffraction study. *Physical Review B*, 87(14):1–6, 2013. doi: 10.1103/PhysRevB.87.140406.

[20] D. Haskel, G. Fabbris, M. Zhernenkov, P. Kong, C. Jin, G. Cao, and M. van Veenendaal. Pressure tuning of the spin-orbit coupled ground state in Sr_2IrO_4. *Physical Review Letters*, 109(2):027204, 2012. doi: 10.1103/PhysRevLett.109.027204.

[21] J. K. Kawasaki, M. Uchida, H. Paik, D. G. Schlom, and K. M. Shen. Evolution of electronic correlations across the rutile, perovskite, and Ruddelsden-Popper iridates with octahedral connectivity. *Physical Review B*, 94(12):121104, 2016. doi: 10.1103/PhysRevB.94.121104.

[22] A. Revelli, M. Moretti Sala, G. Monaco, P. Becker, L. Bohatý, M. Hermanns, T. C. Koethe, T. Fröhlich, P. Warzanowski, T. Lorenz, S. V. Streltsov, P. H. van Loosdrecht, D. I. Khomskii, J. van den Brink, and M. Grüninger. Resonant inelastic X-ray incarnation of Young's double-slit experiment. *Science Advances*, 5 (1):eaav4020, 2019. doi: 10.1126/sciadv.aav4020.

[23] Y. Wang, R. Wang, J. Kim, M. H. Upton, D. Casa, T. Gog, G. Cao, G. Kotliar, M. P. Dean, and X. Liu. Direct Detection of Dimer Orbitals in $Ba_5AlIr_2O_{11}$. *Physical Review Letters*, 122(10):106401, 2019. doi: 10.1103/PhysRevLett.122.106401.

[24] S. Mohapatra, J. van den Brink, and A. Singh. Magnetic excitations in a three-orbital model for the strongly spin-orbit coupled iridates: Effect of mixing between the J=1/2 and 3/2 sectors. *Physical Review B*, 95(9):094435, 2017. doi: 10.1103/PhysRevB.95.094435.

[25] G. L. Stamokostas and G. A. Fiete. Mixing of $t_{2g}-e_g$ orbitals in $4d$ and $5d$ transition metal oxides. *Physical Review B*, 97(8):085150, 2018. doi: 10.1103/PhysRevB.97.085150.

[26] A. Kitaev. Anyons in an exactly solved model and beyond. *Annals of Physics*, 321 (1):2–111, 2006. doi: 10.1016/j.aop.2005.10.005.

[27] L. Savary and L. Balents. Quantum spin liquids: a review. *Reports on Progress in Physics*, 80(1):016502, 2016. doi: 10.1088/0034-4885/80/1/016502.

[28] J. G. Rau, E. K.-H. Lee, and H.-Y. Kee. Generic spin model for the honeycomb iridates beyond the Kitaev limit. *Physical Review Letters*, 112(7):077204, 2014. doi: 10.1103/PhysRevLetters112.077204.

[29] A. Revelli, M. Grüninger, et al. Fingerprints of Kitaev physics in the magnetic excitations of honeycomb iridates. *Physical Review Research*, 2(4):043094, 2020. doi: 10.1103/PhysRevResearch.2.043094.

[30] A. Ruiz, N. P. Breznay, M. Li, I. Rousochatzakis, A. Allen, I. Zinda, V. Nagarajan, G. Lopez, Z. Islam, M. H. Upton, J. Kim, A. H. Said, X.-R. Huang, T. Gog, D. Casa, R. J. Birgeneau, J. D. Koralek, J. G. Analytis, N. B. Perkins, and A. Frano. Magnon-spinon dichotomy in the Kitaev hyperhoneycomb β-Li_2IrO_3. *Physical Review B*, 103(18):184404, 2021. doi: 10.1103/PhysRevB.103.184404.

[31] S. Sachdev. Quantum criticality: Competing ground states in low dimensions. *Science*, 288(5465):475–480, 2000. doi: 10.1126/science.288.5465.475.

[32] S. Sachdev. *Quantum Phase Transitions*. Cambridge University Press, 2 edition, 2011.

[33] S. Sachdev and B. Keimer. Quantum criticality. *Physics Today*, 64(2):29–35, 2011. doi: 10.1063/1.3554314.

[34] B. Michon, C. Girod, S. Badoux, J. Kačmarčík, Q. Ma, M. Dragomir, H. Dabkowska, B. Gaulin, J.-S. Zhou, S. Pyon, T. Takayama, H. Takagi, S. Verret, N. Doiron-Leyraud, C. Marcenat, L. Taillefer, and T. Klein. Thermodynamic

signatures of quantum criticality in cuprate superconductors. *Nature*, 567(7747): 218–222, 2019. doi: 10.1038/s41586-019-0932-x.

[35] P. Gegenwart, Q. Si, and F. Steglich. Quantum criticality in heavy-fermion metals. *Nature Physics*, 4(3):186–197, 2008. doi: 10.1038/nphys892.

[36] Q. Si, R. Yu, and E. Abrahams. High-temperature superconductivity in iron pnictides and chalcogenides. *Nature Reviews Materials*, 1(4):1–15, 2016. doi: 10.1038/natrevmats.2016.17.

[37] C. Liu, P. Bourges, Y. Sidis, T. Xie, G. He, F. Bourdarot, S. Danilkin, H. Ghosh, S. Ghosh, X. Ma, S. Li, Y. Li, and H. Luo. Preferred Spin Excitations in the Bilayer Iron-Based Superconductor $CaK(Fe_{0.96}Ni_{0.04})_4As_4$ with Spin-Vortex Crystal Order. *Physical Review Letters*, 128(13):137003, 2022. doi: 10.1103/PhysRevLett.128.137003.

[38] A. J. Kim, H. O. Jeschke, P. Werner, and R. Valentí. **J**- Freezing and Hund's Rules in Spin-Orbit-Coupled Multiorbital Hubbard Models. *Physical Review Letters*, 118 (8):086401, 2017. doi: 10.1103/PhysRevLett.118.086401.

[39] P. Werner, E. Gull, M. Troyer, and A. J. Millis. Spin freezing transition and non-Fermi-liquid self-energy in a three-orbital model. *Physical Review Letters*, 101(16): 166405, 2008. doi: 10.1103/PhysRevLett.101.166405.

[40] S. Hoshino and P. Werner. Superconductivity from emerging magnetic moments. *Physical Review Letters*, 115(24):247001, 2015. doi: 10.1103/PhysRevLett.115.247001.

[41] J. Als-Nielsen and D. McMorrow. *Elements of Modern X-ray Physics*. John Wiley and Sons, second edition, 2011.

[42] G. L. Squires. *Introduction to the Theory of Thermal Neutron Scattering*. Cambridge University Press, 1978.

[43] S. H. Simon. *The Oxford Solid State Basics*. Oxford University Press, 2013.

[44] F. De Groot and A. Kotani. *Core Level Spectroscopy of Solids*. CRC Press, 2008.

[45] J. Clancy, H. Gretarsson, A. Lupascu, J. Sears, Z. Nie, M. Upton, J. Kim, Z. Islam, M. Uchida, D. Schlom, K. Shen, and Y.-J. Kim. Magnetic Excitations in Square Lattice Iridates: Contrast between Ba_2IrO_4 and Sr_2IrO_4. *arXiv preprint arXiv:2203.13102*, 2022.

[46] L. J. Ament, M. Van Veenendaal, T. P. Devereaux, J. P. Hill, and J. van den Brink. Resonant inelastic X-ray scattering studies of elementary excitations. *Reviews of Modern Physics*, 83(2):705, 2011. doi: 10.1103/RevModPhys.83.705.

[47] S. Di Matteo. Resonant X-ray diffraction: multipole interpretation. *Journal of Physics D: Applied Physics*, 45(16):163001, 2012. doi: 10.1088/0022-3727/45/16/163001.

[48] J. Luo, G. Trammell, and J. Hannon. Scattering operator for elastic and inelastic resonant X-ray scattering. *Physical Review Letters*, 71(2):287, 1993. doi: 10.1103/PhysRevLetters71.287.

[49] B. J. Kim and G. Khaliullin. Resonant inelastic X-ray scattering operators for t_{2g} orbital systems. *Physical Review B*, 96(8):085108, 2017. doi: 10.1103/PhysRevB.96.085108.

[50] A. Jain, M. Krautloher, J. Porras, G. H. Ryu, D. P. Chen, D. L. Abernathy, J. T. Park, A. Ivanov, J. Chaloupka, G. Khaliullin, B. Keimer, and B. J. Kim. Higgs mode and its decay in a two-dimensional antiferromagnet. *Nature Physics*, 13(7):633–637, 2017. doi: 10.1038/nphys4077.

[51] A. Akbari and G. Khaliullin. Magnetic excitations in a spin-orbit-coupled d^4 Mott insulator on the square lattice. *Physical Review B*, 90(3):035137, 2014. doi: 10.1103/PhysRevB.90.035137.

[52] M. Noguchi, A. Nakazawa, S. Oka, T. Arima, Y. Wakabayashi, H. Nakao, and Y. Murakami. Synchrotron X-ray-diffraction study of orbital ordering in YVO_3. *Physical Review B*, 62(14):R9271, 2000. doi: 10.1103/PhysRevB.62.R9271.

[53] V. E. Dmitrienko, K. Ishida, A. Kirfel, and E. N. Ovchinnikova. Polarization anisotropy of X-ray atomic factors and forbidden resonant reflections. *Acta Crystallographica*, A61(5):481–493, 2005. doi: 10.1107/S0108767305018209.

[54] D. H. Templeton and L. K. Templeton. Polarized X-ray absorption and double refraction in vanadyl bisacetylacetonate. *Acta Crystallographica*, A36(2):237–241, 1980. doi: 10.1107/S0567739480000472.

[55] C. Donnerer, M. Rahn, M. Moretti Sala, J. Vale, D. Pincini, J. Strempfer, M. Krisch, D. Prabhakaran, A. Boothroyd, and D. McMorrow. All-in-all-out magnetic order and propagating spin waves in $Sm_2Ir_2O_7$. *Physical Review Letters*, 117(3):037201, 2016. doi: 10.1103/PhysRevLetters117.037201.

[56] R. P. Feynman, R. B. Leighton, and M. Sands. *The Feynman Lectures on Physics: The New Millennium Edition*, volume 3. Basic Books, 2011.

[57] Y. Ma and M. Blume. Interference of fluorescence X-rays and coherent excitation of core levels. *Review of Scientific Instruments*, 66(2):1543, 1995. doi: 10.1063/1.1145903.

[58] J. W. Kim, Y. Choi, J. Kim, J. F. Mitchell, G. Jackeli, M. Daghofer, J. van den Brink, G. Khaliullin, and B. J. Kim. Dimensionality driven spin-flop transition in layered iridates. *Physical Review Letters*, 109(3):037204, 2012. doi: 10.1103/PhysRevLett.109.037204.

[59] D. Mazzone, Y. Shen, H. Suwa, G. Fabbris, J. Yang, S.-S. Zhang, H. Miao, J. Sears, K. Jia, Y. Shi, M. Upton, D. Casa, X. Liu, J. Liu, C. Batista, and M. Dean. Antiferromagnetic excitonic insulator state in $Sr_3Ir_2O_7$. *Nature Communications*, 13(1):1–8, 2022. doi: 10.1038/s41467-022-28207-w.

[60] X. Chen, J. L. Schmehr, Z. Islam, Z. Porter, E. Zoghlin, K. Finkelstein, J. P. Ruff, and S. D. Wilson. Unidirectional spin density wave state in metallic $(Sr_{1-x}La_x)_2IrO_4$. *Nature Communications*, 9(1):1–7, 2018. doi: 10.1038/s41467-017-02647-1.

[61] P. M. Sarte, C. Stock, B. R. Ortiz, K. H. Hong, and S. D. Wilson. Van Vleck excitons in Ca_2RuO_4. *Physical Review B*, 102:245119, 2020. doi: 10.1103/PhysRevB.102.245119.

[62] Gog, Thomas and Casa, Diego M and Knopp, Jonathan and Kim, Jungho and Upton, Mary H and Krakora, Richard and Jaski, Alan and Said, Ayman and Yavaş, Hasan and Gretarsson, Hlynur and Huang, Xian Rong. Performance of quartz-and sapphire-based double-crystal high-resolution (∼10 meV) RIXS monochromators under varying power loads. *Journal of synchrotron radiation*, 25(4):1030–1035, 2018. doi: 10.1107/S1600577518005945.

[63] Shvyd'ko, Yu V and Hill, JP and Burns, CA and Coburn, DS and Brajuskovic, B and Casa, D and Goetze, K and Gog, T and Khachatryan, R and Kim, J-H and others. MERIX Next generation medium energy resolution inelastic X-ray scattering instrument at the APS. *Journal of Electron Spectroscopy and Related Phenomena*, 188:140–149, 2013. doi: 10.1016/j.elspec.2012.09.003.

[64] A. H. Said, T. Gog, M. Wieczorek, X. Huang, D. Casa, E. Kasman, R. Divan, and J. H. Kim. High-energy-resolution diced spherical quartz analyzers for resonant inelastic X-ray scattering. *Journal of Synchrotron Radiation*, 25(2):373–377, 2018. doi: 10.1107/S1600577517018185.

[65] J. Kim, D. Casa, A. Said, R. Krakora, B. J. Kim, E. Kasman, X. Huang, and T. Gog. Quartz-based flat-crystal resonant inelastic X-ray scattering spectrometer with sub-10 meV energy resolution. *Scientific Reports*, 8(1):1–9, 2018. doi: 10.1038/s41598-018-20396-z.

[66] S. W. Lovesey. *Theory of Neutron Scattering from Condensed Matter*, volume 2. Oxford University Press, 1986.

[67] M. Braden, Y. Sidis, P. Bourges, P. Pfeuty, J. Kulda, Z. Mao, and Y. Maeno. Inelastic neutron scattering study of magnetic excitations in Sr_2RuO_4. *Physical Review B*, 66(6):064522, 2002. doi: 10.1103/PhysRevB.66.064522.

[68] Z. Porter, E. Zoghlin, J. L. Schmehr, and S. D. Wilson. Crystal growth of $Sr_2Ir_xRu_{1-x}O_4$ for x$\leq$0.4. *Journal of Crystal Growth*, 578:126432, 2022. doi: 10.1016/j.jcrysgro.2021.126432.

[69] K. Harada, Y. Teramoto, T. Usui, K. Itaka, T. Fujii, T. Noji, H. Taniguchi, M. Matsukawa, H. Ishikawa, K. Kindo, D. S. Dessau, and T. Watanabe. Revised phase diagram of the high-T_c cuprate superconductor Pb-doped $Bi_2Sr_2CaCu_2O_{8+\delta}$ revealed by anisotropic transport measurements. *Physical Review B*, 105(8):085131, 2022. doi: 10.1103/PhysRevB.105.085131.

[70] P. A. Lee, N. Nagaosa, and X.-G. Wen. Doping a Mott insulator: Physics of high-temperature superconductivity. *Reviews of Modern Physics*, 78(1):17, 2006. doi: 10.1103/RevModPhys.78.17.

[71] R. J. Cava, B. Batlogg, K. Kiyono, H. Takagi, J. J. Krajewski, W. F. Peck, L. W. Rupp, and C. H. Chen. Localized-to-itinerant electron transition in $Sr_2Ir_{1-x}Ru_xO_4$. *Physical Review B*, 49(17):11890–11894, 1994. doi: 10.1103/PhysRevB.49.11890.

[72] Y. Sidis, M. Braden, P. Bourges, B. Hennion, S. Nishi Zaki, Y. Maeno, and Y. Mori. Evidence for incommensurate spin fluctuations in Sr_2RuO_4. *Physical Review Letters*, 83(16):3320–3323, 1999. doi: 10.1103/PhysRevLetters83.3320.

[73] F. Servant, S. Raymond, B. Fåk, P. Lejay, and J. Flouquet. Two-dimensional spin fluctuations in Sr_2RuO_4. *Solid State Communications*, 116(9):489–493, 2000. doi: 10.1016/S0038-1098(00)00364-1.

[74] A. Mackenzie, R. Haselwimmer, A. Tyler, G. Lonzarich, Y. Mori, S. Nishizaki, and Y. Maeno. Extremely strong dependence of superconductivity on disorder in Sr_2RuO_4. *Physical Review Letters*, 80(1):161, 1998. doi: 10.1103/PhysRevLetters80.161.

[75] J. E. Ortmann, J. Y. Liu, J. Hu, M. Zhu, J. Peng, M. Matsuda, X. Ke, and Z. Q. Mao. Competition between antiferromagnetism and ferromagnetism in Sr_2RuO_4 probed by Mn and Co doping. *Scientific Reports*, 3:1–7, 2013. doi: 10.1038/srep02950.

[76] M. Zhu, K. V. Shanavas, Y. Wang, T. Zou, W. F. Sun, W. Tian, V. O. Garlea, A. Podlesnyak, M. Matsuda, M. B. Stone, D. Keavney, Z. Q. Mao, D. J. Singh, and X. Ke. Non-Fermi surface nesting driven commensurate magnetic ordering in Fe-doped Sr_2RuO_4. *Physical Review B*, 95(5):2–7, 2017. doi: 10.1103/PhysRevB.95.054413.

[77] P. Battle, J. Gore, and J. Frost. Magnetic properties of $BaRu_{1-x}Rh_xO_3$ and $Sr_2Ru_{1-x}Rh_xO_4$. *Physical Review B*, 51(13):8624, 1995. doi: 10.1103/PhysRevB.51.8624.

[78] M. E. Barber. *Uniaxial Stress Technique and Investigations of Correlated Electron Systems*. Springer, 2018. doi: 10.1007/978-3-319-93973-5.

[79] J. Kwon, B. S. Kim, M. K. Kim, J. Denlinger, A. Bostwick, E. Rotenberg, N. Lee, H. Y. Choi, J. Y. Moon, Y. J. Choi, J. Mun, M. Kim, Y. Yoshida, W. Kyung, and C. Kim. Spin-orbit coupling driven orbital-selective doping effect in $Sr_2Ir_xRu_{1-x}O_4$. *Physical Review B*, 103(8):L081104, 2021. doi: 10.1103/PhysRevB.103.L081104.

[80] K. Shen, N. Kikugawa, C. Bergemann, L. Balicas, F. Baumberger, W. Meevasana, N. Ingle, Y. Maeno, Z.-X. Shen, and A. Mackenzie. Evolution of the Fermi surface and quasiparticle renormalization through a van Hove singularity in $Sr_{2-y}La_yRuO_4$. *Physical Review Letters*, 99(18):187001, 2007. doi: 10.1103/PhysRevLett.99.187001.

[81] N. Kikugawa, C. Bergemann, A. P. Mackenzie, and Y. Maeno. Band-selective modification of the magnetic fluctuations in Sr_2RuO_4: A study of substitution effects. *Physical Review B*, 70(13):134520, 2004. doi: 10.1103/PhysRevB.70.134520.

[82] B. Burganov, C. Adamo, A. Mulder, M. Uchida, P. King, J. Harter, D. Shai, A. Gibbs, A. Mackenzie, R. Uecker, M. Bruetzam, M. Beasley, C. Fennie, D. Schlom, and K. Shen. Strain control of fermiology and many-body interactions in two-dimensional ruthenates. *Physical Review Letters*, 116(19):197003, 2016. doi: 10.1103/PhysRevLetters116.197003.

[83] T. Imai, A. W. Hunt, K. R. Thurber, and F. C. Chou. ^{17}O NMR evidence for orbital dependent ferromagnetic correlations in Sr_2RuO_4. *Physical Review Letters*, 81(14):3006–3009, 1998. doi: 10.1103/PhysRevLetters81.3006.

[84] M. Minakata and Y. Maeno. Magnetic ordering in Sr_2RuO_4 induced by nonmagnetic impurities. *Physical Review B*, 63(18):180504, 2001. doi: 10.1103/PhysRevB.63.180504.

[85] M. Braden, O. Friedt, Y. Sidis, P. Bourges, M. Minakata, and Y. Maeno. Incommensurate Magnetic Ordering in $Sr_2Ru_{1-x}Ti_xO_4$. *Physical Review Letters*, 88(19):4, 2002. doi: 10.1103/PhysRevLett.88.197002.

[86] N. Kikugawa and Y. Maeno. Non-Fermi-Liquid Behavior in Sr_2RuO_4 with Nonmagnetic Impurities. *Physical Review Letters*, 89(11):117001, 2002. doi: 10.1103/PhysRevLett.89.117001.

[87] K. Pucher, J. Hemberger, F. Mayr, V. Fritsch, A. Loidl, E.-W. Scheidt, S. Klimm, R. Horny, S. Horn, S. G. Ebbinghaus, A. Reller, and R. Cava. Transport, magnetic, thermodynamic, and optical properties in Ti-doped Sr_2RuO_4. *Physical Review B*, 65(10):104523, 2002. doi: 10.1103/PhysRevB.65.104523.

[88] J. L. Schmehr, M. Aling, E. Zoghlin, and S. D. Wilson. High-pressure laser floating zone furnace. *Review of Scientific Instruments*, 90(4):043906, 2019. doi: 10.1063/1.5085327.

[89] J. S. Bobowski, N. Kikugawa, T. Miyoshi, H. Suwa, H.-s. Xu, S. Yonezawa, D. A. Sokolov, A. P. Mackenzie, and Y. Maeno. Improved Single-Crystal Growth of Sr_2RuO_4. *Condensed Matter*, 4(1):6, 2019. doi: 10.3390/condmat4010006.

[90] C. McDaniel and S. Schneider. Phase relations in the SrO-IrO_2-Ir system in air. *Journal of Research of the National Bureau of Standards*, 75A(3):185, 1971. doi: 10.6028/jres.075A.019.

[91] Z. Q. Mao, Y. Maenoab, and H. Fukazawa. Crystal growth of Sr_2RuO_4. *Materials Research Bulletin*, 35(11):1813–1824, 2000. doi: 10.1016/S0025-5408(00)00378-0.

[92] F. Lichtenberg, A. Catana, J. Mannhart, and D. G. Schlom. Sr_2RuO_4 : A metallic substrate for the epitaxial growth of $YBa_2Cu_3O_{7-\delta}$. *Applied Physics Letters*, 60(9):1138–1140, 1992. doi: 10.1063/1.106432.

[93] N. Kikugawa, A. P. Mackenzie, and Y. Maeno. Effects of in-plane impurity substitution in Sr_2RuO_4. *Journal of the Physical Society of Japan*, 72(2):237–240, 2003. doi: 10.1143/JPSJ.72.237.

[94] Q. Zhao, J.-H. Sim, Z. Zhang, H. Su, F. Han, Q. Zhang, B. Tian, Q. Xu, M.-J. Han, C.-G. Duan, and J. F. Mitchell. Tetrahedral coordination and low-spin configuration in a 5*d* oxide. *Physical Review Materials*, 3(6):063607, 2019. doi: 10.1103/PhysRevMaterials.3.063607.

[95] A. A. Coelho. `TOPAS` and `TOPAS-Academic`: an optimization program integrating computer algebra and crystallographic objects written in `C++`. *Journal of Applied Crystallography*, 51(1):210–218, 2018. doi: 10.1107/S1600576718000183.

[96] C. McDaniel and S. Schneider. Phase relations in the Ru-Ir-O_2 system in air. *Journal of Research of the National Bureau of Standards*, 73A(2):213, 1969. doi: 10.6028/jres.073a.019.

[97] A. Kanbayasi. Magnetic properties of $SrRuO_3$ single crystal. *Journal of the Physical Society of Japan*, 41(6):1876–1878, 1976. doi: 10.1143/JPSJ.41.1876.

[98] A. Biswas, Y. W. Lee, and Y. H. Jeong. Electronic and magnetic transitions in perovskite $SrRu_{1-x}Ir_xO_3$ thin films. *Journal of Applied Physics*, 118(9):095303, 2015. doi: 10.1063/1.4929966.

[99] M. Hatatani and T. Moriya. Ferromagnetic spin fluctuations in two-dimensional metals. *Journal of the Physical Society of Japan*, 64(9):3434–3441, 1995. doi: 10.1143/jpsj.64.3434.

[100] M. Hatatani, O. Narikiyo, and K. Miyake. A theory of uniform spin susceptibility around the antiferromagnetic quantum critical point. *Journal of the Physical Society of Japan*, 67(12):4002–4005, 1998. doi: 10.1143/JPSJ.67.4002.

[101] N. Shirakawa, K. Murata, Y. Nishihara, S. Nishizaki, Y. Maeno, T. Fujita, J. G. Bednorz, F. Lichtenberg, and N. Hamada. Novel Hall-Coefficient Behavior in Superconducting Sr_2RuO_4. *Journal of the Physical Society of Japan*, 64(4):1072–1075, 1995. doi: 10.1143/JPSJ.64.1072.

[102] A. Mackenzie, N. Hussey, A. Diver, S. Julian, Y. Maeno, S. Nishizaki, and T. Fujita. Hall effect in the two-dimensional metal Sr_2RuO_4. *Physical Review B*, 54(10):7425, 1996. doi: 10.1103/PhysRevB.54.7425.

[103] J. Wu, H. P. Nair, A. T. Bollinger, X. He, I. Robinson, N. J. Schreiber, K. M. Shen, D. G. Schlom, and I. Božović. Electronic nematicity in Sr_2RuO_4. *Proceedings of the National Academy of Sciences*, 117(20):10654–10659, 2020. doi: 10.1073/pnas.1921713117.

[104] F. Herman, J. Buhmann, M. H. Fischer, and M. Sigrist. Deviation from Fermi-liquid transport behavior in the vicinity of a van Hove singularity. *Physical Review B*, 99(18):184107, 2019. doi: 10.1103/PhysRevB.99.184107.

[105] N. Kikugawa, A. P. Mackenzie, C. Bergemann, and Y. Maeno. Low-temperature Hall effect in substituted Sr_2RuO_4. *Physical Review B*, 70(17):174501, 2004. doi: 10.1103/PhysRevB.70.174501.

[106] M. Braden, W. Reichardt, Y. Sidis, Z. Mao, and Y. Maeno. Lattice dynamics and electron-phonon coupling in Sr_2RuO_4: Inelastic neutron scattering and shell-model calculations. *Physical Review B*, 76(1):014505, 2007. doi: 10.1103/PhysRevB.76.014505.

[107] I. Anderson, P. Brown, J. Carpenter, G. Lander, R. Pynn, J. Rowe, O. Schärpf, V. Sears, and B. Willis. *International Tables for Crystallography*. John Wiley and Sons, Inc., 2006.

[108] A. Gukasov, M. Braden, R. Papoular, S. Nakatsuji, and Y. Maeno. Anomalous Spin-Density Distribution on Oxygen and Ru in $Ca_{1.5}Sr_{0.5}RuO_4$: Polarized Neutron Diffraction Study. *Physical Review Letters*, 89(8):087202, 2002. doi: 10.1103/PhysRevLett.89.087202.

[109] N. G. Parkinson, P. D. Hatton, J. A. Howard, C. Ritter, F. Z. Chien, and M.-K. Wu. Crystal and magnetic structures of $A_2YRu_{1-x}Cu_xO_6$ with A= Sr,Ba and x= 0.05 to 0.15. *Journal of Materials Chemistry*, 13(6):1468–1474, 2003. doi: 10.1039/B212123A.

[110] V. Brouet, P. Foulquier, A. Louat, F. Bertran, P. Le Fèvre, J. E. Rault, and D. Colson. Origin of the different electronic structure of Rh-and Ru-doped Sr_2IrO_4. *Physical Review B*, 104(12):L121104, 2021. doi: 10.1103/PhysRevB.104.L121104.

[111] M. Vališka, J. Pospíšil, M. Diviš, J. Prokleška, V. Sechovskỳ, and M. M. Abd-Elmeguid. Evolution of ferromagnetic and non-Fermi-liquid states with doping: The case of Ru-doped UCoGe. *Physical Review B*, 92(4):045114, 2015. doi: 10.1103/PhysRevB.92.045114.

[112] S.-I. Fujimori, Y. Takeda, T. Okane, Y. Saitoh, A. Fujimori, H. Yamagami, Y. Haga, E. Yamamoto, and Y. Ōnuki. Electronic structures of uranium compounds studied by soft X-ray photoelectron spectroscopy. *Journal of the Physical Society of Japan*, 85(6):062001, 2016. doi: 10.7566/JPSJ.85.062001.

[113] L. Ye, S. Fang, M. G. Kang, J. Kaufmann, Y. Lee, J. Denlinger, C. Jozwiak, A. Bostwick, E. Rotenberg, E. Kaxiras, D. C. Bell, O. Janson, R. Comin, and J. G. Checkelsky. A flat band-induced correlated kagome metal. *arXiv preprint arXiv:2106.10824*, 2021.

[114] M. Y. Jeong, S. H. Chang, H. J. Lee, J.-H. Sim, K. J. Lee, E. Janod, L. Cario, A. Said, W. Bi, P. Werner, A. Go, J. Kim, and M. J. Han. $J_{\mathrm{e}}\mathrm{ff} = 3/2$ metallic phase and unconventional superconductivity in $GaTa_4Se_8$. *Physical Review B*, 103 (8):L081112, 2021. doi: 10.1103/PhysRevB.103.L081112.

[115] H. Deng, J. Zhang, M. Y. Jeong, D. Wang, Q. Hu, S. Zhang, R. Sereika, T. Nakagawa, B. Chen, X. Yin, H. Xiao, X. Hong, J. Ren, M. J. Han, J. Chang, H. Weng, Y. Ding, H.-Q. Lin, and H.-K. Mao. Metallization of quantum material $GaTa_4Se_8$ at high pressure. *The Journal of Physical Chemistry Letters*, 12(23):5601–5607, 2021. doi: 10.1021/acs.jpcLetters1c01069.

[116] M. Oda, T. Nakano, Y. Kamada, and M. Ido. Electronic states of doped holes and magnetic properties in $La_{2-x}M_xCuO_4$ (M= Sr, Ba). *Physica C: Superconductivity*, 183(4-6):234–240, 1991. doi: 10.1016/0921-4534(91)90567-I.

[117] C. Kaiser, W. Huang, S. Komiya, N. Hussey, T. Adachi, Y. Tanabe, Y. Koike, and J. Sonier. Curie-like paramagnetism due to incomplete Zhang-Rice singlet formation in $La_{2-x}Sr_xCuO_4$. *Physical Review B*, 86(5):054522, 2012. doi: 10.1103/PhysRevB.86.054522.

[118] H. Miao, G. Fabbris, R. Koch, D. Mazzone, C. Nelson, R. Acevedo-Esteves, G. Gu, Y. Li, T. Yilimaz, K. Kaznatcheev, E. Vescovo, M. Oda, T. Kurosawa, N. Momono, T. Assefa, I. Robinson, E. Bozin, J. Tranquada, P. Johnson, and M. Dean. Charge density waves in cuprate superconductors beyond the critical doping. *npj Quantum Materials*, 6(1):1–6, 2021. doi: 10.1038/s41535-021-00327-4.

[119] G. Ahn, J. Schmehr, Z. Porter, S. Wilson, and S. Moon. Doping and temperature evolutions of optical response of $Sr_3(Ir_{1-x}Ru_x)_2O_7$. *Scientific Reports*, 10(1):1–9, 2020. doi: 10.1038/s41598-020-79263-5.

[120] Y. V. Sushko, B. DeHarak, G. Cao, G. Shaw, D. Powell, and J. Brill. Hydrostatic pressure effects on the magnetic susceptibility of ruthenium oxide $Sr_3Ru_2O_7$: evidence for pressure-enhanced antiferromagnetic instability. *Solid State Communications*, 130(5):341–346, 2004. doi: 10.1016/j.ssc.2004.02.010.

[121] J. Hooper, M. Fang, M. Zhou, D. Fobes, N. Dang, Z. Mao, C. Feng, Z. Xu, M. Yu, C. O'Connor, G. Xu, N. Andersen, and M. Salamon. Competing magnetic fluctuations in $Sr_3Ru_2O_7$ probed by Ti doping. *Physical Review B*, 75(6):060403, 2007. doi: 10.1103/PhysRevB.75.060403.

[122] T. Hogan, L. Bjaalie, L. Zhao, C. Belvin, X. Wang, C. G. Van de Walle, D. Hsieh, and S. D. Wilson. Structural investigation of the bilayer iridate $Sr_3Ir_2O_7$. *Physical Review B*, 93:134110, 2016. doi: 10.1103/PhysRevB.93.134110.

[123] S. Grigera, R. Perry, A. Schofield, M. Chiao, S. Julian, G. Lonzarich, S. Ikeda, Y. Maeno, A. Millis, and A. Mackenzie. Magnetic field-tuned quantum criticality in the metallic ruthenate $Sr_3Ru_2O_7$. *Science*, 294(5541):329–332, 2001. doi: 10.1126/science.1063539.

[124] A. Rost, S. A. Grigera, J. Bruin, R. Perry, D. Tian, S. Raghu, S. A. Kivelson, and A. Mackenzie. Thermodynamics of phase formation in the quantum critical metal $Sr_3Ru_2O_7$. *Proceedings of the National Academy of Sciences*, 108(40):16549–16553, 2011. doi: 10.1073/pnas.1112775108.

[125] C. Lester, S. Ramos, R. Perry, T. Croft, R. Bewley, T. Guidi, P. Manuel, D. Khalyavin, E. Forgan, and S. Hayden. Field-tunable spin-density-wave phases in $Sr_3Ru_2O_7$. *Nature Materials*, 14(4):373–378, 2015. doi: 10.1038/nmat4181.

[126] D. Sun, A. Rost, R. Perry, A. Mackenzie, and M. Brando. Low temperature thermodynamic investigation of the phase diagram of $Sr_3Ru_2O_7$. *Physical Review B*, 97(11):115101, 2018. doi: 10.1103/PhysRevB.97.115101.

[127] C. Lester, S. Ramos, R. Perry, T. Croft, M. Laver, R. Bewley, T. Guidi, A. Hiess, A. Wildes, E. Forgan, and S. Hayden. Magnetic-field-controlled spin fluctuations and quantum criticality in $Sr_3Ru_2O_7$. *Nature Communications*, 12(1):1–6, 2021. doi: 10.1038/s41467-021-26068-3.

[128] Z. Wang, Y. Okada, J. ONeal, W. Zhou, D. Walkup, C. Dhital, T. Hogan, P. Clancy, Y.-J. Kim, Y. Hu, L. Santos, S. Wilson, N. Trivedi, and V. Madhavan. Disorder induced power-law gaps in an insulator-metal Mott transition. *Proceedings of the National Academy of Sciences*, 115(44):11198–11202, 2018. doi: 10.1073/pnas.1808056115.

[129] D. Heidarian and N. Trivedi. Inhomogeneous metallic phase in a disordered Mott insulator in two dimensions. *Physical Review Letters*, 93(12):126401, 2004. doi: 10.1103/PhysRevLett.93.126401.

[130] A. W. Sandvik. Quantum criticality and percolation in dimer-diluted two-dimensional antiferromagnets. *Physical Review Letters*, 96(20):207201, 2006. doi: 10.1103/PhysRevLett.96.207201.

[131] Y. Cao, X. Liu, W. Xu, W. G. Yin, D. Meyers, J. Kim, D. Casa, M. H. Upton, T. Gog, T. Berlijn, G. Alvarez, S. Yuan, J. Terzic, J. M. Tranquada, J. P. Hill, G. Cao, R. M. Konik, and M. P. M. Dean. Giant spin gap and magnon localization in the disordered Heisenberg antiferromagnet $Sr_2Ir_{1-x}Ru_xO_4$. *Physical Review B*, 95(12):121103, 2017. doi: 10.1103/PhysRevB.95.121103.

[132] X. Chen, Y. He, S. Wu, Y. Song, D. Yuan, E. Bourret-Courchesne, J. P. Ruff, Z. Islam, A. Frano, and R. J. Birgeneau. Structural and magnetic transitions in the planar antiferromagnet $Ba_4Ir_3O_{10}$. *Physical Review B*, 103(22):224420, 2021. doi: 10.1103/PhysRevB.103.224420.

[133] J. P. Clancy, H. Gretarsson, E. K. Lee, D. Tian, J. Kim, M. H. Upton, D. Casa, T. Gog, Z. Islam, B. G. Jeon, K. H. Kim, S. Desgreniers, Y. B. Kim, S. J. Julian, and Y. J. Kim. X-ray scattering study of pyrochlore iridates: Crystal structure, electronic, and magnetic excitations. *Physical Review B*, 94(2):024408, 2016. doi: 10.1103/PhysRevB.94.024408.

[134] A. Paramekanti, D. J. Singh, B. Yuan, D. Casa, A. Said, Y. J. Kim, and A. D. Christianson. Spin-orbit coupled systems in the atomic limit: Rhenates, osmates, iridates. *Physical Review B*, 97(23):235119, 2018. doi: 10.1103/PhysRevB.97.235119.

[135] H. Gretarsson, H. Suzuki, H. Kim, K. Ueda, M. Krautloher, B. J. Kim, H. Yava, G. Khaliullin, and B. Keimer. Observation of spin-orbit excitations and Hund's multiplets in Ca_2RuO_4. *Physical Review B*, 100(4):045123, 2019. doi: 10.1103/PhysRevB.100.045123.

[136] J. Kim, A. H. Said, D. Casa, M. H. Upton, T. Gog, M. Daghofer, G. Jackeli, J. van den Brink, G. Khaliullin, and B. J. Kim. Large spin-wave energy gap in the bilayer iridate $Sr_3Ir_2O_7$: Evidence for enhanced dipolar interactions near the

Mott metal-insulator transition. *Physical Review Letters*, 109(15):157402, 2012. doi: 10.1103/PhysRevLett.109.157402.

[137] S. Calder, J. Vale, N. Bogdanov, X. Liu, C. Donnerer, M. Upton, D. Casa, A. Said, M. Lumsden, Z. Zhao, J.-Q. Yan, D. Mandrus, S. Nishimoto, J. van den Brink, J. Hill, D. McMorrow, and A. Christianson. Spin-orbit-driven magnetic structure and excitation in the $5d$ pyrochlore $Cd_2Os_2O_7$. *Nature Communications*, 7(1):1–8, 2016. doi: 10.1038/ncomms11651.

[138] H. Takahashi, H. Suzuki, J. Bertinshaw, S. Bette, C. Mühle, J. Nuss, R. Dinnebier, A. Yaresko, G. Khaliullin, H. Gretarsson, T. Takayama, H. Takagi, and B. Keimer. Nonmagnetic $J = 0$ State and Spin-Orbit Excitations in K_2RuCl_6. *Physical Review Letters*, 127(22):227201, 2021. doi: 10.1103/PhysRevLett.127.227201.

[139] J. Bertinshaw, S. Mayer, F.-U. Dill, H. Suzuki, O. Leupold, A. Jafari, I. Sergueev, M. Spiwek, A. Said, E. Kasman, X. Huang, B. Keimer, and H. Gretarsson. IRIXS Spectrograph: an ultra high-resolution spectrometer for tender RIXS. *Journal of Synchrotron Radiation*, 28(4), 2021. doi: 10.1107/S1600577521003805.

[140] C. Peterson, M. W. Swift, Z. Porter, R. J. Clément, G. Wu, G. H. Ahn, S. J. Moon, B. C. Chakoumakos, J. P. C. Ruff, H. Cao, C. Van de Walle, and S. D. Wilson. $Sr_3Ir_2O_7F_2$: Topochemical conversion of a relativistic Mott state into a spin-orbit driven band insulator. *Physical Review B*, 98:155128, 2018. doi: 10.1103/PhysRevB.98.155128.

[141] G. Khaliullin. Excitonic magnetism in Van Vleck-type d^4 Mott insulators. *Physical Review Letters*, 111(19):197201, 2013. doi: 10.1103/PhysRevLett.111.197201.

[142] O. N. Meetei, W. S. Cole, M. Randeria, and N. Trivedi. Novel magnetic state in d^4 Mott insulators. *Physical Review B*, 91(5):054412, 2015. doi: 10.1103/PhysRevB.91.054412.

[143] A. Abragam and B. Bleaney. *Electron Paramagnetic Resonance of Transition Ions*. Oxford University Press, 2012.

[144] A. Louat, F. Bert, L. Serrier-Garcia, F. Bertran, P. Le Fèvre, J. Rault, and V. Brouet. Formation of an incoherent metallic state in Rh-doped Sr_2IrO_4. *Physical Review B*, 97(16):161109, 2018. doi: 10.1103/PhysRevB.97.161109.

[145] J. Clancy, A. Lupascu, H. Gretarsson, Z. Islam, Y. Hu, D. Casa, C. Nelson, S. LaMarra, G. Cao, and Y.-J. Kim. Dilute magnetism and spin-orbital percolation effects in $Sr_2Ir_{1-x}Rh_xO_4$. *Physical Review B*, 89(5):054409, 2014. doi: 10.1103/PhysRevB.89.054409.

[146] J. Nelson, C. Parzyck, B. Faeth, J. Kawasaki, D. Schlom, and K. Shen. Mott gap collapse in lightly hole-doped $Sr_{2-x}K_xIrO_4$. *Nature Communications*, 11(1):1–6, 2020. doi: 10.1038/s41467-020-16425-z.

[147] C. G. Fatuzzo, M. Dantz, S. Fatale, P. Olalde-Velasco, N. E. Shaik, B. Dalla Piazza, S. Toth, J. Pelliciari, R. Fittipaldi, A. Vecchione, N. Kikugawa, J. S. Brooks, H. M. Rønnow, M. Grioni, C. Rüegg, T. Schmitt, and J. Chang. Spin-orbit-induced orbital excitations in Sr_2RuO_4 and Ca_2RuO_4: A resonant inelastic X-ray scattering study. *Physical Review B*, 91(15):155104, 2015. doi: 10.1103/PhysRevB.91.155104.

[148] S. Nakatsuji, S.-i. Ikeda, and Y. Maeno. Ca_2RuO_4: New Mott Insulators of Layered Ruthenate. *Journal of the Physical Society of Japan*, 66(7):1868–1871, 1997. doi: 10.1143/JPSJ.66.1868.

[149] X. Li, H. Ning, O. Mehio, H. Zhao, M.-C. Lee, K. Kim, F. Nakamura, Y. Maeno, G. Cao, and D. Hsieh. Keldysh Space Control of Charge Dynamics in a Strongly Driven Mott Insulator. *Physical Review Letters*, 128(18):187402, 2022. doi: 10.1103/PhysRevLett.128.187402.

[150] M. Kusch, V. M. Katukuri, N. A. Bogdanov, B. Büchner, T. Dey, D. V. Efremov, J. E. Hamann-Borrero, B. H. Kim, M. Krisch, A. Maljuk, M. Moretti Sala, S. Wurmehl, G. Aslan-Cansever, M. Sturza, L. Hozoi, J. van den Brink, and J. Geck. Observation of heavy spin-orbit excitons propagating in a nonmagnetic background: The case of $(Ba,Sr)_2YIrO_6$. *Physical Review B*, 97(6):064421, 2018. doi: 10.1103/PhysRevB.97.064421.

[151] N. R. Davies, C. V. Topping, H. Jacobsen, A. J. Princep, F. K. Kirschner, M. C. Rahn, M. Bristow, J. G. Vale, I. Da Silva, P. J. Baker, C. J. Sahle, Y. F. Guo, D. Y. Yan, Y. G. Shi, S. J. Blundell, D. F. McMorrow, and A. T. Boothroyd. Evidence for a J_{eff}=0 ground state and defect-induced spin glass behavior in the pyrochlore osmate $Y_2Os_2O_7$. *Physical Review B*, 99(17):174442, 2019. doi: 10.1103/PhysRevB.99.174442.

[152] J. P. Clancy, H. Gretarsson, M. H. Upton, J. Kim, G. Cao, and Y. J. Kim. Magnetic excitations in hole-doped Sr_2IrO_4: Comparison with electron-doped cuprates. *Physical Review B*, 100(10):104414, 2019. doi: 10.1103/PhysRevB.100.104414.

[153] K. Ishii, I. Jarrige, M. Yoshida, K. Ikeuchi, J. Mizuki, K. Ohashi, T. Takayama, J. Matsuno, and H. Takagi. Momentum-resolved electronic excitations in the Mott insulator Sr_2IrO_4 studied by resonant inelastic X-ray scattering. *Physical Review B*, 83(11):115121, 2011. doi: 10.1103/PhysRevB.83.115121.

[154] V. M. Katukuri, H. Stoll, J. van den Brink, and L. Hozoi. Ab initio determination of excitation energies and magnetic couplings in correlated quasi-two-dimensional

iridates. *Physical Review B*, 85(22):220402, 2012. doi: 10.1103/PhysRevB.85.220402.

[155] J. Jeanneau, P. Toulemonde, G. Remenyi, A. Sulpice, C. Colin, V. Nassif, E. Suard, E. Salas Colera, G. R. Castro, F. Gay, C. Urdaniz, R. Weht, C. Fevrier, A. Ralko, C. Lacroix, A. A. Aligia, and M. Núñez-Regueiro. Singlet Orbital Ordering in Bilayer $Sr_3Cr_2O_7$. *Physical Review Letters*, 118(20):207207, 2017. doi: 10.1103/PhysRevLett.118.207207.

[156] D. Reznik, P. Bourges, H. F. Fong, L. P. Regnault, J. Bossy, C. Vettier, D. L. Milius, I. A. Aksay, and B. Keimer. Direct observation of optical magnons in $YBa_2Cu_3O_{6.2}$. *Physical Review B*, 53(22):R14741, 1996. doi: 10.1103/PhysRevB.53.R14741.

[157] T. G. Perring, D. T. Adroja, G. Chaboussant, G. Aeppli, T. Kimura, and Y. Tokura. Spectacular doping dependence of interlayer exchange and other results on spin waves in bilayer manganites. *Physical Review Letters*, 87(21):217201, 2001. doi: 10.1103/PhysRevLett.87.217201.

[158] B. Yuan, J. P. Clancy, A. M. Cook, C. M. Thompson, J. Greedan, G. Cao, B. C. Jeon, T. W. Noh, M. H. Upton, D. Casa, T. Gog, A. Paramekanti, and Y. J. Kim. Determination of Hund's coupling in $5d$ oxides using resonant inelastic X-ray scattering. *Physical Review B*, 95(23):235114, 2017. doi: 10.1103/PhysRevB.95.235114.

[159] Z. Porter, E. Zoghlin, S. Britner, S. Husremovic, J. P. Ruff, Y. Choi, D. Haskel, G. Laurita, and S. D. Wilson. Evolution of structure and magnetism across the metal-insulator transition in the pyrochlore iridate $(Nd_{1-x}Ca_x)_2Ir_2O_7$. *Physical Review B*, 100(5):054409, 2019. doi: 10.1103/PhysRevB.100.054409.

[160] T. Fujita, Y. Kozuka, M. Uchida, A. Tsukazaki, T.-h. Arima, and M. Kawasaki. Odd-parity magnetoresistance in pyrochlore iridate thin films with broken time-reversal symmetry. *Scientific Reports*, 5:9711, 2015. doi: 10.1038/srep09711.

[161] A. B. Sushkov, J. B. Hofmann, G. S. Jenkins, J. Ishikawa, S. Nakatsuji, S. Das Sarma, and H. D. Drew. Optical evidence for a Weyl semimetal state in pyrochlore $Eu_2Ir_2O_7$. *Physical Review B*, 92(24):241108, 2015. doi: 10.1103/PhysRevB.92.241108.

[162] K. Ueda, J. Fujioka, and Y. Tokura. Variation of optical conductivity spectra in the course of bandwidth-controlled metal-insulator transitions in pyrochlore iridates. *Physical Review B*, 93(24):245120, 2016. doi: 10.1103/PhysRevB.93.245120.

[163] K. Ueda, R. Kaneko, H. Ishizuka, J. Fujioka, N. Nagaosa, and Y. Tokura. Spontaneous Hall effect in the Weyl semimetal candidate of all-in all-out pyrochlore iridate. *Nature Communications*, 9(1):3032, 2018. doi: 10.1038/s41467-018-05530-9.

[164] X. Wan, A. M. Turner, A. Vishwanath, and S. Y. Savrasov. Topological semimetal and Fermi-arc surface states in the electronic structure of pyrochlore iridates. *Physical Review B*, 83(20):205101, 2011. doi: 10.1103/PhysRevB.83.205101.

[165] W. Witczak-Krempa and Y. B. Kim. Topological and magnetic phases of interacting electrons in the pyrochlore iridates. *Physical Review B*, 85(4):45124, 2012. doi: 10.1103/PhysRevB.85.045124.

[166] L. Savary and L. Balents. Coulombic quantum liquids in spin half pyrochlores. *Physical Review Letters*, 108(3):037202, 2012. doi: 10.1103/PhysRevLett.108.037202.

[167] I. Kimchi and A. Vishwanath. Kitaev-Heisenberg models for iridates on the triangular, hyperkagome, kagome, fcc, and pyrochlore lattices. *Physical Review B*, 89 (1):14414, 2014. doi: 10.1103/PhysRevB.89.014414.

[168] L. Savary, E. G. Moon, and L. Balents. New type of quantum criticality in the pyrochlore iridates. *Physical Review X*, 4(4):041027, 2014. doi: 10.1103/PhysRevX.4.041027.

[169] J. S. Gardner, M. J. Gingras, and J. E. Greedan. Magnetic pyrochlore oxides. *Reviews of Modern Physics*, 82(1):53–107, 2010. doi: 10.1103/RevModPhys.82.53.

[170] K. Matsuhira, M. Wakeshima, R. Nakanishi, T. Yamada, A. Nakamura, W. Kawano, S. Takagi, and Y. Hinatsu. Metal-insulator transition in pyrochlore iridates $Ln_2Ir_2O_7$ (Ln = Nd, Sm, and Eu). *Journal of the Physical Society of Japan*, 76(4):43706, 2007. doi: 10.1143/JPSJ.76.043706.

[171] K. Matsuhira, M. Wakeshima, Y. Hinatsu, and S. Takagi. Metal-insulator transitions in pyrochlore oxides $Ln_2Ir_2O_7$. *Journal of the Physical Society of Japan*, 80 (9):094701, 2011. doi: 10.1143/JPSJ.80.094701.

[172] K. Ueda, J. Fujioka, C. Terakura, and Y. Tokura. Pressure and magnetic-field effects on metal-insulator transitions of bulk and domain-wall states in pyrochlore iridates. *Physical Review B*, 92(12):1–5, 2015. doi: 10.1103/PhysRevB.92.121110.

[173] K. Ueda, J. Fujioka, C. Terakura, and Y. Tokura. Pressure and magnetic field effects on metal-insulator transitions of bulk and domain wall states in pyrochlore iridates. *Physical Review B*, 92(12):121110, 2015. doi: 10.1103/PhysRevB.92.121110.

[174] Y. Machida, S. Nakatsuji, S. Onoda, T. Tayama, and T. Sakakibara. Time-reversal symmetry breaking and spontaneous Hall effect without magnetic dipole order. *Nature*, 463(7278):210, 2010. doi: 10.1038/nature08680.

[175] M. Nakayama, T. Kondo, Z. Tian, J. J. Ishikawa, M. Halim, C. Bareille, W. Malaeb, K. Kuroda, T. Tomita, S. Ideta, K. Tanaka, M. Matsunami, S. Kimura, N. Inami, K. Ono, H. Kumigashira, L. Balents, S. Nakatsuji, and S. Shin. Slater to Mott Crossover in the Metal to Insulator Transition of $Nd_2Ir_2O_7$. *Physical Review Letters*, 117(5):056403, 2016. doi: 10.1103/PhysRevLett.117.056403.

[176] K. Tomiyasu, K. Matsuhira, K. Iwasa, M. Watahiki, S. Takagi, M. Wakeshima, Y. Hinatsu, M. Yokoyama, K. Ohoyama, and K. Yamada. Emergence of magnetic long-range order in frustrated pyrochlore $Nd_2Ir_2O_7$ with metal-insulator transition. *Journal of the Physical Society of Japan*, 81(3):034709, 2012. doi: 10.1143/JPSJ.81.034709.

[177] R. Kaneko, M.-T. Huebsch, S. Sakai, R. Arita, H. Shinaoka, K. Ueda, Y. Tokura, and J. Fujioka. Enhanced thermopower in the correlated semimetallic phase of hole-doped pyrochlore iridates. *Physical Review B*, 99(16):161104, 2019. doi: 10.1103/PhysRevB.99.161104.

[178] E. Zoghlin, Z. Porter, S. Britner, S. Husremovic, Y. Choi, D. Haskel, G. Laurita, and S. D. Wilson. Mapping the structural, magnetic and electronic behavior of $(Eu_{1-x}Ca_x)_2Ir_2O_7$ across a metal-insulator transition. *Journal of Physics: Condensed Matter*, 33(5):055601, 2020. doi: 10.1088/1361-648X/abbf2b.

[179] W. Zhu, M. Wang, B. Seradjeh, F. Yang, and S. Zhang. Enhanced weak ferromagnetism and conductivity in hole-doped pyrochlore iridate $Y_2Ir_2O_7$. *Physical Review B*, 90(5):054419, 2014. doi: 10.1103/PhysRevB.90.054419.

[180] A. Banerjee, J. Sannigrahi, S. Giri, and S. Majumdar. Observation of non-Fermi liquid behavior in hole-doped $Eu_2Ir_2O_7$. *Physical Review B*, 96(22):224426, 2017. doi: 10.1103/PhysRevB.96.224426.

[181] P. Telang, K. Mishra, A. K. Sood, and S. Singh. Dilute stuffing in the pyrochlore iridate $Eu_2Ir_2O_7$. *Physical Review B*, 97:235118, 2018. doi: 10.1103/PhysRevB.97.235118.

[182] J. N. Millican, R. T. Macaluso, S. Nakatsuji, Y. Machida, Y. Maeno, and J. Y. Chan. Crystal growth and structure of $R_2Ir_2O_7$ (R= Pr, Eu) using molten KF. *Materials Research Bulletin*, 42(5):928–934, 2007. doi: 10.1016/j.materresbull.2006.08.011.

[183] A. Hammersley, S. Svensson, M. Hanfland, A. Fitch, and D. Hausermann. Two-dimensional detector software: from real detector to idealised image or two-theta scan. *International Journal of High Pressure Research*, 14(4-6):235–248, 1996. doi: 10.1080/08957959608201408.

[184] X. Qiu, J. W. Thompson, and S. J. Billinge. PDFgetX2: a GUI-driven program to obtain the pair distribution function from X-ray powder diffraction data. *Journal of Applied Crystallography*, 37(4):678–678, 2004. doi: 10.1107/S0021889804011744.

[185] C. Farrow, P. Juhas, J. Liu, D. Bryndin, E. Božin, J. Bloch, T. Proffen, and S. Billinge. PDFfit2 and PDFgui: computer programs for studying nanostructure in crystals. *Journal of Physics: Condensed Matter*, 19(33):335219, 2007. doi: 10.1088/0953-8984/19/33/335219.

[186] H. Takatsu, K. Watanabe, K. Goto, and H. Kadowaki. Comparative study of low-temperature X-ray diffraction experiments on $R_2Ir_2O_7$ (R= Nd, Eu, and Pr). *Physical Review B*, 90(23):235110, 2014. doi: 10.1103/PhysRevB.90.235110.

[187] S. M. Disseler, C. Dhital, T. C. Hogan, A. Amato, S. R. Giblin, C. De La Cruz, A. Daoud-Aladine, S. D. Wilson, and M. J. Graf. Magnetic order and the electronic ground state in the pyrochlore iridate $Nd_2Ir_2O_7$. *Physical Review B*, 85(17):174441, 2012. doi: 10.1103/PhysRevB.85.174441.

[188] H. Guo, K. Matsuhira, I. Kawasaki, M. Wakeshima, Y. Hinatsu, I. Watanabe, and Z.-A. Xu. Magnetic order in the pyrochlore iridate $Nd_2Ir_2O_7$ probed by muon spin relaxation. *Physical Review B*, 88(6):060411, 2013. doi: 10.1103/PhysRevB.88.060411.

[189] D. Haskel, Y. Tseng, J. Lang, and S. Sinogeikin. Instrument for X-ray magnetic circular dichroism measurements at high pressures. *Review of Scientific Instruments*, 78(8):083904, 2007. doi: 10.1063/1.2773800.

[190] J. Clancy, N. Chen, C. Kim, W. Chen, K. Plumb, B. Jeon, T. Noh, and Y.-J. Kim. Spin-orbit coupling in iridium-based $5d$ compounds probed by X-ray absorption spectroscopy. *Physical Review B*, 86(19):195131, 2012. doi: 10.1103/PhysRevB.86.195131.

[191] M. A. Laguna-Marco, D. Haskel, N. Souza-Neto, J. Lang, V. Krishnamurthy, S. Chikara, G. Cao, and M. van Veenendaal. Orbital magnetism and spin-orbit effects in the electronic structure of $BaIrO_3$. *Physical Review Letters*, 105(21):216407, 2010. doi: 10.1103/PhysRevLett.105.216407.

[192] B. Thole, P. Carra, F. Sette, and G. van der Laan. X-ray circular dichroism as a probe of orbital magnetization. *Physical Review Letters*, 68(12):1943, 1992. doi: 10.1103/PhysRevLett.68.1943.

[193] B. Ravel and M. Newville. ATHENA, ARTEMIS, HEPHAESTUS: data analysis for X-ray absorption spectroscopy using IFEFFIT. *Journal of Synchrotron Radiation*, 12(4):537–541, 2005. doi: 10.1107/S0909049505012719.

[194] Z. Tian, Y. Kohama, T. Tomita, H. Ishizuka, T. H. Hsieh, J. J. Ishikawa, K. Kindo, L. Balents, and S. Nakatsuji. Field-induced quantum metal-insulator transition in the pyrochlore iridate $Nd_2Ir_2O_7$. *Nature Physics*, 12(2):134, 2016. doi: 10.1038/nphys3567.

[195] K. Ueda, J. Fujioka, B. J. Yang, J. Shiogai, A. Tsukazaki, S. Nakamura, S. Awaji, N. Nagaosa, and Y. Tokura. Magnetic Field-Induced Insulator-Semimetal Transition in a Pyrochlore $Nd_2Ir_2O_7$. *Physical Review Letters*, 115(5):056402, 2015. doi: 10.1103/PhysRevLett.115.056402.

[196] E. Y. Ma, Y.-T. Cui, K. Ueda, S. Tang, K. Chen, N. Tamura, P. M. Wu, J. Fujioka, Y. Tokura, and Z.-X. Shen. Mobile metallic domain walls in an all-in-all-out magnetic insulator. *Science*, 350(6260):538–541, 2015. doi: 10.1126/science.aac8289.

[197] I. Kapon, C. W. Rischau, B. Michon, K. Wang, B. Xu, Q. Yang, S. Nakatsuji, and D. van der Marel. Magnetic field tuning of valley population in the Weyl phase of $Nd_2Ir_2O_7$. *Physical Review Research*, 4(2):023056, 2022. doi: 10.1103/PhysRevResearch.4.023056.

[198] S. H. Chun, B. Yuan, D. Casa, J. Kim, C.-Y. Kim, Z. Tian, Y. Qiu, S. Nakatsuji, and Y.-J. Kim. Evolution of Magnetic Excitations Across the Metal-Insulator Transition in a Pyrochlore Iridate $Eu_2Ir_2O_7$. *Physical Review Letters*, 120:177203, 2018. doi: 10.1103/PhysRevLett.120.177203.